2008

Numerical investigation of roughness effects in aircraft icing calculations

Brian Daniel Matheis
Iowa State University

Numerical investigation of roughness effects in aircraft icing calculations

by

Brian Daniel Matheis

A dissertation submitted to the graduate faculty

in partial fulfillment of the requirements for the degree of

DOCTOR OF PHILOSOPHY

Major: Aerospace Engineering

Program of Study Committee:
Alric Rothmayer, Major Professor
Fred L. Haan Jr.
Tom I.-P. Shih
Richard Pletcher
Eugene S. Takle

Iowa State University

Ames, Iowa

2008

A conversation with my dad, circa 1994:

So Brian, what are you going to study when you go to college this year?
I don't know.
Well, you're pretty good at math, how about engineering?
Ok.
What type of engineering would you like to study?
Hmm.
Well, you really like airplanes, how about aerospace engineering?
That sounds good, think I can finish that in four years?

In memory of my dad, Rick Matheis.

TABLE OF CONTENTS

ACKNOWLEDGMENTS

In an effort such as this there are always more people to thank than you can remember. I don't think I would have made it to this point without the support of my wife Jill. She continually encouraged me and showed a great deal of understanding when things didn't go according to plan. In addition, I want to thank Erik and Ella for being willing to give up a little play time so that dad could have time to "finish school". In addition I want to thank my family, my mom, brothers and sisters for their belief in me and their encouragement to keep moving forward.

There is little doubt that I could not have accomplished this without the advise and guidance of my advisor, Dr. Alric Rothmayer. Indeed I would likely not have considered a graduate degree without his encouragement. I appreciate the honest and helpful critique of all of my research and papers and making sure I was headed down the correct path. I also appreciate his willingness to take several trips to Minnesota to review the dissertation with me.

I would also like to thank Dr. Paul Tsao and Dr. Wade Huebsch for their help and assistance during many phases of this study when things were stuck. Their help, whether providing advise or access to computational resources is very much appreciated.

Finally, I would like to thank Tom Bond and Dr. Mark Potapczuk of the NASA Glenn Research Center Icing Branch for financial support of this research. This work was partly funded by the Graduate Student Researchers Program (GSRP) under contract NGT3-52380.

ABSTRACT

Icing codes are playing a role of increasing significance in the design and certification of ice protected aircraft surfaces. However, in the interest of computational efficiency certain small scale physics of the icing problem are grossly approximated by the codes. One such small scale phenomena is the effect of ice roughness on the development of the surface water film and on the convective heat transfer. This study uses computational methods to study the potential effect of ice roughness on both of these small scale phenomena.

First, a two-dimensional condensed layer code is used to examine the effect of roughness on surface water development. It is found that the Couette approximation within the film breaks down as the wall shear goes to zero, depending on the film thickness. Roughness elements with initial flow separation in the air induce flow separation in the water layer at steady state, causing a trapping of the film. The amount of trapping for different roughness configurations is examined.

Second, a three-dimensional incompressible Navier-Stokes code is developed to examine large scale ice roughness on the leading edge. The effect on the convective heat transfer and potential effect on the surface water dynamics is examined for a number of distributed roughness parameters including Reynolds number, roughness height, streamwise extent, roughness spacing and roughness shape. In most cases the roughness field increases the net average convective heat transfer on the leading edge while narrowing surface shear lines, indicating a choking of the surface water flow. Both effects show significant variation on the scale of the ice roughness. Both the change in heat transfer as well as the potential change in surface water dynamics are presented in terms of the development of singularities

in the surface shear pattern. Of particular interest is the effect of the smooth zone upstream of the roughness which shows both a relatively large increase in convective heat transfer as well as excessive choking of the surface shear lines at the upstream end of the roughness field. A summary of the heat transfer results is presented for both the averaged heat transfer as well as the maximum heat transfer over each roughness element, indicating that the roughness Reynolds number is the primary parameter which characterizes the behavior of the roughness for the problem of interest.

CHAPTER 1. INTRODUCTION

Aircraft Icing and Icing Codes

Any vehicle which flies through the atmosphere can be subject to icing of the vehicle's structure during flight. In-flight icing occurs when small liquid supercooled water droplets are suspended in the atmosphere. These droplets constitute what is known as an icing cloud. As a flight vehicle or aircraft flies through the icing cloud, the small droplets impact on various critical surfaces. If the temperature of the air is low enough and the surface is unprotected/unheated, the droplets may freeze immediately upon impact forming what is known as rime ice. At warmer temperatures the droplets may hit the surface but remain in liquid form, at least for a time. The liquid water may freeze soon after impact, or run along the surface for a certain distance before freezing and forming what is known as glaze ice.

When significant ice forms on a critical surface the result is typically a loss of aircraft performance, i.e. decreased lift, increased drag, an alteration in the aircraft's handling characteristics or a combination of all three (see, for example, [1],[2], [3]). Ice which forms on a surface and then sheds due to aerodynamic forces has the potential to be ingested by an engine and cause damage or loss of engine performance (see, for example, [4]). In addition, any other flight critical parts which are on the exterior of an aircraft are at potential risk for damage or decreased performance due to icing. As a result, the Federal Aviation Administration's (FAA) Federal Air Regulations (FAR) Part 25.1419[5] specify the requirements for certification of a commercial transport category airplane with respect to aircraft icing and ice protection. The requirements state that it is the responsibility of the

airframe manufacturer to verify that the airplane can safely operate within the icing envelope defined in FAR Part 25[5]. In particular, FAR Part 25.1419[5] requires 1) an analysis be performed to show that the ice protection system is adequate and 2) icing or dry air flight or wind tunnel tests to verify the analysis and check for anomalies. The purpose of the analysis is to determine if ice will accrete with the ice protection system operative. Items of interest may include size and shape of ice in the protected area or ice further aft on the surface after liquid water has run back. In addition, the analysis may need to assess the size and shape of ice that would accrete if the ice protection system were inoperative due to a system malfunction.

One of the primary methods for carrying out the ice protection system analysis is the use of ice accretion codes. Many icing codes have been developed and used in the aviation industry throughout the world, however the main code used in the U.S. is known as LEWICE[6] and was developed by the NASA Glenn (formerly Lewis) Research Center Icing Branch. As with most icing codes, LEWICE is based on the Messinger[7] control volume icing model which sets up mass and energy balances on control volumes which are defined along the surface of interest. A significant advantage of using this model is that it allows very rapid icing analyses to be performed on modern desktop PC's. This is important because the code can be used to assess performance in a large combination of icing conditions, flight conditions and aircraft configurations. LEWICE and other icing codes based on the Messinger[7] model have proved to be very successful in numerically reproducing ice shapes generated in icing tunnels and flight tests for rime ice and a number of glaze ice conditions. However, like most other icing codes, the accuracy of LEWICE in the cases of warmer temperatures and higher liquid water content (LWC) has not been as

successful. This is likely due to small scale effects of the icing process which must be modeled in the control volume approach.

The general time stepping solution procedure of the LEWICE code is shown in Figure 1. The simulation starts with the flow solution over the clean aircraft or component. This flow solution is then used as an input to a water droplet trajectory calculation which determines where droplets of various sizes impact the surface. The next step is a heat transfer calculation in which the contribution of the various heat transfer modes are determined, including convective heat transfer, cooling due to the impacting droplets, various latent heats and others. The heat transfer calculation is combined with a mass balance in the next step to determine the amount of ice that accumulates in a given time step in each control volume. This "new" ice is added to the clean airfoil or existing ice shape from the previous time step and a modified geometry is created. The process is then repeated until the total icing time has been reached. There are various small scale processes contained in the blocks of Figure 1 which are modeled in a simple manner in the icing code in order to maintain computational efficiency. These effects become more significant at warmer temperatures and higher liquid water contents (LWC) and are not completely understood. As a result LEWICE, along with some other icing codes, is not as accurate in predicting ice shapes for glaze ice conditions. In 1999, Potapczuk[8] of NASA Glenn, in an overview of the status of the LEWICE code, listed the advances in surface modeling which are required for better prediction of glaze ice accretion. These include:

1. Dynamics of unfrozen water on a rough surface
2. Impact of small scale roughness on convective heat transfer augmentation
3. Effect of droplet splashing on surface water transport

Two of the three advances mentioned by Potapczuk[8] are directly linked to a better

understanding of the effects of surface roughness. This is the focus of the current study.

Ice Roughness

Extensive research has been conducted to examine the effect of roughness on the convective heat transfer. For example Schlichting[9] gives a detailed method for determining the augmentation to the convective heat transfer for sand grain roughness. However the majority of this research has focused on the scenario of roughness which lies on a flat plate and well within the thickness of an approaching turbulent boundary layer. As the next few sub-sections highlight, these conditions are not applicable to ice roughness.

Experimental Evidence

There are currently no broadly accepted mechanisms for the formation of ice roughness. Proposed theories include an instability between the air/water/ice interfaces or a reaction of the water film to the air boundary-layer transitioning from laminar to turbulent flow. Tsao & Rothmayer[10] examined the formation of ice roughness in terms of a stability problem in the context of the triple-deck boundary-layer structure. The study showed that in the case of wall cooling, which is the typical case for ice formation, instabilities occur which permit the formation of initially shallow ice roughness elements on the surface. A subsequent study by Tsao & Rothmayer[11] showed favorable comparisons of the predicted roughness element diameters with experimental observations of Anderson *et al*.[12]. Additional studies which have focused on ice layer instability as a mechanism for large ice roughness formation near stagnation lines include Rothmayer[13] and Shourya & Rothmayer[14].

As a result of the lack of understanding of the ice roughness formation mechanism, most icing codes do not include a model for roughness formation even though capturing the effects of the roughness is essential for correctly predicting glaze ice shapes. The alternative,

as is done with LEWICE, is to calibrate the code against known experimental shapes (see Ruff and Berkowitz[6]). That is, for a given icing condition, the roughness parameter within the LEWICE code is varied until the computational ice shape agrees with the experimental one. The result is a correlation of roughness characteristics (height) as a function of the icing condition. However, this is applicable only to airfoil leading edges and may not allow an accurate glaze ice prediction on other shapes without a priori knowledge of the roughness characteristics. Therefore, a better understanding of the formation of ice roughness is required.

The main evidence for the character of ice roughness has come from icing experiments. Shin[15] and Anderson *et al*.[12] have both characterized ice roughness in glaze icing conditions based on icing tests conducted in NASA's Icing Research Tunnel (IRT). Figure 2 from Anderson *et al*.[12] shows a typical example of ice roughness near the leading edge. The stagnation line is shown as the line in the middle of the figure. On either side of the stagnation line, extending approximately 5-6mm downstream, there is a region of smooth, clear ice. This is simply known as the smooth zone and is typical of glaze ice over two-dimensional airfoils. The size of this zone is dependent on the icing/flight condition and may not be present at all for swept wing icing. At the edge of the smooth zone the appearance of ice roughness is sudden. Shin[15] characterized ice roughness elements such as these in terms of the size, shape and location of the roughness elements relative to the leading edge. Subsequently, Kerho[16] used the data obtained by Shin[15] and a boundary-layer code to determine flow conditions at the location of the roughness without the roughness elements present. The results are shown in Table 1.1 which is taken from Winkler[17].

Re_c	k/δ	Re_k
$2.76x10^6$	2.7 - 4.8	1500 - 3300
$3.68x10^6$	3.1 - 5.5	2000 - 4400
$4.60x10^6$	3.5 - 6.1	2500 - 5500

Table 1.1: Typical conditions for glaze ice roughness. From Winkler[17]

The left column gives the three chord Reynolds numbers examined by Shin[15] and the other two columns give ranges of 1) ratio of the roughness height, k, to local boundary-layer thickness, δ and 2) the roughness Reynolds number, Re_k. The roughness Reynolds number is defined as

$$Re_k = \frac{u_k k}{\nu} \quad , \tag{1.1}$$

where u_k is the local streamwise velocity at a height k from the surface without the roughness present. The two parameters k/δ and Re_k are thought to be the most important parameters in terms of characterizing the flow over roughness, and the majority of roughness research uses one or both of these parameters when analyzing results. Because most of this research focuses on roughness buried deep within the boundary-layer, the parameter of choice has typically been Re_k. However, as Table 1.1 shows, ice roughness on an airfoil leading edge is typically three to six times larger than the local boundary-layer thickness. As a result, both of these parameters may play important roles in characterizing ice roughness effects for parameters such as the convective heat transfer.

Characteristics of Isolated Roughness

Although the practical application of isolated roughness is limited, it is typically studied as a building block to the understanding of distributed roughness fields. As mentioned previously, a large body of work exists for the case of roughness which is

contained well within an approaching turbulent boundary-layer. Instead of focusing on this extensive list of literature, the main goal of this and the next section is to examine what has been learned from research concerned with roughness which has a height equal to or greater than the thickness of an approaching laminar boundary-layer.

Any roughness element with an O(1) aspect ratio will typically lead to premature transition, compared to the roughness not being present. At extremely low Reynolds numbers this may not be the case and even at moderately low Reynolds numbers the roughness will only begin the amplification of flow instabilities and transition may still occur far downstream from the roughness. As the flow velocity is increased, for example increasing Re_k, this transition point will begin to move upstream. At some critical value, $Re_{k,crit}$, the transition point moves rapidly upstream to approach the roughness, with only small changes in the value of Re_k. Extensive studies performed for roughness on a flat plate indicate that the value of $Re_{k,crit}$ is 600, though it is not clear if this is valid for larger roughness elements. When an isolated roughness element is placed on an airfoil leading edge, Bragg *et al.*[18] has shown that this value could be as high as 1500, owing to the favorable pressure gradient. Below $Re_{k,crit}$ the flow in the vicinity of the roughness can be considered to be laminar. Therefore the laminar flow regime is of significant importance for flow over ice roughness.

Mason & Morton[19] have conducted Navier-Stokes simulations for flow over O(1) aspect ratio roughness in addition to water channel tests with dye visualization. While the presented results are nearly all qualitative, the study serves to highlight the flow structures that are generated by this type of roughness in the laminar flow regime. The flow structures

are significant because they determine the potential effect of the roughness on heat transfer and surface water flow. For example, flow structures which tend to move the outer flow closer to the surface are likely to lead to increased heat transfer. Similarly, flow structures which have an influence on the surface shear pattern may have an effect on the distribution of the surface water film.

Figure 3 and Figure 4 show various flow structures typical of laminar flow over an isolated roughness element based on a computation from the current study. The color contours on the surface of the roughness in these figures show the convective heat transfer coefficient. In this case the outer flow is colder than the temperature of the wall and blue contours indicate regions of increased cooling while red contours indicate regions of decreased cooling, but still cooling nonetheless. The baseline convective heat transfer that would exist without the presence of the roughness is evident from examining the surface upstream of the roughness element. The lines shown on the surface are the surface shear lines (or limiting streamlines) which are constructed from the three-dimensional skin friction field on the surface. The color contours on the symmetry plane are the streamwise velocity over the roughness element, while the lines on the symmetry plane are the streamlines which are determined from the flow velocity components. The general features of laminar flow over a roughness element can be understood by examining Figure 3 and Figure 4.

The surface shear pattern for the flow over the roughness element exhibits a number of shear singularities which were first studied by Lighthill[20]. The study of these singularities is significant because it can itself reveal a good deal about the flow interior and general properties of the flow. Nodal points are singularities into which all nearby shear lines converge. Focal points are a type of nodal point, however in this case the shear lines

converge by spiraling around the singularity. Nodal points and focal points can either be points of separation or points of attachment depending on whether the shear lines are moving into or away from the singularity, respectively. Finally, saddle points are points through which only two shear lines pass. All three of these types of singular points are evident in Figure 3 and Figure 4. Lighthill[20] developed a rule which governs the number of singular points which can occur on a surface. In particular, the number of saddle points on the surface must always be equal to the number of nodal and focal points on the surface. Looking at Figure 3a there are three nodal points and two focal points (the symmetric focal point is not shown) for a total of five. There are also five saddle points, again with symmetric saddle points not shown. Therefore Lighthill's[20] rule is satisfied for the roughness element in Figure 3.

Nodal or focal points of attachment are locations where the outer fluid is impinging on the surface (i.e. stagnation points). If the outer flow is colder than the wall, this results in an increased cooling of the surface at these types of singularities. This is in fact the case for the three nodal points on the roughness center-line in Figure 3a (although the nodal point on the downstream top part of the roughness is a nodal point of separation). Nodal or focal points of separation are locations where the fluid is being lifted away from the wall. This tends to move the outer fluid further from the wall, thereby decreasing the heat transfer at the singularity. This is the case for the focal point in Figure 3a which is a focal point of separation and shows a decreased cooling of the wall relative to the approaching flow.

Saddle points do not have as direct an effect on the convective heat transfer. The significance of saddle points is that the shear lines which emanate from them act as dividing lines on the surface. These are often separation lines in three-dimensional separated flows.

Chapter 2 of this study discusses the role that the surface shear plays in being the predominant driver of unfrozen surface water. As a result, the dividing of the surface shear lines due to the presence of saddle points is significant because it acts to determine where the surface water generally can or cannot go. For example, for the shear lines which are approaching the roughness element from upstream, none of them will actually reach the roughness element due to the saddle point which is just upstream of the roughness. Half of the shear lines move around the roughness element and toward the focal point where they terminate after spiraling in. This is a location at which unfrozen surface water can begin to pool since the shear lines are leaving the surface at this location. The other half move around the roughness element and simply continue downstream.

Like the surface shear pattern, the streamlines in the symmetry plane also contain singularities. Each nodal point in the surface shear which lies on the symmetry plane shows up as a saddle point in the streamline pattern on the symmetry plane. Similar to the saddle points on the surface, these saddle points also act to split the flow. Consider, for example, the saddle point in the symmetry plane on the upstream face of the roughness. There is a dividing streamline which originates at this saddle point and extends upstream. Any streamlines which originate below this dividing streamline will get caught up in the horse-shoe vortex structure which sets up at the base of the roughness. The horse-shoe vortex structure is evident in the spiraling streamlines at the upstream base of the roughness. This vortex structure wraps "legs" around the roughness element which extend downstream, typically causing downwash along the roughness center-line. The number of horse-shoe vortices in front of a roughness element can vary and typically increase with increasing Re_k. The behavior of streamlines which enter the horse-shoe vortex structure is shown in Figure

3b. The streamline which begins near the dividing streamline in the symmetry plane is brought down to the surface by the horse-shoe vortex. This streamline then follows the structure around the side of the roughness and gets caught up in the roughness wake. The horse-shoe vortex structure is primarily fed by the streamlines which originate near the dividing streamline in the symmetry plane. Other streamlines which originate further away from the symmetry plane are actually lifted away from the surface by the presence of the horse-shoe vortex. This tends to have an insulating effect on the surface, assuming that the freestream air is colder than the wall. As a result, the cooling at the base of the roughness is decreased, as indicated in Figure 3.

A second type of roughness induced vortex structure, first observed experimentally by Gregory & Walker[21], typically occurs at higher values of Re_k and/or for "sharper" roughness elements, such as that shown in Figure 3. Gregory & Walker[21] referred to these as chimney vortices as they initially appear just downstream of the roughness, on both sides of the center-line, rising vertically from the surface. These vortices are formed by shear layers separating from the sides of the roughness element and rolling up just downstream of the roughness. The on-wall signature of the chimney vortices are the focal points shown in Figure 3. Figure 4a shows a streamline which originates near the wall upstream of the roughness element and is captured by the chimney vortex in the roughness wake. The streamline is lifted from the surface in a swirling motion. As mentioned previously, this contributes to the decreased cooling on the surface at the focal point.

Finally, returning to the streamline pattern on the symmetry plane, streamlines which originate above the dividing streamline from the upstream saddle point will pass over the top of the roughness element. This is the case for the streamline shown in Figure 4b. As it

passes over the roughness, this streamline is very near the roughness surface and separates into the wake as part of the shear layer. Once in the wake the streamline becomes subject to the downward motion of the main wake vortex, then the upward motion of the chimney vortices, and so forth until it exits the wake entirely. Since the majority of the streamlines which enter the roughness wake come from near the roughness surface, the convective cooling in this region is decreased, as indicated in Figure 4.

The effect of isolated roughness elements in a flat plate laminar boundary-layer on the convective heat transfer was examined experimentally by Henry *et al.*[22]. Heat transfer data was obtained by infrared imaging of the surface to determine the mean surface temperature. For all roughness elements tested, a maximum heat transfer enhancement occurred about one-half roughness height upstream from the maximum height. Only the smallest roughness element examined in this study was below $Re_{k,crit}$. This case showed a factor of two relative increase in the heat transfer over the clean plate value, while downstream of the roughness the heat transfer quickly returned to the flat plate value. For the other roughness elements which were above $Re_{k,crit}$ the maximum relative heat transfer over the roughness element was as high as 8.5 while the relative heat transfer in the roughness wake was typically 50% of the maximum value. The results of Henry *et al.*[22] also indicated a significant k/δ effect. In particular, once the height of the roughness was equal to the height of the local boundary-layer or larger, the maximum heat transfer over the roughness element began to increase significantly. This was likely due to the top of the roughness element being exposed to the free-stream air.

Poinsatte *et al.*[23] examined distributed roughness elements on the leading edge of an airfoil, however the roughness spacing was quite large such that the roughness elements

essentially behaved as isolated roughness elements. The roughness element sizes and Reynolds numbers investigated were consistent with those listed in Table 1.1. Heat transfer data was obtained from heat flux gauges mounted in the surface of the airfoil. Roughness elements placed right at the stagnation point locally increased the heat transfer by about 10% but did not significantly alter downstream heat transfer values. Roughness elements placed further downstream had a significant effect in increasing the heat transfer on and immediately downstream of the roughness. However, for the lower Reynolds numbers tested the heat transfer returned to the value corresponding to the clean leading edge. Meanwhile, the heat transfer data for some of the higher Reynolds numbers tested indicated that the roughness may have initiated transition to turbulent flow.

Other than these two studies there is no other known data which examines the effect of heat transfer due to large isolated roughness in a laminar boundary-layer. Experimental studies, such as that by Acarlar & Smith[24] and Winkler[17] for isolated roughness on a flat plate well above $Re_{k,crit}$ have looked at the unsteady flow-field about isolated roughness. For the Winkler[17] study in particular, the purpose was to better understand the flow mechanisms on the scale of the roughness which lead to heat transfer augmentation. In this case vortex structures were identified both upstream and downstream of the roughness which could affect the convective heat transfer. However, there were no corresponding heat transfer measurements to confirm the resulting hypothesis.

There are no known studies which examine the effect of large isolated roughness elements on the development of surface water films.

Characteristics of Distributed Roughness

As multiple isolated roughness elements are moved closer together, the individual

vortex structures of the individual elements will begin to interact. In some cases this leads to mutual destruction of certain vortex structures while in other cases it leads to an increase in the intensity of a particular vortex structure. Detailed experimental studies of large distributed roughness have been conducted by Winkler[17] for a flat plate and Kerho[16] for an airfoil leading edge. The Kerho[16] study is particularly interesting in that it examined the method in which distributed roughness on an airfoil leading edge promotes transition. For the lowest chord Reynolds number tested, 750,000, all but the largest distributed roughness fields placed approximately three leading edge radii of curvature downstream maintained laminar flow. However, even for the higher Reynolds numbers up to 2.25 million, the roughness did not initiate an immediate transition to turbulence. Instead, the turbulence intensity values were seen to start small at the trailing edge of the roughness field and grow in a linear fashion moving downstream, not reaching fully turbulent levels until approximately 40% chord. Though turbulence intensity values were not obtained directly over/in the roughness field itself, trends from downstream of the roughness indicate that the levels within the field were low. As a result, two of Kerho's[16] conclusions regarding the implications for convective heat transfer were

> *"Large increases in local convective heat transfer required by the accretion process are not thought to be driven by boundary-layer transition or transitional flow"*

and

> *"It is speculated that the ice accretion process is governed by very local effects on the scale of the size of individual roughness elements"*

Lee[25] used the same experimental setup of Kerho[16] but added infrared imaging

of the surface in order to obtain mean surface temperatures and mean relative heat transfer coefficients. For the lowest Reynolds number cases investigated by Kerho[16] in which the flow remained laminar, the heat transfer was found to increase by 25-70% depending on the height of the roughness. For the higher Reynolds number cases the heat transfer was increased by up to 300%. In all cases the heat transfer increased with increasing streamwise distance immediately over the roughness field. At the downstream end of the roughness field the heat transfer rapidly decreased to a much lower level but this level was typically still significantly higher than the clean airfoil value. A significant question which is left unanswered by the Kerho[16] and Lee[25] studies is whether or not the laminar flow over a distributed roughness field can account for the large increases seen in the convective heat transfer immediately over the roughness field.

Henry *et al*.[22] also examined the effect of large distributed roughness on a flat plate on the convective heat transfer. However the flow approaching the roughness field was purposefully tripped to be turbulent and therefore does not have as direct an application to the case of leading edge roughness.

While the Kerho[16] and Lee[25] studies examined regularly spaced hemispherical roughness elements on an airfoil leading edge, other studies have examined the effect of actual ice roughness on leading edge heat transfer. Dukhan *et al.*[26] used castings of experimental ice shapes, both with and without the roughness intact, in order to look at the effect of real ice roughness. For the "smooth glaze" type roughness examined in that study which is most applicable to the current study, increases of relative heat transfer of 300-500%, depending on free-stream velocity, were observed. In most cases the heat transfer profiles were similar to the smooth model heat transfer over the upstream part of the roughness,

however moving downstream the heat transfer would either gradually or suddenly increase, possibly indicating a transition to turbulent flow. The start of this "transition" region for the smooth glaze roughness occurred at a local Reynolds number based on distance from the leading edge of approximately 60,000. Other roughness shapes examined by Dukhan *et al.*[26] which were more extreme in terms of the roughness height and shape produced even larger relative increases in the convective heat transfer. For the icing conditions investigated by Dukhan *et al.*[26], these more extreme shapes were associated with longer icing exposure time.

There is little experimental evidence concerning the effect of large distributed roughness on surface water dynamics. Detailed examinations of the surface physics during ice accretion have been performed by Olsen & Walker[27] and Hansman & Turnock[28]. The Hansman & Turnock[28] experiments with high resolution video of the ice surface showed that the previously mentioned smooth zone appeared to be uniformly wetted by liquid water. A number of theoretical studies have examined modeling the surface water dynamics in this smooth wall region. For example, Nelson *et al*.[29], Rothmayer & Tsao[30] and Timoshin[31] have all developed surface water models in the context of the icing problem. However once the rough zone was reached, the water tended to coalesce into stationary hemispherical beads and thus the surface was no longer uniformly wetted. In this case the previously mentioned studies may not be directly applicable. It was noted by Hansman & Turnock[28] that the forward part of this rough zone slowly migrated upstream as the icing exposure time continued. For some cases investigated, downstream of the rough zone there appeared water runback in the form of rivulets. Modeling of the rivulets for the icing problem has been addressed by a large number of studies, for example Al-Khalil *et*

al.[32],[33] and Wang & Rothmayer[34],[35].

Purpose of the Current Study

The purpose of the current study is to build on experimental studies which have been completed to date. This is done by examining local effects about the roughness elements, as suggested by Kerho[16], and how they affect the convective heat transfer. In addition, a qualitative assessment of the effect of roughness fields on surface shear patterns and surface water dynamics is also undertaken. In both cases it is hoped that understanding these basic issues will eventually lead to new models for icing codes which properly account for the small scale physics.

The method used in this study to achieve these goals is the numerical solution of the Navier-Stokes equations for flow over leading edge roughness, which can provide a complete flow map of the roughness field. There are many different possible parameters which collectively define a roughness field, such as roughness height, shape, spacing and extent. In addition, both Re_k and k/δ may have independent effects which alter the way in which the roughness affects the flow field. The numerical solution must therefore also be able to efficiently analyze the range of these parameters appropriate to aircraft icing and the flow regimes which they induce. In particular, since there are no turbulence models which are known to accurately model the transitional flow state caused by large leading edge roughness, the code should be capable of directly capturing the range of spatial scales via direct computation. In the present study, while the numerical solution is developed with this fact in mind, the focus is on the case of laminar/steady flow over leading edge roughness. There are two main reasons for this. First, computation of the laminar/steady flow is a logical first step in understanding the complete flow map for leading edge roughness.

Second, the laminar/steady flow case has some practical application to aircraft icing calculations. As indicated by the Kerho[16] experiments, even at chord Reynolds numbers up to 2.25 million, the turbulence intensities in the vicinity of the roughness field appear to be small enough that the roughness effects may be dominated by the basic steady flow over the roughness field. This is true for roughness on the nominal leading edge with its strong favorable pressure gradient. For ice shapes which have developed glaze ice horns such as that shown in Figure 5, this "approximation" is expected to be even more valid for roughness elements upstream of the horns which are essentially in a stagnation point/low speed flow. Therefore, most of the cases investigated in this study are purposefully chosen to be steady/laminar flow cases. This is assured by computing cases which have Reynolds numbers and/or roughness heights well below those cases which produced no transition in the Kerho[16] study. Each of these cases are investigated to assess their effect on the convective heat transfer as well as their potential effect on the surface water dynamics.

Layout of the Dissertation

The dissertation is laid out as follows. In Chapter 2, a two-dimensional asymptotic theory is exploited to gain insight into the effects of roughness on surface water dynamics. The results for this particular sub-class of roughness problems are analyzed and potential implications for large scale three-dimensional roughness are discussed.

In Chapter 3, the numerical method for solving the Navier-Stokes flow field over large distributed leading edge roughness is detailed. The code which has been developed based on this method is validated in Chapter 4 using three distinct/separate cases for flow over isolated roughness.

Chapter 5 goes through a systematic variation of the various parameters which define

a leading edge roughness field and the associated flow conditions in order to investigate the effect of each parameter. The two parameters of interest for this investigation are the augmentation to the convective heat transfer and the influence on the surface water dynamics. For this latter case the effects are analyzed in terms of the impact of the roughness on the surface shear patterns, based on the implications drawn from Chapter 2.

Finally, Chapter 6 summarizes the significant conclusions from this study and gives suggestions for future research.

CHAPTER 2. IMPACT OF SHALLOW TWO-DIMENSIONAL ROUGHNESS ON UNFROZEN SURFACE WATER DYNAMICS

In the context of the Messinger[7] model for aircraft ice accretion a simple water mass balance at the surface gives the following equation for the film thickness, *h*,

$$\rho_w \frac{\partial h}{\partial t} + \frac{\partial}{\partial s}\left[\dot{m}_R\right] = \dot{m}_w \quad , \tag{2.1}$$

where $\dot{m}_R$ is the mass flux of water on the surface due to runback along the surface and $\dot{m}_w$ is the mass flux of water to/from the surface due to droplet impingement, evaporation / condensation and freezing / melting. Clearly there is potential for surface roughness to impact $\dot{m}_w$ by affecting water freezing rates through modification of the surface heat transfer. This potential will be addressed in Chapter 5. In addition there is also significant potential for roughness to alter the runback mass flux of the water, $\dot{m}_R$. Typically, this effect of a roughness field on the surface water runback is not addressed in icing codes.

Figure 5a shows the aircraft icing problem on the scale of the airfoil leading edge including an assumed thin water film with mass flux $\dot{m}_R$. The most simplistic model for evaluating $\dot{m}_R$ in an icing code is to assume that any unfrozen water runs back to the next computational cell at the next time step. Slightly more sophisticated models assume a Couette flow within the film in order to analytically obtain the value of $\dot{m}_R$. A number of different types of flow solvers can be used to calculate the flow over the ice shape to determine the wall shear which would be used in a Couette film model. Figure 5b shows local surface effects which may impact $\dot{m}_R$ but are not accounted for in a purely Couette

flow film model. This schematic shows a water film being driven by an air viscous sub-layer. There are waves on the surface of the film and initial ice roughness under-lying the film. As the ice roughness grows, experimental evidence suggests that the roughness height will become significantly larger than the thickness of the water film. In this case, not only $\dot{m}_R$ may be affected but the general distribution of the water as well. That is, the film may break up or pool and stop flowing downstream altogether. The goal of this chapter is to examine how this larger small scale surface roughness alters the Couette film model. For simplicity and computational efficiency the roughness effects in this chapter are examined in terms of a condensed layer structure which has previously been used by Rothmayer & Tsao[30] and Matheis & Rothmayer[36] to examine other small scale effects of surface water films.

The Condensed Layer Approach

The condensed layer asymptotic structure is derived in Rothmayer & Tsao[30] for describing the interaction between an air boundary-layer and dynamic surface water. In particular, the theory describes the scales at which both air shear and air pressure gradients are of the same order in driving the water motion, termed Stage II, as well as the scales which describe air shear dominated water motion (Stage I) and air pressure gradient dominated water motion (Stage III). Here we will make no assumption about whether the water film is being more shear driven or pressure gradient driven and will therefore use the more generally applicable Stage II. Figure 5b shows the relevant spatial scales for the Stage II asymptotic structure relative to the various scales of the problem. Note that Re is the usual Reynolds number while σ is a non-dimensional surface tension given by

$$\sigma = \frac{\sigma^*}{V_\infty \mu_\infty} \quad , \tag{2.2}$$

where σ^* is the dimensional surface tension. As it turns out, the range of film thicknesses and values of surface tension which can be appropriately examined by the Stage II structure are in-between the Navier-Stokes and Triple-Deck scales and are applicable to the aircraft icing problem with initial ice roughness. The main restriction in this regard is that the roughness elements must be shallow with aspect ratios of approximately 0.1 for typical icing conditions. For example, if we consider a 100 knot flight condition for a one meter chord airfoil at 0°C, then using Figure 5b we get streamwise and vertical scales which are on the order of 0.4mm and 0.04mm, respectively. Increasing the airspeed to 200 knots changes these scales to approximately 0.2mm and 0.02mm, respectively. These streamwise scales are on the order of what has been observed for ice roughness from icing tunnel experiments. The vertical scales, while smaller than the typical observed ice roughness may still be representative of early roughness formation. In any case, it should be noted that typical film thickness for aircraft icing near the leading edge is only on the order of several microns. Therefore the Stage II structure admits realistic icing scenarios in which the ice roughness height is significantly larger than the film thickness. In terms of dimensional variables, the Stage II film thickness is given by

$$h = \sigma^{-1/7} Re^{5/7} L^{-1} h^* \quad . \tag{2.3}$$

When the scales for Stage II shown in Figure 5b are substituted into the Navier-Stokes equations and proper considerations are given for matching to the global air flow, the result is (in two-dimensions),

$$\begin{gathered} U_X + V_Y = 0 \\ R_B\left[U\,U_X + V\,U_Y\right] = -P_X + \mu_{air}\,U_{YY} \\ P_Y = 0 \quad , \end{gathered} \tag{2.4}$$

for the air viscous sub-layer. In (2.4) R_B is the non-dimensional air density at the air/water interface and μ_{air} is the non-dimensional air viscosity. A set of equations similar to (2.4) also exists in the general Stage II structure for the water layer. Boundary conditions include the no-slip condition at the wall for the water layer and an asymptote to the global air solution at large Y in the air viscous sub-layer. A shearing transformation is introduced into the governing equations to account for varying film thickness and under-lying ice roughness. These terms show up in the boundary condition at large Y. A full stress match at the air / water interface in Stage II results in

$$\mu_{water}\left[\frac{\partial U_w}{\partial Y}\left(X, F_{water}\right)\right]=\mu_{air}\left[\frac{\partial U}{\partial Y}\left(X, F_{water}\right)\right]$$
$$P_w\left(X, F_{water}\right)=P\left(X, F_{water}\right)-\frac{\partial^2 F_{water}}{\partial X^2} \quad , \tag{2.5}$$

where F_{water} is the time and space varying film height above the global ice surface. This parameter is found from a kinematic condition

$$V_w\left(X, F_{water}\right)=\frac{\partial F_{water}}{\partial T}+U_w\left(X, F_{water}\right)\frac{\partial F_{water}}{\partial X} \quad . \tag{2.6}$$

As is often done for thin water films being driven by an air flow, a lubrication approximation is made within the water film which results in all of the convective terms being neglected. This results in a Couette-Poeusille flow in the water layer which is being driven by the air via (2.5). The velocities in the water can then be written in terms of the air variables in (2.5). Substituting the resulting solution into (2.6) gives

$$\mu_{water}\frac{\partial F_{water}}{\partial T}+\frac{\partial}{\partial X}\left[\mu_{air}\tau_{wx}\frac{F^2}{2}-\left(\frac{\partial P}{\partial X}-\frac{\partial^3 F_{water}}{\partial X^3}\right)\frac{F^3}{3}\right]=0 \quad , \tag{2.7}$$

where

$$\tau_{wx} = \left(\frac{\partial U}{\partial Y} \right)_{air} \left(X , F_{water} \right) \tag{2.8}$$

and

$$F = F_{water} - F_{ice} \quad , \tag{2.9}$$

with F_{ice} defining the shape of the ice roughness under the water film.

(2.4) and (2.7) are the governing equations being solved in the current study to examine a thin water film being driven by an air layer over ice roughness. Because of the lubrication approximation, the air layer effectively sees the water layer as being stationary so that no-slip conditions in the air are sufficient at the air/water interface. The boundary condition in the air at large Y including a shearing transformation is

$$U = \lambda \left(Y + F_{water} - h_{II} \right) \quad \text{as} \quad Y \to \infty \quad , \tag{2.10}$$

where λ is the local wall shear from the global air flow solution over the global ice surface.

Numerical Implementation

A set of equations similar to that given here has been solved by Matheis & Rothmayer[36] to examine the effect that surface waves have on the water film to increase the mass flux within the film. That study initially looked at a primitive variable form of the equations for the numerical implementation, however the combination of the dynamic air/water interface, periodic boundary conditions and the continuity equation created numerical oscillations in the solution that could not be damped by the numerics. As a result, a streamfunction/vorticity method was used to solve the air layer. The same approach is being used in the current study. All terms in the equations are second order central differenced with the exception of the convective terms in the vorticity transport equation and the temporal term in (2.7). The convective terms in the vorticity transport equation are

second order upwind differenced while the temporal term in (2.7) is second order backward differenced. Grid stretching is applied in the vertical direction in order to adequately resolve critical regions of the flow and grid independence was periodically checked throughout the course of this study. The reader is referred to Matheis & Rothmayer[36] for full details of the numerics. In addition, the appendix lists the final equations being solved in this study.

Discussion of Thin Films Flowing Over Shallow Roughness

Before presenting the full numerical results for films flowing over ice roughness, the equations are examined in order to provide some insight into the impact of the ice roughness on very thin films. First, consider the water height to be some small perturbation from the ice roughness surface, that is

$$F_{water} = F_{ice} + h f \quad , \tag{2.11}$$

where h is the small uniform thickness in Stage II scales. Examining (2.7) in light of (2.11) the order of magnitude of the various terms are

$$\underset{O(h)}{\mu_{water}\frac{\partial F_{water}}{\partial T}} + \frac{\partial}{\partial X}\left[\underset{O(h^2)}{\mu_{air}\tau_{wx}\frac{F^2}{2}} - \left(\underset{O(h^3)}{\frac{\partial P}{\partial X}} - \underset{O(h^4)}{\frac{\partial^3 F_{water}}{\partial X^3}}\right)\frac{F^3}{3}\right] = 0 \quad . \tag{2.12}$$

As $h \to 0$ the first balance that is picked up is between the first and second terms in (2.12) when $T \sim h^{-1}$. The new form of (2.12) then becomes

$$\mu_{water}\frac{\partial f}{\partial T} + \frac{\partial}{\partial X}\left[\mu_{air}\tau_{wx}\frac{f^2}{2}\right] = 0 \quad . \tag{2.13}$$

Note that (2.13) is simply the unsteady Couette flow approximation within the film. That is, when the under-lying roughness is "shallow" the Couette flow model may still be valid. In the steady state limit, (2.13) can be solved directly for the film thickness, f. Figure 6 shows a comparison of the solution of the steady form of (2.13) with two full non-linear Stage II

calculations for two different values of h. Recall the example of a one meter chord airfoil in a 100 knot air flow. The vertical Stage II scale in this example is about 0.04mm or 40 microns. If we assume that typical film thicknesses are on the order of a few to several microns, then h values on the order of 0.1 are reasonable. Figure 6 shows that for this scenario the simple Couette model is as accurate as the full Stage II model which includes pressure and surface tension effects. For the particular example given in Figure 6, the roughness changes the film thickness by up to 30%, however the total mass flux of water remains constant.

The time scale for the film evolution in Stage II is given by

$$t \sim Re^{-3/7}\sigma^{2/7}M \quad , \tag{2.14}$$

where M is the water to air viscosity ratio. For the example that has been carried through this section the film development time scale is about 0.01 seconds for film thicknesses which are O(1) in Stage II scales. However, for the thin film example of h=0.1, the time scale to achieve the steady Couette flow is on the order of 0.1 seconds. Therefore as the film thickness becomes smaller the time scale increases to the point where the film may not reach steady-state before freeze out.

Returning to (2.12) it is conceivable that the air wall shear, τ_{wx}, may be small enough such that other terms in (2.12) must also be included in the thin film limit. Indeed, using τ_{wx} =0 in the Couette model would result in an infinite film thickness, which is not physically possible. It is expected that this situation would arise as the roughness height increases and the air flow over the roughness separates. For a single two-dimensional separation region this would result in two points on the surface at which the wall shear would

be zero. The question then becomes "at what point does the Couette model for film flow over a roughness element actually break down?". This question can be answered by examining an asymptotic structure for a roughness element which induces a minimum shear point on the downstream face of the roughness. This situation is shown schematically on the left side of Figure 7 which actually shows the wall shear going to zero (incipient separation) though this is not a requirement for the following discussion. In particular the goal is to examine the film response in the region around the minimum shear point and to find when the solution first departs from the Couette model. The key here is that away from this minimum shear point the film must return to a shear driven film. In other words, the Couette model must become valid far from the minimum shear point. The streamwise length scale is set to Δ, and the wall shear is expanded about the minimum shear point in a Taylor series. The result is that

$$\frac{\partial U}{\partial Y} \sim \Delta^2 \quad . \tag{2.15}$$

Maintaining proper balances in the air layer immediately adjacent to the film results in

$$Y \sim \Delta^2 \quad , \tag{2.16}$$

and matching to the Couette film at large X gives

$$F \sim h\Delta^{-1} \quad . \tag{2.17}$$

Substituting these scales into the Stage II kinematic condition, (2.12), results in the orders of magnitude for each term shown in (2.18),

$$\underset{h\Delta^{-1}T^{-1}}{\mu_{water}\frac{\partial F_{water}}{\partial T}} + \frac{\partial}{\partial X}\left[\underset{h^2\Delta^{-1}}{\mu_{air}\tau_{wx}\frac{F^2}{2}} - \underset{h^3\Delta^{-4}}{\frac{\partial P}{\partial X}\frac{F^3}{3}} + \underset{h^4\Delta^{-8}}{\frac{\partial^3 F}{\partial X^3}\frac{F^3}{3}} + \underset{h^3\Delta^{-4}}{\frac{\partial^3 F_{ice}}{\partial X^3}\frac{F^3}{3}}\right] = 0 \quad . \tag{2.18}$$

As is typical, some trial and error with the correct balancing is necessary and the result is that the air shear term must match the surface tension term (the circled terms in (2.18)). The result of this balance is that

$$\Delta \sim h^{2/7} \tag{2.19}$$

and the resulting scales in both the air and water film layers are shown in the right of Figure 7. Note that a Couette-Poiseuille flow governs the air layer adjacent to the film which leads to (2.20) for the film thickness,

$$\mu_{water}\frac{\partial \bar{F}}{\partial \bar{T}}+\frac{\partial}{\partial \bar{X}}\left[\mu_{air}k(\bar{X})\frac{\bar{F}^2}{2}+\frac{\partial^3 \bar{F}}{\partial \bar{X}^3}\frac{\bar{F}^3}{3}\right]=0 \quad , \tag{2.20}$$

where

$$k(\bar{X})=\frac{\partial U}{\partial Y}(X_0,0)+\frac{1}{2}\frac{\partial^3 U}{\partial X^2 \partial Y}(X_0,0)\bar{X}^2+\ldots \quad . \tag{2.21}$$

Note that since the water film scale is smaller than the vertical scale in the air layer, it is valid to evaluate the derivatives in (2.21) at the ice roughness surface neglecting the presence of the film (instead of at the air/water film interface).

Possibly the most critical aspect of this minimum shear structure is that it occurs when

$$\frac{\partial U}{\partial Y}(X_0,0)\sim h^{4/7} \quad . \tag{2.22}$$

This is the point at which the Couette model within the film first breaks down and additional terms from the interface stress balance are required in the film equation. As increased ice roughness height leads to lower shear on the downstream face of the roughness, the result is a bulging of the film thickness which is maintained by the surface tension. Solutions for this asymptotic structure are shown in Figure 8 for flow over a roughness element which induces

incipient separation and has a wall shear curvature of 0.303 in Stage II scales. Also shown in Figure 8 are numerical results for the full Stage II non-linear problem, which compare well with the minimum shear structure as $h \to 0$. The Stage II numerical results reveal that the mass flux within the water film does not change from the Couette model, however there is a small separation region within the film which locally traps water near the minimum shear point. This separation region gets smaller as $h \to 0$. That is, as the minimum shear structure is approached by the full non-linear Stage II solutions, the separation region within the film layer gets smaller. This is consistent with the minimum shear structure itself which does not admit separation within the film. In order to continue studying the effect of roughness as the air flow changes from incipient separation to full separation a model which admits separation within the film is required. This suggests returning to the full Stage II model and examining numerical results of that model.

Results for Thin Films Flowing Over Shallow Roughness

When the ice roughness height becomes larger than that required for incipient separation the air flow becomes fully separated behind the roughness. In this scenario it is necessary to resort to the full Stage II model to solve the air/water interaction. Figure 9a shows a typical scenario in which a roughness which induces a full two-dimensional separation on its downstream face has an initially thin uniform film over its surface. The film is assumed to have a constant mass flux of water at the upstream boundary. Since this initial film is thin it is primarily driven by the shear from the adjacent air layer. Upstream of the separation point, the film is being driven toward the separation point. The initial film within the air separation region will also be driven

downstream. The result is an initial pooling of water at the separation point and a thinning of the film at the re-attachment location. The pooling of the film at the separation point has a feedback effect on the air layer, causing the initial separation point to move a little bit downstream. The water then begins to pool at this new separation point which causes the separation point to continue to move downstream. This process continues until eventually a condition is reached in which the air flow is completely attached over the roughness element. At this point there is an excess of water which has accumulated on the downstream face of the roughness and a pocket of water is forced downstream by the air. However, as shown in Figure 9b, even after both the air flow and film have reached a steady state condition, there is still a pocket of water within the film which is recirculating on the downstream face of the roughness, as evidenced by the streamlines within the film. Therefore during this process the separation region has moved from the air to the water film layer. This process has previously been observed by Timoshin[37]. The water mass flux over the roughness in this steady state condition is necessarily equal to the upstream reference mass flux. However the total mass of water which is present on the surface has increased significantly. For this particular case the total amount of water present within the computational domain has increased by about 130%.

In order to more completely map the effect of roughness on the amount of water that locally accumulates on an airfoil surface, a study is performed in which the height of a single roughness element is varied while the wavelength/diameter is held nearly fixed. This is accomplished by using a Gaussian roughness shape which is the same as the shape used in Figure 9b. Starting from a very shallow roughness element, the roughness height is gradually increased. For each case, an initially thin uniform film is allowed to reach a steady state

condition. For each solution a water mass trapping factor, G, is found. G is defined as the ratio of water mass with roughness present to water mass without roughness present (i.e. a uniform thin film). The result is shown in Figure 10 for a film thickness of h=0.1. The dashed line in Figure 10 is the value of G for Couette flow which traps no additional water on the surface. The first point in the figure has a roughness height such that the minimum shear in the air over the roughness element is $h^{4/7}$. The previous section indicated that this was the point at which the Couette flow approximation first breaks down. The second point in Figure 10 is the incipient separation case where the air flow first separates as the roughness height is increased. All roughness elements with heights greater than this value have fully separated air flow and as the roughness height increases the amount of trapped water increases. The solid line in the figure is a parabolic curve fit to the numerical data. Though Figure 10 is generated for a specific roughness shape at a constant wavelength it is expected that results would be similar for more general roughness shapes.

The picture for the fully separated roughness remains essentially the same as the film thickness is decreased. That is, all cases tested continue to show a separated region of water behind the roughness element and re-attachment of the air flow with no alteration to the steady state film mass flux. The numerical results as well as preliminary asymptotic analysis show that time and spatial scales are altered as the film thickness is changed. For example, an order of magnitude decrease in the film thickness corresponds to an order of magnitude increase in the time it takes for the steady film to develop. Since all steady calculations were a long time limit of unsteady calculations this means a large increase in computer resources is required as the film thickness is decreased. The amount of water (or percentage change of water) trapped by the surface roughness also changes with the film thickness. Typically, as

the film thickness decreases, less water is trapped by a given roughness element.

Effects of Distributed Roughness

When multiple roughness elements are considered the effect on the amount of water that is trapped by the elements is cumulative. That is, if all roughness elements have separated air flow, then the film must re-establish the mass flux at the first roughness element in a manner similar to that outlined for single roughness elements in the previous section. Once this is done the film can re-establish itself at the second roughness element and so on until the mass flux is constant over the entire roughness field. If the spacing between roughness elements is large then the total amount of water trapped will be equal to the sum of water trapped by each roughness element as if it were considered in isolation. If the roughness elements are moved closer together then the separation region of upstream elements is affected by the presence of downstream elements, leading to a change in the amount of trapped water. This is illustrated by the results shown in Figure 11a. The roughness elements which make up the roughness field in Figure 11a correspond to $\Delta_{ice}=2$ in Figure 10. Therefore, the isolated roughness element would have a trapping factor of G=1.18. As the distance between roughness elements is increased such that each element acts as an individual roughness element then it is expected that G=1 + 3x0.18 = 1.54. In Case A of Figure 11a the roughness elements are moved closer together which results in a small increase in the degree of separation behind each roughness element. As a result, the amount of water trapped by each roughness element is also increased and the value of G increases slightly to 1.58. In Case B, the roughness elements are moved closer together, to the point where each roughness element now limits the degree of separation of the roughness in front of it. In fact, there is no separation here behind the first two roughness elements and

most of the water is trapped by the last element. The result is a decrease in the value of G to 1.33.

Figure 11b shows a multiple roughness case similar to Case B in Figure 11a but with the roughness height increased. The air flow over the steady state film between the roughness elements is still separated, however the mass flux through the film is still constant. Surface tension in the film between the roughness elements allows the water to flow downstream even though the shear forcing from the air flow is in the upstream direction. Therefore, it is possible for the air flow to remain separated and the film to establish a constant mass flux simultaneously when multiple roughness elements are present.

Conclusions for Thin Film with Shallow Two-Dimensional Roughness

In studying the impact of shallow two-dimensional roughness elements on thin films in the condensed layer structure the key findings are that:

1. The film distribution can be computed using a Couette flow approximation when the roughness elements are sufficiently shallow. This approximation breaks down when the minimum shear stress over the roughness is on the order of $h^{4/7}$, where h is the film thickness.

2. When the minimum shear falls below the minimum for which (1) is valid, then the film and the air flow interact to maintain a constant mass flux within a steady film while the amount of water over the roughness increases. This water is trapped in separation bubbles within the film and the amount of trapped water increases as the separation over the bare roughness element increases. The trapped water has a feedback effect on the air flow, causing the initial separation region within the air to disappear as the air flow re-attaches at steady state.

3. When multiple roughness elements are present, the amount of water trapped by the roughness can increase or decrease depending on the spacing between roughness elements. In addition, it is possible that closely spaced roughness elements will still allow separation in the air at steady state.

Implications for Three-Dimensional Roughness

The general trends observed in the previous sections are expected to extend at least to some degree to large scale three-dimensional roughness as well. For example, in the three-dimensional version of Stage II, spanwise terms appear in the various equations which are essentially identical to the corresponding streamwise terms. The same scalings which take the streamwise components from the Navier-Stokes equations to the Stage II equations apply to the spanwise components as well. The three-dimensional counterpart to (2.13) is

$$\mu_{water}\frac{\partial f}{\partial T}+\frac{\partial}{\partial X}\left[\mu_{air}\tau_{wx}\frac{f^2}{2}\right]+\frac{\partial}{\partial Z}\left[\mu_{air}\tau_{wz}\frac{f^2}{2}\right]=0 \quad , \tag{2.23}$$

and the Couette approximation still holds. Similarly, (2.22) is still valid as the rule for limiting the Couette approximation and introducing surface tension effects. However, in the three-dimensional case (2.22) is

$$\sqrt{\left[\frac{\partial U}{\partial Y}\left(X_0,0,Z_0\right)\right]^2+\left[\frac{\partial W}{\partial Y}\left(X_0,0,Z_0\right)\right]^2}\sim h^{4/7} \tag{2.24}$$

for the limit of the Couette approximation for $h^{4/7}\to 0$. In three-dimensional separated flows, the magnitude of the surface shear approaching zero occurs only at a finite number of points within the flow, which are the singular points (see Tobak & Peake[38]) previously mentioned. Recall that the singular points consist of nodal points, saddle point and focal points, and each of these types of singular points can be seen in Figure 3 for flow over an

isolated roughness element. From (2.23) we know that the surface water is going to be driven primarily by the surface shear. That is, the direction of the surface water flow will generally be in the direction of the surface shear lines. Near the surface singularities, (2.23) will break down according to (2.24). At nodal points and focal points of separation, water will be continually driven toward the singularity resulting in an increase in the film thickness. As with the two-dimensional case, surface tension effects will act to limit the total film thickness.

As mentioned previously, the key characteristic of a saddle point is that it divides the flow into four parts. Imagine a surface film which is being driven by the surface shear and approaching the roughness element in Figure 3a. The saddle point which is farthest downstream from the roughness acts to split the upstream flow into two regions. Half of the upstream flow is "captured" by the roughness and funneled toward the focal point, while the other half of the upstream flow simply moves past the roughness element. While these types of general trends are expected, surface tension would likely alter this picture somewhat.

In summary, it is expected that for initially thin films at early time the surface shear will be the primary driver for a three-dimensional film. At long time, surface tension will come into play and the surface water will alter the air flow. However, this is beyond the scope of this study. Therefore, in analyzing the impact of three-dimensional distributed roughness on surface water the surface shear patterns will be investigated in lieu of a full multi-phase calculation. In this regard, the turning and blocking of surface shear lines in the shear topology will be interpreted as potential turning and blocking of the early thin surface film.

CHAPTER 3. NUMERICAL SOLUTION OF THE NAVIER-STOKES EQUATIONS OVER LARGE THREE-DIMENSIONAL ROUGHNESS

The main goal of this study is to obtain numerical solutions to the incompressible three-dimensional Navier-Stokes equations for flow over O(1) aspect ratio three-dimensional roughness on an airfoil leading edge. In order to provide a more realistic picture of the effects of distributed roughness on the convective heat transfer and the surface water motion, the roughness geometries included in this study are closer to typical ice roughness than the roughness elements examined in the previous chapter. The purpose of this chapter is to describe the process for obtaining the solution, including geometry setup, grid generation, formulation and transformation of the governing equations and differencing strategies.

Geometry Modeling & Grid Generation

The two aspects of the problem that need to be modeled geometrically are a three-dimensional roughness element and an airfoil leading edge.

The Base Geometry Model

The leading edge is approximated using a parabolic cylinder with a short spanwise length (i.e. small spanwise strip). The parabolic approximation works well for many symmetric airfoils within about the first 5% chord of the leading edge, including a NACA 0012 airfoil (see Abbott & Von Doenhoff[39]). The parabola is specified via a conformal mapping, given by

$$u = \frac{1}{2} w^2 \quad , \tag{3.1}$$

where

$$u = x + iy \qquad \text{and} \qquad w = \xi' + i\,\eta' \quad . \tag{3.2}$$

This leads to a relationship between the Cartesian (*x,y*) and conformal (ξ' , η') coordinates given by

$$x=\frac{1}{2}\left(\xi'^2-\eta'^2\right) \qquad \text{and} \qquad y=\xi'\eta' \quad . \tag{3.3}$$

Parabolas of varying thickness are accommodated by varying the minimum value of η', η'_{min} . In particular, the relationship between η'_{min} and the parabola leading edge radius of curvature, *R*, is

$$\eta'_{min}=R^{1/2} \quad . \tag{3.4}$$

Note that *R* is also used as the reference length when non-dimensionalizing the governing equations. When *R* = 1, (3.3) gives the standard parabola in non-dimensional coordinates. As $R\rightarrow 0$, (3.3) approximates a flat plate leading edge. This is useful since a lot of experimental roughness work is for roughness on a flat plate and so the basic form of (3.3) allows these cases to be approximated as well. As $R\rightarrow \infty$, (3.3) approximates a stagnation point geometry.

In addition to being an orthogonal transformation, conformal mappings have the advantage that harmonic functions remain harmonic under the transformation. Thus, a potential flow which is governed by Laplace's equation, i.e.

$$\nabla^2\phi=0 \quad , \tag{3.5}$$

continues to have the same form when the coordinates are transformed via a conformal mapping. This is advantageous in the current study in which the flow is effectively being split into viscous and inviscid parts, with the inviscid part being governed by (3.5). However, as will be seen later, a conformal mapping also tends to maintain the form of the

equations governing the viscous part as well, in particular the vorticity transport equations. It should be noted that the conformal mapping being applied in this study is in two-dimensions only, with the third dimension not being transformed conformally. In this situation, the full benefits of using conformal mappings are not realized, however their use still tends to decrease the total number of terms to be evaluated and tends to maintain the Cartesian form of the governing equations.

The transformation in (3.3) is made three-dimensional in the current study by simply adding a third computational coordinate given by

$$z = \zeta' \quad , \tag{3.6}$$

where z is the Cartesian spanwise coordinate.

Roughness Models

Surface roughness is incorporated into the numerical solution via a shearing transformation. The grid is shifted in the η' direction by applying the equation

$$\eta = \eta' - f(\xi', \zeta') \quad , \tag{3.7}$$

which is known as a Prandtl transposition. In the new coordinate system, (ξ , η , ζ), the no-slip boundary condition is applied at $\eta = \eta_{min}$. In (3.7), f is the equation which gives the roughness shape. The tangential wall coordinates in the new coordinate system are given by

$$\xi = \xi' \qquad \text{and} \qquad \zeta = \zeta' \quad . \tag{3.8}$$

The purpose of using the shearing transformation to model the roughness is so that a structured grid can be maintained for the flow solver while eliminating the need to manually generate complex grids for each roughness field to be studied. In addition, it offers a natural extension for a future study to examine the effects of the air flow on the temporal evolution

of growing surface ice roughness as well as the dynamics of surface water.

Surface roughness comes in many different shapes and forms. Therefore, in order to examine the effects of surface roughness it is desirable to model a number of idealized roughness shapes while maintaining certain properties of the roughness geometry which make their integration into the flow solver via a Prandtl transposition possible. In the present work the most important geometrical feature of the roughness model is "smoothness", either numerical or analytical. By analytical smoothness it is meant that the derivatives of the roughness are continuous up to a certain order. By numerical smoothness it is meant that regions of significant geometry change have sufficient grid resolution in that region. The strategy used in the present study is to use smooth functions which can approximate a given roughness shape and then ensure that the grid resolution is sufficient to properly capture the flow effects induced by the roughness.

The four different shapes for individual roughness elements used in this study are shown in Figure 13. The first roughness shape is a simple three-dimensional quartic bump given by the equation

$$f = k\left[1-\left(2\frac{s-s_0}{\lambda_s}\right)^2\right]^m\left[1-\left(2\frac{\zeta-\zeta_0}{\lambda_\zeta}\right)^2\right]^m \quad , \tag{3.9}$$

where k is the maximum height of the bump, s is the non-dimensional arc-length along the parabola, and the λ's are proportional to the streamwise and spanwise wavelengths of the bump. Note that s is directly related to the parabolic streamwise coordinate and the leading edge radius of curvature by the equation

$$s = \frac{1}{2}\left[\xi\sqrt{\xi^2+R}+R\ln\left(\sqrt{\xi^2+R}+\xi\right)\right]-\frac{1}{2}R\ln\left(\sqrt{R}\right) \quad . \tag{3.10}$$

Equation (3.10) allows (3.9) to be cast in a form suitable for (3.7). There is a discontinuity in the m^{th} derivative where the roughness shape given by (3.9) intersects the flat surface (f=0), resulting in a non-smooth function. By setting the value of m large enough (typically m=10 in the current study) the intersection of the roughness and the parabola surface is smooth enough for purposes of a numerical solution.

A second roughness model which is useful for comparison with older numerical studies is a secant bump given by the equation

$$f = k\, sech\left(\lambda_s\left(s - s_0\right)\right) sech\left(\lambda_\zeta\left(\zeta - \zeta_0\right)\right) \quad . \tag{3.11}$$

In addition, many experimental roughness studies have used hemispheres as the shape of the roughness. Hemispheres pose a challenge numerically because derivatives are not finite and they are discontinuous where the hemisphere intersects the surface. In the present study the goal is to approximate a hemisphere with a function which has finite and continuous derivatives over the entire surface. An example is a simple exponential decay function,

$$f(r) = k \exp\left(A_1 r + A_2 r^2 + ...\right) \quad , \tag{3.12}$$

where r is a radial coordinate from the center of the roughness being approximated and the A_i's are coefficients which are to be determined. The Taylor series of (3.12) is given by

$$f(r) = k\left(1 + A_1 r + \left(A_2 + \frac{1}{2} A_1^2\right) r^2 + ...\right) \quad . \tag{3.13}$$

The function in (3.12) is made to approximate a given shape by comparing (3.13) with the Taylor series of the desired shape and matching coefficients. In the case of a hemisphere the shape is given by

$$f(r)=\left(k^2-r^2\right)^{1/2} \quad , \tag{3.14}$$

which has a Taylor series

$$f(r)=k-\frac{1}{2k}r^2-\frac{1}{8k^2}r^4+\ldots \quad . \tag{3.15}$$

Comparing (3.13) and (3.15) including higher order terms and using induction it is found that all A_i's with odd i vanish (since the hemisphere is axially symmetric) and the A_i's for even i are given by

$$A_i=\frac{-1}{ik^i} \quad . \tag{3.16}$$

The form of (3.12) used to approximate a hemisphere is then

$$f(r)=k\exp\left(\sum_{i=0}^{m}\frac{-r^{2i}}{2\,i\,k^{2i}}\right) \quad , \tag{3.17}$$

where the coefficients in (3.17) have been modified to account for the fact that all odd terms vanish. The parameter m in (3.17) is used as a trade-off between function smoothness and how well (3.17) approximates a hemisphere. When m is small the shape is very smooth and Gaussian-like. As m becomes large the approximation of the hemisphere improves. However, at large m the corners of the shape become sharp and an increasing number of grid points are required to adequately resolve the flow in this area. In addition, because the Prandtl transposition is a shearing transformation, increasing the value of m will lead to grids with higher skewness. Figure 12 shows the progression of (3.17) from the Gaussian shape to the true hemisphere as m goes to infinity.

The last shape which is incorporated within the code is an approximation of a three-dimensional cylinder or disk. For this shape the transition from the roughness to the clean surface is made by using hyperbolic tangent functions. The cylinder shape is given by

$$f(r)=\frac{k}{4}\left[1-\tanh\left(\frac{r-D/2}{a}\right)\right]\left[1+\tanh\left(\frac{r+D/2}{a}\right)\right] \quad , \tag{3.18}$$

where D is the diameter of the cylinder and a is a non-integer smoothness parameter. As $a \rightarrow 0$ the transition becomes sharper, eventually approaching a 90 degree angle.

The code is capable of placing uniform and non-uniform distributions of roughness elements which consist of one or more different types of roughness on the surface. In addition, since all roughness elements are defined analytically, more complex roughness shapes can be created by superposition of the basic roughness elements shown in Figure 13. An example of the types of roughness shapes that are possible using this technique is shown in Figure 14. The roughness shape in Figure 14 is meant to represent a typical glaze ice shape and was constructed using a superposition of two large two-dimensional quartic humps and multiple hemispheres which have random size and placement. Figure 14 shows an iso-metric view, a two-dimensional view and a close-up of the roughness with a surface mesh.

Grid Stretching

The final step in geometry creation and grid generation is the setup of grids which have adequate resolution for viscous flow effects in regions of interest but coarser grids in outer regions of the flow. Many different types of grid stretching can be applied in each coordinate direction. These include uniform grids and stretching about a single point. For example, in the ξ direction the grid stretching

$$\xi=\xi_0+\left(\xi_{max}-\xi_0\right)\frac{\sinh\left(a_\xi\bar{\xi}\right)}{\sinh\left(a_\xi\right)} \quad , \tag{3.19}$$

stretches the grid about the point ξ_0 with the degree of stretching given by a_ξ. $\bar{\xi}$ is the computational coordinate in the streamwise direction. Typically $-1 \le \bar{\xi} \le 1$, however when

using (3.19) the value of $\bar{\xi}_{min}$ must be modified so that $\xi_{min}=-\xi_{max}$ and the parabola is symmetric. The result is that $\bar{\xi}_{min}$ must be set to the value

$$\bar{\xi}_{min}=\frac{1}{a_\xi}\sinh^{-1}\left(\sinh(a_\xi)\frac{(-\xi_{max}-\xi_0)}{(\xi_{max}-\xi_0)}\right) \quad . \tag{3.20}$$

Grid stretching similar to (3.19) can also be applied in the wall-normal and spanwise directions as well, with the exception that the wall-normal grid is typically stretched about the surface, $\eta=-\eta_{min}$.

For Navier-Stokes calculations it is often desirable to have a uniform grid in the wall-tangential coordinate directions in order to minimize the effect of the grid on the solution. However, it would be impractical to cover the entire parabola with a uniform grid in the streamwise direction. One solution is to construct a grid transformation which uses a uniform grid over a region of interest and stretches the grid on either side of this uniform grid region, to the outer boundaries of the flow domain. The method for constructing such a grid was developed by Bhaskaran[40] and is reviewed here for reference. The uniform grid region, denoted as Region 2, is defined by $\xi_{M1}\le\xi\le\xi_{M2}$ where ξ is given by the grid law

$$\xi=\xi_{M1}+\left(\frac{\xi_{M2}-\xi_{M1}}{\bar{\xi}_{M2}-\bar{\xi}_{M1}}\right)(\bar{\xi}-\bar{\xi}_{M1}) \quad . \tag{3.21}$$

In the region upstream of Region 2 (Region 1) the grid is stretched to the boundary of the flow domain. This is accomplished using a hyperbolic sine function

$$\frac{\xi_{M1}-\xi}{\xi_{M1}-\xi_{min}}=\frac{\sinh\left[a_{\xi 1}\left(\frac{\bar{\xi}_{M1}-\bar{\xi}}{\bar{\xi}_{M1}-\bar{\xi}_{min}}\right)\right]}{\sinh(a_{\xi 1})} \quad . \tag{3.22}$$

Similarly in the region downstream from Region 2 (Region 3) the grid law is

$$\frac{\xi-\xi_{M2}}{\xi_{max}-\xi_{M2}}=\frac{\sinh\left[a_{\xi 3}\left(\frac{\bar{\xi}-\bar{\xi}_{M2}}{\bar{\xi}_{max}-\bar{\xi}_{M2}}\right)\right]}{\sinh\left(a_{\xi 3}\right)} \quad . \tag{3.23}$$

The stretching factors for these two regions, $a_{\xi 1}$ and $a_{\xi 3}$ are chosen such that the first order grid metrics are continuous where Region 1 and Region 3 meet Region 2. The result is a transcendental equation for the stretching factors, for example,

$$\frac{\sinh(a_{\xi 3})}{a_{\xi 3}}=\frac{\xi_{max}-\xi_{M2}}{\bar{\xi}_{max}-\bar{\xi}_{M2}} \tag{3.24}$$

which must be solved numerically for $a_{\xi 3}$. A similar grid stretching strategy can be applied in the spanwise direction. A typical three-dimensional viscous grid with a uniform grid region in the streamwise direction is shown in Figure 15. The uniform grid region is the area in which the roughness is placed.

An overview of the method of geometry modeling and grid generation which has been described in this section is summarized in Figure 16, which is taken from Huebsch[41].

Formulation of the Navier-Stokes Equations

The goal of the current study is to develop a robust flow solver for the three-dimensional Navier-Stokes equations to examine the flow over three-dimensional roughness on an airfoil leading edge. The resulting flow solver should be both accurate and relatively free of numerical dissipation. It is the author's experience in previous numerical studies that in two dimensions, streamfunction/vorticity methods can overcome some of the stability issues associated with primitive variable solvers and can produce a robust flow solver. In addition, previous studies of Navier-Stokes flow over two-dimensional roughness by Huebsch[41] used a streamfunction/vorticity approach. As a result, this study uses a similar approach in three dimensions. In three dimensions, the velocity/vorticity approach or vector-

potential/vorticity approach requires the solution of six unknowns compared with the customary four for primitive variables. However, a streamfunction-like/vorticity method was developed by Davis *et al.*[42] to solve the Thin Layer Navier-Stokes (TLNS) equations for steady flow over shallow bumps. The present study starts with this method and modifies it slightly to solve for the contravariant vector components of the full Navier-Stokes equations. The Prandtl transposition and standard grid stretching are then applied to the governing equations. An incompressible form of the energy equation is also developed in order to study the effect of roughness on heat transfer. A brief review of the derivation of the vorticity transport and vector potential equations is given in the next section in order to provide context for the remaining discussion.

Streamfunction-Like / Vorticity Formulation in Cartesian Coordinates

The primitive variable form of the continuity equation is given by

$$\frac{\partial u_i}{\partial x_i}=0 \quad . \tag{3.25}$$

In (3.25) and in what follows in this sub-section we use Cartesian tensor notation to illustrate the development of the method. The incompressible form of the Navier-Stokes (momentum) equations is given by

$$\frac{\partial u_i}{\partial t}+u_j\frac{\partial u_i}{\partial x_j}=-\frac{\partial p}{\partial x_i}+Re^{-1}\frac{\partial^2 u_i}{\partial x_i^2} \quad . \tag{3.26}$$

Note that (3.26) can also be written as

$$\frac{\partial u_i}{\partial t}+\frac{\partial}{\partial x_i}\left(\frac{u_j u_j}{2}\right)-\epsilon_{imn}\epsilon_{njk}u_m\frac{\partial u_k}{\partial x_j}=-\frac{\partial p}{\partial x_i}+Re^{-1}\frac{\partial^2 u_i}{\partial x_i^2} \quad , \tag{3.27}$$

where ϵ_{ijk} is the permutation symbol. That (3.27) is equal to (3.26) can easily be shown if the following property of ϵ_{ijk} is used

$$\epsilon_{imn}\epsilon_{jkn}=\delta_{ij}\delta_{mn}-\delta_{ik}\delta_{jm} \quad . \tag{3.28}$$

Taking the curl of (3.27) gives

$$\epsilon_{opi}\frac{\partial}{\partial x_p}\left(\frac{\partial u_i}{\partial t}\right)-\epsilon_{opi}\epsilon_{imn}\epsilon_{njk}\frac{\partial}{\partial x_p}\left(u_m\frac{\partial u_k}{\partial x_j}\right)=Re^{-1}\epsilon_{opi}\frac{\partial}{\partial x_p}\left(\frac{\partial^2 u_i}{\partial x_i^2}\right) \quad , \tag{3.29}$$

where the second and fourth terms in (3.27) have dropped out because the curl of the gradient of any scalar quantity is zero (see Karamcheti[43]). Note that by using continuity (3.29) can be rewritten as

$$\frac{\partial}{\partial t}\left(\epsilon_{opi}\frac{\partial u_i}{\partial x_p}\right)-\epsilon_{opi}\epsilon_{imn}\frac{\partial}{\partial x_p}\left(u_m\epsilon_{njk}\frac{\partial u_k}{\partial x_j}\right)=Re^{-1}\frac{\partial^2}{\partial x_i^2}\left(\epsilon_{opi}\frac{\partial u_i}{\partial x_p}\right) \quad . \tag{3.30}$$

Introducing the definition of vorticity,

$$\omega_i=\epsilon_{ijk}\frac{\partial u_k}{\partial x_j} \quad , \tag{3.31}$$

the above equation can be written as

$$\frac{\partial \omega_o}{\partial t}-\epsilon_{opi}\epsilon_{imn}\frac{\partial}{\partial x_p}\left(u_m\omega_n\right)=Re^{-1}\frac{\partial^2\omega_o}{\partial x_i^2} \quad . \tag{3.32}$$

Once again (3.28) is used to write (3.32) as

$$\frac{\partial \omega_o}{\partial t}-\frac{\partial}{\partial x_n}\left(u_o\omega_n\right)+\frac{\partial}{\partial x_m}\left(u_m\omega_o\right)=Re^{-1}\frac{\partial^2\omega_o}{\partial x_i^2} \quad . \tag{3.33}$$

Expanding the derivatives in (3.33) gives

$$\frac{\partial \omega_o}{\partial t}-\omega_n\frac{\partial u_o}{\partial x_n}-u_o\frac{\partial \omega_n}{\partial x_n}+\omega_o\frac{\partial u_m}{\partial x_m}+u_m\frac{\partial \omega_o}{\partial x_m}=Re^{-1}\frac{\partial^2\omega_o}{\partial x_i^2} \quad . \tag{3.34}$$

The fourth term in (3.34) is zero due to (3.25). The third term in (3.34) is also zero due to the solenoidality condition, which is identical to (3.25) but with ω_i replacing u_i (this equation

is found by taking the curl of (3.31)). The final form of the vorticity transport equation is then

$$\frac{\partial \omega_i}{\partial t} + u_j \frac{\partial \omega_i}{\partial x_j} = \omega_j \frac{\partial u_i}{\partial x_j} + Re^{-1} \frac{\partial^2 \omega_i}{\partial x_j^2} \quad . \tag{3.35}$$

The three-dimensional vorticity transport equation is identical to its two-dimensional counterpart with the exception of the first term on the right-hand-side of (3.35). These are commonly labeled the vortex stretching/turning terms. Vortex turning is the physical mechanism whereby vorticity in one coordinate direction is converted into vorticity in another coordinate direction by turning of the flow. Vortex stretching is the mechanism whereby a vortex line, when it is stretched via flow dynamics, increases in vorticity magnitude due to conservation of angular momentum.

In two dimensions, the purpose of the streamfunction is to define a function which exactly satisfies continuity and then construct a condition which relates streamfunction to vorticity. In three dimensions the idea is the same. In general, mass conservation can be satisfied by writing the velocity vector in terms of a vector potential using the relation (again the curl of a gradient field of a scalar is always zero, see Karamcheti[43])

$$u_i = \epsilon_{ijk} \frac{\partial A_k}{\partial x_j} \quad . \tag{3.36}$$

The relationship between the vector potential and the vorticity vector is found using (3.31) and (3.36), in which case

$$\omega_m = \epsilon_{mni} \epsilon_{ijk} \frac{\partial^2 A_k}{\partial x_n \partial x_j} \quad . \tag{3.37}$$

Once again, using the identity in (3.28) and doing a bit of rewriting this can be simplified to

$$\omega_i = \frac{\partial}{\partial x_j}\left(\frac{\partial A_j}{\partial x_i} - \frac{\partial A_i}{\partial x_j}\right) \quad . \tag{3.38}$$

(3.35) and (3.38) along with appropriate boundary conditions form the general vector potential/vorticity method in three dimensions. This general system requires the solution of six equations with six unknowns. In order for this method to be computationally competitive with the primitive variable approach, which solves four equations for four unknowns, the size of the system must be reduced. This is accomplished in the method of Davis *et al.*[42] by assuming the form of the vector potential, A_i, to be

$$A_i = \begin{Bmatrix} -\theta \\ 0 \\ \psi \end{Bmatrix} \quad . \tag{3.39}$$

Note that (3.39) is simply a consequence of the gauge invariance of the vector potential, which says that A_i only has two independent components. At this point it is possible to depart from the general method and write the equations in terms of specific components of the vorticity vector and the vector A_i in a Cartesian coordinate system. Substituting (3.39) into (3.38) would result in Poisson equations for each of the streamfunction-like parameters, θ and ψ. However the approach here will be to transform the equations to solve for the contravariant vector components.

Transformation to Contravariant Coordinates

The current study extends the method of Davis *et al.*[42] by transforming the governing equations to contravariant coordinates for the full Navier-Stokes equations. The reason for doing this is to maintain a flow solution which, from a computational domain perspective, has similarities to a flat plate flow solution. This generally simplifies the form of the governing equations and allows numerical methods applicable to flat plate flow

solutions to be used. At this point it is possible to continue with tensor notation in deriving the contravariant form of the governing equations. However, in dealing with an orthogonal coordinate system it is actually simpler and more informative to write the equations using vector notation. The governing equations in vector notation are the vorticity transport equation

$$\frac{\partial \vec{\omega}}{\partial t}+\vec{V}\cdot\nabla\vec{\omega}=\vec{\omega}\cdot\nabla\vec{V}+Re^{-1}\nabla^2\vec{\omega} \quad , \tag{3.40}$$

which corresponds to (3.35), and the kinematic condition

$$\vec{\omega}=\nabla\times\nabla\times\vec{A} \quad , \tag{3.41}$$

which corresponds to (3.37). Breaking these equations into the component equations simply involves using the proper relationships for the various vector operations. For example, in a general orthogonal coordinate system

$$\nabla\phi=\frac{1}{h_1}\frac{\partial\phi}{\partial x_1}\hat{e}_1+\frac{1}{h_2}\frac{\partial\phi}{\partial x_2}\hat{e}_2+\frac{1}{h_3}\frac{\partial\phi}{\partial x_3}\hat{e}_3 \tag{3.42}$$

and

$$\nabla\cdot\vec{\Phi}=\frac{1}{h_1h_2h_3}\left\{\frac{\partial}{\partial x_1}\left(h_2h_3\Phi_1\right)+\frac{\partial}{\partial x_2}\left(h_1h_3\Phi_2\right)+\frac{\partial}{\partial x_3}\left(h_1h_2\Phi_3\right)\right\} \quad . \tag{3.43}$$

It should be noted that when terms are evaluated in this manner, the Φ's are the vector components in the chosen orthogonal coordinate system. Combining (3.42) and (3.43) gives

$$\nabla^2\phi=\nabla\cdot\nabla\phi=\frac{1}{h_1h_2h_3}\left\{\frac{\partial}{\partial x_1}\left(\frac{h_2h_3}{h_1}\frac{\partial\phi}{\partial x_1}\right)+\frac{\partial}{\partial x_2}\left(\frac{h_1h_3}{h_2}\frac{\partial\phi}{\partial x_2}\right)+\frac{\partial}{\partial x_3}\left(\frac{h_1h_2}{h_3}\frac{\partial\phi}{\partial x_3}\right)\right\} \quad , \tag{3.44}$$

where the h_i's are the grid scale factors, that is, the diagonal components of the Jacobian matrix. For any conformal mapping in two dimensions $h_1=h_2=h$. In addition, since

$x_3=\zeta'=z$, $h_3=1$. This allows (3.44) to be simplified to

$$\nabla^2\phi=\frac{1}{h^2}\left\{\frac{\partial^2\phi}{\partial x_1^2}+\frac{\partial^2\phi}{\partial x_2^2}+h^2\frac{\partial^2\phi}{\partial x_3^2}\right\} \quad , \tag{3.45}$$

since *h* is not a function of x_3. This example shows the advantage of using a conformal coordinate system in that the Laplacian has a form which is very similar to the Laplacian in a Cartesian coordinate system and the total number of terms is kept to a minimum. The gradient of a vector is found using the following relation from Karamcheti[43]

$$\nabla\times\left(\vec{A}\times\vec{B}\right)=\vec{A}\left(\nabla\cdot\vec{B}\right)+\left(\vec{B}\cdot\nabla\right)\vec{A}-\vec{B}\left(\nabla\cdot\vec{A}\right)-\left(\vec{A}\cdot\nabla\right)\vec{B} \quad , \tag{3.46}$$

or solving for the part of interest

$$\left(\vec{A}\cdot\nabla\right)\vec{B}-\left(\vec{B}\cdot\nabla\right)\vec{A}=-\nabla\times\left(\vec{A}\times\vec{B}\right)+\vec{A}\left(\nabla\cdot\vec{B}\right)-\vec{B}\left(\nabla\cdot\vec{A}\right) \quad . \tag{3.47}$$

Notice that the left side of (3.47) is equivalent to the second and third terms in (3.40) if the third term is brought to the left-hand-side and $\vec{A}=\vec{V}$ and $\vec{B}=\vec{\omega}$. (3.47) then becomes

$$\left(\vec{V}\cdot\nabla\right)\vec{\omega}-\left(\vec{\omega}\cdot\nabla\right)\vec{V}=-\nabla\times\left(\vec{V}\times\vec{\omega}\right)+\vec{V}\left(\nabla\cdot\vec{\omega}\right)-\vec{\omega}\left(\nabla\cdot\vec{V}\right) \quad . \tag{3.48}$$

The last two terms in (3.48) are zero because of the solenoidality condition and continuity, respectively. Plugging the remaining term into (3.40) gives an alternative form of the vorticity transport equations

$$\frac{\partial\vec{\omega}}{\partial t}-\nabla\times\left(\vec{V}\times\vec{\omega}\right)=Re^{-1}\nabla^2\vec{\omega} \quad . \tag{3.49}$$

This equation can easily be evaluated in terms of known vector operations for orthogonal coordinate systems and an equation for each of the three vorticity components can be written. For example, carrying out the operations and doing some simplifying for the first vorticity transport equation gives

$$\frac{\partial(h\omega_1)}{\partial t}+\frac{\partial}{\partial \eta'}(V_2\omega_1-V_1\omega_2)+\frac{\partial}{\partial \zeta'}(hV_3\omega_1-hV_1\omega_3)$$
$$=Re^{-1}\frac{\partial}{\partial \eta'}\left\{\frac{1}{h^2}\left[\frac{\partial}{\partial \eta'}(h\omega_1)-\frac{\partial}{\partial \xi'}(h\omega_2)\right]\right\}+\frac{\partial}{\partial \zeta'}\left\{\frac{1}{h^2}\left[\frac{\partial}{\partial \zeta'}(h\omega_1)-\frac{\partial}{\partial \xi'}(h\omega_3)\right]\right\} \quad (3.50)$$

Again, it is noted that these are the components in the contravariant (i.e. conformal) coordinate system. In a similar manner, carrying out the vector operations in (3.41), the equation for the third component of the vector potential, $\vec{A}$, is

$$\frac{\partial^2\psi}{\partial \xi'^2}+\frac{\partial^2\psi}{\partial \eta'^2}+\frac{\partial^2(h\theta)}{\partial \xi'\partial \zeta'}=-h^2\omega_3 \quad . \quad (3.51)$$

The system is closed by adding additional equations for ω_3 and θ and substituting for the velocity components in (3.50) in terms of ψ and θ, given in the appendix. These velocity components are given by

$$\vec{V}=\frac{1}{h}\frac{\partial\psi}{\partial \eta'}\hat{e}_1+\frac{1}{h}\left[-\frac{\partial(h\theta)}{\partial \zeta'}-\frac{\partial\psi}{\partial \xi'}\right]\hat{e}_2+\frac{1}{h^2}\frac{\partial(h\theta)}{\partial \eta'}\hat{e}_3 \quad . \quad (3.52)$$

There are a couple of additional simplifications which can be made in order to reduce the total number of terms in the equations as well as improve convergence. First, convergence rates are often limited by slow convergence of the inviscid part of the flow which requires boundary conditions being transferred all the way through the solution domain. Therefore, this study follows the two-dimensional study of Baskharan[40] and splits the flow into a viscous part and an inviscid part, with the inviscid solution given by the potential flow solution over the base two-dimensional geometry (i.e. without the roughness present). The "viscous" part of the flow is then responsible for capturing both the viscous effects as well as any changes in the inviscid flow due to the presence of roughness. Second, it is noted by

examining (3.50) and (3.51) that many of the vector components responsible for the three-dimensionality of the flow-field are multiplied by the scale factor, *h*. Therefore, a transformation is used in which the computational components are equal to the physical component times the scale factor. The complete set of transformations being used here is then

$$\begin{Bmatrix} \psi \\ h\theta \\ h\omega_1 \\ h\omega_2 \\ \omega_3 \end{Bmatrix} = \begin{Bmatrix} \Psi \\ \Theta \\ \Omega_1 \\ \Omega_2 \\ \Omega_3 \end{Bmatrix} + \begin{Bmatrix} \bar{\psi} \\ 0 \\ 0 \\ 0 \\ 0 \end{Bmatrix} \quad , \tag{3.53}$$

where the first vector on the right-hand-side is the set of computational components being used in this study, and the second vector on the right-hand-side is the potential flow solution over the base two-dimensional geometry. Making these substitutions, (3.50) and (3.51) become

$$\begin{aligned} &\frac{\partial \Omega_1}{\partial t} + \frac{\partial}{\partial \eta'}\left(\frac{1}{h}V_2\Omega_1 - \frac{1}{h}V_1\Omega_2\right) + \frac{\partial}{\partial \zeta'}\left(V_3\Omega_1 - hV_1\Omega_3\right) \\ &= Re^{-1}\frac{\partial}{\partial \eta'}\left\{\frac{1}{h^2}\left[\frac{\partial \Omega_1}{\partial \eta'} - \frac{\partial \Omega_2}{\partial \xi'}\right]\right\} + \frac{1}{h^2}\left[\frac{\partial^2 \Omega_1}{\partial \zeta'^2} - \frac{\partial^2 (h\Omega_3)}{\partial \xi' \partial \zeta'}\right] \end{aligned} \tag{3.54}$$

and

$$\frac{\partial^2 \Psi}{\partial \xi'^2} + \frac{\partial^2 \Psi}{\partial \eta'^2} + \frac{\partial^2 \Theta}{\partial \xi' \partial \zeta'} = h^2 \Omega_3 \quad , \tag{3.55}$$

respectively.

The final step before differencing the governing equations is to apply the transformations for introduction of the roughness as well as the grid stretching in each direction. This follows the standard chain rule for changing coordinate systems in which a

derivative is being evaluated and the details of the derivation will not be given here. The development and listing of the final complete set of equations which are being solved in this study are given in the appendix.

Boundary Conditions

Appropriate boundary conditions are necessary in order for the solution in the domain interior to simulate the desired physics. At the parabola surface the usual no-slip boundary condition is applied, where all velocity components are set to zero. At the η' far-field it is assumed that both the wall and the roughness have no impact on the flow so that the two-dimensional inviscid potential solution is recovered there. Far downstream, on the top and bottom of the parabola, an outflow condition must be specified without influencing the flow in the region of interest. In the present study this boundary is placed a large distance away from the region of interest where the grid has coarsened significantly moving downstream, see Figure 15. This very coarse grid region acts as built-in numerical dissipation, regardless of the differencing scheme, so that as the flow moves from the fine grid region through the coarse grid region both the flow three-dimensionality as well as flow unsteadiness are gradually dissipated. As a result, a two-dimensional steady boundary condition can be used at the far downstream boundary. Since the viscous flow over a parabola is known to asymptote to a flat plate solution far away from the leading edge, it is possible to apply a two-dimensional Blasius solution at this downstream boundary. Finally, in the spanwise direction a number of different boundary conditions can be applied. These include flow periodicity, flow symmetry and a boundary-layer type approximation.

The no-slip boundary condition at the surface requires that all velocity components vanish. In the primitive variable formulation this is trivial. However, in the current

formulation the appropriate conditions on the streamfunction-like components and vorticity components must be found. Specifying values for the velocity components leads to conditions on the streamfunctions only. Appropriate conditions for the vorticity components must therefore be derived and this has been the subject of much research over the years, see for example Napolitano *et al*.[44] and Souli[45]. The present study uses the well known coupled method in which the boundary conditions for the velocity components are used to specify the streamfunction-like components and their derivatives on the surface with the Poisson equations solved at the surface to find a kinematically compatible condition for the vorticity components. The goal here is to show that the well known conditions on the streamfunction in two-dimensions also hold for the streamfunction-like components in three-dimensions.

In particular, consider the no-slip boundary condition applied to the surface given by η'=const. The continuity equation in contravariant coordinates is solved for the wall-normal derivative of the second velocity component

$$\frac{\partial}{\partial \eta'}\left(h V_2\right)=-\frac{\partial}{\partial \xi'}\left(h V_1\right)-\frac{\partial}{\partial \zeta'}\left(h^2 V_3\right). \tag{3.56}$$

From (3.52), the velocity components, written in terms of the vector potential, A_i, are given by

$$\begin{aligned} h V_1 &= \frac{\partial A_3}{\partial \eta'}-\frac{\partial}{\partial \zeta'}\left(h A_2\right) \\ h V_2 &= \frac{\partial}{\partial \zeta'}\left(h A_1\right)-\frac{\partial A_3}{\partial \xi'} \\ \text{and}\quad h^2 V_3 &= \frac{\partial}{\partial \xi'}\left(h A_2\right)-\frac{\partial}{\partial \eta'}\left(h A_1\right) \end{aligned} \quad , \quad . \tag{3.57}$$

Substituting (3.57) into (3.56) gives

$$\frac{\partial}{\partial \eta'}(hV_2) = -\frac{\partial^2 A_3}{\partial \xi' \partial \eta'} + \frac{\partial^2 (hA_2)}{\partial \xi' \partial \zeta'} - \frac{\partial^2 (hA_2)}{\partial \xi' \partial \zeta'} + \frac{\partial^2 (hA_1)}{\partial \eta' \partial \zeta'} \quad . \tag{3.58}$$

Note that the middle two terms on the right-hand-side cancel each other. Integrating the remaining equation in η' gives an expression for V_2,

$$hV_2 = -\frac{\partial A_3}{\partial \xi'} + \frac{\partial (hA_1)}{\partial \zeta'} + g(\xi', \zeta') \quad , \tag{3.59}$$

where *g* is an arbitrary constant resulting from the integration. Note that without loss of generality (3.59) can be written as

$$hV_2 = -\frac{\partial}{\partial \xi'}\left(A_3 - g_1(\xi', \zeta')\right) + \frac{\partial}{\partial \zeta'}\left(hA_1 - g_2(\xi', \zeta')\right) \quad . \tag{3.60}$$

In general, it might be expected that A_1 and A_3 will be non-zero on the surface, $\eta' = \sqrt{R}$. However, if we pick

$$g_2(\xi', \zeta') = h(\xi', \sqrt{R}) A_1(\xi', \sqrt{R}, \zeta') \tag{3.61}$$

and

$$g_1(\xi', \zeta') = A_3(\xi', \sqrt{R}, \zeta') \tag{3.62}$$

then we can define a new vector potential, $\vec{A}'$, given by

$$A_i' = \begin{Bmatrix} A_1 - h(\xi', \sqrt{R}) A_1(\xi', \sqrt{R}, \zeta') \\ A_2 \\ A_3 - A_3(\xi', \sqrt{R}, \zeta') \end{Bmatrix} \tag{3.63}$$

which automatically satisfies $V_2 = 0$ on the surface because the first and third components are zero on the surface. The first and third components of (3.63) are analogous to the gauge transformation used in the vector potential method. Note that using $\vec{A}'$ in place of $\vec{A}$ does not change the form of (3.36) so that all of the governing equations in their given forms

remain valid when written in terms of $\vec{A}'$. Therefore, dropping the prime we can solve the governing equations with $A_1 = A_3 = 0$ on the surface to satisfy $V_2 = 0$ there. The other condition on the vector potential which is a result of the no-slip condition comes from setting the first and third components of (3.36) to zero so that

$$\frac{\partial A_3}{\partial \eta'} = \frac{\partial (h A_2)}{\partial \zeta'} \tag{3.64}$$

and

$$\frac{\partial (h A_2)}{\partial \xi'} = \frac{\partial (h A_1)}{\partial \eta'} \tag{3.65}$$

on the surface. Applying the specific form of the vector potential given in (3.39) to the general no-slip boundary conditions developed here gives

$$\psi = \theta = \frac{\partial \psi}{\partial \eta'} = \frac{\partial (h\theta)}{\partial \eta'} = 0 \tag{3.66}$$

Applying the transformations specified in (3.53), the final no-slip boundary conditions specified on the streamfunction-like components are

$$\Psi = -\bar{\psi} \tag{3.67}$$

and

$$\frac{\partial \Psi}{\partial \eta} = -\frac{\partial \bar{\psi}}{\partial \eta'} \tag{3.68}$$

for Ψ, and

$$\Theta = 0 \tag{3.69}$$

and

$$\frac{\partial \Theta}{\partial \eta} = 0 \tag{3.70}$$

for Θ. The value of the vorticity at the surface is calculated by solving the Poisson

equations, (3.41), at the surface.

Far downstream the flow exits to a two-dimensional Blasius condition. The third component of the streamfunction-like vector used here, namely ψ, is equivalent to the traditional two-dimensional streamfunction if $\Theta = \Omega_1 = 0$. In a Blasius flow this streamfunction is given by

$$\psi = \sqrt{2s} f_b(\eta_b) \quad , \tag{3.71}$$

where s is the arc length along the parabola, f_b is the Blasius function and η_b is the Blasius coordinate given by

$$\eta_b = \frac{h_w \eta_w'}{\sqrt{2s}} \quad . \tag{3.72}$$

Noting that

$$\frac{\partial^2 \psi}{\partial \eta'^2} = -h^2 \omega_3 \tag{3.73}$$

in the boundary-layer, we can use (3.71) and differentiate it to find

$$h^2 \omega_3 = h_w \frac{f_b(\eta_b)}{\sqrt{2s}} \quad . \tag{3.74}$$

The non-dimensional arc length along the parabola surface is given by

$$s = \frac{1}{2}\left[\xi\sqrt{\xi^2 + R} + R\ln\left(\sqrt{\xi^2 + R} + \xi\right)\right] - \frac{1}{2} R\ln\left(\sqrt{R}\right) \quad . \tag{3.75}$$

To leading order, at large ξ' the arc length is given by

$$s \sim \frac{1}{2}\xi'^2 + \ldots \tag{3.76}$$

and the Blasius coordinate is

$$\eta_b \sim h_w \frac{\eta_w}{\xi'} + \ldots \quad . \tag{3.77}$$

Substituting (3.76) into (3.71) gives

$$\psi \sim \xi' f_b(\eta_b) + \ldots \quad . \tag{3.78}$$

Differentiating with-respect-to ξ' gives

$$\frac{\partial \psi}{\partial \xi'} \sim f_b(\eta_b) - \frac{\eta_w'}{\xi'} f_b'(\eta_b) + \ldots \quad . \tag{3.79}$$

However in the limit as $\xi' \to \infty$

$$\frac{\partial \psi}{\partial \xi'} \sim f_b(\eta_b) = \frac{\psi}{\xi'} \quad . \tag{3.80}$$

Differentiating (3.79) with-respect-to ξ' and again taking the limit as $\xi' \to \infty$ results in

$$\frac{\partial^2 \psi}{\partial \xi'^2} \sim 0 \quad . \tag{3.81}$$

A similar analysis can be done for ω_3 which results in

$$\omega_3 \sim \frac{f_b(\eta_b)}{\xi'} \tag{3.82}$$

and

$$\frac{\partial \omega_3}{\partial \xi'} \sim -\frac{\omega_3}{\xi'} \tag{3.83}$$

for the first derivative and

$$\frac{\partial^2 \omega_3}{\partial \xi'^2} \sim \frac{2\omega_3}{\xi'^2} \tag{3.84}$$

for the second derivative. (3.80), (3.81), (3.83) and (3.84) are used to evaluate derivatives at the downstream boundaries which are placed at large absolute values of ξ'.

At the far-field, the two-dimensional potential flow solution is recovered, since it is unaffected by the roughness at the surface. Therefore, all vorticity components at this boundary vanish, i.e.

$$\Omega_1 = \Omega_3 = 0 \quad . \tag{3.85}$$

In addition, the parts of the streamwise and spanwise velocity components not written in terms of the potential flow solution are set to zero, i.e.

$$\frac{\partial \Psi}{\partial \eta} = \frac{\partial \Theta}{\partial \eta} = 0 \quad . \tag{3.86}$$

This procedure recovers the potential flow solution at the far-field, with the exception that any flow displacement in the wall-normal direction due to the presence of the roughness is allowed because the streamwise and spanwise derivates of Ψ and Θ which effect the wall-normal velocity are non-zero.

Finally, the main boundary condition used in this study at the spanwise boundaries is a symmetry flow condition. For this condition, any variables which would exist in a two-dimensional flow (Ψ and Ω_3) have a vanishing first derivative normal to the boundary. Meanwhile, any variables which do not exist in a two-dimensional flow (Θ and Ω_1) are themselves equal to zero on the spanwise boundary.

The Energy Equation

In Cartesian tensor form, the general form of the non-dimensional compressible energy equation is given by

$$\begin{aligned} \rho\left(\frac{\partial T}{\partial t} + u_j \frac{\partial T}{\partial x_j}\right) = &-(\gamma - 1)\left[1 + \gamma M_\infty^2 P\right]\frac{\partial u_j}{\partial x_j} + \gamma(\gamma - 1) Re^{-1} M_\infty^2 \Phi \\ &+ \gamma Re^{-1} \frac{\partial}{\partial x_j}\left[\frac{\mu}{Pr}\frac{\partial T}{\partial x_j}\right] \quad , \end{aligned} \tag{3.87}$$

where the viscous dissipation term is

$$\Phi = -\frac{2}{3}\mu\left(\frac{\partial u_j}{\partial x_j}\right)^2 + \mu\frac{\partial u_k}{\partial x_j}\left(\frac{\partial u_j}{\partial x_k} + \frac{\partial u_k}{\partial x_j}\right) \quad . \tag{3.88}$$

In the study of incompressible flows it is customary to assume that fluid properties are constant throughout the flow while still allowing temperature variation (see Schlichting[9]). That is, in terms of non-dimensional variables it is assumed that

$$\rho = \mu = k = 1 \quad . \tag{3.89}$$

The form of the energy equation model used in this study is determined by substituting (3.89) into (3.87) and (3.88). In addition, since the focus here is on the effects of the roughness fields in incompressible flow, this study sets $M_\infty = 0$ so that the pressure term and the dissipation term vanish in (3.87). Continuity results in the first term on the right side of (3.87) vanishing as well. The final form of the energy equation model being examined in this study is then

$$\frac{\partial T}{\partial t} + u_j\frac{\partial T}{\partial x_j} = \gamma\, Re^{-1} Pr^{-1}\frac{\partial^2 T}{\partial x_j^2} \quad . \tag{3.90}$$

Schlichting[9] has shown that when (3.89) is used the energy equation becomes decoupled from the flow field so that the velocity components can be determined first and then these values are treated as known quantities in solving for the temperature with (3.90). This is the approach taken in the current study.

Since water exists in both liquid and solid form at the surface during glaze ice accretion, the surface temperature is likely the freezing point of water, or 0°C. Therefore, the temperature boundary condition used at the surface in this study is held fixed at this value. At the far-field, the temperature should recover to the corresponding inviscid temperature

since the grids used in this study do not extend out of the domain of influence of the parabola. In general, for a compressible flow, the inviscid temperature at any given point is determined by the equation

$$T\left(1+\frac{\gamma-1}{2}M^2\right)=T_\infty\left(1+\frac{\gamma-1}{2}M_\infty^2\right) \quad , \tag{3.91}$$

where M is the local Mach number in the inviscid flow at the point of interest. Again, this study uses M_∞=0 so that (3.91) simply reduces to

$$T=T_\infty \quad . \tag{3.92}$$

This is the boundary condition on the temperature at the far-field used in this study. Differencing of the energy equation is done in a manner which is similar to the differencing of the main flow equations and is described in the next section.

Differencing of the Governing Equations

This section describes the differencing schemes that are used for discretization of the governing equations. In addition, the method by which the discretized equations are solved is also described.

Temporal Integration Schemes

Consider a symbolic form of the vorticity transport equations, (3.40), given by

$$\frac{\omega_i^n-\omega_i^{n-1}}{\Delta t}+C_i=S_i+D_i \quad , \tag{3.93}$$

where the subscript indicates the particular vorticity component and the superscript n denotes the current time level during an unsteady solution of the governing equations. The letters C, S and D in (3.93) denote the convection, vortex stretching and diffusion terms, respectively, in the governing equations regardless of the spatial differencing scheme used. The time level at which these terms are evaluated determines the method of temporal integration being used

and the stability properties of the resulting algorithm. For example, if all terms are evaluated at the current time level,

$$\frac{\omega_i^n - \omega_i^{n-1}}{\Delta t} + C_i^n = S_i^n + D_i^n \tag{3.94}$$

then the resulting scheme is fully implicit and the algorithm is unconditionally stable for linear problems (neglecting the stability issues resulting from applying the boundary conditions). This allows a relatively large time step to be taken during the numerical solution to arrive quickly at the final time-averaged quantities or a steady-state solution. Note that the temporal discretization term in (3.94) must be written using values from the n-2 time level in order for the solution to be second order accurate in time. This can be avoided by evaluating the other terms in (3.94) as an average of the current time level and the previous time level,

$$\frac{\omega_i^n - \omega_i^{n-1}}{\Delta t} + \frac{1}{2}\left(C_i^n + C_i^{n-1}\right) = \frac{1}{2}\left(S_i^n + S_i^{n-1}\right) + \frac{1}{2}\left(D_i^n + D_i^{n-1}\right) \quad . \tag{3.95}$$

This is the second order accurate Crank-Nicholson scheme. This scheme is also unconditionally stable for linear problems and has the advantage of containing information of the time rate of change of vorticity from the previous time level during the solution of the vorticity at the current time level. While both (3.94) and (3.95) allow large time steps to be taken, a dis-advantage is that both are computationally expensive per iteration. This is because all terms in (3.93) must be evaluated at each iteration and the non-linear terms require more iterations to achieve convergence. For Direct Numerical Simulation (DNS) type calculations the large time step advantage may be lost because such calculations often require accuracy over a large range of time scales (see Moin & Mahesh[46]). However, evaluating all terms in (3.93) at the n-1 time level (the fully explicit approach) requires a very

large reduction in the time step in order to maintain numerical stability, about three orders of magnitude in the experience of the author, with the current problem of interest. A compromise is to evaluate the convection and vortex stretching terms explicitly using the Adams-Bashforth method while evaluating the diffusion terms implicitly using the Crank-Nicholson method, i.e.

$$\frac{\omega_i^n - \omega_i^{n-1}}{\Delta t} + \frac{1}{2}\left(3C_i^{n-1} - C_i^{n-2}\right) = \frac{1}{2}\left(3S_i^{n-1} - S_i^{n-2}\right) + \frac{1}{2}\left(D_i^n + D_i^{n-1}\right) \quad . \tag{3.96}$$

This temporal integration scheme is often called the semi-implicit scheme or the implicit-explicit scheme (see Moin & Mahesh[46]). Using (3.96) requires a reduction of the time step by about one and a half orders of magnitude in comparison to the fully implicit scheme to maintain numerical stability. However this time step reduction is also usually required when solving for all possible turbulence time scales in the flow, thus it is often the temporal integration method of choice for DNS calculations. For example, variations of this scheme were used by Joslin & Grosch[47] and Tufo *et al*.[48] for DNS of flow over roughness of different scales. Furthermore, (3.96) can be modified so that only the wall-normal diffusion terms are evaluated implicitly while streamwise and spanwise diffusion terms are evaluated explicitly. Doing so typically does not require a further reduction in the time step to ensure stability, and applying this new scheme to the incompressible energy equation model allows the temperature field to be solved in a single sweep of the flow domain.

Because of the different advantages of each temporal integration scheme (i.e. fully implicit, Crank-Nicholson and semi-implicit) all three schemes are implemented in the code that has been written for the current study. This will allow the code to be extended to study flow conditions of varying time scales including vortex shedding, break down to turbulence,

leading edge pitching, and dynamic surface water development.

For unsteady calculations, the governing equations are iterated at each time step until the changes in the flow variables from one iteration to the next are less than a specified convergence criteria. A satisfactory convergence criteria for the vorticity components is found to be 10^{-2}. Convergence is accelerated at each time step by providing an improved initial guess of the flow-field using the solution from the previous time step. For example, before iterating upon the governing equations at time level n+1, an initial guess is made for Ω_3 using the equation

$$\Omega_3^{n-1} = \Omega_3^n + \beta\left(\Omega_3^n - \Omega_3^{n-1}\right) \quad . \tag{3.97}$$

This equation is a first order Taylor series with a discretized first order derivative. The β term is used to relax the prediction. Typically β =1, however sometimes it may be advantageous to use a value slightly less than one to avoid "shooting" past the final solution at the next time step. A prediction is made for all four variables, both streamfunction-like components and both vorticity components using (3.97), for each time step. Applying this method was found to result in only about 1/3 as many iterations being required per time step to converge to the chosen convergence level, compared to no convergence acceleration being applied.

Differencing of Non-Convection Terms

The diffusion and vortex stretching terms in the vorticity transport equations and all terms in the streamfunction-like Poisson equations are discretized using second order accurate central differences, see Tannehill *et al*.[49].

Differencing of Convection Terms

One of the more critical aspects of any numerical algorithm is the method used to

discretize the convective terms. The differencing scheme which is applied to these terms impacts the overall accuracy of the solution, the amount of artificial dissipation present in the solution and the scheme's stability properties. Viewing the current study as an extension of the two-dimensional study of Huebsch & Rothmayer[50] to three dimensions, the baseline approach is to use central differencing for all convection terms, like that used in Huebsch & Rothmayer[50]. This method works for most steady three-dimensional calculations, however for some three-dimensional steady calculations and most unsteady calculations the solver cannot tolerate oscillations in the solution the way that two-dimensional calculations can. One of the primary sources of oscillations in the flow field during iteration is the interaction of the Prandtl transposition used to model the roughness and the shear layer downstream of the roughness. Figure 17 shows the vorticity immediately downstream of a single roughness element. Also shown is the grid and a grid line of constant η (dark line). The shear layer, or high gradient region, is clearly visible in Figure 17 between the dark blue and yellow/green regions. Because of the Prandtl transposition, the grid slopes down the back side of the roughness instead of remaining parallel to the shear layer. As a result, the grid in the wake of the roughness is skewed relative to the local flow, with high gradients in the shear layer. When central differencing is used for the convective terms in this scenario, oscillations can result which may grow during the iterative process and cause the solution to become unstable. To counter this problem, a number of upwinding methods are implemented in the code. Upwinding is chosen because it is a natural way to introduce varying levels of numerical dissipation into the solution without requiring extra dissipation specific terms or user knowledge of allowable dissipation coefficients.

The second differencing method for the convection terms implemented within the

code is the Essentially Non-Oscillatory (ENO) and Weighted ENO (WENO) methods for discretization of the convection terms. Details of the WENO scheme are not given here and the reader is referred to more comprehensive sources on the subject such as Liu *et al*.[51]. Both the ENO and WENO schemes consider the three possible third order upwind difference stencils about grid point i. These are

$$\Psi_{\bar{\xi}}^{1}=\frac{11\Psi_{ijk}-18\Psi_{i-1\mathrm{jk}}+9\Psi_{i-2\mathrm{jk}}-2\Psi_{i-3\mathrm{jk}}}{6\Delta\bar{\xi}},$$
$$\Psi_{\bar{\xi}}^{2}=\frac{2\Psi_{i+1\mathrm{jk}}+3\Psi_{ijk}-6\Psi_{i-1\mathrm{jk}}+\Psi_{i-2\mathrm{jk}}}{6\Delta\bar{\xi}} \qquad (3.98)$$
$$\text{and}\quad \Psi_{\bar{\xi}}^{3}=\frac{-\Psi_{i+2\mathrm{jk}}+6\Psi_{i+1\mathrm{jk}}-3\Psi_{ijk}-2\Psi_{i-1\mathrm{jk}}}{6\Delta\bar{\xi}},$$

where i-1 is in the upwind direction. Note that each successive difference approximation becomes more skewed towards the downwind direction. The stencil which is chosen by the ENO scheme is the one whose corresponding polynomial interpolates the function in the smoothest manner using a complicated polynomial reconstruction process. The WENO scheme recognizes the fact that, at least in smooth regions of the flow, to pick just one of the stencils in (3.98) is overkill. Rather a weighting of the three different stencils is used. The result is that in smooth regions the scheme can be up to fifth order accurate while in regions of high gradients, where one of the stencils is chosen predominantly over the other two in order to avoid oscillations, the scheme still remains at least third order accurate. However, the smoothing process employed by the WENO scheme can tend to introduce too much artificial dissipation into the flow.

As a compromise between the oscillations of central differencing and the potential for excessive dissipation of the WENO scheme, a third method for calculating the convection terms is implemented. This third method for differencing convection terms is a simple blend

of a second order central difference and a second order upwind difference given by

$$\Psi_{\bar{\xi}} = \lambda \Psi_{ud} + (1-\lambda)\Psi_{cd} \quad , \tag{3.99}$$

where "ud" and "cd" denote standard second order upwind and central differences, respectively. The λ is included to be able to vary the degree of upwinding and avoid excessive numerical dissipation beyond what is required for stability. Choosing $\lambda = 1/3$ gives a third order approximation known as the QUICK scheme which is identical to the second equation in (3.98).

Figure 18 shows a qualitative comparison of the three convection differencing schemes (central, WENO and QUICK) using a particular test case for an unsteady flow solution over an isolated two-dimensional roughness element. The lines in Figure 18 show contours of the spanwise vorticity, Ω_3. Figure 18a shows the central differencing scheme. The advantage of the central difference scheme is low numerical dissipation and low computation time. However, just downstream of the roughness peak oscillations are apparent in the solution. These oscillations can cause the three-dimensional flow solver to become unstable. Figure 18b shows the vorticity contours for the WENO scheme. Figure 18b is a smooth solution. However, the WENO solutions have a high level of numerical dissipation. Finally, Figure 18c shows the QUICK scheme which uses (3.99) with $\lambda = 1/3$. The shapes of the vortices are very similar to Figure 18a which indicates that numerical dissipation is low. However, enough dissipation has been introduced so that the oscillations downstream of the roughness are avoided. It should be noted that if λ is increased to unity in (3.99), the vorticity contours look similar to Figure 18c with a small increase in evident numerical dissipation. The flow upstream of the roughness element in Figure 18, which is periodic and unsteady, is not significantly affected by the varying levels of numerical dissipation of the

various schemes.

Because of the clear advantages of the QUICK scheme over either second order central differencing or the WENO scheme, the QUICK method of convective discretization is used for the majority of calculations in this study. For some higher Re_k flows the WENO scheme is used to obtain a qualitative picture of the flow over the roughness.

One important aspect of any upwind differencing scheme is to determine the proper upwinding direction. Typically, the physical velocity is simply used as an indication of the local flow direction. The characteristic (see Tannehill *et al*.[49]) direction, however, is with respect to the grid and not necessarily the physical domain. It turns out that when the shearing transformation is applied the two are not the same in the wall-normal direction. The physical velocity in contravariant coordinates is given by (3.52). Applying (3.53) and the shearing transformation to this equation results in

$$\begin{aligned} U &= \frac{1}{h}\left(\frac{\partial \Psi}{\partial \eta} + \frac{\partial \bar{\psi}}{\partial \eta}\right) \quad , \\ V &= \frac{1}{h}\left[-\frac{\partial(\Theta)}{\partial \zeta} + f_\zeta \frac{\partial(\Theta)}{\partial \eta} - \frac{\partial \Psi}{\partial \xi} + f_\xi \frac{\partial \Psi}{\partial \eta} - \frac{\partial \bar{\psi}}{\partial \xi'}\right] \\ \text{and} \quad W &= \frac{1}{h^2}\frac{\partial(\Theta)}{\partial \eta} \quad . \end{aligned} \tag{3.100}$$

Conversely, velocities can be defined with respect to the grid. Taking guidance from (3.52) and starting with the coordinate system after the shearing transformation, the grid-based velocity components are found to be

$$\hat{U} = \frac{1}{h}\left(\frac{\partial \psi}{\partial \eta}\right) \quad ,$$
$$\hat{V} = \frac{1}{h}\left[-\frac{\partial (h\theta)}{\partial \zeta} - \frac{\partial \psi}{\partial \xi}\right] \qquad (3.101)$$
$$\text{and} \quad \hat{W} = \frac{1}{h^2}\frac{\partial (h\theta)}{\partial \eta} \quad .$$

Since the inviscid derivatives of the streamfunction are defined with respect to the primed coordinates it is necessary to go backwards through the shearing transformation. Doing this gives

$$\hat{U} = \frac{1}{h}\left(\frac{\partial \Psi}{\partial \eta} + \frac{\partial \bar{\psi}}{\partial \eta'}\right) \quad ,$$
$$\hat{V} = \frac{1}{h}\left[-\frac{\partial (\Theta)}{\partial \zeta} - \frac{\partial \psi}{\partial \xi} - \frac{\partial \bar{\psi}}{\partial \xi'} + f_{\xi}\frac{\partial \bar{\psi}}{\partial \eta'}\right] \qquad (3.102)$$
$$\text{and} \quad \hat{W} = \frac{1}{h^2}\frac{\partial (\Theta)}{\partial \eta} \quad .$$

Comparing (3.100) and (3.102) it can be seen that there is no difference between the grid and physical streamwise and spanwise velocities. Therefore, using the sign of the physical velocity will not cause any problems. For the wall-normal velocity, however, there are differences between the terms which are being multiplied by roughness derivatives. Though the differences are small they can lead to a different sign of the grid wall-normal velocity, $\hat{V}$, compared to the physical wall normal velocity, V, in regions where the roughness derivatives are large. If an upwinding scheme is used in the wall normal direction, using the physical wall normal velocity to determine differencing direction may lead to an instability in the algorithm. This is consistent with observations that were made using two-dimensional calculations from this study. That is, choosing the upwinding direction of the wall-normal velocity using (3.100) resulted in instabilities that originated at the maximum slope of the roughness. This is resolved by using the grid wall normal velocity as defined by (3.102)

instead.

It is also worth noting that, as it is written, (3.54) allows a conservative differencing approach for both the convection as well as vortex stretching terms (i.e. the nonlinear terms). This would be accomplished by defining the differences using the product of the velocity components with the respective vorticity component. If a vorticity-velocity approach were being used this would be more feasible. However, it would require the solution of six equations for six unknowns. In the current streamfunction-like / vorticity framework, the conservative differencing approach was attempted but proved to require too much memory and was considerably more expensive per iteration. Instead, the derivatives in (3.54) are evaluated using a chain rule to arrive at a non-conservative form of the vorticity transport equations (see the appendix for the final form of the equations being used in this study).

Method of Solution

Regardless of the method of temporal integration and the spatial differencing scheme used, the basic methodology for solving the resulting system of equations is the same and uses an ADI-like iteration procedure. The discretized equations at each grid point are written in the form

$$A_i \Psi_{i-1} + B_i \Psi_i + C_i \Psi_{i+1} = D_i \quad . \tag{3.103}$$

In the current study the ADI scheme is actually a block ADI scheme, and all four equations are coupled and solved simultaneously. Therefore the A, B and C in (3.103) are 4x4 arrays and D is a four element vector. If the indices i,j,k define a given point in the structured grid, then for a given j,k (constant vertical and spanwise grid lines) (3.103) is written for each i along with appropriate boundary conditions. This forms a system of linear equations which is inverted via a modified Thomas algorithm (see Tannehill *et al.*[49]). The iteration then

proceeds to grid point j+1,k where the process is repeated. This procedure is carried out for all j,k. Following inversion in the streamwise direction, the solution is marched for all i,k with inversion of (3.103) in the j direction. This is followed with inversion in the spanwise direction as well. This entire procedure constitutes one iteration of the flow field. The iteration process is repeated until the change in flow variables from one iteration to the next is less than a specified tolerance. Monitoring of the vorticity components was found to be the best indicator of whether or not a flow field is converged. For steady flows, an absolute maximum error convergence criterion of 10^{-4} is typically found to be more than sufficient. If a steady solution is being sought then the solution is complete when this convergence criteria is reached, for unsteady flows the solution moves on to the next time step.

For each situation where the convection or vortex stretching terms are being treated implicitly, these terms are linearized by applying a Newton linearization. For example,

$$\frac{\partial \Psi}{\partial \eta}\frac{\partial \Omega_3}{\partial \eta} = \left(\frac{\partial \Psi}{\partial \eta}\right)^g \frac{\partial \Omega_3}{\partial \eta} + \frac{\partial \Psi}{\partial \eta}\left(\frac{\partial \Omega_3}{\partial \eta}\right)^g - \left(\frac{\partial \Psi}{\partial \eta}\right)^g \left(\frac{\partial \Omega_3}{\partial \eta}\right)^g \quad , \tag{3.104}$$

where the superscript *g* indicates that the term is evaluated based on "guessed" values from the previous iteration.

The ADI method is an efficient algorithm for the implicit solution of finite difference equations. While it is more efficient than fully coupled methods, it often does not have as good a convergence rate. This is primarily due to the fact that the flow field is only being coupled in one direction at a time (the inversion direction). This can be at least partly overcome by employing multi-grid type techniques to communicate boundary condition information to the interior of the flow domain more quickly. In the current study coarse grids are used to provide initial solutions for finer grid calculations. The typical procedure is to

start with a grid which has half the resolution of the final grid to be used. The flow solution is fully converged on this coarse grid. Following this, a second grid is constructed which has a resolution which is half way between the coarse grid and the final grid. The initial condition for the second grid is the converged solution from the coarse grid which is linearly interpolated onto this second grid. The solution is also fully converged on the second grid. Finally, this second grid solution is linearly interpolated onto the final grid as the starting solution for the final grid computation. While not a true multi-grid method, this simple procedure is found to decrease the solution time by about 60% compared to a single grid solution.

Parallel Processing

Due to the large computational requirements of three-dimensional solutions, a multi-processor approach is necessary for efficient computations. The main consideration in the design of the parallel processing capabilities of the code is the ability to run efficiently on large clusters of workstations or PC's (so-called Beo-Wulf clusters) which have become increasingly available and economical. Such a design would necessarily be a distributed memory architecture where each processor has its own block of data to operate on. The design should also limit message passing between processors as much as possible and instead opt for more computation per processor. This takes advantage of the fast speeds of the newer PC processors while avoiding overloading parallel clusters with lower network bandwidth.

When designing a distributed memory parallel code, the most important decision is how to divide up the grid among the processors. To avoid complexity, the code divides the grid up in only one coordinate direction instead of multiple coordinate directions. The desire to avoid large gradients along the partitioned direction typically rules out partitioning the grid

normal to the wall. Of the remaining two directions, streamwise and spanwise, the current application typically has many more grid points in the streamwise direction, so partitioning the grid in this direction will lead to improved scalability for large numbers of processors. In addition, a spanwise partitioning scheme would require extra communication between processors due to the periodic boundary conditions being applied in that direction. Finally, partitioning in the spanwise direction also requires passing larger blocks of data between processors, for the current application. A schematic of the streamwise grid partitioning scheme is shown in Figure 19a.

Each processor is assigned its own block of data on which to operate. Locally, each processor carries out the method of solution described in the previous section, in which the governing equations are inverted in one of the coordinate directions while marching in the other two coordinate directions. After the inversion over the entire grid block is complete, each processor passes data to neighboring processors in preparation for inversion in the next coordinate direction. Figure 19b shows the message passing pattern between neighboring processors after each sweep of the grid. Processor i marches/inverts the data between the dashed grid lines. At the edges of each data block is a buffer region of grid points which contains data from the neighboring processor. Figure 19b shows a buffer region containing two grid points, which is the minimum required for the QUICK scheme. Note that because each processor effectively operates independently from the neighboring processor, a discontinuity can exist in the data between processors which can lead to reduced convergence rates. One method of counter-acting this problem is to add a ghost region for each processor. A ghost region is an extension of a processor's grid block into the neighboring processor's grid block. In the case of Figure 19b, when marching in the direction of increasing ξ,

processor i receives the ghost region from processor i-1. Processor i then starts the sweep in ξ at the beginning of this ghost region before sweeping over its own data. The ghost region effectively provides improved guess values for the data owned by processor i. After the sweep of the grid block is complete, the ghost region is updated with data from processor i-1. Even though the computational cost per iteration increases slightly when using ghost regions, convergence rates typically increase. Ghost regions containing a few grid points are typically the most efficient.

Keeping data local to each processor minimizes communication between neighboring processors and typically leads to good scalability. Scalability performance of the code was measured by running a three-dimensional test case on the Itanium NCSA cluster at the University of Illinois. The cluster consists of 800 MHz Itanium processors running the Linux operating system and connected by a Myrinet high speed network. The calculation was run out to 200 iterations on a 1024x101x91 grid with the number of processors increasing for each run. The parallel performance of the code is shown in Figure 20. The speedup in Figure 20 is defined to be

$$Speedup = \frac{T_s}{T_p} , \tag{3.105}$$

where T_s is the serial run time on a single processor and T_p is the run time on p processors. Since the test problem could not be run on a single processor because of memory limitations, the serial run time was obtained by finding T_4 (the run time on four processors) and multiplying by four (i.e. assuming a linear relationship for small numbers of processors). As the number of processors was increased, the amount of memory required per processor decreased. This results in a larger portion of the problem residing in the high speed cache

and registers. This leads to super-linear speedup for the current problem below about 32 processors. As the number of processors is increased beyond this amount, this effect is counter-acted by the increase in inter-processor communication per grid point and the resulting speedup is less than the theoretical maximum. Note that the design of the parallel architecture which minimizes inter-processor communication allows good speedup to be maintained through 128 processors. From Figure 20 it can be seen that the speedup for 128 processors is still about 84% of the theoretical maximum despite the fact that this case has just eight streamwise grid points per processor (and larger communication to computation ratio). As the problem size increases the scalability is expected to remain closer to the theoretical value for larger numbers of processors.

CHAPTER 4. VALIDATION OF THE NAVIER-STOKES FLOW SOLVER

In this chapter the Navier-Stokes code is validated by comparing results with existing numerical results, new results from a commercial CFD code and experimental results. In addition, the validation cases cover three different roughness/flow regimes of a) steady flow over shallow roughness, b) steady flow over O(1) aspect ratio roughness and c) unsteady flow over O(1) aspect ratio roughness.

Comparison with Previous Numerical Results for Shallow Roughness

The logical place to start the code validation is the numerical test case which was performed by Davis *et al*.[42], who developed the numerical method upon which the present study is patterned. It should be noted that because the roughness elements are shallow, Davis *et al*.[42] used a thin-layer Navier-Stokes implementation of the algorithm. Also, that study used a first-order upwinding technique for the convection terms. Ddue to the relatively benign flow conditions the solution is not expected to be affected greatly by the increased numerical dissipation.

The 3% bump of Davis *et al*.[42] is a secant function (see (3.11)) with k=0.03, λ_s = λ_ζ =4, s_0 =2.5 and ζ_0 =0.

Figure 21 shows the streamwise skin friction down the roughness center-line. The circles are the data from Davis *et al*.[42] which is for the shallow three-dimensional roughness on a flat plate at a freestream Reynolds number of 60,000. The lines are from the present study for the same roughness element placed on parabolas with varying leading edge radius of curvature, R. Recall that as $R \to 0$ the parabola better approximates a flat plate. For each value of R, the roughness position is chosen so that the approaching streamwise skin

friction is the same as that seen in the Davis *et al.*[42] data. For R=0.1 there are two curves. The solid curve uses a coarse grid while the dashed curve uses a fine grid which has approximately twice the grid resolution of the coarse grid. All other calculations use the coarse grid.

Figure 21a shows that as $R \to 0$ the current study compares well with the Davis *et al.*[42] data. In particular, the R=0.01 data is the only case to capture the negative skin friction just downstream of the roughness. For the typical parabola with R=1, the favorable pressure gradient prevents the flow from decelerating to the point where the skin friction changes sign.

Figure 21b shows the spanwise skin friction at the spanwise plane ζ =0.3. Once again, both the coarse grid and fine grid results are shown for R=0.1. In this case reducing R to 0.1 is sufficient to calculate the spanwise skin friction. Note that the spike in the Davis *et al.*[42] data upstream of the roughness is due to the upstream boundary condition used in that study.

A second comparison case with Davis *et al.*[42] is for a 6% dent which has the same geometrical parameters as the 3% bump except that now k=-0.06. In addition, for this case the Reynolds number is reduced to 8,000. The result is a larger region of separation as well as an opposite sign of the spanwise skin friction for a given spanwise plane. Figure 22a shows the streamwise skin friction down the dent center-line. Over the majority of the dent the present study agrees well with the Davis *et al.*[42] data for R=0.01. Away from the dent the two curves diverge slightly due to the differences in the base geometry (i.e. flat plate vs. thin parabola). Figure 22b shows the spanwise skin friction at the ζ =0.3 plane. As mentioned, the sign of the spanwise skin friction of the dent is opposite to that of the bump as

the flow is first turned inward toward the plane of symmetry and then turned outward on the lee side of the dent. Once again, the shape of the spanwise skin friction from the current study is close to the Davis *et al.*[42] data with a slight offset between the two curves, likely due to the difference in the base geometry.

As a final check, a comparison of two streamwise velocity profiles for the 6% dent are shown in Figure 23. Figure 23a shows a comparison at the dent's maximum depth on the roughness center-line. The separation region clearly shows up as a region of negative streamwise velocity. Figure 23b shows a comparison at the same streamwise location but away from the symmetry plane at ζ =0.3. In both cases, the comparison between the current study and the Davis *et al.*[42] data is good.

Comparison with Fluent Results

In order to fully validate the code for flow over steady roughness, a more detailed comparison for flow over O(1) aspect ratio roughness is required. Existing numerical studies for this type of flow are scarce. Therefore, the commercial code Fluent is used to generate the results for comparison. In this case, the roughness and base geometries near the roughness element are identical. A quartic roughness element (see (3.9)) is used and placed on the R=1 parabola leading edge at s=1 (i.e. one leading edge radius of curvature from the stagnation point). In this case the roughness is defined by k=0.05, $\lambda_s = \lambda_\zeta$ =0.2 and m=10. These parameters give the roughness on the parabolic leading edge shown in Figure 24. This figure includes a close-up of the single roughness element, including the surface mesh used. The surface geometry from the fine mesh region was imported into Gambit, the pre-processor for Fluent, in order to match the roughness shape as closely as possible between the two codes. Additional surface geometry and boundaries were then added to complete the

flow domain to be used by Fluent.

Originally, both codes were used to solve for the flow over half of the roughness, with a symmetry boundary condition applied at both spanwise boundaries shown in Figure 24. However, it was realized that the Fluent calculations did not seem to treat the symmetry condition properly, with certain contour lines not approaching the symmetry plane perpendicular to the plane itself. As a result, the spanwise domain of the Fluent calculation was doubled so that the symmetry condition at the roughness center plane was not necessary. It is not expected that the remaining symmetry conditions at the spanwise boundaries in the Fluent calculation have a significant effect on the flow over the roughness element itself.

The total number of grid points and mesh spacing used for the Fluent half domain is similar to the grid used in the current study.

In all cases of problem setup, every attempt was made to use the same numerical options in the Fluent calculation as are used in the current study. For example, the QUICK scheme was used in the Fluent calculation for differencing the convective terms, while the current study also uses the QUICK scheme in the streamwise and spanwise directions. However, it is noted that the general approach taken by the two codes in solving the incompressible Navier-Stokes equations is different. Fluent is a finite volume based code which solves the primitive variable form of the Navier-Stokes equations in Cartesian coordinates. As detailed in the previous chapter, the current study is a finite difference code which solves a streamfunction-like / vorticity form of the Navier-Stokes equations in contravariant coordinates. The effect of the roughness in the current study is captured directly via explicit terms which appear in the governing equations. The effect of the roughness in the Fluent code is captured via the shape and boundary condition at the wall and

is subsequently propagated into the flow interior.

Figure 25 through Figure 28 show a comparison for the three Cartesian vorticity components at various locations over the roughness. Vorticity is chosen as the variable of comparison because it is the basis of the numerical method used in the current study and it tends to amplify differences between codes. At the top of each figure is a slice of the roughness at a given spanwise plane. Contours of the particular component of vorticity are shown on this plot as well for both the Fluent calculation and the current study. For example, Figure 25 shows contours of the spanwise vorticity (z-vorticity) at the top of the page. Other figures show the vorticity which is aligned with the Cartesian x-axis (x-vorticity) or with the Cartesian y-axis (y-vorticity). Also shown in each figure are profile comparisons of each particular vorticity component at various streamwise locations for the given spanwise plane. The location of the profiles relative to the roughness is also shown as the vertical lines in the plot at the top of each page.

In most cases, the comparison between the Fluent calculation and the current study agree fairly well. On the roughness center-plane (z=-0.05), Figure 25 shows a comparison of the z-vorticity. Upstream of the roughness the contours from the two codes are identical. Downstream of the roughness there is some difference between the two codes for small magnitude of the vorticity. However, the profile shown at x=-0.08 shows a relatively good agreement between the codes. At z=-0.03, Figure 26, the comparison of the z-vorticity is actually a little bit better, likely due to the fact that the gradients of the z-vorticity in this plane are smaller.

Figure 27 shows the x-vorticity also at the z=-0.03 plane. There are small differences in the outer-most contour in the top plot. In addition, the profile at x=-0.12 shows a fairly

significant difference between the two codes near the surface. By examining the plot at the top of the figure it can be seen that differences between the codes in this profile are amplified due to the fact that this profile is in a high gradient region. This is demonstrated by also plotting a profile from the current study at x=-0.119, that is a profile which is only slightly shifted from the nominal profile at x=-0.12. Both lines are shown in the top plot of Figure 27 (x=-0.119 is a dotted line) however they are nearly indistinguishable from each other. The x-vorticity at x=-0.119, shown as open squares, nearly directly coincides with the x-vorticity at x=-0.12 from the Fluent calculation, shown as open circles. Thus it is concluded that the differences between the two codes at x=-0.12 are exaggerated by the large gradients.

Finally, Figure 28 shows the y-vorticity at the z=-0.03 plane. There are again some small differences noted in the contours as well as in the profiles. In general, however, the two codes are in good agreement.

The conclusion from the comparison with Fluent, which is a well validated commercial CFD package, is that the code developed for the current study is fully capable of accurately simulating flows over O(1) aspect ratio roughness on the leading edge.

Comparison with Experiment for Unsteady Flow Upstream of Roughness

Winkler[17] experimentally examined both isolated and distributed roughness placed on a flat plate. The purpose of the experiments was to identify flow mechanisms which may be responsible for the increased convective heat transfer seen just downstream of roughness elements, although the corresponding heat transfer data was not obtained. The data acquired included smoke visualization images and velocity profiles obtained with Laser Doppler Velocimetry (LDV). Because of the desire to obtain results applicable to aircraft icing the experiments were run at relatively high Re_k. For the isolated roughness experiment, which

is the case being simulated here, the value of Re_k is 3700 and the ratio of roughness height to boundary layer thickness, k/δ, is 2.5. In order to assure that a flow solution can be obtained at these conditions without numerical instability the WENO differencing scheme is used for the convection terms. In this situation, in which the WENO scheme is used to calculate unsteady flow, the algorithm is similar to a Monotonically Integrated Large Eddy Simulation (MILES) approach which is an LES scheme that uses excessive numerical dissipation as the filtering scheme. The goal of applying this scheme is to perform a preliminary test of the ability of the algorithm to capture unsteady vortex shedding and qualitative flow behavior.

The current study uses a parabola with R=0.1 to approximate the flat plate used by Winkler[17]. The roughness height is set at k=0.4 and the freestream Reynolds number is Re_R=9320. With the roughness placed at the appropriately scaled distance from the leading edge, the ratio of roughness height to boundary layer thickness computed by the code is k/δ =2.74 which is close to the value reported by Winkler[17].

The geometry and surface grid used in the calculation are shown in Figure 29. Note that in order to keep the computational grid to a manageable size, the spanwise extent of the flow domain is limited to three roughness heights. The dense grid region used in the calculation has a length of 25 roughness heights, with the downstream boundary of the dense grid region located 20 roughness heights downstream from the roughness itself. The dense grid uses 615 grid points in the streamwise direction, which is equivalent to 24.6 grid points per roughness height in the streamwise direction. The grid uses 101 grid points in both the wall-normal and spanwise directions.

Because of limited computational resources a full three-dimensional grid

independence study could not be performed. However, a series of two-dimensional calculations were performed to test the streamwise and wall-normal grid resolution to some extent. Figure 30 shows the effect of increasing the resolution in the wall-normal direction using the time-averaged streamwise skin friction. About 2.5k downstream from the roughness, the coarse grid (which is used in the three-dimensional calculation) is slightly out of agreement with the other two grids. Figure 31 shows the impact of increasing the resolution in the streamwise direction. Once again the coarse grid is the one used in the three-dimensional calculation. Note that this grid is not grid independent. Increasing the resolution to 110 grid points per k is still not sufficient for this high Re_k case. In particular, there are differences in the small scale structures 1k downstream from the roughness when compared with the finest grid.

Because the three-dimensional calculation is not grid resolved and because the WENO scheme causes excessive numerical dissipation, the results should be evaluated mostly on a qualitative level. Figure 30 and Figure 31 show that at least in terms of a two-dimensional analysis, the grid being used for the three-dimensional calculation is likely sufficient in the region upstream of the roughness. The solution will be compared with experiment in this region.

Figure 32 shows a comparison of time-averaged streamlines from the current calculation with an instantaneous smoke visualization taken from the experiment of Winkler[17] upstream of the roughness. The smoke visualization shows three primary vortices upstream of the roughness, which are labeled as such in the figure. In the experiment the instantaneous number of vortices present changed periodically with time from three to two and back to three again. The streamlines in Figure 32 from the simulation show

the existence of three vortices upstream of the roughness along with two secondary vortices. Though the secondary vortices are not labeled in the smoke visualization image their presence can be inferred. The shape and size of the vortex structures predicted by the computation differs from the experiment and this difference is likely due to a difference in the geometry at the roughness-plate juncture as well as the slightly favorable pressure gradient which exists on the thin parabola.

Figure 33 shows streamwise velocity contours near the leading edge of the roughness taken from both the Winkler[17] experiment and the three-dimensional calculation. The computation is able to predict the separated region upstream of the roughness as well as the "bulge" in the streamwise velocity contours on the roughness leading edge. This bulge is not evident in the two-dimensional calculation and appears to be a three-dimensional effect.

Figure 34 shows wall-normal velocity contours near the leading edge of the roughness. Once again the computation does a good job of predicting both the size as well as the location of the various structures.

Figure 35 shows a comparison of the time-averaged streamwise and wall-normal velocity profiles approaching the roughness element for both the experiment and the computation. Also shown by the dashed lines are the velocity profiles for a two-dimensional computation using the same parameters as the three-dimensional computation. The Δx in Figure 35 gives the distance upstream from the reference point, in roughness heights. Thus Δx =-1.5 is 1.5k upstream of the reference point, which as shown in Figure 33 is just the leading edge of the roughness. The experimental and computational curves clearly show the separation region upstream of the roughness. The separation region predicted by the two-dimensional computation is significantly larger, extending further vertically from the wall

and further upstream from the roughness. Near the roughness, however, the magnitude of the reversed flow from the three-dimensional computation is larger, indicating a larger skin-friction magnitude as well. In general, the comparison between the three-dimensional computational profiles and the experimental profiles is good, except very near the roughness. The difference in this region is possibly due to differences in the geometry being used. Recall that the computations use a filleted hemisphere which has a smooth transition to the base geometry, while the experiment used a hemisphere which intersects the flat plate at a right angle. As a result of the fillet used in the computations, the point at which the roughness computational model intersects the plate is not the same as in the experiment. Changing the reference point used to determine the streamwise location of the profiles from the computation to be the location at which the roughness model intersects the plate (or is within 1% of the maximum roughness height since it's asymptotic) gives the profiles shown in Figure 36. When the streamwise shift is applied, both the streamwise and the wall-normal velocity profiles show an improved agreement with experiment. In particular, the wall-normal velocity computed by the code now has the same sign as the experimental data. Some profiles are still under-predicted in velocity magnitude and this could again be a result of using a hemisphere which has a smooth transition to the flat plate.

As mentioned previously, the flow downstream of the roughness is excessively dissipated by the WENO differencing scheme. Again, the goal here is to demonstrate the basic capability of the code to capture unsteady vortex shedding and generating flow structures in the wake which at least have a turbulent-like appearance. This step is viewed as a pre-curser to an accurate calculation of unsteady flow in the roughness wake at high Re_k.

Figure 37 shows the development of the flow spanwise vorticity over the roughness.

Upstream of the roughness element, where a two-dimensional boundary-layer exists, the spanwise vorticity varies only with distance outward from the wall, with a maximum at the wall and decreasing to zero in the freestream. Thus, a vorticity iso-surface appears as a two-dimensional sheet. The iso-surface shown in Figure 37 is Ω_3=-1. As the flow approaches the roughness, this sheet is lifted from the surface by the presence of the roughness element. Below the sheet and along the side of the roughness there exists smaller scale iso-surfaces for Ω_3=-1 which indicates production of vorticity at the surface due to the pressure gradients which are generated by the roughness element itself. The vortex sheet is warped and twisted as it passes over the roughness element until shortly after entering the roughness wake it becomes mixed with other vorticity layers and the vorticity which is produced at the surface. At this point, it is difficult to tell which part of the iso-surfaces are due to the upstream vortex sheet and which parts are due to fresh vorticity being produced at the wall. Also shown in Figure 37 is a close-up view of the vorticity in the immediate roughness wake along with a grid overlay on the iso-surface. Though it is recognized that the flow solution is not grid independent in the roughness wake, the figure shows that there are a reasonable number of grid points within the flow structures shown in the figure. That is, there are typically several grid points per iso-surface structure.

Figure 38 shows two-dimensional slices of the flow at constant spanwise stations, again showing spanwise vorticity. At the roughness center-plane, except for the vortex rolling up on the downstream side of the roughness, there is relatively little variation in the vorticity. Moving out from the roughness center-plane an increasing level of mixing can be seen, with turbulent-like structures appearing stronger at the spanwise boundary.

Figure 39 shows a comparison of the time-averaged streamwise velocity over the

entire roughness element, including the roughness wake. As expected, the comparison in the roughness wake is not good and the excessive dissipation of the WENO scheme in this region is evident. In particular, the nearly vertical contours in the Winkler[17] figure are not reproduced by the computation.

The purpose of simulating the Winkler[17] isolated roughness experiment is to examine the ability of the code to calculate high Re_k flows over roughness. To this end the WENO scheme was applied in order to maintain numerical stability, despite the high numerical dissipation levels. The flow upstream of the roughness shows that this scheme is sufficient to capture the horseshoe flow structures and quantitatively capture the flow approaching the roughness element. Downstream of the roughness the quantitative comparison is not good. However the computational results did show the ability to capture unsteady vortex shedding and vorticity breakdown, including the computation of turbulent-like structure in the roughness wake.

CHAPTER 5. RESULTS FOR FLOW OVER THREE-DIMENSIONAL DISTRIBUTED ROUGHNESS

As indicated in Chapter 1, the most significant unknown effects of ice roughness on the icing process are the role that roughness plays in the convective heat transfer and its effect on surface water dynamics. The purpose of this chapter is to examine the effect that various distributed roughness patterns have on these two items. In particular, the study focuses on distributed roughness and properties such as the Reynolds number and roughness height, shape, spacing and streamwise extent. In all cases, the impact of the roughness on heat transfer is examined by comparing the convective heat transfer over the rough surface to the clean parabolic leading edge heat transfer.

For the effect of roughness on surface water dynamics the analysis is more qualitative. The current solutions are single phase and a true assessment of the impact of roughness on surface water dynamics requires a full multi-phase solution. This is the case in Chapter 2, which examined the effect of two-dimensional roughness elements on thin water films. The results from that chapter show that thin films are primarily air shear driven, with alterations due to pressure gradients and surface tension in areas where the air shear goes to zero. Therefore, to assess the impact of roughness on surface water dynamics the limiting streamlines (i.e. wall shear patterns) are examined in order to gain insight into the initial motion of very thin films.

Clean Leading Edge Heat Transfer

The next few sections examine the impact of various properties of distributed roughness fields on the convective heat transfer and the wall shear patterns. In examining the convective heat transfer, all of the roughness effects are presented relative to the clean

leading edge heat transfer. Therefore, it is worthwhile to briefly examine the clean leading edge heat transfer and a comparison of the code with experimental data.

Poinsatte *et al*.[52] experimentally examined the convective heat transfer in the vicinity of the leading edge of a NACA 0012 airfoil. Both flight and wind tunnel tests were performed in order to determine the potential impact that turbulence intensity could have on heat transfer. The results showed that the leading edge convective heat transfer for the airfoil was a little higher in the tunnel than in free flight owing to the increased turbulence intensities in the tunnel. However in both cases, the convective heat transfer was significantly less than the analytical result for a cylinder found by Frossling[53], which is often used in icing codes near the stagnation region of an airfoil.

Figure 40 shows a comparison of the Poinsatte *et al*.[52] free flight heat transfer data with results from the code for various Reynolds numbers. The results are presented in terms of the Frossling number, which is defined as the Nusselt number divided by the square root of the Reynolds number. In this case the reference length is the chord of the NACA 0012 airfoil. The figure shows the Reynolds number used in the code based on the leading edge radius of curvature. The value for Re_R of 15000 corresponds to a chord Reynolds number of 943,000, which is a little lower than the minimum Reynolds number tested by Poinsatte *et al*.[52] of 1.2 million. Analysis of the flight test method used indicates that the Mach number for these low Reynolds number tests was approximately 0.1 to 0.15. This is sufficiently low to be considered incompressible and using M_∞=0 in the code is justified. A freestream-to-wall temperature difference of 10ºC was used for all cases and studies of the effect of the temperature difference show that the heat transfer is not significantly affected by this parameter.

All of the curves for the various Reynolds numbers essentially collapse to a single curve when plotted as a Frossling number. This is consistent with the flight test data and it is the main reason for presenting the heat transfer data in this manner. Near the stagnation point, the code tends to under-predict the heat transfer, whereas further aft of the leading edge the code slightly over-predicts the heat transfer. Poinsatte *et al*.[52] did not have an explanation for the discontinuity in the flight test data. It is worth pointing out that the last three points in Figure 40 agree very well with laminar flat plate theory, as would be expected on an airfoil away from the stagnation point.

In the sections to follow, the effect of various roughness parameters on the convective heat transfer are examined. In all cases the augmentation of the heat transfer is assessed. The purpose of Figure 40 is to show that the clean leading edge heat transfer predicted by the code is representative of actual airfoil leading edge heat transfer. Though the flow is being solved over a parabolic leading edge and not a complete airfoil, the heat transfer data will continue to be presented as a Frossling number based on airfoil chord length. This is done by using the ratio of leading edge radius of curvature, R, to chord length, c, for a NACA 0012 airfoil which is 0.0159. However, as opposed to the case shown in Figure 40, the data will be plotted against an arc-length which is non-dimensionalized by R.

Effect of the Reynolds Number on the Base Roughness Pattern

The baseline distributed roughness pattern used in this study is shown in Figure 41. This roughness field consists of three-dimensional quartic roughness elements defined by (3.9), where $\lambda_s = \lambda_\zeta = 0.2$, m=10 and k=0.05, that is the roughness height is 5% of the leading edge radius of curvature, R. For example, for a 21" NACA 0012 airfoil, which is a standard airfoil used in icing research, this represents a roughness height of approximately 0.42mm.

Figure 42 shows a comparison of the baseline roughness pattern and the clean leading edge two-dimensional laminar boundary-layer thickness at Reynolds numbers of 1000, 5000, 10000 and 15000. At the lower Reynolds numbers the roughness field is completely submerged within the boundary-layer. At the higher Reynolds numbers tested in this study the roughness penetrates the boundary-layer and is as high as approximately twice the boundary-layer thickness near the stagnation point.

For the quartic roughness element defined by (3.9) there is no well defined diameter. However, if it is arbitrarily assumed that the diameter is defined as the point at which the roughness height is 1% of the maximum roughness height, then the diameter of the roughness shown in Figure 41 is D=0.12. The uniform spacing between roughness elements in Figure 41 is Δs =0.115, that is the spacing is approximately one roughness diameter. This value is a little smaller than observed "typical" ice roughness spacing from experimental data. However as mentioned previously, the intent here is to examine the overall effect that these various parameters have on the surface flow properties of the roughness fields.

The strip in the middle of the roughness field of Figure 41 is the baseline mesh used for the computations in this study. The flow is solved in the meshed region only, and symmetry boundary conditions are applied at each of the spanwise planes. The larger roughness field is being shown for clarity.

Figure 43 shows streamwise and spanwise skin-friction contours for flow over the roughness field at Re=5000. Both components of the skin friction increase for roughness elements which are further downstream. This is due primarily to the increasing skin-friction from the base leading edge flow which reaches a maximum on the clean leading edge at approximately x=-0.2. This corresponds to the second-to-last row of roughness elements in

Figure 43 (see Figure 42).

Figure 44 shows that there is a correlation between the skin friction and the surface heat transfer induced by the roughness, as might be expected from a Reynold's analogy. The heat transfer, presented as the Frossling number, is largest over the peaks of the roughness elements where the skin friction is largest. As seen from the plots on the right of Figure 44 this also corresponds to locations where the thermal boundary-layer is very thin, as would be expected for a roughness element which protrudes through the clean leading edge boundary-layer. The separation region which is induced between roughness elements maintains a larger region between the cold outer flow and the warmer wall (increased thermal boundary-layer thickness), and the heat transfer in these separated regions is reduced. Therefore, it is expected that the heat transfer augmentation which is caused by the roughness field depends on the magnitude of the skin friction over the tops of the roughness elements and the size of the separation regions between the roughness elements.

This correlation between the skin friction and the convective heat transfer is also seen to some degree in Figure 45. Each spike in the streamwise skin friction, C_{fs}, is accompanied by a corresponding spike in the Frossling number. However, it can be seen that the correlation is not proportional along the entire roughness field. Rather, the maximum Frossling number over the roughness asymptotes at about the sixth roughness element while the maximum streamwise skin friction continues to increase at approximately a linear rate. The continual increase of the skin friction is due to the continually increasing inviscid velocity which is driving the flow. This velocity field can be seen in the contours in the upper right plot of Figure 44. This increase in the skin friction tends to increase the convective heat transfer by the Reynolds analogy. Conversely, the roughness elements

further downstream are submerged deeper in the base thermal boundary-layer. This tends to decrease the convective heat transfer over the roughness element because the roughness is further from the cold outer flow. The net result is that these two effects somewhat offset each other for the downstream roughness elements and the effect of the roughness on the convective heat transfer asymptotes to a constant.

Also shown in Figure 45 is a comparison of C_{fs} with a fine grid solution which has 25% more grid points in each coordinate direction compared to the base grid. There is no distinguishable difference between the two curves, thus the rest of this study uses the base grid for the remaining calculations, however it should be noted that grid checks were performed periodically throughout the course of this study.

The heat transfer and streamwise skin friction for an increased Reynolds number of 10,000 is shown in Figure 46. The skin friction profile is similar to the profile seen in Figure 45 for *Re*=5000. However, the Frossling number shows a different character. Instead of an asymptote to a constant value downstream, the Frossling number for *Re*=10,000 continues to increase with downstream distance. As before, the increasing skin friction lends itself to increased convective heat transfer. At the increased Reynolds number, however, the downstream roughness elements are very near the height of the base thermal boundary-layer. Thus, there is not the associated decreased in the convective heat transfer as was seen for the *Re*=5000 case. The net result is that for *Re*=10,000, the downstream roughness elements continue to increase the convective heat transfer as shown in the Frossling number in Figure 46.

The same trends hold for Reynolds numbers lower and higher than those shown in Figure 45 and Figure 46. For the case of *Re*=1000 the effect of the roughness actually

decreases moving downstream. For *Re*=15,000 the trend is similar to that seen in Figure 46 with the magnitude of the effect of the roughness increased further, owing primarily to the thinner base thermal boundary-layer. These trends can also be seen in Figure 65 which summarizes all of the results from the chapter in terms of the correlation of the maximum heat transfer over the roughness with respect to the roughness Reynolds number, Re_k, and the roughness height to boundary-layer thickness ratio, k/δ.

The effect of doubling the spanwise extent of the computational domain is shown in Figure 47. The solid and dashed lines in Figure 47 show the streamwise skin-friction and convective heat transfer, respectively, at the right symmetry plane for the meshed domain shown in Figure 41. Also shown, by the symbols, are the same parameters from a computation with double the spanwise extent. In this calculation, the spanwise slice shown in Figure 47 is not at the right symmetry plane but in the middle of the computational domain. For both parameters, the two calculations are indistinguishable, therefore it is concluded that using the reduced spanwise extent with the symmetry boundary conditions is sufficient for capturing the roughness effects in the steady laminar flow.

One of the challenges in analyzing the heat transfer results of this chapter is determining how to put the data in a format which might be applicable to heat transfer modeling for icing codes. Typical icing codes will not resolve flow features on the scale of the roughness elements and the effect of the roughness would tend to show up as an averaged augmentation of the heat transfer of a computational cell adjacent to the surface. The method used here is to first take an area-weighted spanwise average of the convective heat transfer computations at a given streamwise location. That is, for a given spanwise strip, the spanwise average is given by

$$Fr_{span\,ave} = \frac{1}{A}\int_{\zeta_{min}}^{\zeta_{max}} Fr\, dA \quad , \tag{5.1}$$

where A is the total surface area over the roughness for the spanwise strip. The spanwise averaged *Fr* does not include the effect of the increased surface area due to the roughness, which would also tend to increase the heat transfer (as an example, for the roughness shown in Figure 41 the leading edge surface area is increased by about 30% due to the roughness). Rather, only the effect of the altered flow field is being examined. This allows a direct comparison of roughness fields of different sizes and surface areas in the following sections.

Figure 48 shows the spanwise averaged heat transfer as a function of streamwise location for the *Re*=5000 calculation. Because of the pattern of the roughness used here there is still a significant amount of variation in the spanwise averaged data. Therefore, a rolling streamwise average is applied to the spanwise averaged data. The averaging "window" for the rolling average is chosen based on trial and error to produce a smooth curve while still capturing the significant trends of the data. For the present study this averaging window is equal to the roughness spacing. The same averaging window is used for all Reynolds numbers. This rolling average data is also shown in Figure 48, along with a comparison to the clean leading edge heat transfer. Note that for this particular case the net effect of the roughness is to slightly decrease the leading edge convective heat transfer. This effect remains relatively constant over the entire length of the roughness field. This can be seen more clearly examining what will be called the relative heat transfer, Fr_p / Fr_u, where Fr_p is the heat transfer over the roughness field (perturbed region) and Fr_u is the heat transfer over the clean leading edge (unperturbed region). This relative increase in the convective heat transfer is shown in Figure 49 for all Reynolds numbers investigated in this

study. As noted previously, the *Re*=5000 data shows a constant small decrease in the heat transfer, while the *Re*=1000 data shows a similar trend with a larger relative decrease in the heat transfer. By contrast, for the *Re*=10,000 and *Re*=15,000 cases, though the heat transfer is decreased near the stagnation point, the average leading edge heat transfer increases when moving downstream. The sudden drop in the relative heat transfer for all Reynolds numbers seen in Figure 49 is due to the larger separation region downstream of the last row of roughness elements.

Figure 50 shows the surface shear lines, that is limiting streamlines, for all four Reynolds numbers of the base roughness pattern. As mentioned before, for thin films on the surface it is expected that the liquid water would be driven primarily by the air shear. Therefore, the motion of the surface film is primarily in the direction of the shear lines shown in Figure 50. Chapter 2 showed that in two-dimensions this approximation breaks down when the magnitude of the surface shear is small which occurs near singularities in the wall shear pattern.

For all four Reynolds numbers shown in Figure 50, the primary direction of the air shear over the first two rows of roughness elements is in the downstream direction. Therefore, any droplets which impinge in this region and do not freeze are driven back over the roughness. Further downstream, saddle points of separation develop at locations where the flow is separated between roughness elements. From these saddle points, separation lines emanate which divide the surface flow. A purely shear driven film will not be able to cross these separation lines. For a Reynolds number of 1000 (the left most plot) the first saddle point appears in front of the fourth streamwise roughness element on the right side of the pattern. This saddle point forces the surface shear lines toward the middle of the roughness

pattern. Subsequent saddle points in front of downstream roughness elements have a similar effect, forcing the surface shear lines toward the middle of the roughness pattern. The result is that a "river" of surface shear lines (or water) flows down the middle of the roughness pattern. This is a potential mechanism by which surface water finds its way through a roughness field. Note that for a Reynolds number of 1000 the saddle points are "weak" in that the resulting flow separation region evident from the surface shear pattern is small. For the higher Reynolds number cases the saddle points begin one roughness element further upstream and tend to be stronger, in that the resulting separation regions are larger. This leads to larger spanwise components of the shear vector inside the separation region which, in turn, leads to stronger forcing of the main shear lines toward the middle of the roughness pattern. The result is that the "river" which flows down the middle of the roughness is narrower for the higher Reynolds numbers. This would likely lead to either higher film velocities or thicker films in this region. The highest Reynolds number case of 15,000 at the far right of Figure 50 shows that the downstream flow is nearly choked off by the roughness field.

Figure 51 shows contours of the convective heat transfer (i.e. Frossling number) for each of the cases shown in Figure 50. In this figure, the blue regions are the regions of increased cooling (increased heat transfer) while the red regions are regions of decreased cooling (decreased heat transfer). The heat transfer for the Re=1000 case is relatively unremarkable. As expected, there is an increase in heat transfer over the peak of each roughness element. As the Reynolds number increases, the size of this region on the peak of each roughness element also increases. At the same time, owing to increased flow separation between the roughness elements, the heat transfer between the roughness elements decreases

(the color scale is the same for each plot). These regions of decreased heat transfer seem to correlate with the emergence of singularities in the surface streamline pattern. This is consistent with the previous discussion of heat transfer over an isolated roughness element.

Effect of Roughness Height

This section investigates the effect of roughness height on the convective heat transfer and surface shear lines. The roughness pattern is identical to that in the previous section, however in this case, in addition to a roughness height of k=0.05, roughness heights of k=0.03 and k=0.01 are also investigated. The Reynolds number for these cases is held constant at a value of 10,000, which is the case which showed moderate increase in the convective heat transfer in the previous section.

The relationship between roughness height and boundary-layer height for the various roughness patterns is shown in Figure 52. As before, the largest roughness of k=0.05 is a little higher than the boundary-layer thickness at the downstream edge of the roughness. The roughness height of k=0.03 is equal to the boundary-layer thickness at the trailing edge of the field, while the roughness height of k=0.01 is submerged well within the boundary-layer. In this regard, these latter two cases are similar to the Reynolds numbers of 5000 and 1000, respectively, of the previous section.

Figure 53 shows the relative heat transfer over the clean leading edge for the various roughness heights. Of course, the curve for k=0.05 corresponds to the Re=10,000 curve in Figure 49. The k=0.01 curve has essentially no effect on the convective heat transfer. For k=0.03, there is a decrease in the convective heat transfer near the stagnation point. Moving downstream the relative heat transfer gradually increases to a maximum of approximately 1.1 at the trailing edge of the roughness. This trend is very similar to the Re=5000 curve shown

in Figure 49 which has a similar roughness height to boundary-layer thickness ratio.

Figure 54 shows the surface shear lines for the various roughness heights. The plot on the left is for k=0.01 and shows that all surface shear lines generally flow downstream. As a result, it is expected that there would not be a significant effect on the distribution of the water film other than small changes in the film thickness due to variation in the surface shear. For k=0.03, saddle points begin to appear in front of the fourth roughness element on the right side of the roughness pattern. This is similar to the Re=1000 case shown in Figure 50, however the surface shear pattern for k=0.03 is somewhere in between the surface shear pattern for Re=1000 and Re=5000 in Figure 50. The surface shear lines originating at the stagnation point are again forced toward the center in a "river" of surface shear lines which is not as narrow as the case for larger roughness height, k=0.05.

Effect of Roughness Streamwise Extent

In many glaze icing experiments a smooth region free from roughness is known to exist near the stagnation point and this region can extend several millimeters away from the stagnation point. The baseline distributed roughness pattern examined thus far starts immediately at the stagnation point and does not include a smooth region. In this section, the starting point of the roughness field is gradually moved downstream to examine the effect of a smooth region. All of these cases are run at Re=10,000. For each new case, the starting point of the roughness is moved downstream by about 23% of the leading edge radius of curvature. This corresponds to approximately 2 millimeters on the standard 21 inch NACA 0012 airfoil. Note that instead of shifting the entire roughness field downstream, the roughness elements at the beginning of the roughness field are removed so that the streamwise extent of the field is shortened. For each new case, this involves removing four

roughness elements from the roughness field.

Figure 55 shows the relative heat transfer for the four cases being investigated in this section. The value of Δs is the distance, as a fraction of the leading edge radius of curvature, from the stagnation point to the start of the roughness field. The curve for Δs=0 corresponds to the *Re*=10,000 curve of Figure 49. For Δs=0.23, as the flow approaches the starting point of the roughness, a spike is seen in the relative heat transfer. Initially there is a sharp drop in the relative heat transfer due to the "blockage" that the roughness creates in decelerating the approaching flow from the clean leading edge flow. However, compared to the fifth row of roughness elements for Δs=0, the leading roughness elements for Δs=0.23 which are at the same streamwise location see a significantly higher flow speed. As a result, the relative heat transfer over these roughness elements is increased compared to the fifth row of roughness elements for Δs=0. This trend continues for Δs=0.46 and Δs=0.69 with the magnitude of the spike increasing as the size of the smooth region increases. This corresponds to the start of each roughness field effectively seeing a higher local velocity as Δs is increased. For each roughness field, the relative heat transfer over the roughness elements quickly returns to the baseline curve of Δs=0 after the first one or two rows of elements. Therefore, the leading roughness effect may not be that significant, as it occurs only over a relatively short distance compared to the entire roughness field length. However, this would depend on the total size of the roughness field.

Figure 56 shows surface shear lines for increasing values of Δs from left to right. As was seen in the third plot of Figure 50, for Δs=0 there is a small "river" of shear lines which is able to wind its way through the roughness field, becoming thinner as it moves downstream. For Δs=0.23 the trend is similar, with a sharper line dividing sections of the

surface flow just downstream of the first roughness element. For Δs=0.46, this feature has evolved into a saddle point just downstream of the second roughness element and divides the approaching surface flow into two parts. The first part moves to the right of the saddle point and continues to move downstream in a "river" similar to that seen in the previous two plots. However, a greater portion of the approaching surface flow is divided off to the left where it is driven towards the peak of the second roughness element. For Δs=0.69, this saddle point increases in strength, to the point where all of the surface flow approaching the roughness field is prevented from moving downstream and is instead driven toward the second roughness element. As a result, the "river" of streamlines which appeared in previous plots has been annihilated and only makes a brief appearance in the middle of the roughness field. As mentioned before, this type of scenario may lead to local increases in the film thickness or even pooling, but would not necessarily completely prevent the downstream flow of a surface water film through the roughness field.

Figure 57 shows the convective heat transfer contours for the cases shown in Figure 56. Because the starting point of the roughness field is different in each plot, the heat transfer approaching each roughness field is slightly different. The contour scale used in Figure 57 is the same as the scale used in Figure 51. As before, the regions of increased heat transfer (blue regions) are greatest for those roughness elements which protrude through the boundary-layer and also for those roughness elements which experience a flow stagnation point due to direct impingement, as evidenced by a nodal point of attachment near the peak of the roughness. The regions of decreased heat transfer (dark regions) again correlate with the presence of singularities in the surface shear pattern. For example, for the right-hand plot in Figure 57, the first two red regions correspond to two saddle points which have set up

behind the first two roughness elements.

Effect of Roughness Spacing

This section investigates the effect of the roughness spacing. The center-to-center spacing between roughness elements used in the nominal roughness pattern shown in Figure 49 and Figure 50 is approximately equal to one roughness diameter. As the roughness spacing increases it would be expected that the flow over the roughness elements would start behaving like the flow over an isolated roughness element. Figure 58 shows the relative heat transfer for roughness fields which have center-to-center spacing of 1.0, 1.5 and 2.0 roughness diameters. Recall that both the heat transfer with roughness present, Fr_p, as well as the heat transfer without the roughness present, Fr_u, use the total surface area of the roughened surface to compute the heat transfer. As a result, there is little difference between the three sets of curves. In fact, near the stagnation point the less dense roughness patterns have higher relative heat transfers. The less dense roughness patterns have fewer separation regions near the stagnation point which leads to the slightly higher relative heat transfer, similar to Figure 53. Near the downstream ends of the roughness fields the higher density roughness fields have a slightly larger relative heat transfer. In this region, both the high density and low density roughness fields induce flow separation. However, the separation regions for the lower density roughness fields have greater streamwise extent. Therefore, the regions which have lower heat transfer, the separation regions, cover more of the surface than the regions which have higher heat transfer, i.e. the roughness elements themselves. As a result, the relative heat transfer decreases near the downstream boundary of the roughness field.

Figure 59 shows the surface streamlines for the same three roughness fields near the

stagnation point. This figure shows how decreasing the density of the roughness causes the initial separation regions to move further downstream. It is also clear that the "river" of surface streamlines which is present in the middle of the roughness field becomes wider as the density of the roughness pattern is decreased. Individual roughness elements still set up separation regions with corresponding limiting streamlines which would prevent water from flowing behind the roughness element. However, because the roughness spacing is larger, these limiting streamlines would likely not pose nearly as much of a restriction on the downstream flow of water as those of the higher density roughness fields.

Figure 60 shows the convective heat transfer contours for each case plotted in Figure 59. The color scaling for this figure is the same as was used for the previous heat transfer figures. As expected, the variation in the convective heat transfer becomes smaller as the roughness spacing is increased. The regions of increased heat transfer on the peak of the roughness elements are larger for larger roughness spacing because each roughness element effectively sees a higher speed flow. In addition, as before, the regions of decreased heat transfer correlate with surface shear singularities. However, in this case the number of singularities is reduced as the roughness spacing is increased. Therefore, there are no extensive regions of decreased heat transfer for larger roughness spacing.

Effect of Roughness Shape

This section investigates the effect of the roughness shape. Up to this point, all of the roughness studies have used the quartic roughness shape defined by (3.9). The other two roughness shapes investigated in this section are the hemispherical shape given by (3.17) and the cylindrical shape given by (3.18). In all cases, the height of the roughness is held fixed at k=0.05 and the height to diameter ratio is approximately one half. Since the quartic

roughness elements have a "peaky" shape the decrease in roughness height when moving away from the maximum height is much more rapid than for the other two roughness shapes. As a result, even though the roughness diameters are the same, the quartic roughness elements present a smaller flow restriction than the other shapes. In fact, if the hemispherical roughness shapes are used, with a roughness spacing of one roughness diameter, the roughness elements would overlap each other. Therefore the nominal roughness spacing chosen for this study is ds/D=1.5 which, for the quartic roughness element, corresponds to the middle plot of Figure 59. As with Figure 59 the Reynolds number used for the shape study is 10,000.

The relative heat transfer for the three roughness shapes is shown in Figure 61. The quartic and hemispherical roughness elements have essentially the same relative heat transfer and the maximum relative heat transfer is approximately 1.3. The cylindrical shape has an increased heat transfer when compared to these other two, and a corresponding maximum relative heat transfer of about 1.5.

Figure 62 shows the surface shear patterns for the three different roughness shapes. As seen previously in Figure 59, the quartic roughness field shown on the left of Figure 62 permits a wide "river" of shear lines to flow unobstructed down the middle of the roughness field. By contrast, the larger flow restriction of the hemispherical roughness elements in the middle plot causes this "river" to narrow much quicker. This is partly affected by the separation in front of the third roughness element on the right side which is not present for the quartic roughness field. The separation regions begin even sooner for the cylindrical roughness field, starting behind the first roughness element on the left side. In fact, a focus of separation can be seen in this region which is closely coupled with a saddle point. The

"river" of surface shear lines for the cylindrical elements is smaller still. However, the difference from the hemispherical roughness does not appear to be that significant. Therefore, it appears that the hemisphere and cylindrical roughness elements present approximately the same level of blockage to the downstream flow of surface water.

Figure 63 shows the surface heat transfer map for each of the roughness shape patterns shown in Figure 62. The scale for the heat transfer coefficient is the same for each plot. The effect of the roughness shape on the maximum heat transfer over a given roughness element is apparent. In particular, peaky type roughness elements produce larger values of the maximum heat transfer (the blue regions). That is, the quartic roughness elements produce the highest maximum heat transfer while the hemispherical roughness elements, which have a constant curvature, produce the smallest. In addition, the effect of the roughness shape on the minimum heat transfer coefficient is also apparent. As mentioned previously, a focal point on the surface tends to lift the flow away from the surface producing a region of low heat transfer. Roughness shapes which have the largest slope on the side of the roughness produce the strongest focal points and chimney vortices because of the strong shear layer which separates from the sides of the roughness. The cylindrical roughness element produces the strongest chimney vortices, followed by the hemisphere and the quartic roughness element. This is consistent with Figure 63 which shows large regions of decreased heat transfer just downstream of the cylindrical roughness elements, at the same location at which focal points exist.

Summary of the Various Roughness Effects

This section revisits the question of whether Re_k or k/δ is the primary parameter controlling roughness effects, by correlating the results from the previous sections using

these two parameters. Once again, the primary roughness effect of interest is the relative heat transfer.

Figure 64 shows the spanwise and streamwise averaged relative heat transfer (which has been presented in the previous figures) in terms of Re_k and k/δ. A direct correlation is not evident from this figure, however the data does tend to collapse toward a single curve when plotted as a function of Re_k. As a result, if this study is supplemented with a more complete data set, it may be possible to determine a simple curve fit as a function of Re_k which can be incorporated within an icing code to account for the effects of roughness fields on heat transfer. Note that the roughness does not act to increase the averaged heat transfer until Re_k has reached a value of approximately 200. The spread in the data is likely due to small differences in the geometry or the flow conditions of the different cases. There does not appear to be a direct correlation with k/δ indicating that this parameter is likely a secondary effect at best.

Figure 65 shows the maximum relative heat transfer over each individual roughness element as a function of Re_k and k/δ. This data tends to be cleaner than the plots of the averaged relative heat transfer in Figure 64 because it does not include the effect of separation regions which can vary in size and strength. The maximum heat transfer increases significantly with increasing Re_k. Also evident from Figure 65 is the effect of roughness shape on the maximum relative heat transfer. Peaky type roughness elements tend to produce large values of the maximum relative heat transfer for a given Re_k. Hemispheres produce the smallest maximum values, while the quartic roughness elements produce the largest. In addition, there appears to be a k/δ effect on the maximum relative heat transfer.

For example, considering the four cases that were run at four different Reynolds numbers, for a given Re_k, maximum relative heat transfer decreases as the value of k/δ increases.

CHAPTER 6. CONCLUSIONS AND RECOMMENDATIONS FOR FURTHER STUDY

The purpose of this study was to examine the potential impact of surface ice roughness on the convective heat transfer and the motion of unfrozen surface water in an attempt to ascertain the significance of ice roughness on the ice accretion process. This study focused mainly on low Reynolds number cases, which result in steady flow over roughness fields.

The first part of the investigation used a condensed layer structure to compute the multi-phase flow of thin liquid films which are driven over shallow two-dimensional roughness elements. Limiting structures were developed in addition to direct computation of the governing equations. This study showed that:

- the film distribution can be computed using a Couette flow approximation when the minimum magnitude of the surface shear over the roughness, τ_{min}, satisfies $\tau_{min} \gg h^{4/7}$, where h is the film thickness.
- when $\tau_{min} \leq h^{4/7}$ then the film distribution in the vicinity of this point violates a Couette flow assumption. A separation bubble forms within the film which traps water locally. The amount of trapped water increases as the size of the air flow separation region increases.
- when multiple roughness elements are present, the amount of water trapped by the roughness can increase or decrease depending on the spacing between roughness elements. In addition, if the roughness elements are closely spaced a separation region can be maintained within the air at steady state.

Therefore it was determined that the thin films were primarily driven by the air shear

with the size of air flow separation regions playing a significant role in determining the actual amount of water present on the surface. Thus, in the Navier-Stokes portion of the study, the three-dimensional surface shear lines were used to interpret the potential effect of a roughness field on the surface water distribution.

This part of the study examined the single phase air flow over roughness fields near an airfoil leading edge by solving the Navier-Stokes equations. The study included systematic variation of the Reynolds number, the roughness height, the smooth zone extent, the roughness spacing and the roughness shape. The net effect of the roughness fields on the relative heat transfer are shown in Figure 64 and Figure 65. While the maximum heat transfer over the roughness element was always greater than the clean leading edge value, the average relative heat transfer did not go above one until Re_k reached approximately 200.

Most roughness fields examined in this study started at the stagnation point, and the effect of those surface roughness fields is to converge the shear lines which originate at the stagnation point into narrow "rivers" of shear lines. In the context of surface water, this would tend to move the water towards the center of the roughness field and possibly trap water between the roughness elements. This effect of narrowing the "river" of surface shear lines tends to increase with increasing roughness height, roughness density, roughness shape surface slope and Reynolds number.

Of particular interest is the effect of the smooth zone, or starting point of the roughness field, on the surface shear lines and heat transfer. As the extent of the smooth zone increases, the effective local flow velocity at the beginning of the roughness field also increases and the effect on the surface shear lines becomes more severe. Separation regions set up behind the first row of roughness elements. The strength of these regions grow as the

length of the smooth zone increases and, eventually, the approaching surface shear lines are blocked altogether. The result is that any surface shear lines that originated at the stagnation point do not penetrate the roughness field. The implication is that the presence of the smooth zone affects the distribution of water within the roughness field. This may be consistent with the experimental observations of Olsen & Walker[27] and Hansman[28] which indicated a thin uniform film in the smooth zone region but only local pockets or pools of water within the roughness field. The computations performed in this study did not include a solution for the water film layer, so it is not possible at this time to develop a water trapping model for three-dimensional roughness fields which could answer these questions. However, this study has pointed out the likely key parameters which could impact the surface water processes and it is recommended that full three-dimensional multi-phase calculations be carried out in the future to develop such a model.

As with the surface shear line study, the smooth zone extent has the most interesting effect on the relative heat transfer. As the length of the smooth zone increases, the local velocity approaching the roughness increases and the heat transfer over the first couple rows of roughness elements increases significantly. The relative heat transfer has a value of one approaching the roughness field with a large spike over the initial part of the roughness field. The size of this spike grows larger as the length of the smooth zone increases. Downstream of the spike, the relative heat transfer quickly returns to the value which corresponds to a roughness field which starts at the stagnation point.

To complete the data set which would be required for developing an icing code model, it is recommended that calculations be performed at higher Reynolds numbers, which would likely require unsteady computations.

REFERENCES

[1] Bragg, M.B., *Rime Ice Accretion and Its Effect on Airfoil Performance*, PhD Dissertation, The Ohio State University, 1981.

[2] Bragg, M.B, & Khodadoust, A., "Effect of Simulated Glaze Ice on a Rectangular Wing", AIAA Paper 89-0750, *27th AIAA Aerospace Sciences Meeting & Exhibit*, 1989.

[3] Kwon, O., & Sankar, L.N., "Numerical Investigation of Performance Degradation of Wings and Rotors Due to Icing", AIAA Paper 92-0412, *30th AIAA Aerospace Sciences Meeting & Exhibit*, 1992.

[4] FAA Technical Center, Aircraft Icing Handbook, Vol. 2, 1991.

[5] Federal Aviation Administration, Federal Air Regulations, Part 25.1419.

[6] Ruff, G.A., & Berkowitz, B.M., Users Manual for the NASA Lewis Ice Accretion Prediction Code (LEWICE), *NASA CR 185129*, 1990.

[7] Messinger, B.L., "Equilibrium Temperature of an Unheated Icing Surface as a Function of Airspeed," *Journal of the Aeronautical Sciences*, Vol. 20, No. 1, 1953, pp. 29-42.

[8] Potapczuk, M.G., "A Review of NASA Lewis' Development Plans for Computational Simulation of Aircraft Icing", AIAA Paper 99-0423, *37th AIAA Aerospace Sciences Meeting & Exhibit*, 1999.

[9] Schlichting, H., *Boundary-Layer Theory*. McGraw-Hill, New York, 1979.

[10] Tsao, J.C., & Rothmayer, A.P., "A Mechanism for Ice Roughness Formation on an Airfoil Leading Edge, Contributing to Glaze Ice Accretion", AIAA Paper 98-0485, *36th AIAA Aerospace Sciences Meeting & Exhibit*, 1998.

[11] Tsao, J.C., & Rothmayer, A.P., "Triple-Deck Simulation of Surface Glaze Ice Accretion", AIAA Paper 00-0234, *38th AIAA Aerospace Sciences Meeting & Exhibit*, 2000.

[12] Anderson, D.N., Hentschel, D.B., & Ruff, G.A., "Measurement and Correlation of Ice-Accretion Roughness", AIAA Paper 98-0486, *36th AIAA Aerospace Sciences Meeting & Exhibit*, 1998.

[13] Rothmayer, A.P., "Stagnation Point Icing", AIAA Paper 2006-1081, *44th AIAA Aerospace Sciences Meeting & Exhibit*, 2006.

[14] Shourya, S.P., & Rothmayer, A.P., "Instability of Stagnation Line Icing," *Computers & Fluids*, 2008, to appear.

[15] Shin, J., "Characteristics of Surface Roughness Associated with Leading Edge Ice Accretion", AIAA Paper 94-0799, *32nd AIAA Aerospace Sciences Meeting and Exhibit*, 1994.

[16] Kerho, M.F., *Effect of Large Distributed Roughness Near an Airfoil Leading Edge on Boundary-Layer Development and Transition*, PhD Dissertation, University of Illinois at

Urbana-Champaign, 1995.

[17] Winkler, J.F., *Local Flowfield About Large Distributed Roughness Elements in a Laminar Boundary Layer*, PhD Dissertation, University of Illinois at Urbana-Champaign, 1996.

[18] Bragg, M., Kerho, M., & Cummings, M., "Airfoil Boundary-Layer due to Large Leading-Edge Roughness", AIAA Paper 95-0536, *33rd AIAA Aerospace Sciences Meeting & Exhibit*, 1995.

[19] Mason, P.J., & Morton, B.R., "Trailing Vortices in the Wakes of Surface-Mounted Obstacles," *Journal of Fluid Mechanics*, Vol. 175, 1987, pp. 247-293.

[20] Lighthill, M.J., *Laminar Boundary Layers*. Oxford University Press, Oxford, 1963.

[21] Gregory, N., & Walker, W.S., The Effect of Transition of Isolated Surface Excrescensces in the Boundary Layer, *British ARC Research Memo 2779*, 1956.

[22] Henry, R.C., Hansmann Jr., R.J., & Breuer, K.S., "Heat Transfer Variation on Protuberances and Surface Roughness Elements," *Journal of Thermophysics and Heat Transfer*, Vol. 9, No. 1, 1995, pp. 175-180.

[23] Poinsatte, P.E., Van Fossen, G.J., & De Witt, K.J., "Roughness Effects on Heat Transfer from a NACA 0012 Airfoil," *Journal of Aircraft*, Vol. 28, No. 12, 1991, pp. 908-911.

[24] Acarlar, M.S., & Smith, C.R., "A Study of Hairpin Vortices in a Laminar Boundary Layer. Part 1. Hairpin Vortices Generated by a Hemisphere Protuberance," *Journal of Fluid Mechanics*, Vol. 175, 1987, pp. 1-41.

[25] Lee, S., *Heat Transfer on an Airfoil with Large Distributed Leading-Edge Roughness*, PhD Dissertation, University of Illinois at Urbana-Champaign, 1997.

[26] Dukhan, N., Masiulaniec, K.C., De Witt, K.J., & Van Fossen Jr., G.J., "Experimental Heat Transfer Coefficients from Ice-Roughened Surfaces for Aircraft Deicing Design," *Journal of Aircraft*, Vol. 36, No. 6, 1999, pp. 948-956.

[27] Olsen, W., & Walker, E., Experimental Evidence for Modifying the Current Physical Model for Ice Accretion on Aircraft Surfaces, *NASA TM-87184*, 1986.

[28] Hansman, R.J., & Turnock, S.R., "Investigation of Surface Water Behavior During Glaze Ice Accretion", AIAA Paper 88-0115, *26th AIAA Aerospace Sciences Meeting & Exhibit*, 1988.

[29] Nelson, J.J., Alving, A.E. & Joseph, D.D., "Boundary-Layer Flow over Air Over Water on a Flat Plate," *Journal of Fluid Mechanics*, Vol. 284, No. 159, 1995, pp. 159-169.

[30] Rothmayer, A.P., & Tsao, J.C., "Water Film Runback on an Airfoil Surface", AIAA Paper 2000-0237, *36th AIAA Aerospace Sciences Meeting & Exhibit*, 2000.

[31] Timoshin, S.N., "Instabilities in a High Reynolds-Number Boundary Layer on a Film-Coated Surface," *Journal of Fluid Mechanics*, Vol. 353, No. 163, 1997, pp. 163-195.

[32] Al-Khalil, K.M., Keith, T.G., & De Witt, K.J., "New Concept in Runback Water

Modeling for Anti-Iced Aircraft Surfaces," *Journal of Aircraft*, Vol. 30, No. 41, 1993, pp. 41-49.

[33] Al-Khalil, K.M., Keith, T.G., & De Witt, K.J., "Development of an Improved Model for Runback Water on Aircraft Surfaces," *Journal of Aircraft*, Vol. 31, No. 271, 1994, pp. 271-278.

[34] Wang, G., & Rothmayer, A.P., "Air Driven Water Flow Past Small Scale Roughness ", AIAA Paper 2005-0653, *43rd AIAA Aerospace Sciences Meeting & Exhibit*, 2005.

[35] Wang, G., & Rothmayer, A.P., "Properties of Thin Water Films Driven by Air Through Surface Roughness", AIAA Paper 2007-0901, *45th AIAA Aerospace Sciences Meeting & Exhibit*, 2007.

[36] Matheis, B.D., & Rothmayer, A.P., "Numerical Simulation of Thin Air Driven Films", AIAA Paper 2002-0525, *40th AIAA Aerospace Sciences Meeting & Exhibit*, 2002.

[37] Timoshin, S.N., *Private Communication,* 1997.

[38] Tobak, M., & Peake, D.J., "Topology of Three-Dimensional Separated Flows," *Annual Review of Fluid Mechanics*, Vol. 14, 1982, pp. 61-85.

[39] Abbott, I.H, & Von Doenhoff, A.E., *Theory of Wing Sections*. Dover Publications, New York, 1959.

[40] Bhaskaran, R., *Unsteady Incompressible Viscous Flow Past Stationary, Pitching or Oscillating Airfoil Leading Edges*, PhD Dissertation, Iowa State University, 1996.

[41] Huebsch, W.W., *Numerical Investigation on the Interaction Between Surface Roughness and Viscous Flows*, PhD Dissertation, Iowa State University, 2000.

[42] Davis, R.L., Carter, J.E. & Hafez, M., "Three-Dimensional Viscous Flow Solutions with a Vorticity-Stream Function Forumulation," *AIAA Journal*, Vol. 27, No. 7, 1988, pp. 892-900.

[43] Karamcheti, K., *Principles of Ideal-Fluid Aerodynamics*. Krieger Publishing Company, Malabar, Florida, 1966.

[44] Napolitano, M., Pascazio, G., & Quartapelle, L., "A Review of Vorticity Conditions in the Numerical Solution of the Zeta-Psi Equations," *Computers & Fluids*, Vol. 28, 1999, pp. 139-185.

[45] Souli, M., "Vorticity Boundary Conditions for Navier-Stokes Equations," *Computer Methods in Applied Mechanics and Engineering*, Vol. 134, 1996, pp. 311-323.

[46] Moin, P., & Mahesh, K., "Direct Numerical Simulation: A Tool in Turbulence Research," *Annual Review of Fluid Mechanics*, Vol. 30, 1998, pp. 539-578.

[47] Joslin, R.D., & Grosch, C.E., "Growth Characteristics Downstream of a Shallow Bump: Computation and Experiment," *Physics of Fluids*, Vol. 7, No. 12, 1995, pp. 3042-3047.

[48] Tufo, H.M., Fischer, P.F., Papka, M.E., & Blom, K., "Numerical Simulation and Immersive Visualization of Hairpin Vortices", Article No. 62, *Proceedings of the IEEE/ACM*

SC99 Conference, 1999.

[49] Tannehill, J.C., Anderson, D.A., & Pletcher, R.H., *Computational Fluid Mechanics and Heat Transfer*. Taylor & Francis, New York, 1997.

[50] Huebsch, W.W., & Rothmayer, A.P., "Unsteady Navier-Stokes Simulation of Flow Past Surface Ice Geometries", AIAA Paper 2000-0232, *38th AIAA Aerospace Sciences Meeting & Exhibit*, 2000.

[51] Liu, X.D., Osher, S., & Chan, T., "Weighted Essentially Non-Oscillatory Schemes," *Journal of Computational Physics*, Vol. 115, No. 1, 1994, pp. 200-212.

[52] Poinsatte, P.E., Van Fossen, G.J. & Newton, J.E., "Heat Transfer Measurements from a Smooth NACA 0012 Airfoil," *AIAA Journal of Aircraft*, Vol. 28, No. 12, 1991, pp. 892-898.

[53] Frossling, N., Evaporation, Heat Transfer, and Velocity in Two-Dimensional and Rotationally Symmetrical Laminar Boundary Layer Flow, *NACA TM-1432*, 1958.

FIGURES

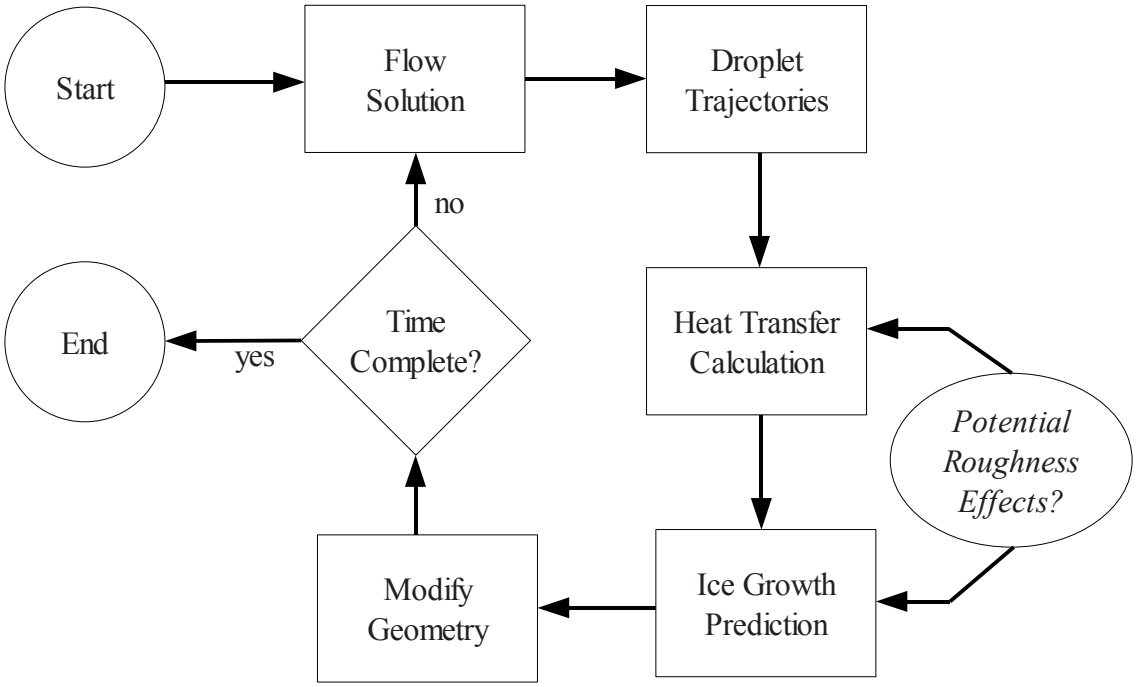

Figure 1: Time stepping procedure used in Messinger[7] based ice accretion codes.

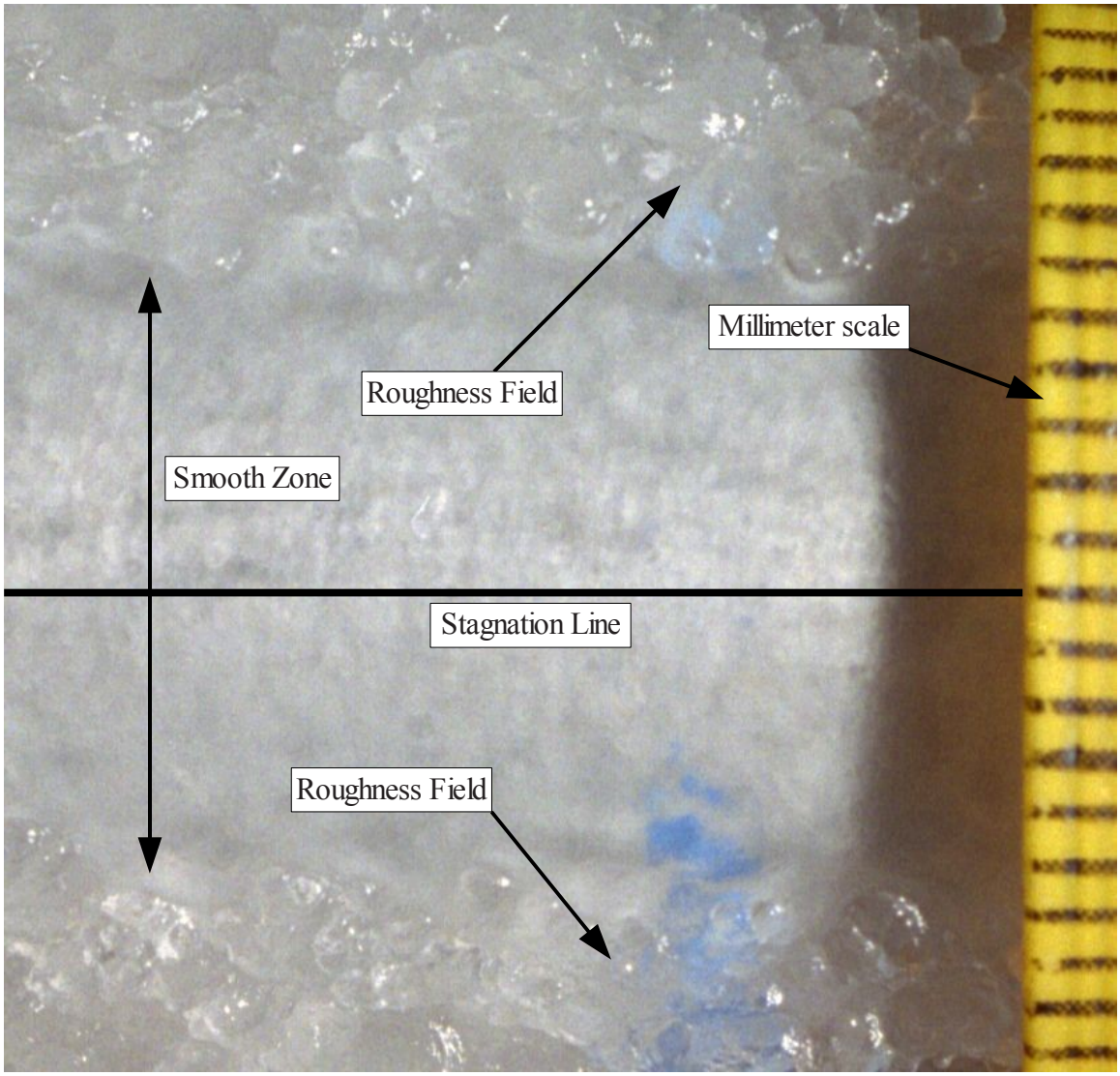

Figure 2: Close-up of ice roughness near an airfoil leadinge edge. From Anderson[12], reproduced with permission.

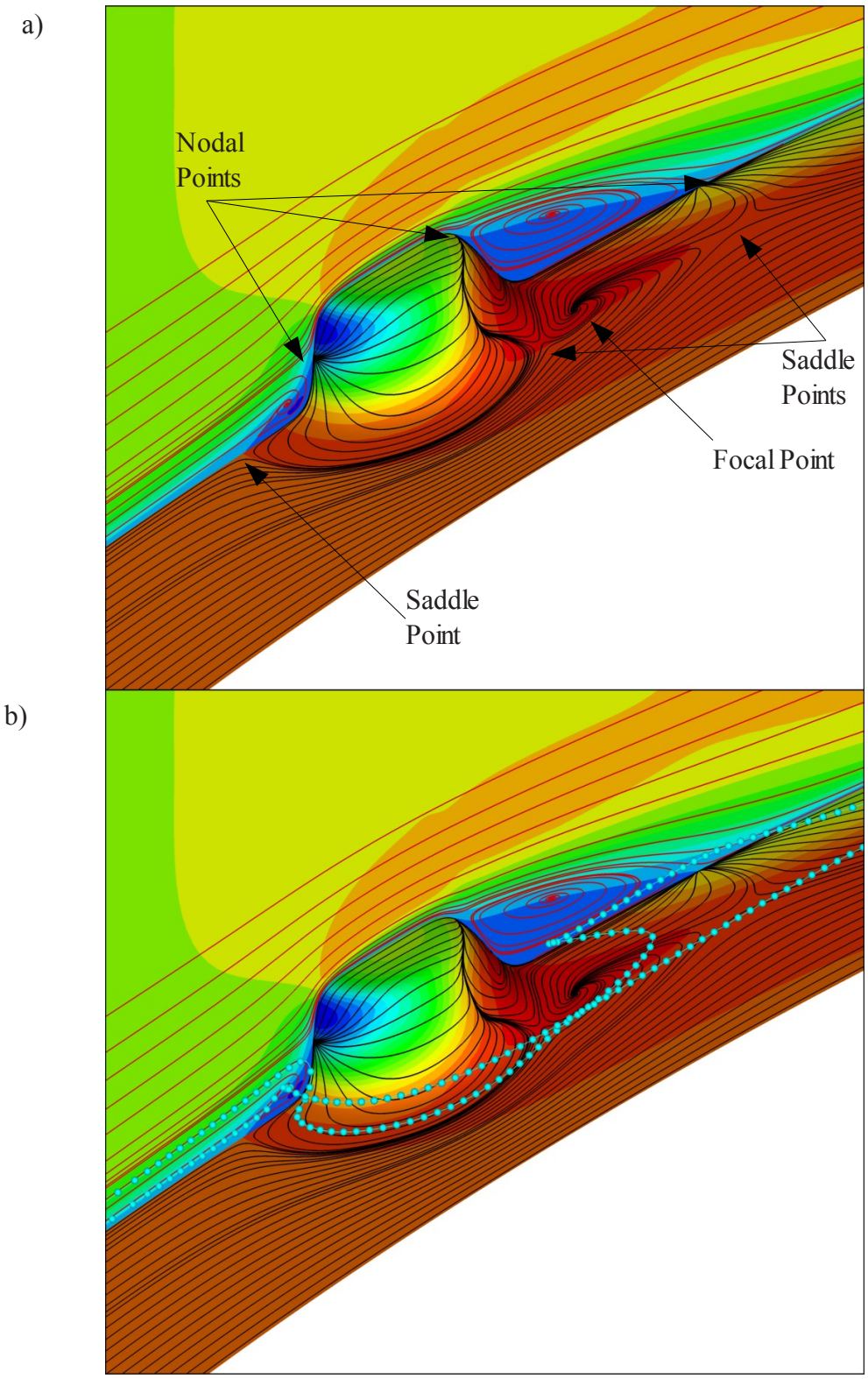

Figure 3: Typical flow structures for laminar flow over an O(1) aspect ratio isolated roughness element, a) surface shear and symmetry velocity patterns, b) streamlines which are part of the upstream horseshoe vortex system.

a)

b)

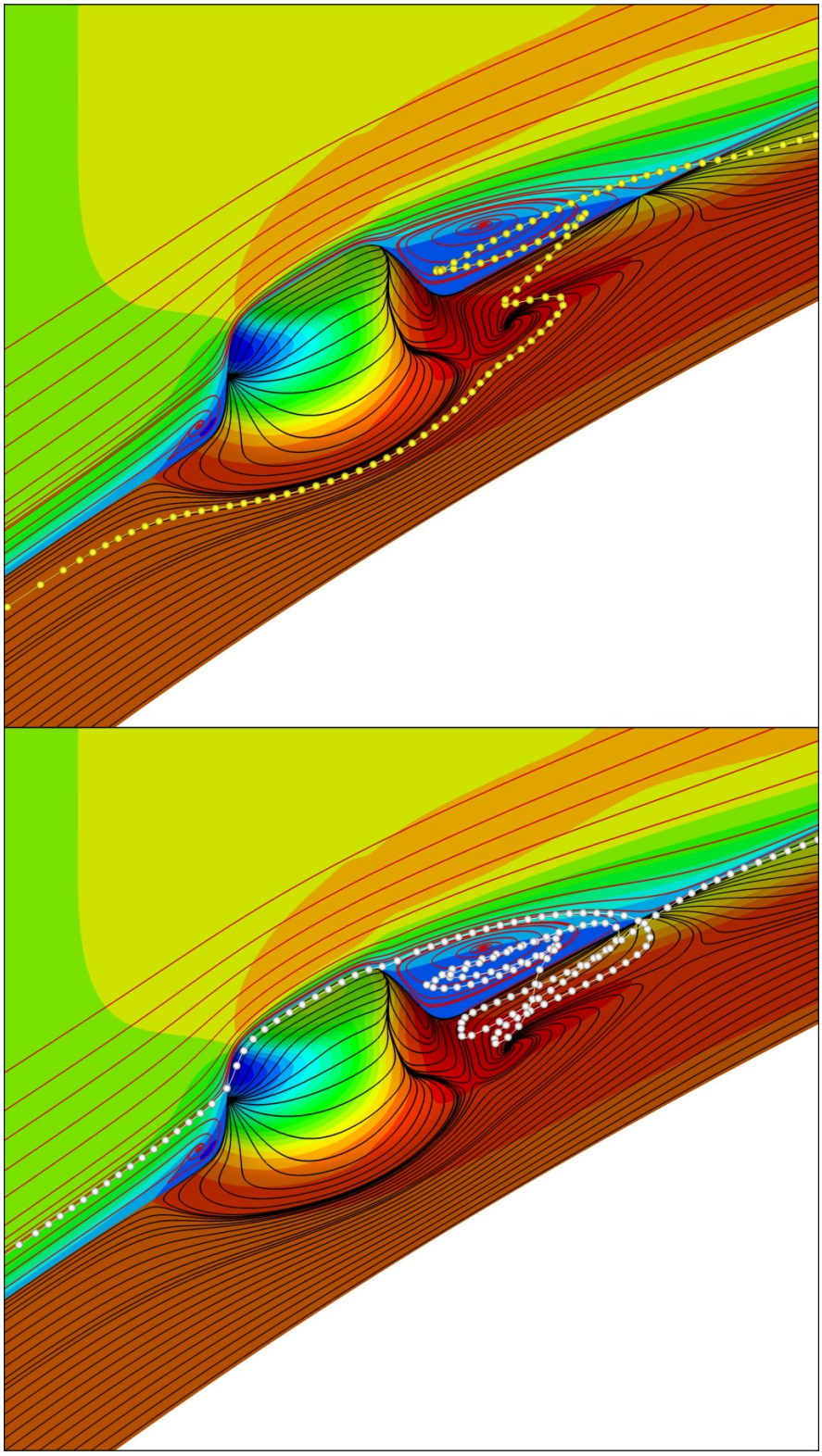

Figure 4: Typical flow structures for laminar flow over an O(1) aspect ratio isolated roughness element, a) streamlines which are part of the chimney vortex structure, b) streamlines which are part of the wake vortex.

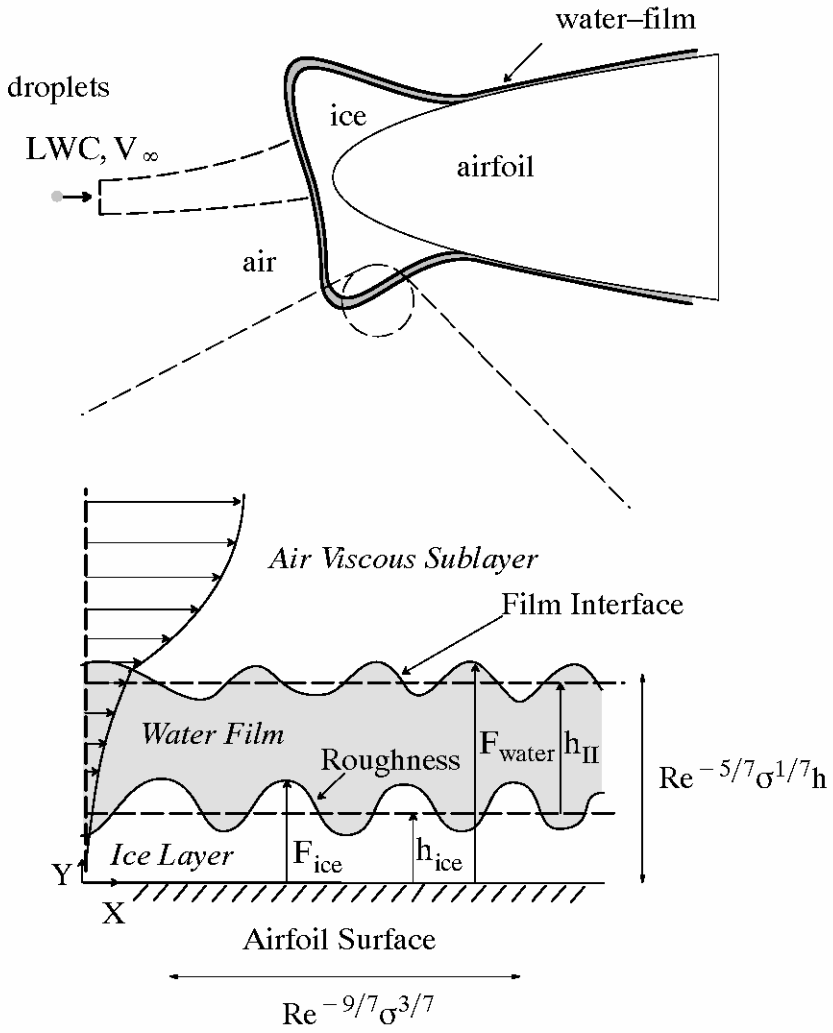

Figure 5: Schematic of the global scale and local scale multi-phase icing problem.

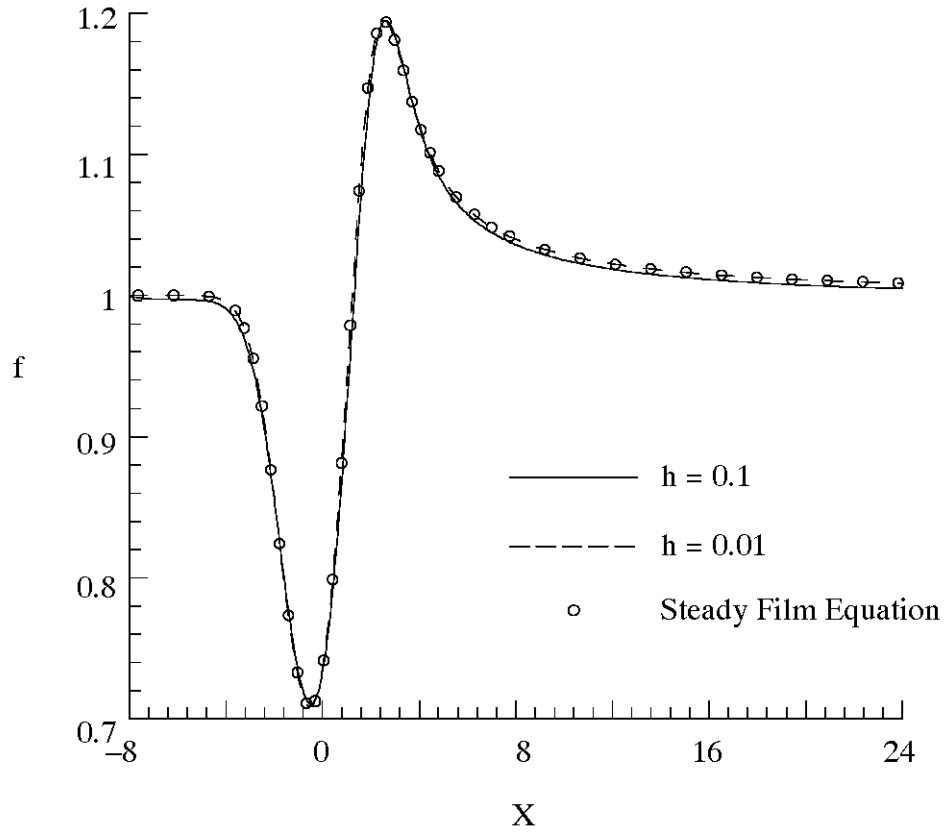

Figure 6: Comparison of the full Stage II numerical solutions and the steady film equation from (2.13) for film flow over a roughness element with an attached airflow.

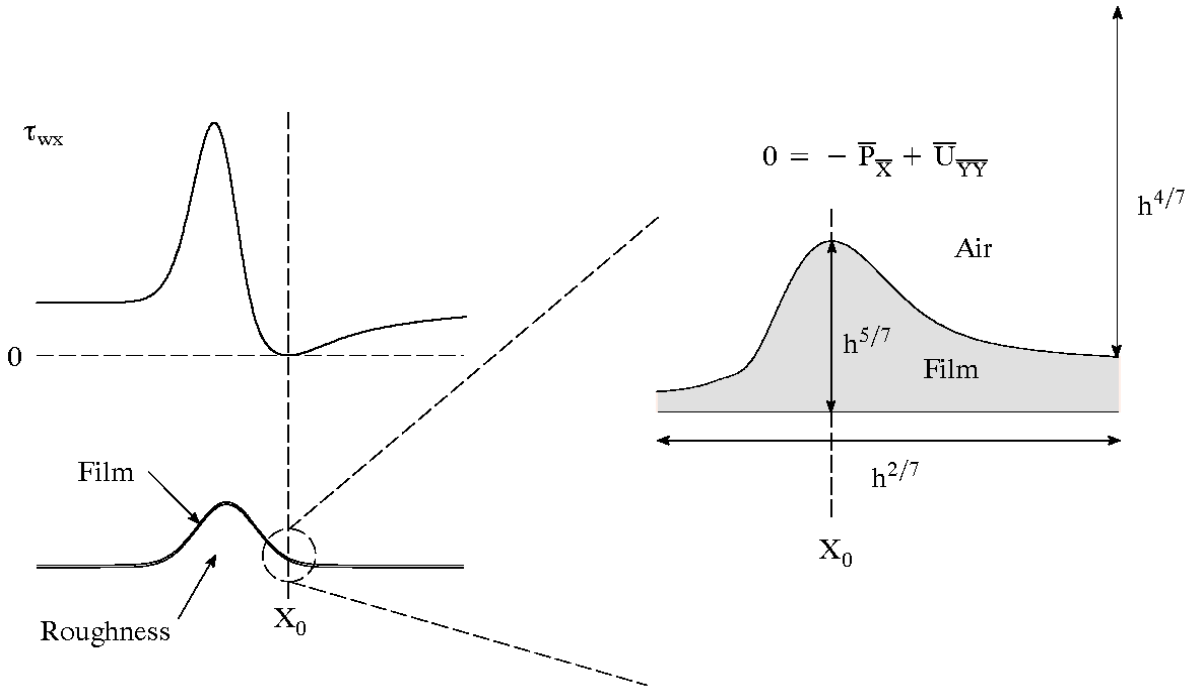

Figure 7: Spatial scales applicable to the low shear structure for an air/water film interaction induced by the presence of a roughness element.

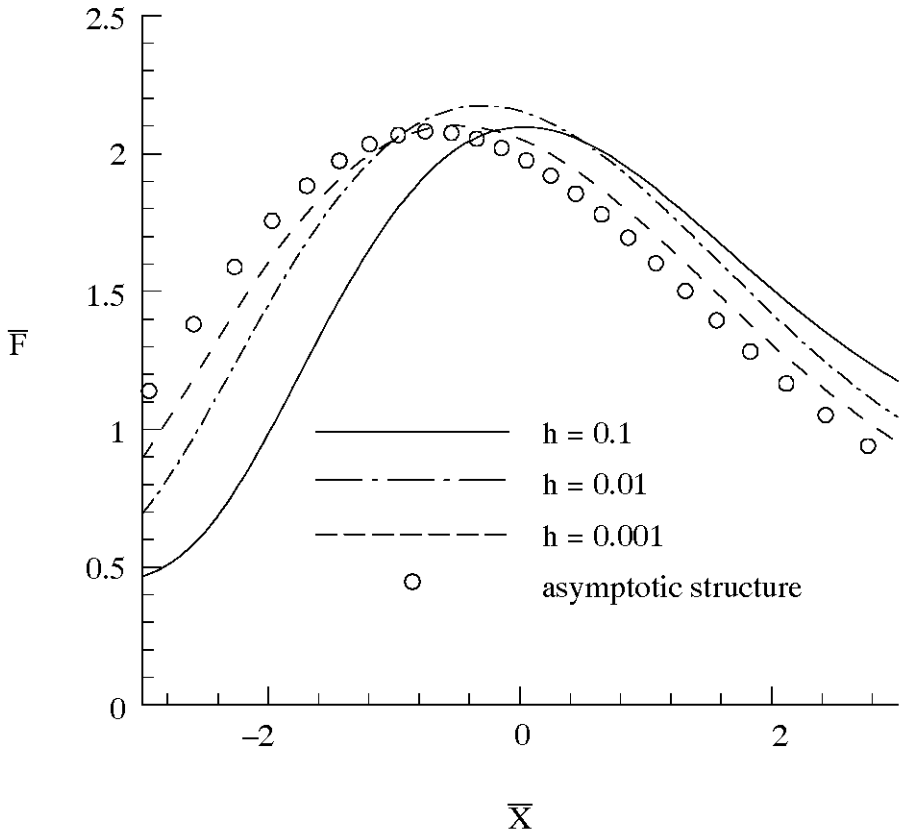

Figure 8: Scaled film thickness near the incipient separation point induced by a roughness element. Comparison of asymptotic theory and full Stage II numerical results.

a) T=0

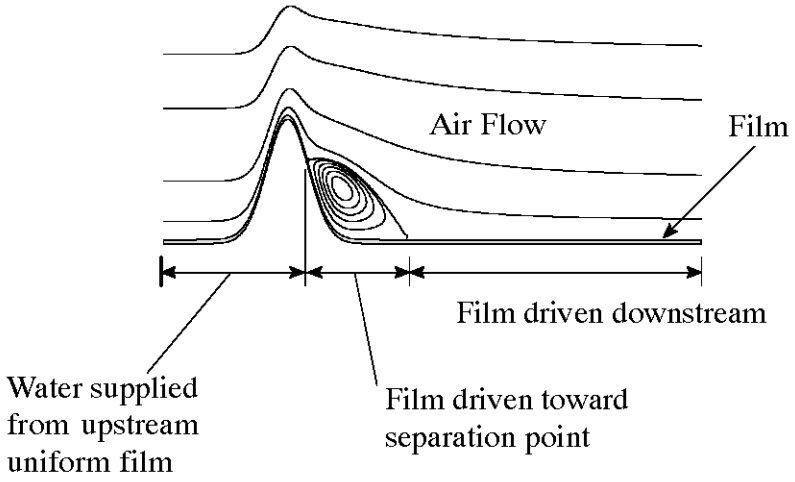

b) T→∞

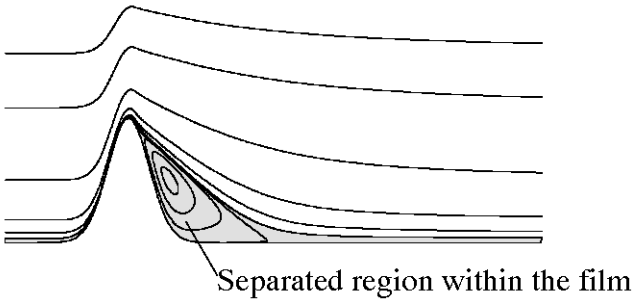

Figure 9: Development of a thin water film flowing over a roughness element which has an initial two-dimensional separation in the air. a) initial condition, b) final steady state solution.

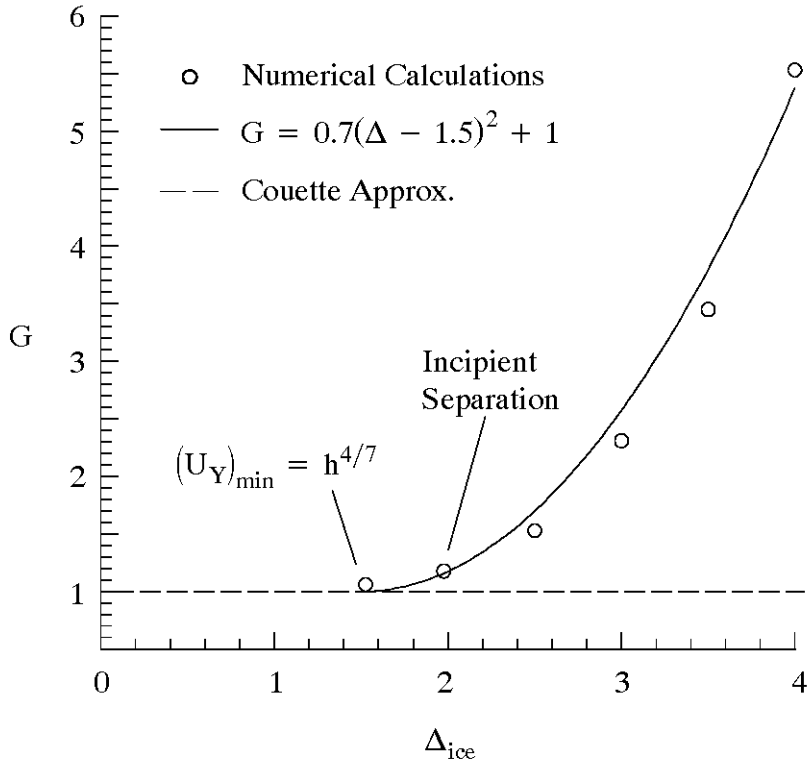

Figure 10: Trapping factor for thin film flow over a roughness element of constant wavelength. Δ is the roughness height, h=0.1.

a)

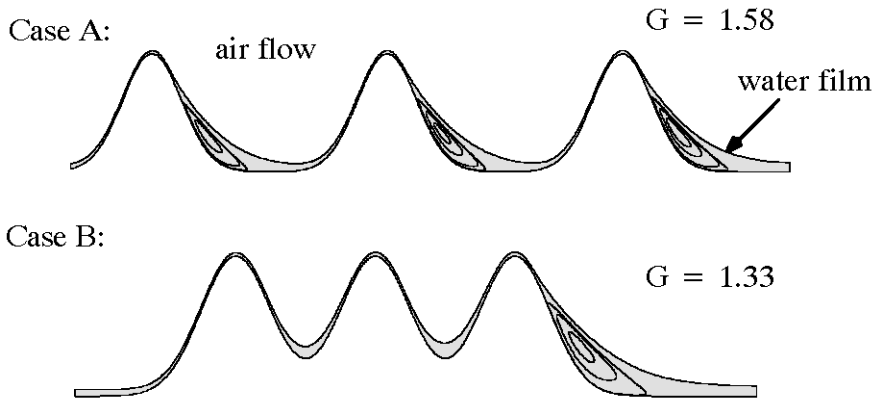

b)

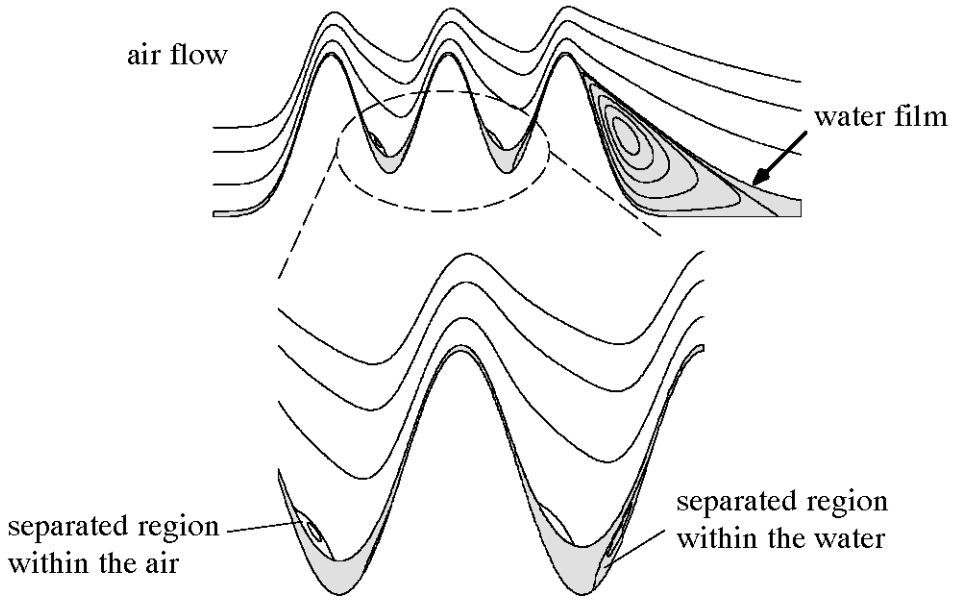

Figure 11: Effect of distributed roughness on water trapping. a) decreasing water trapping as roughness elements are moved closer together. b) effect of distributed roughness in allowing steady state separation within the air flow.

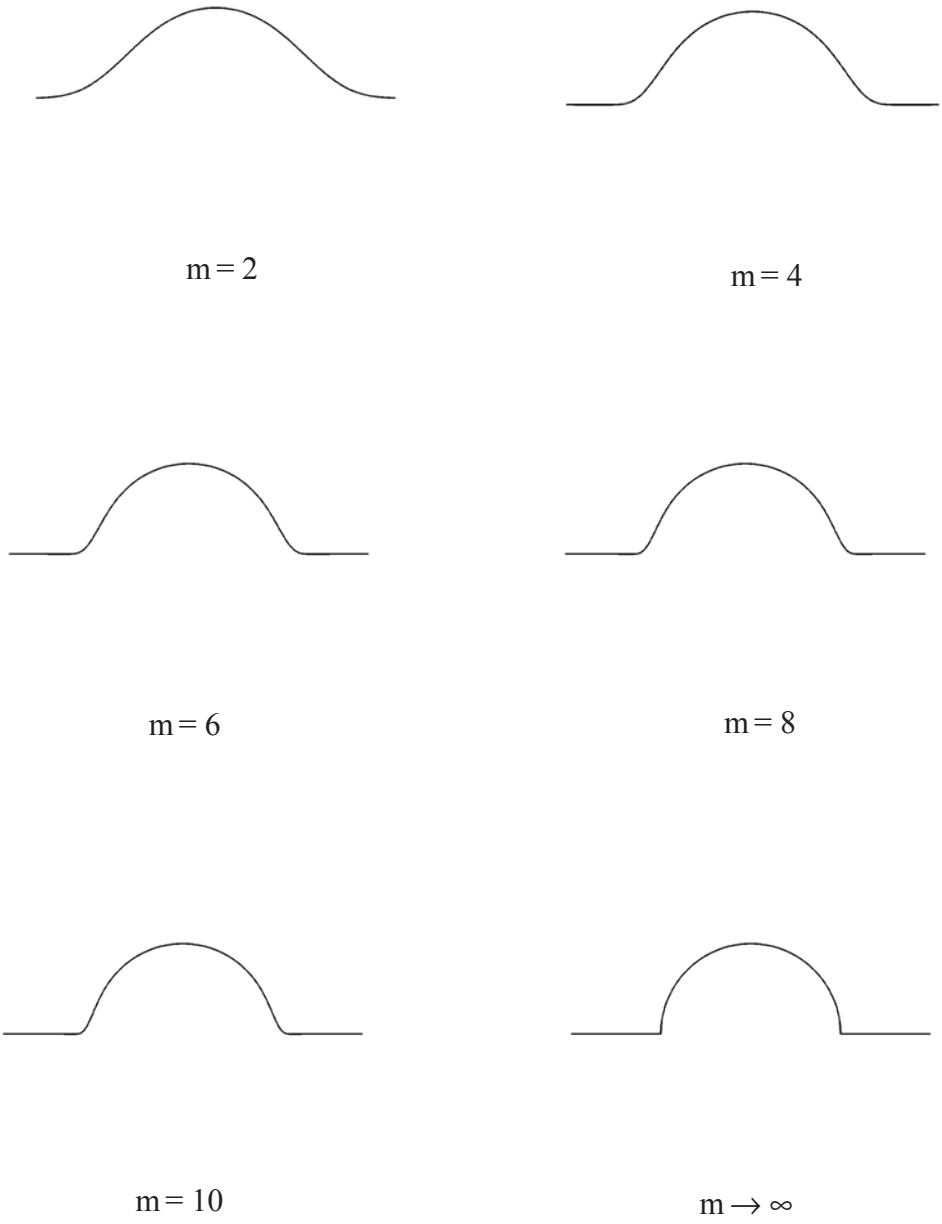

Figure 12: Evolution of the approximate hemisphere roughness model as m goes to infinity.

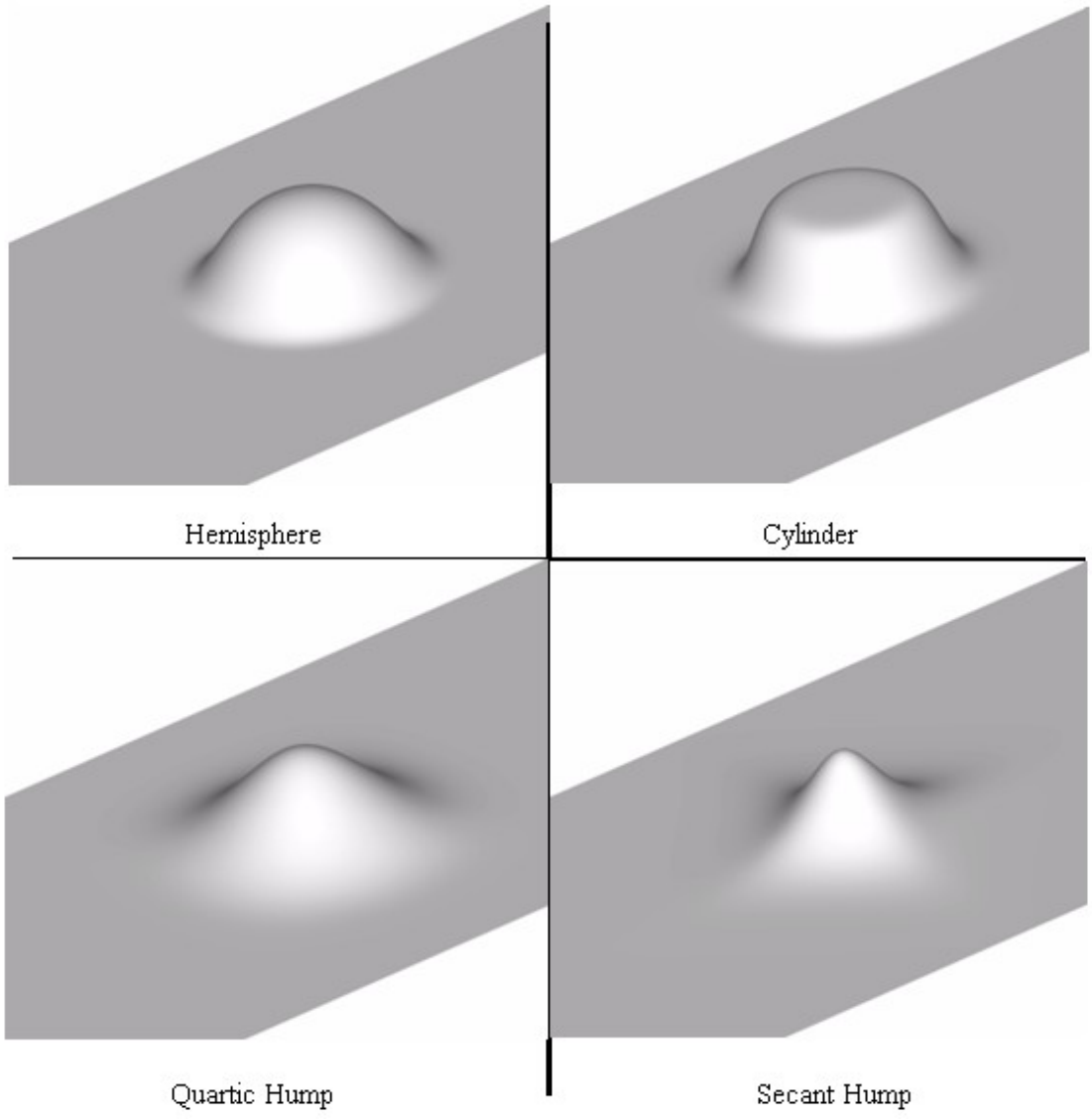

Figure 13: Roughness shapes currently implemented in the Navier-Stokes code.

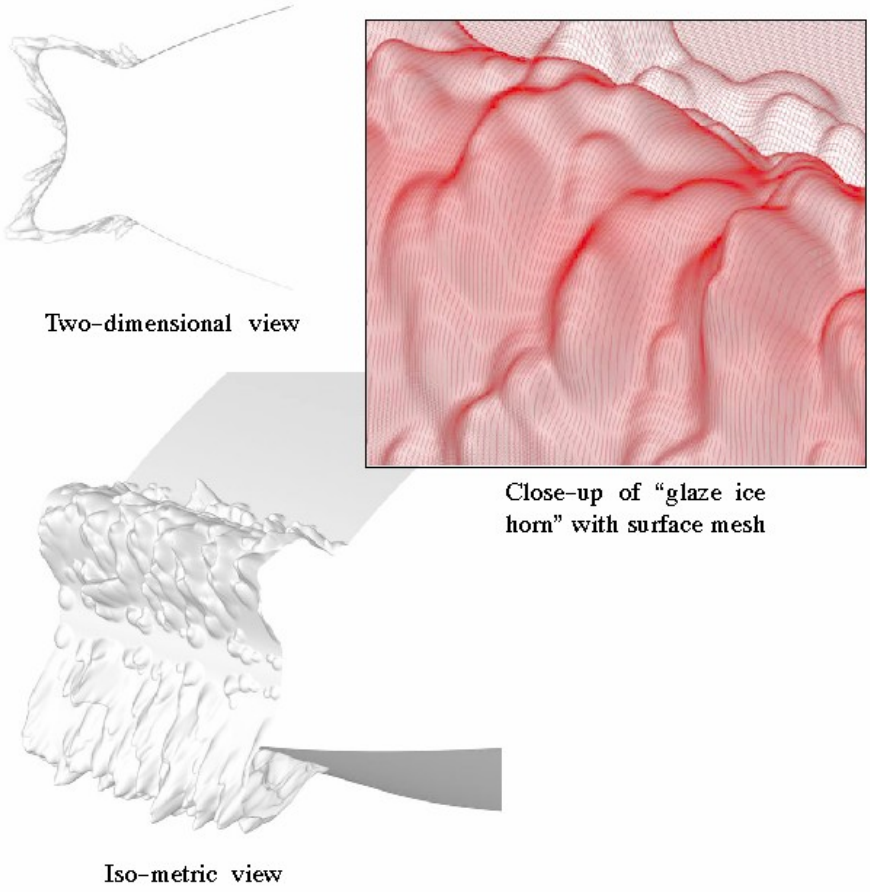

Figure 14: Example of a complex ice shape created by the superposition of basic shapes.

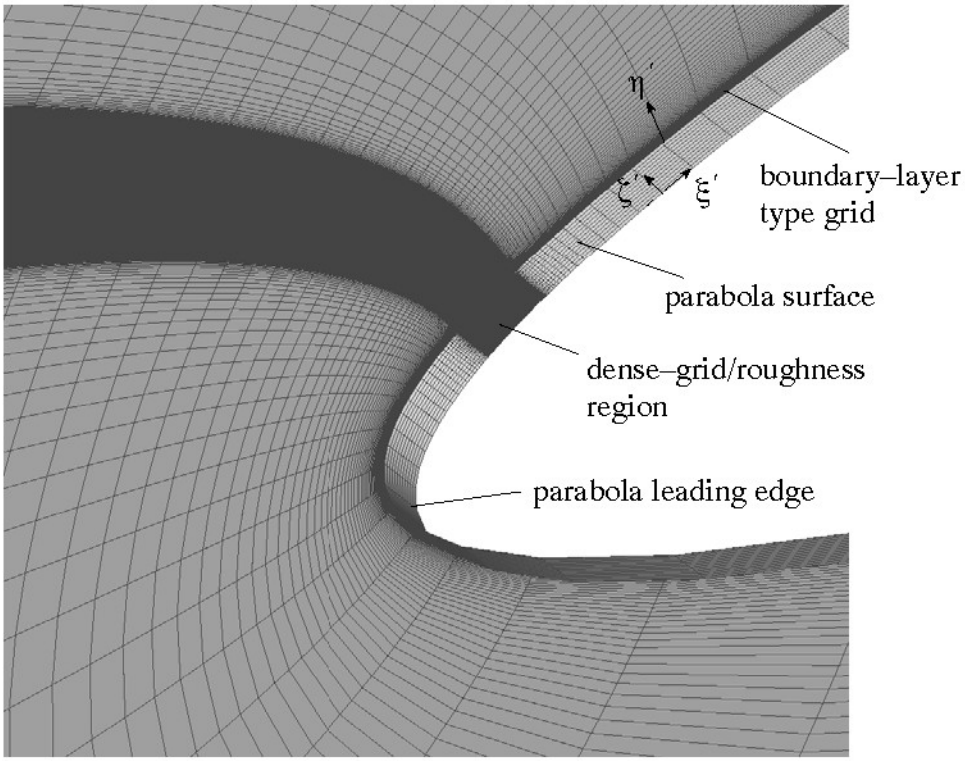

Figure 15: Grid terminology and typical grid setup for the roughness problem.

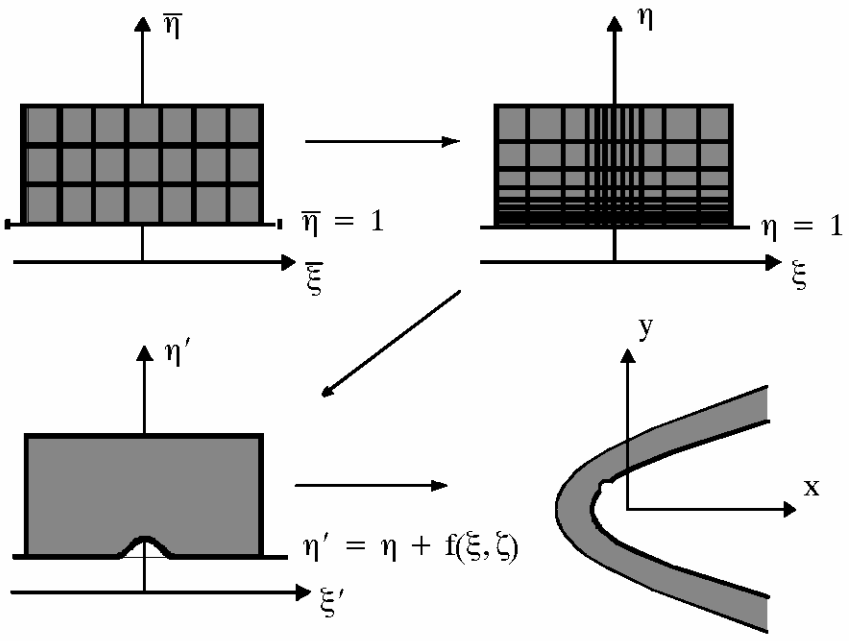

Figure 16: Summary of the geometry and grid generation process. Taken from Huebsch[41], reproduced with permission.

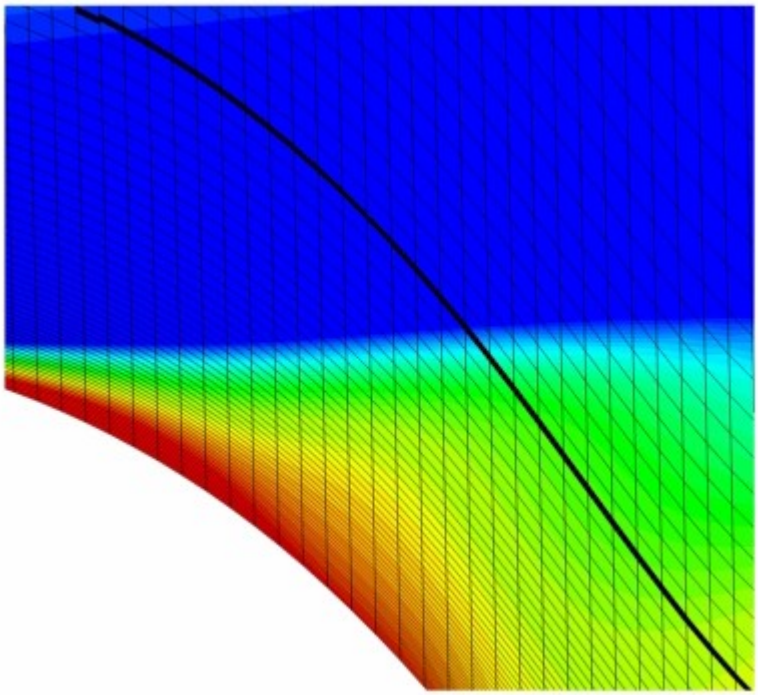

Figure 17: Vorticity immediately downstream of a roughness peak.

a) Central

b) WENO

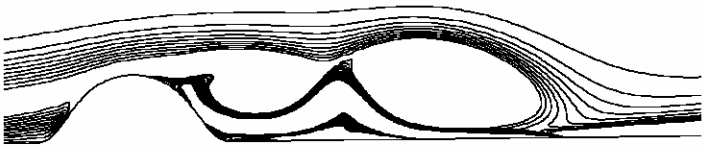

c) QUICK

Figure 18: Comparison of the three different convection differencing schemes. a) central differencing, b) WENO, c) QUICK.

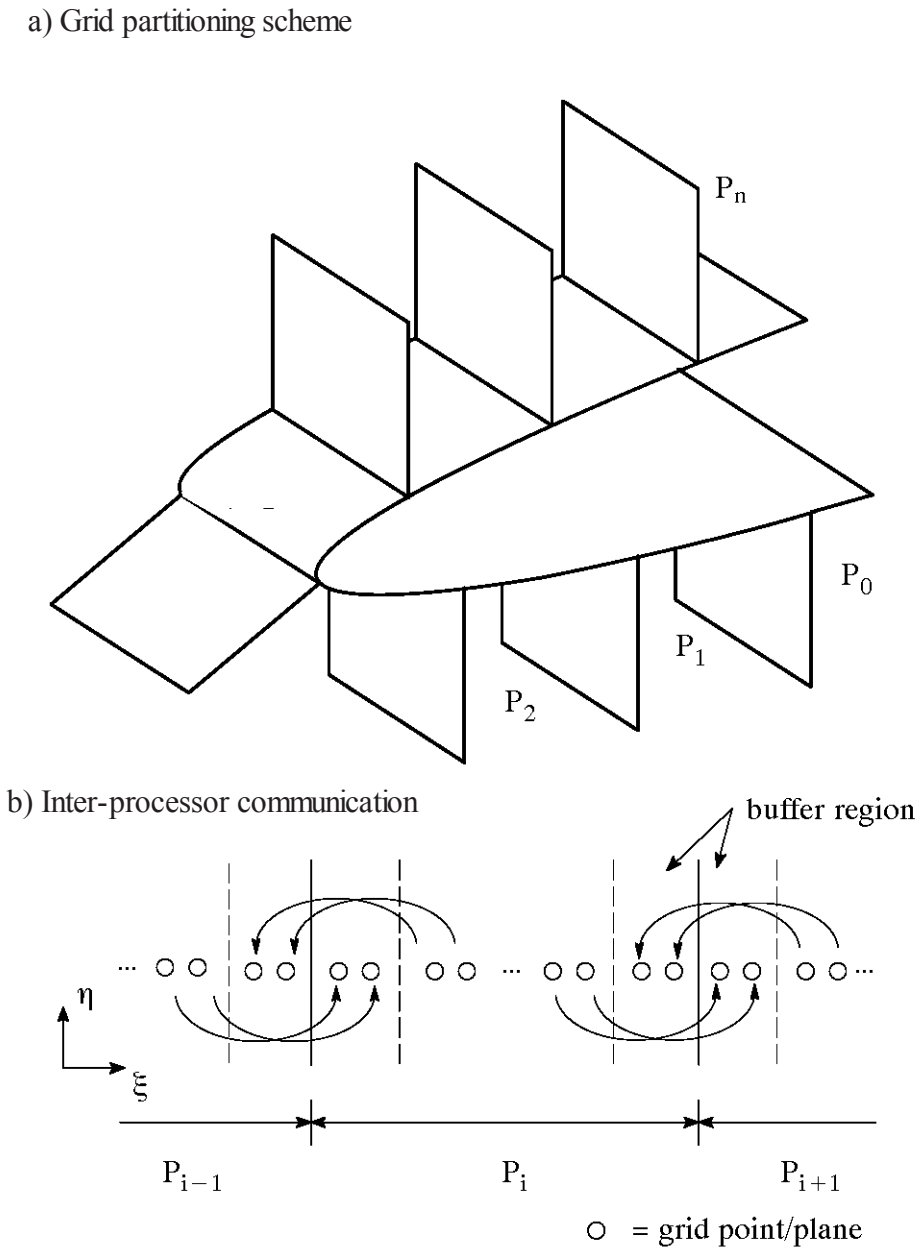

Figure 19: Schematic of a) the grid partitioning scheme and b) the inter-processor communication.

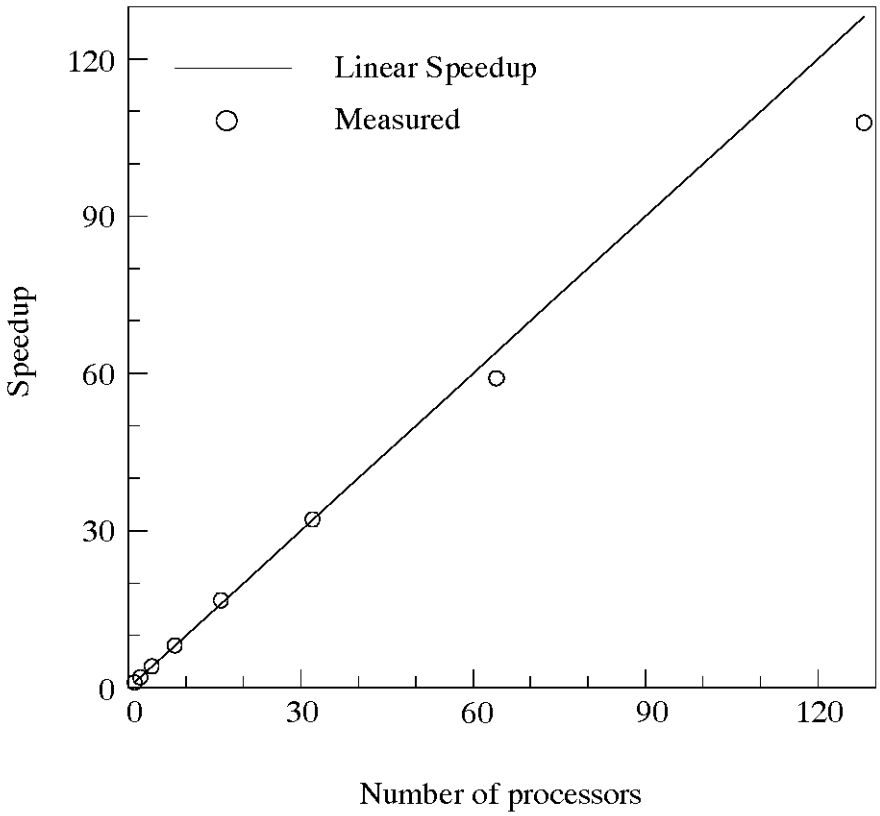

Figure 20: Computed parallel speedup compared to linear speedup.

a)

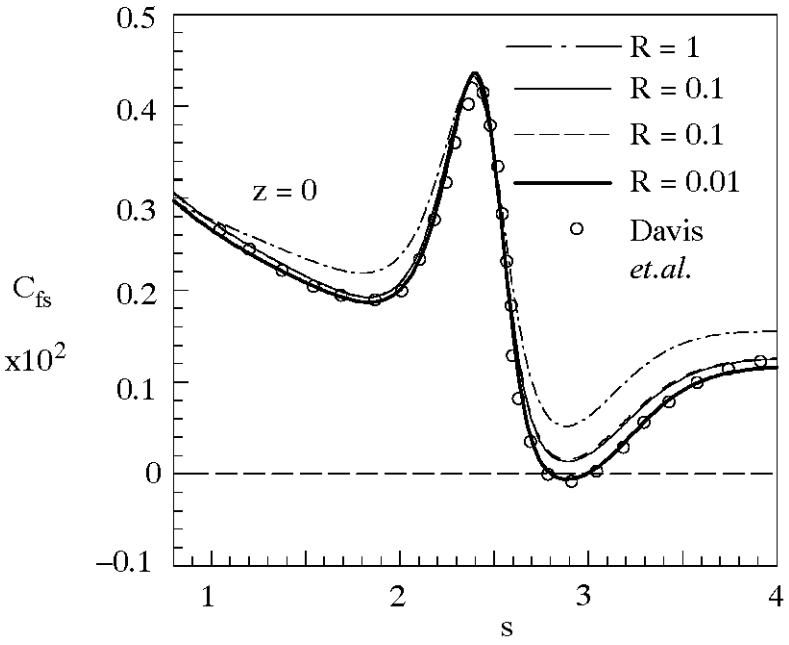

b)

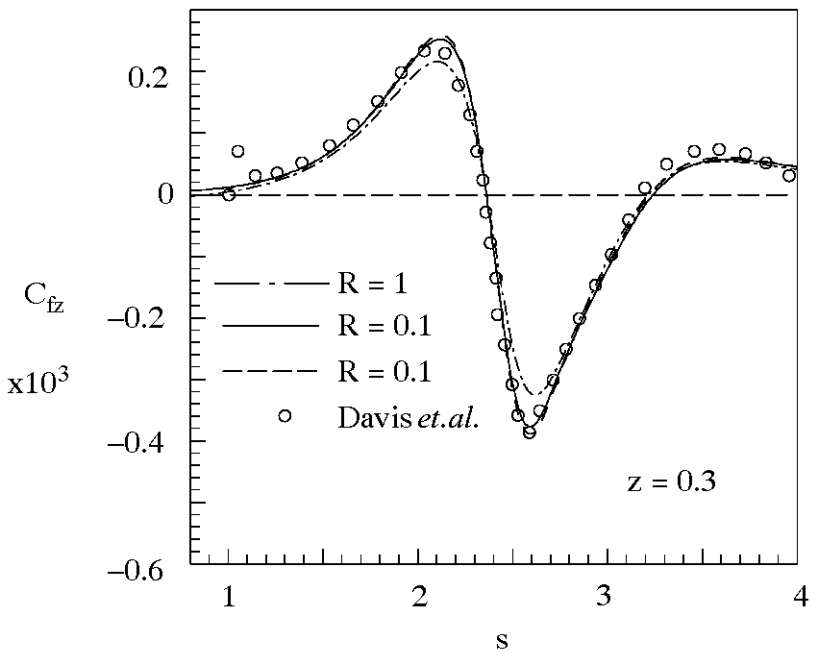

Figure 21: Comparison of the, a) streamwise skin friction down the roughness center-line and b) spanwise skin friction at the ζ =0.3 plane; with the Davis *et al*.[42] computations for a 3% bump. Present results are for parabolas of varying "thickness", R. The dashed curve with R=0.1 is a fine grid solution.

a)

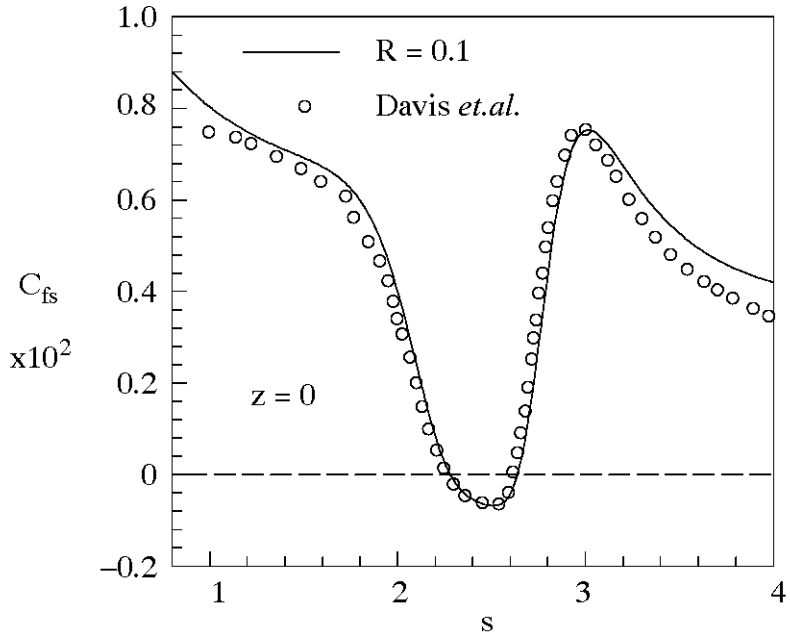

b)

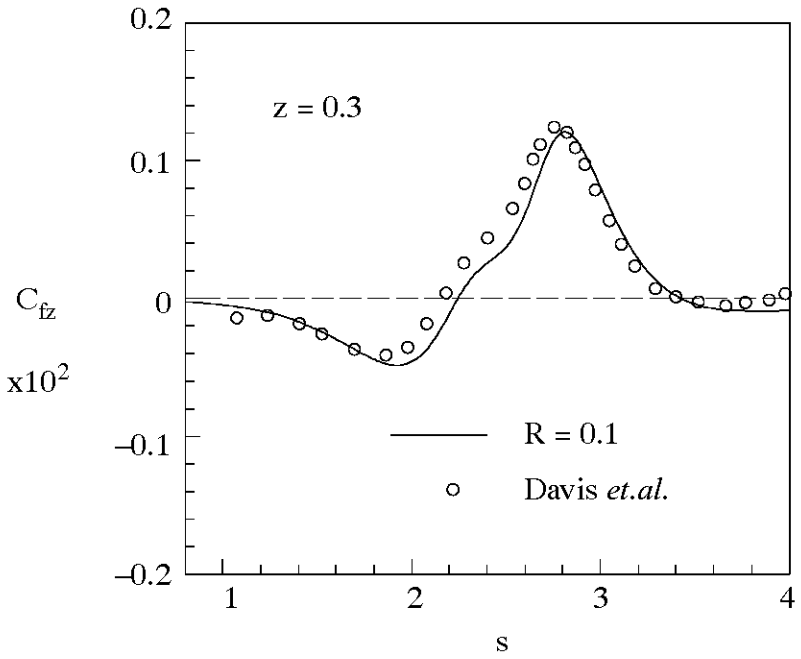

Figure 22: Comparison of the, a) streamwise skin friction down the roughness center-line and b) spanwise skin friction at the ζ =0.3 plane; with the Davis *et al*.[42] computations for a 6% dent.

a)

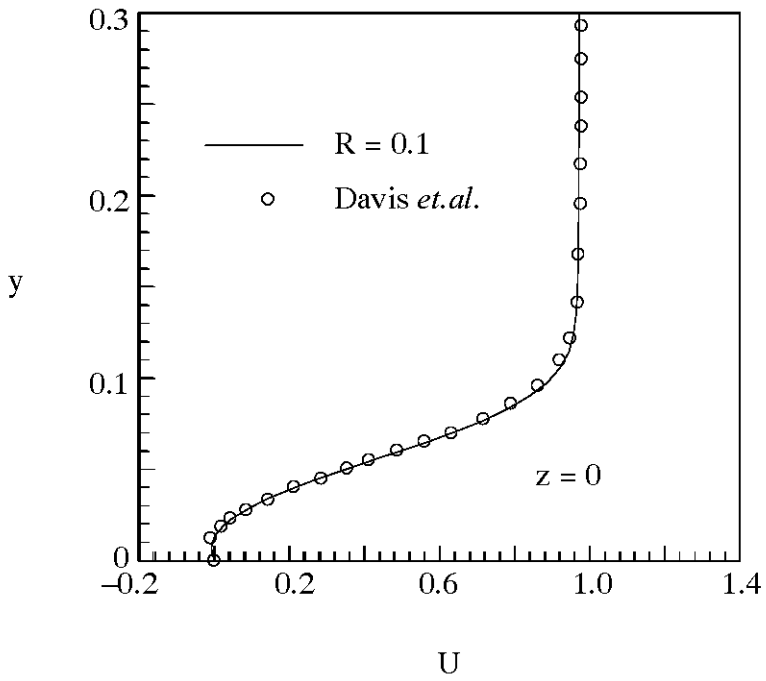

b)

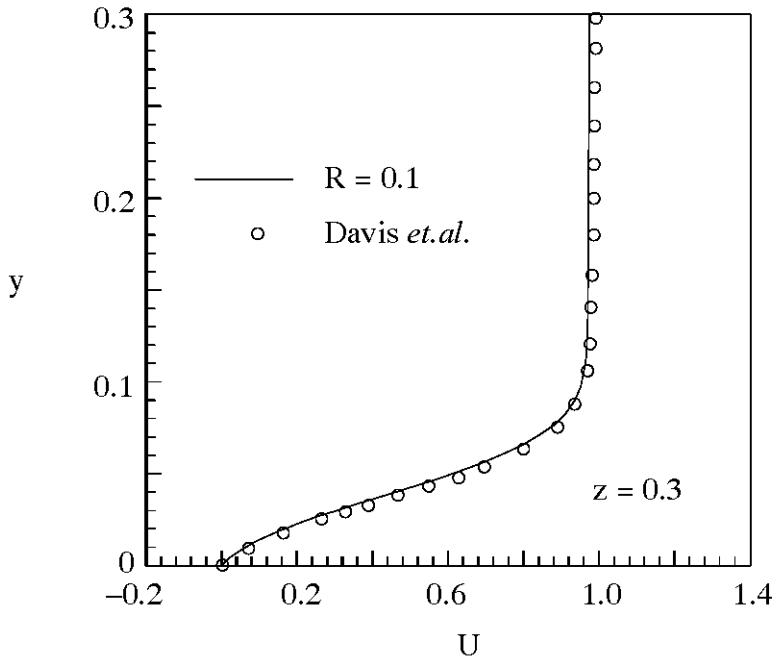

Figure 23: Comparison of the streamwise velocity with the Davis *et al.*[42] computations a) at the dent maximum depth, b) same streamwise location and ζ =0.3

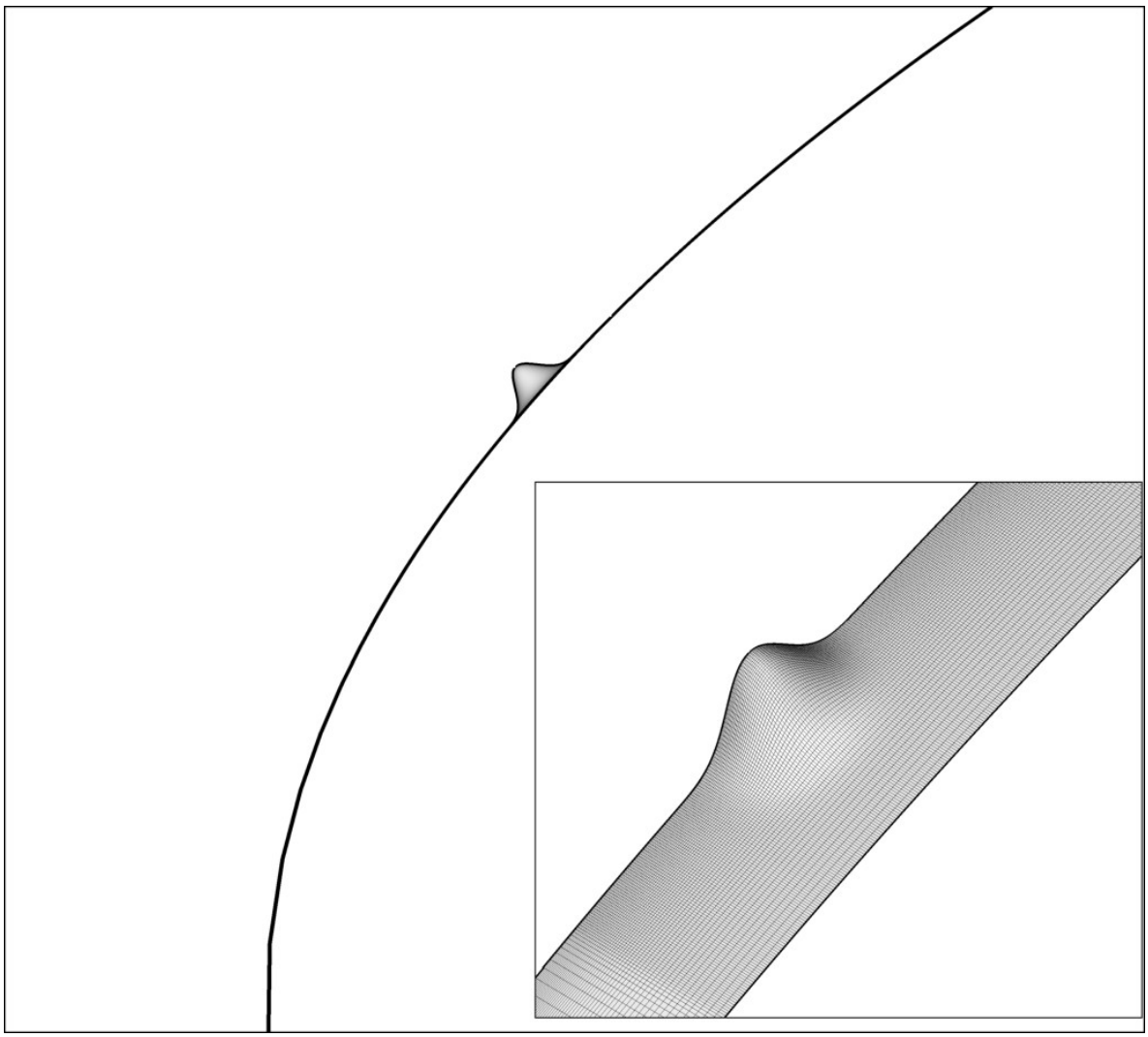

Figure 24: Roughness used for the Fluent comparison study.

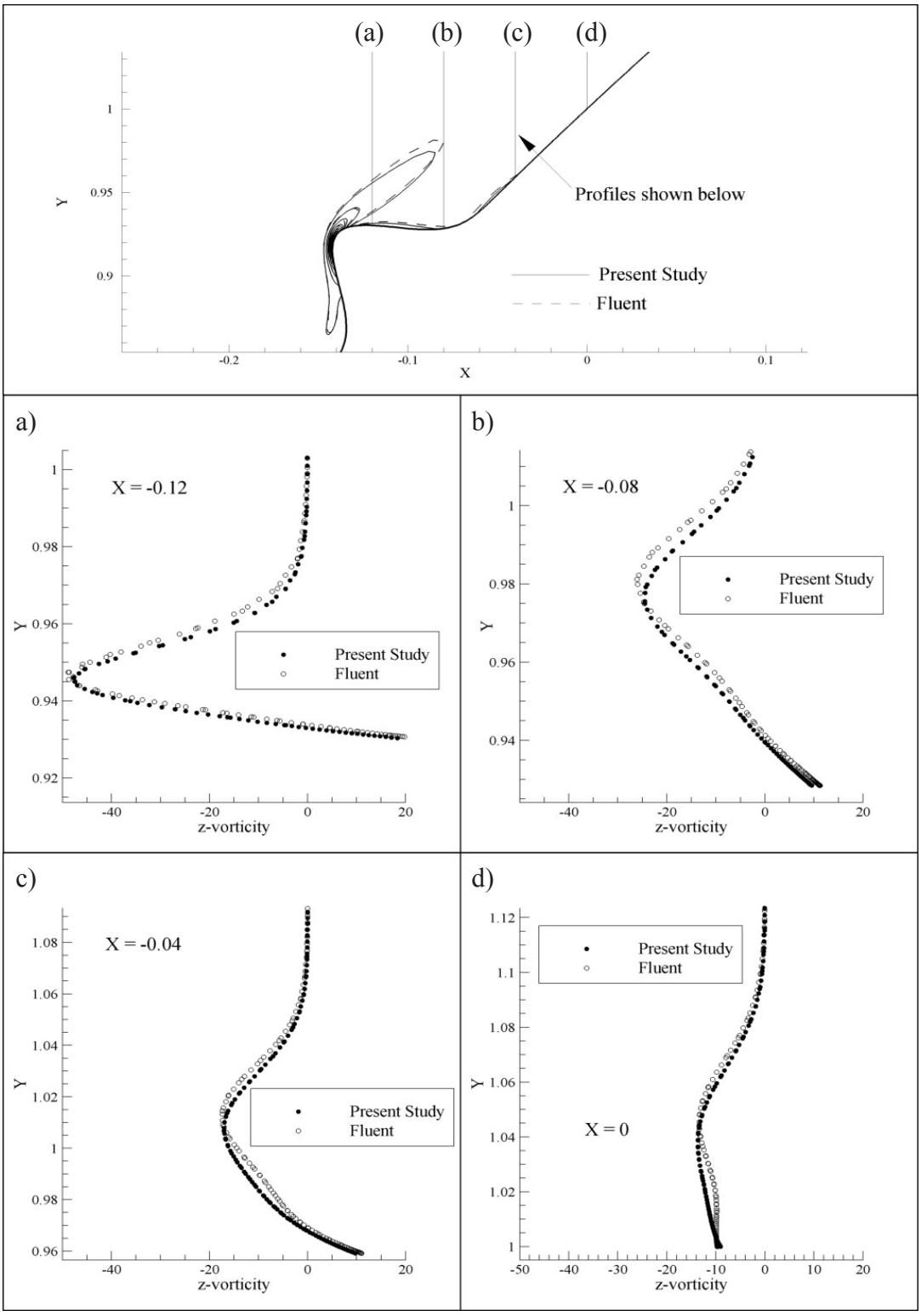

Figure 25: Comparison of z-vorticity at z = -0.05

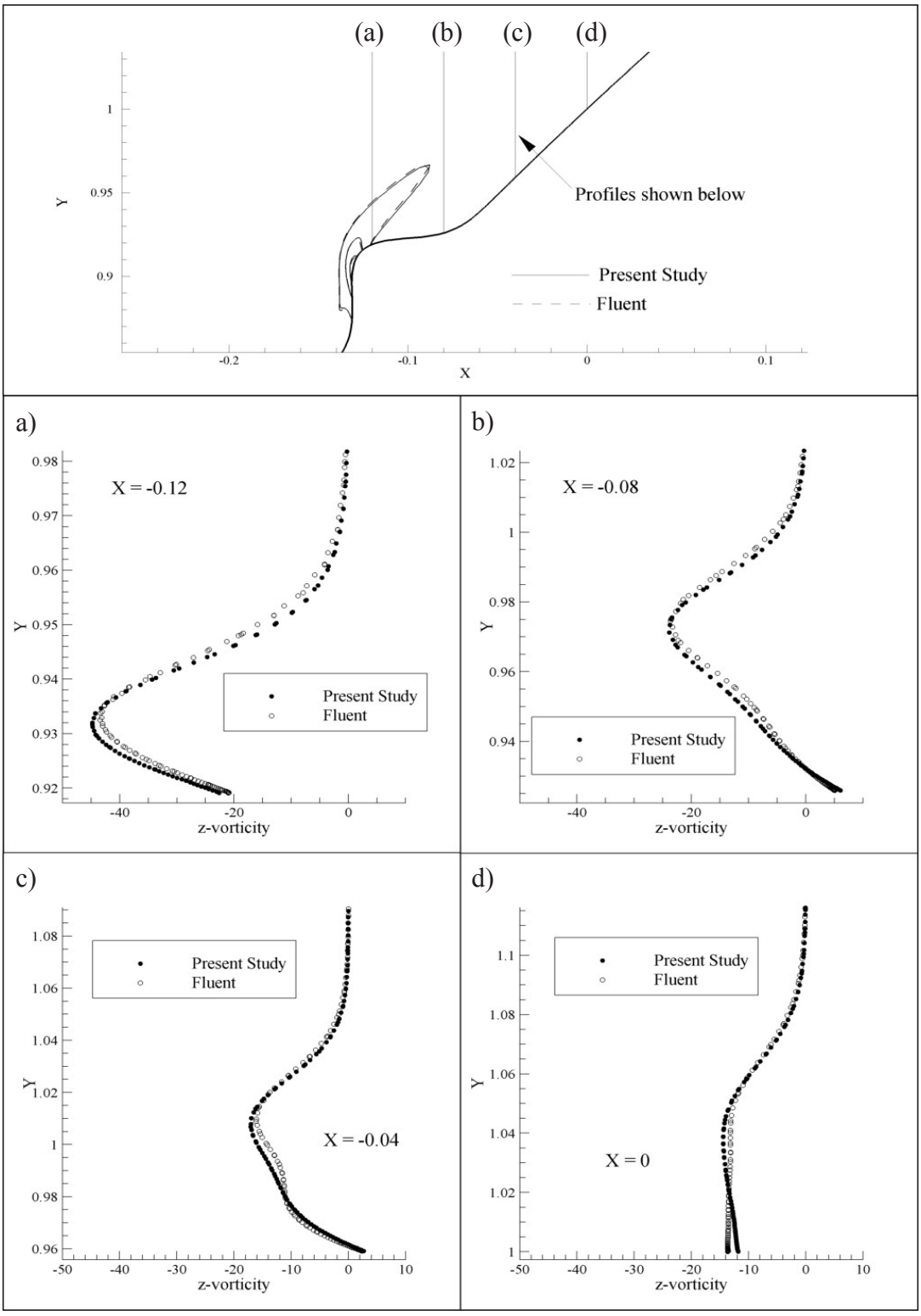

Figure 26: Comparison of z-vorticity at z = -0.03

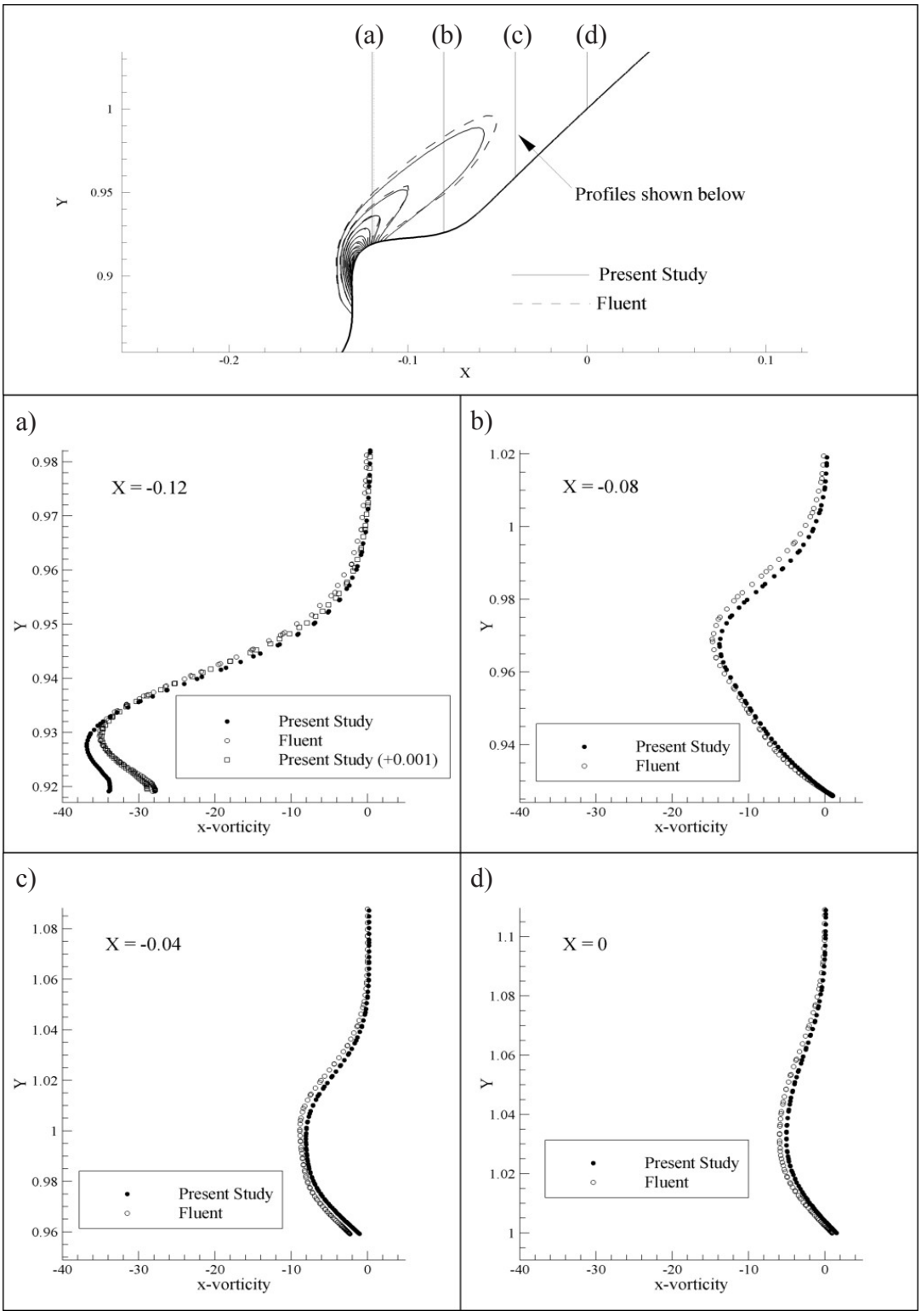

Figure 27: Comparison of x-vorticity at z = -0.03

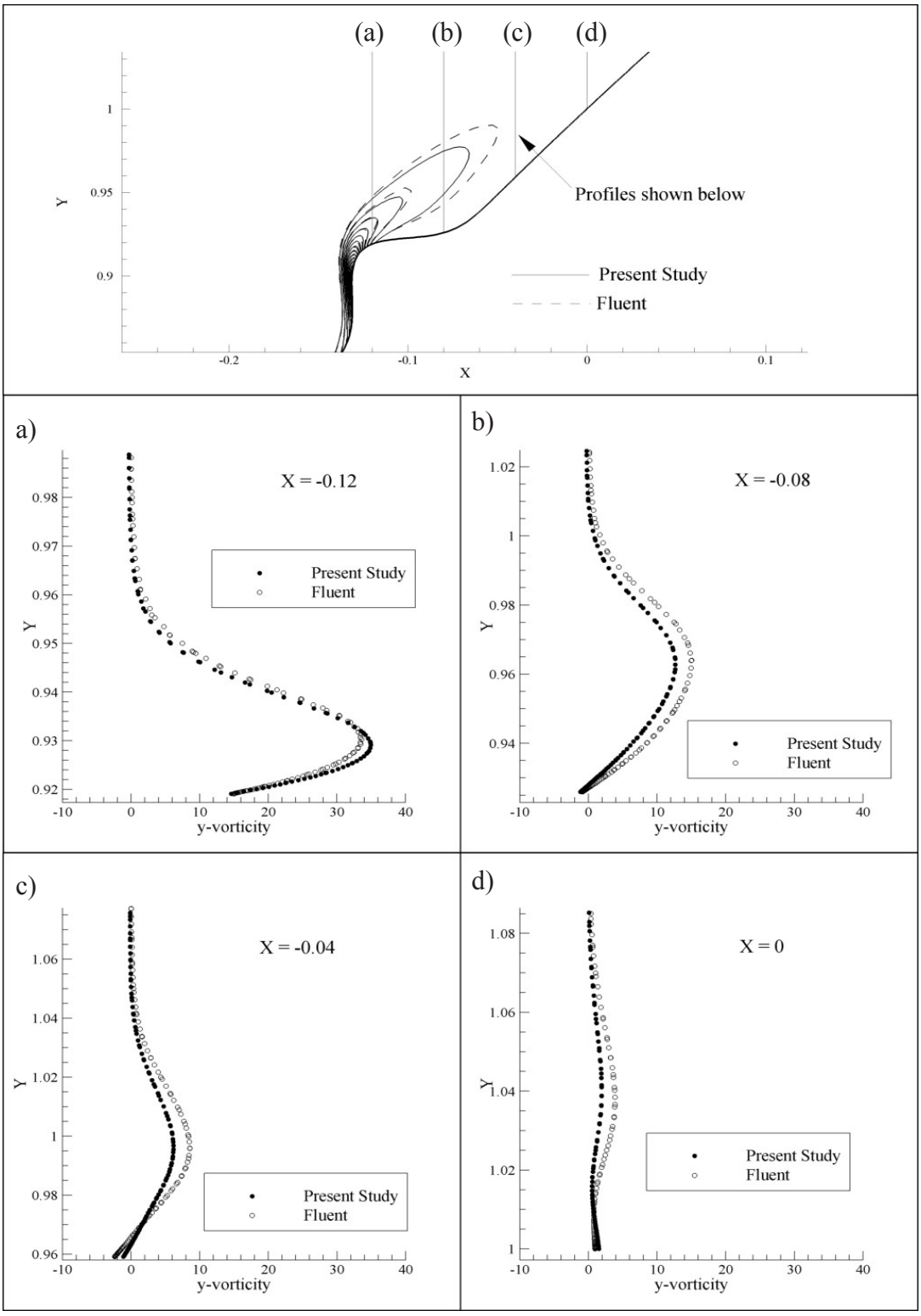

Figure 28: Comparison of y-vorticity at z = -0.03

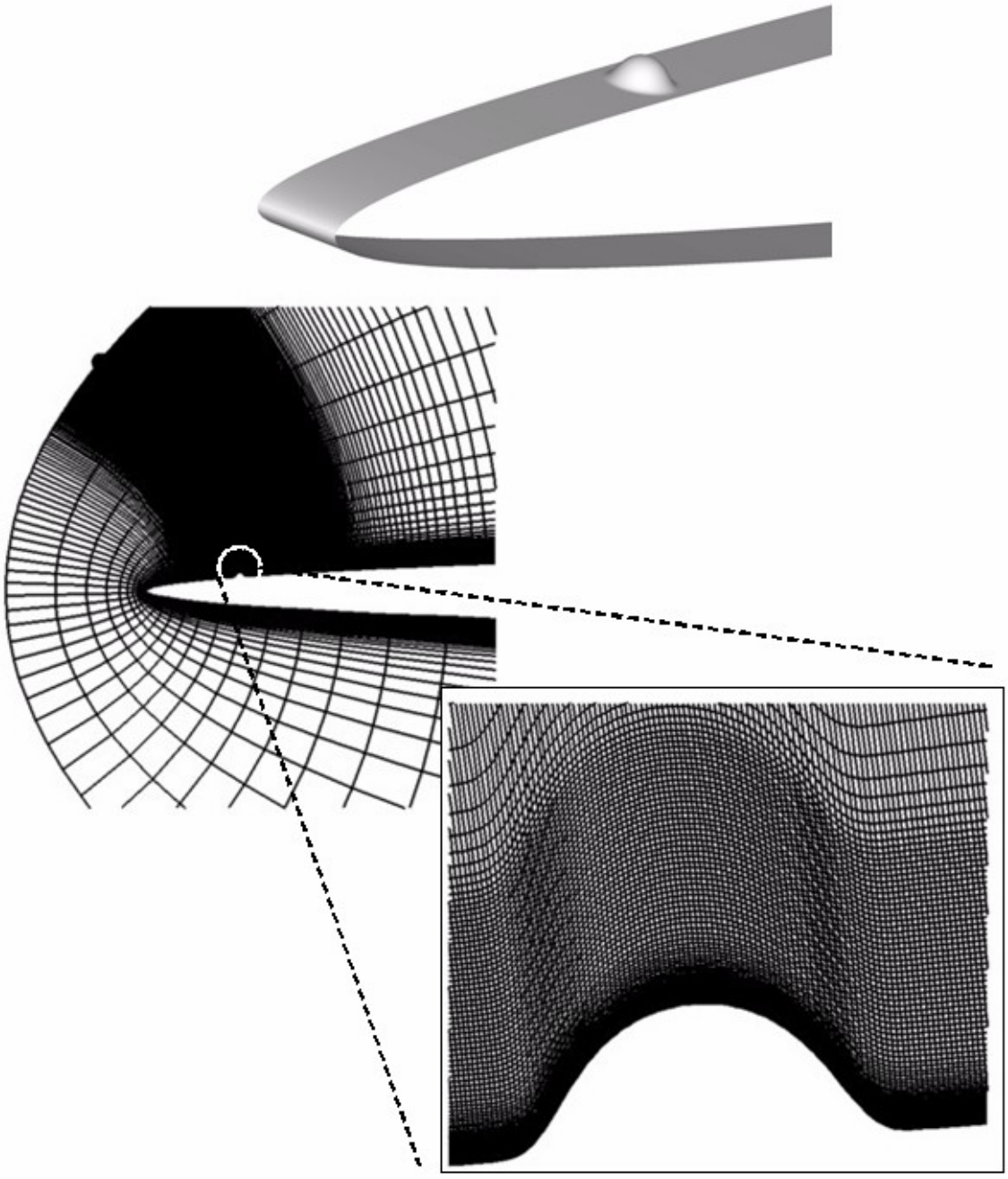

Figure 29: Model geometry and grid used to reproduce the Winkler[17] experiment.

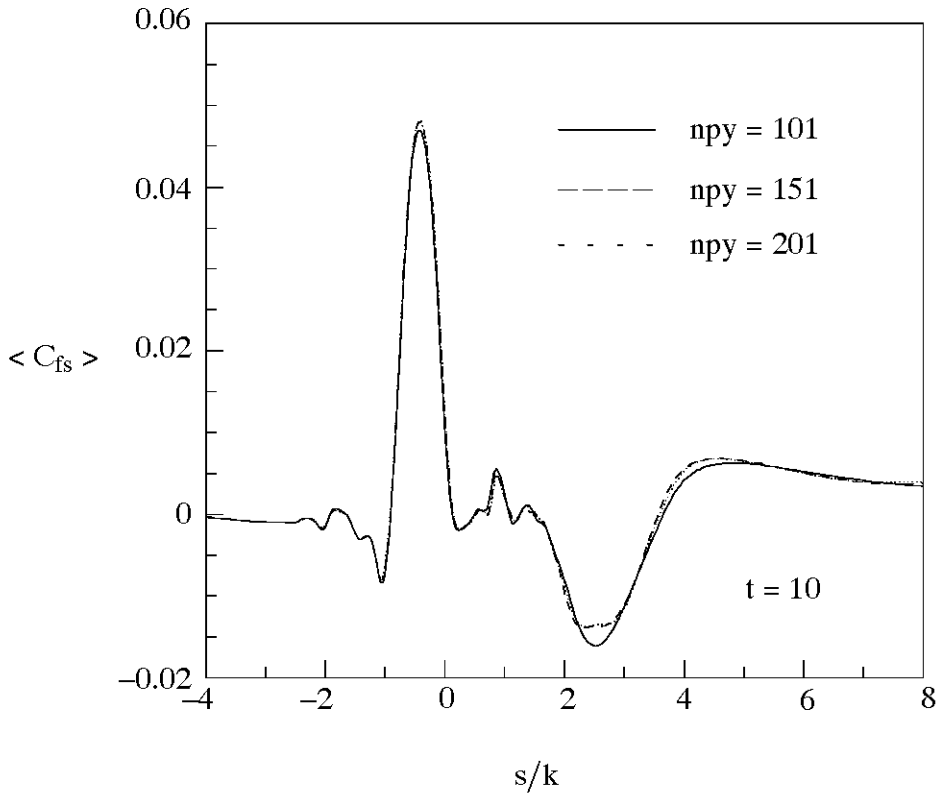

Figure 30: Effect of increasing the wall-normal grid resolution on the time-averaged streamwise skin friction, $<C_{fs}>$, for a two-dimensional calculation of the Winkler[17] experiment.

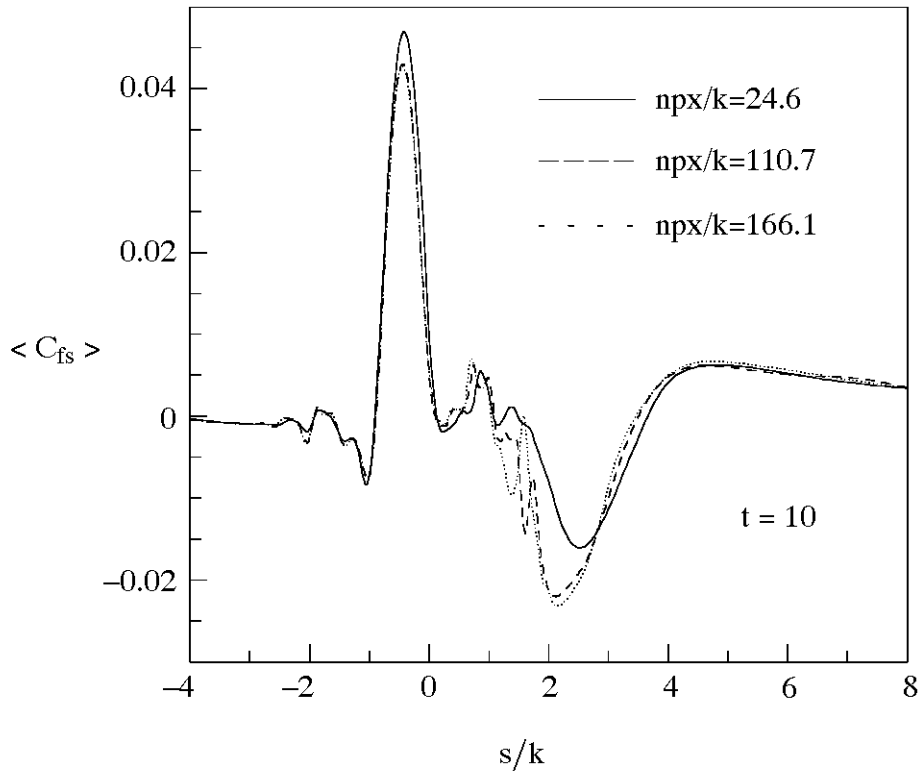

Figure 31: Effect of increasing the streamwise grid resolution on the time-averaged streamwise skin friction, $<C_{fs}>$, for a two-dimensional calculation of the Winkler[17] experiment.

Experiment

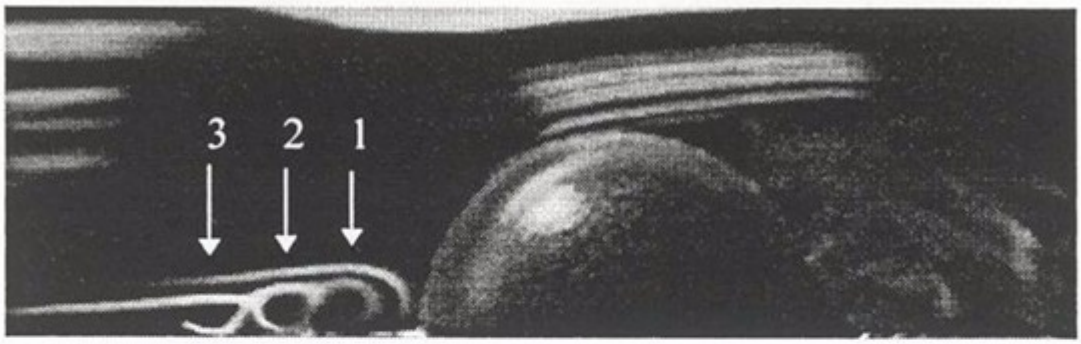

Three-dimensional Computation

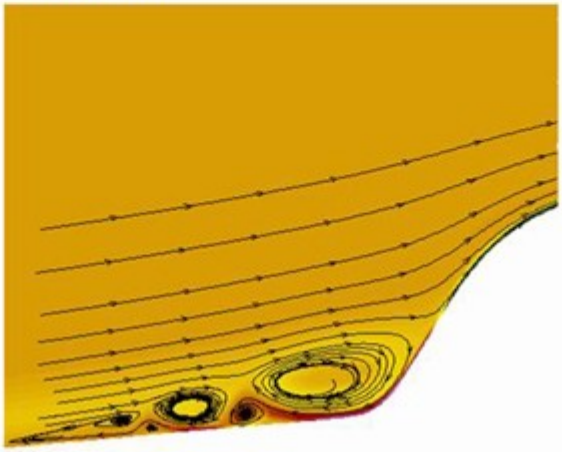

Figure 32: Comparison of experimental smoke visualization and computational time-averaged streamlines upstream of the roughness element. Experiment figure is taken from Winkler[17], reproduced with permission.

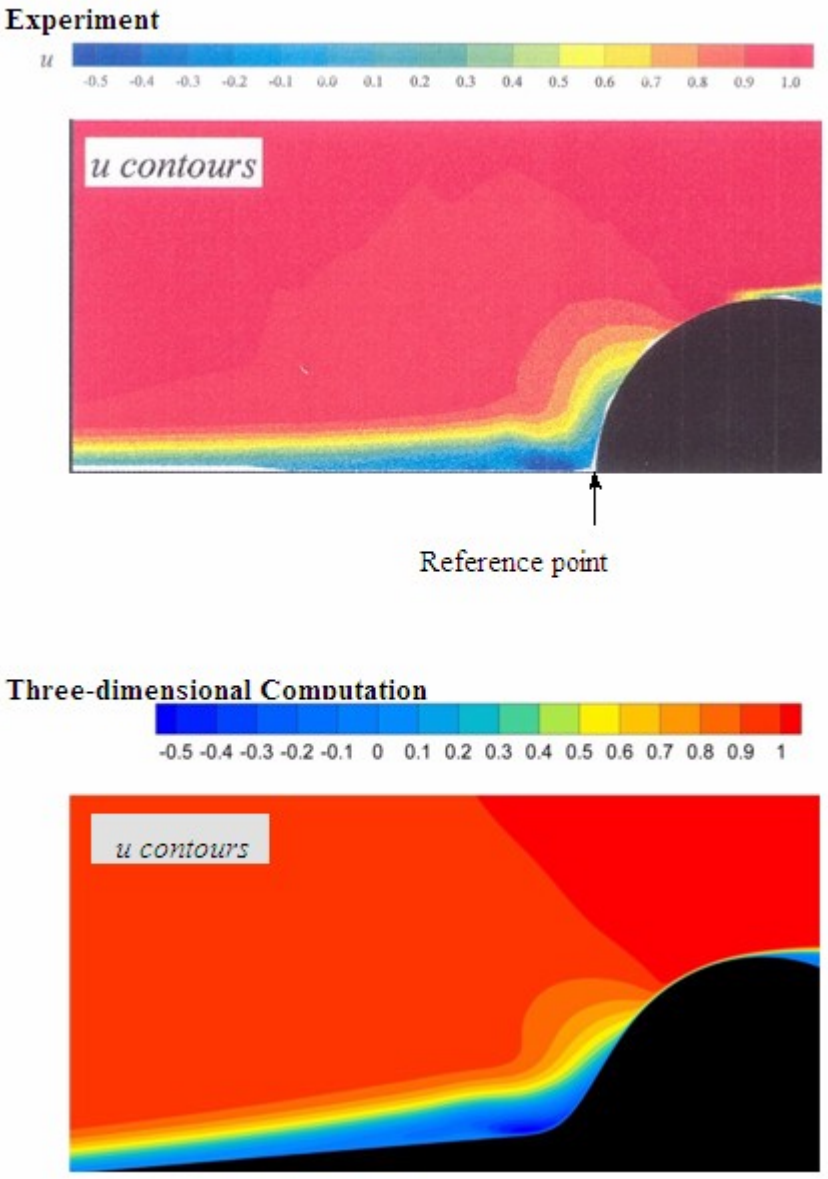

Figure 33: Comparison of time-averaged streamwise velocity contours near the leading edge of the roughness. Experiment figure is taken from Winkler[17], reproduced with permission.

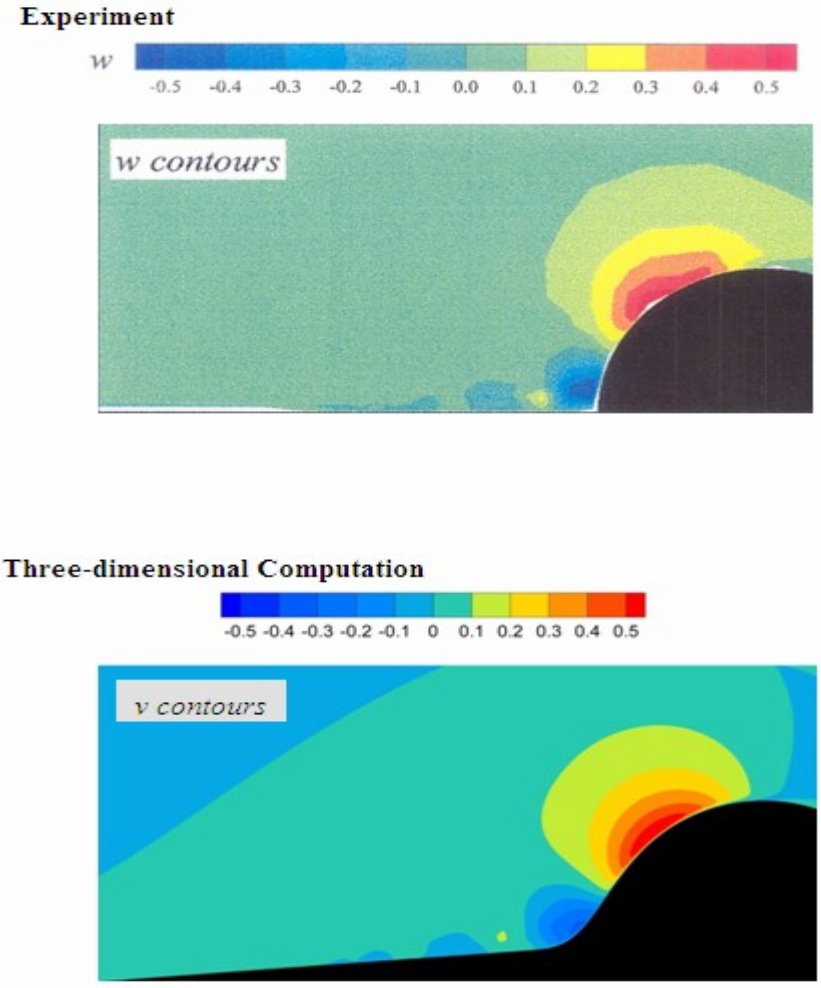

Figure 34: Comparison of time-averaged wall-normal velocity contours near the leading edge of the roughness. Experiment figure is taken from Winkler[17], reproduced with permission.

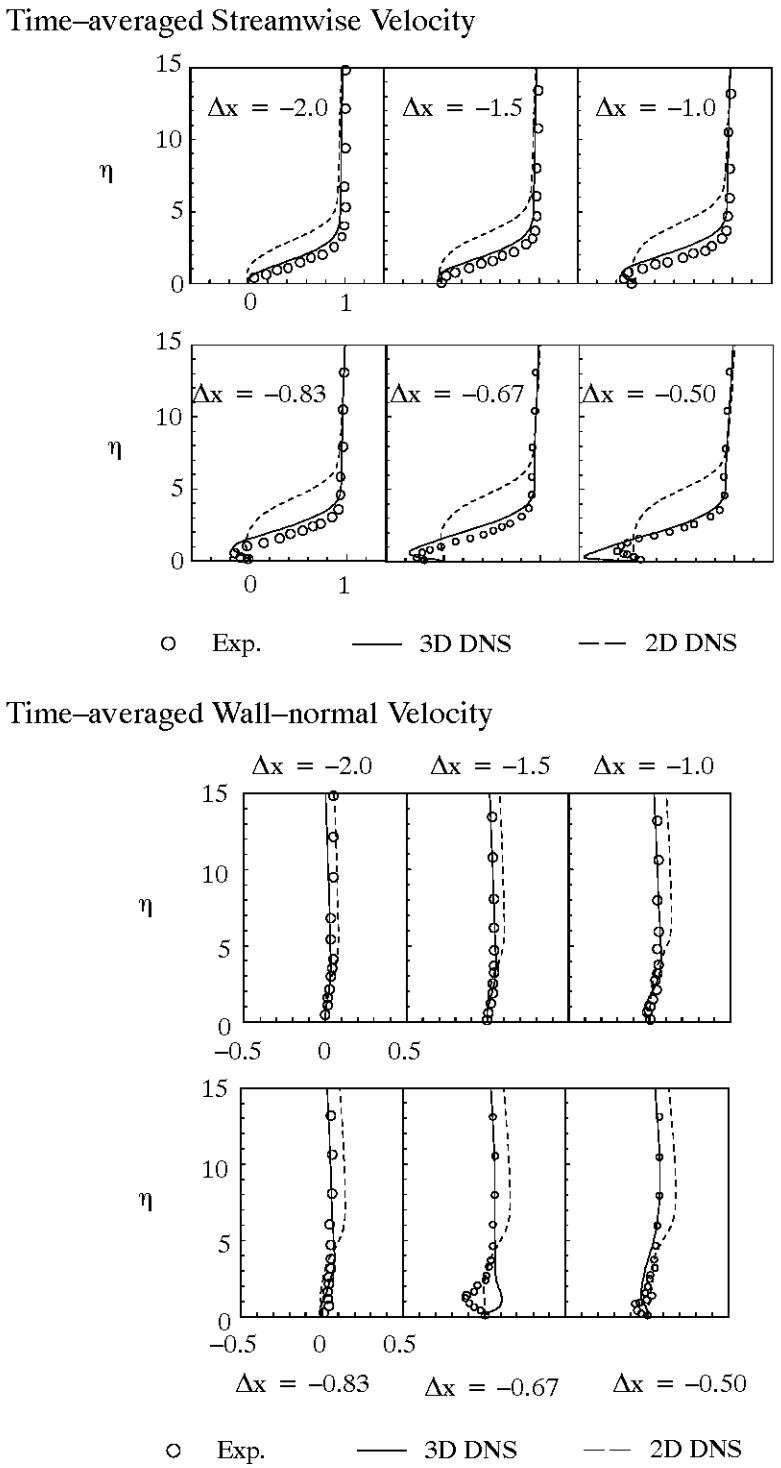

Figure 35: Time-averaged velocity profiles approaching the roughness element. Comparison between experiment of Winkler[17] and computation.

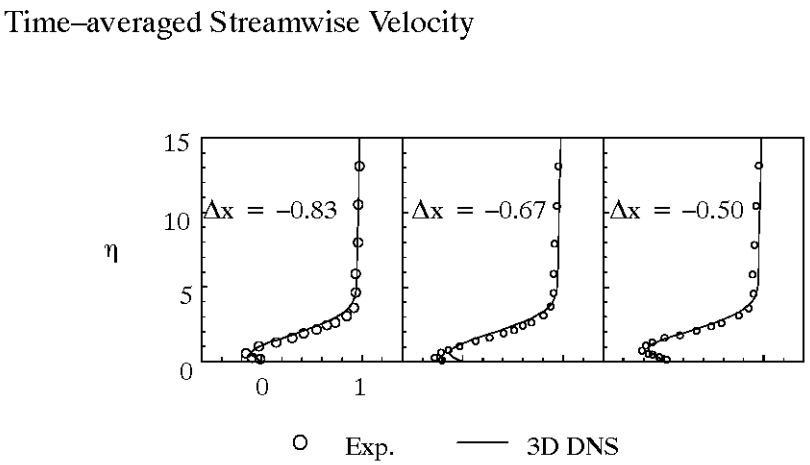

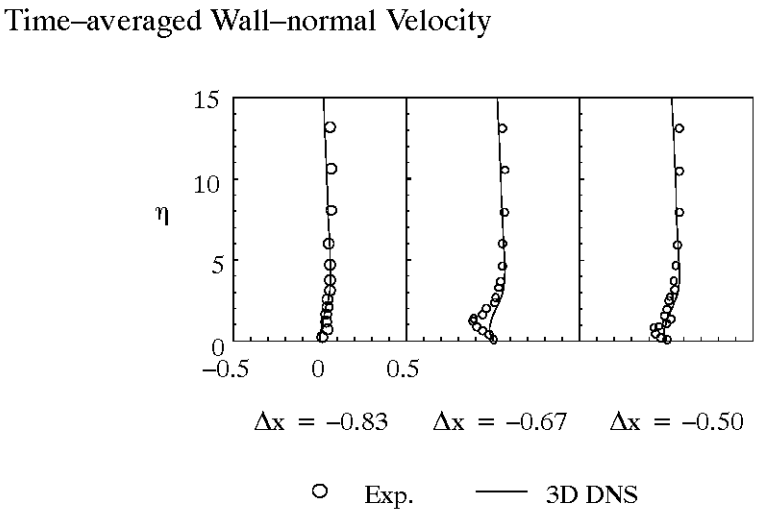

Figure 36: Shifted time-averaged velocity profiles approaching the roughness element. Comparison between experiment of Winkler[17] and computation.

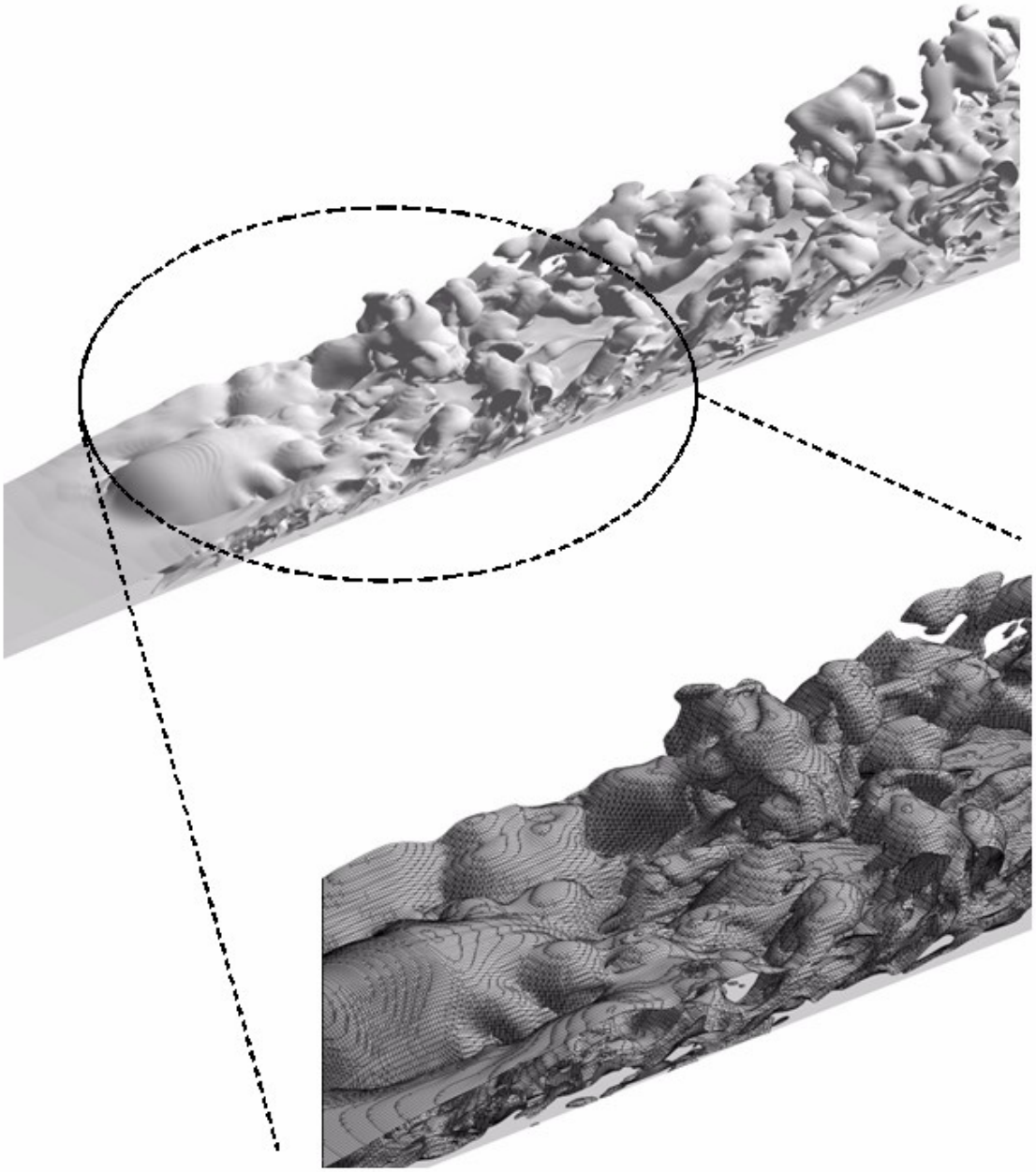

Figure 37: Iso-surface of spanwise vorticity, showing flow development over the isolated roughness. Also shown is a close-up immediately downstream of the roughness element with grid overlay.

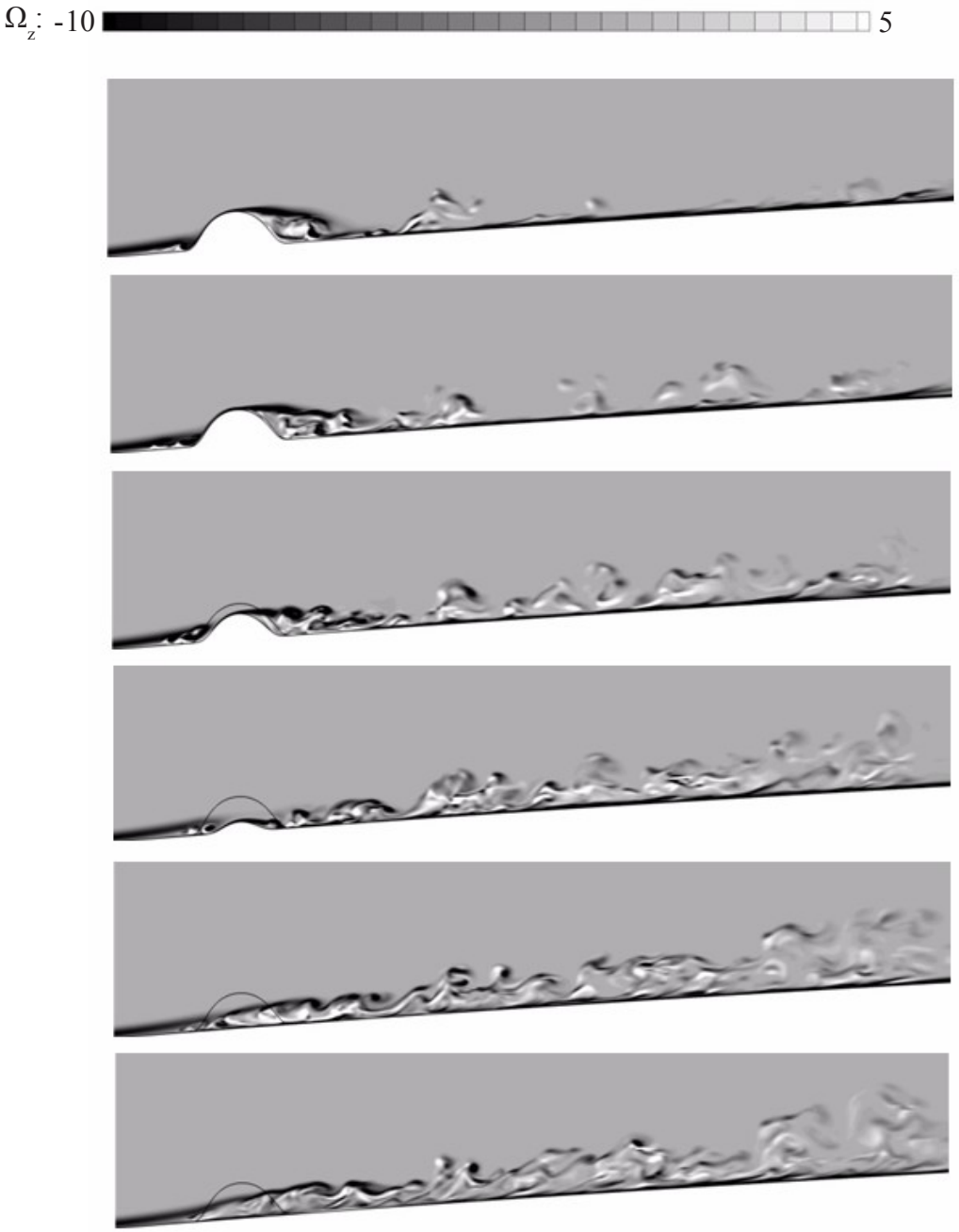

Figure 38: Contours of spanwise vorticity at various spanwise locations. The top plot is at the roughness center plane. The bottom plot is approximately two roughness heights from the center plane.

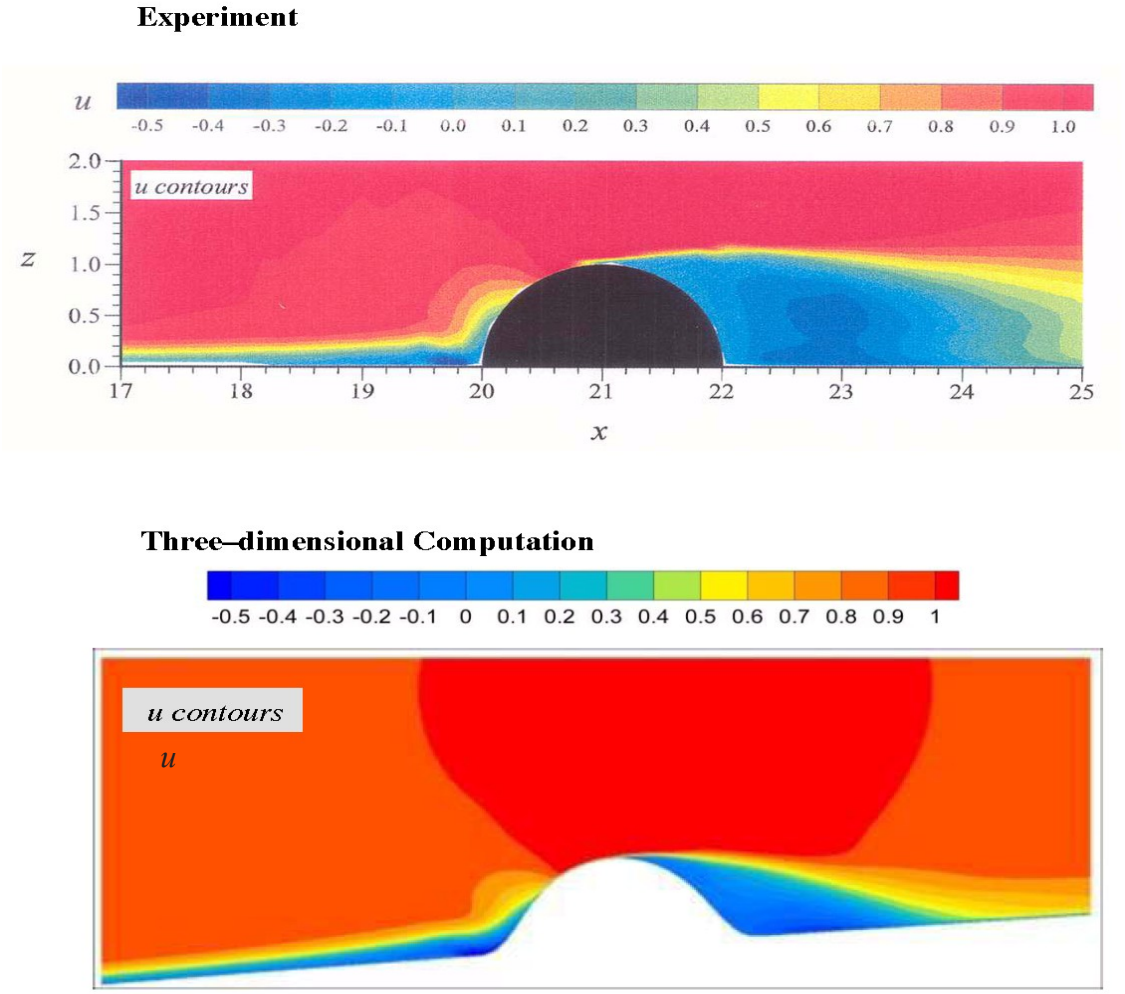

Figure 39: Comparison of time-averaged streamwise velocity contours over the entire isolated roughness. Numerical solutions are not grid resolved and contain excessive numerical dissipation. Experiment figure is taken from Winkler[17], reproduced with permission.

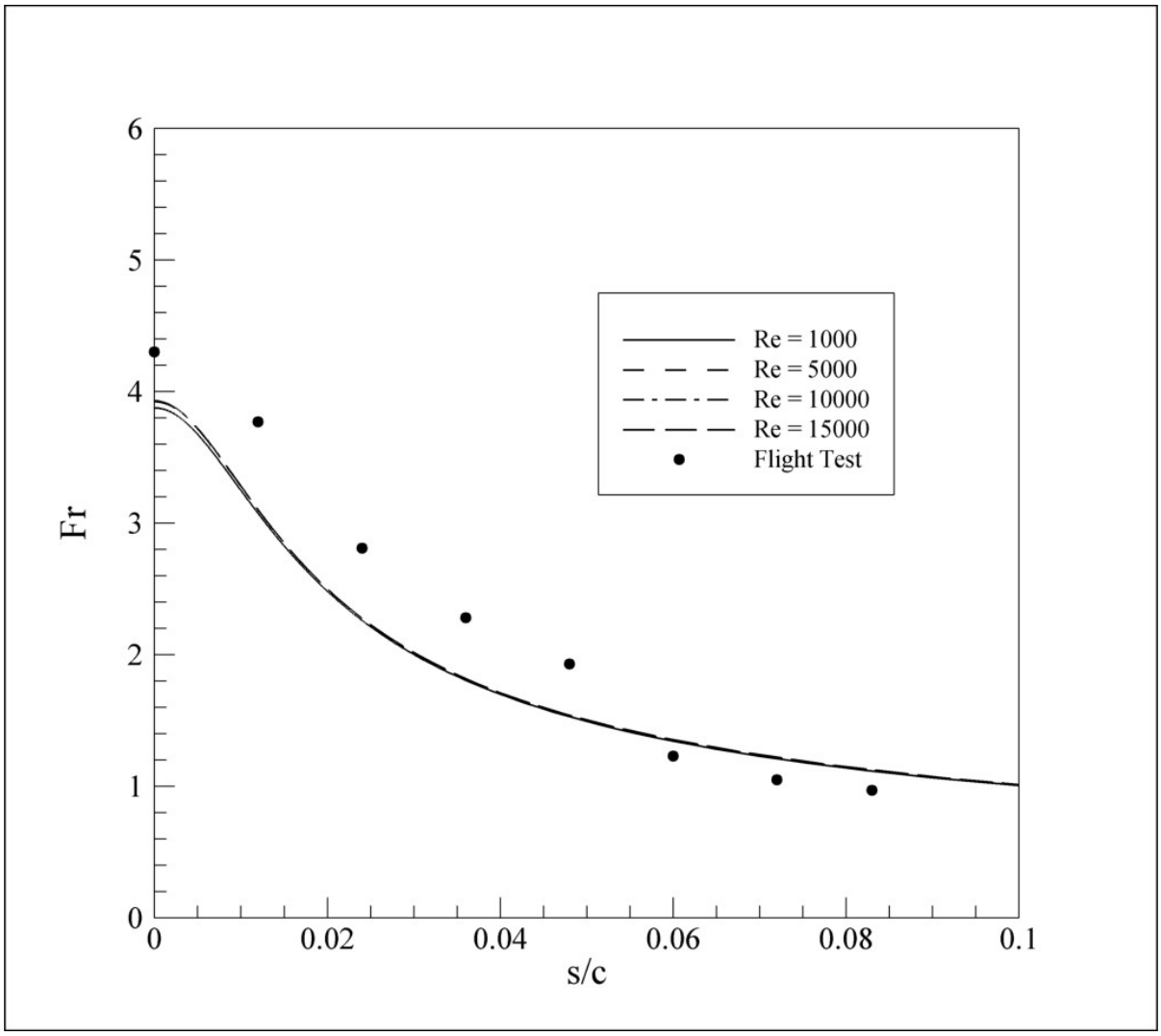

Figure 40: Frossling number on the leading edge. Comparison with leading edge NACA 0012 flight test data of Poinsatte *et al.*[52]

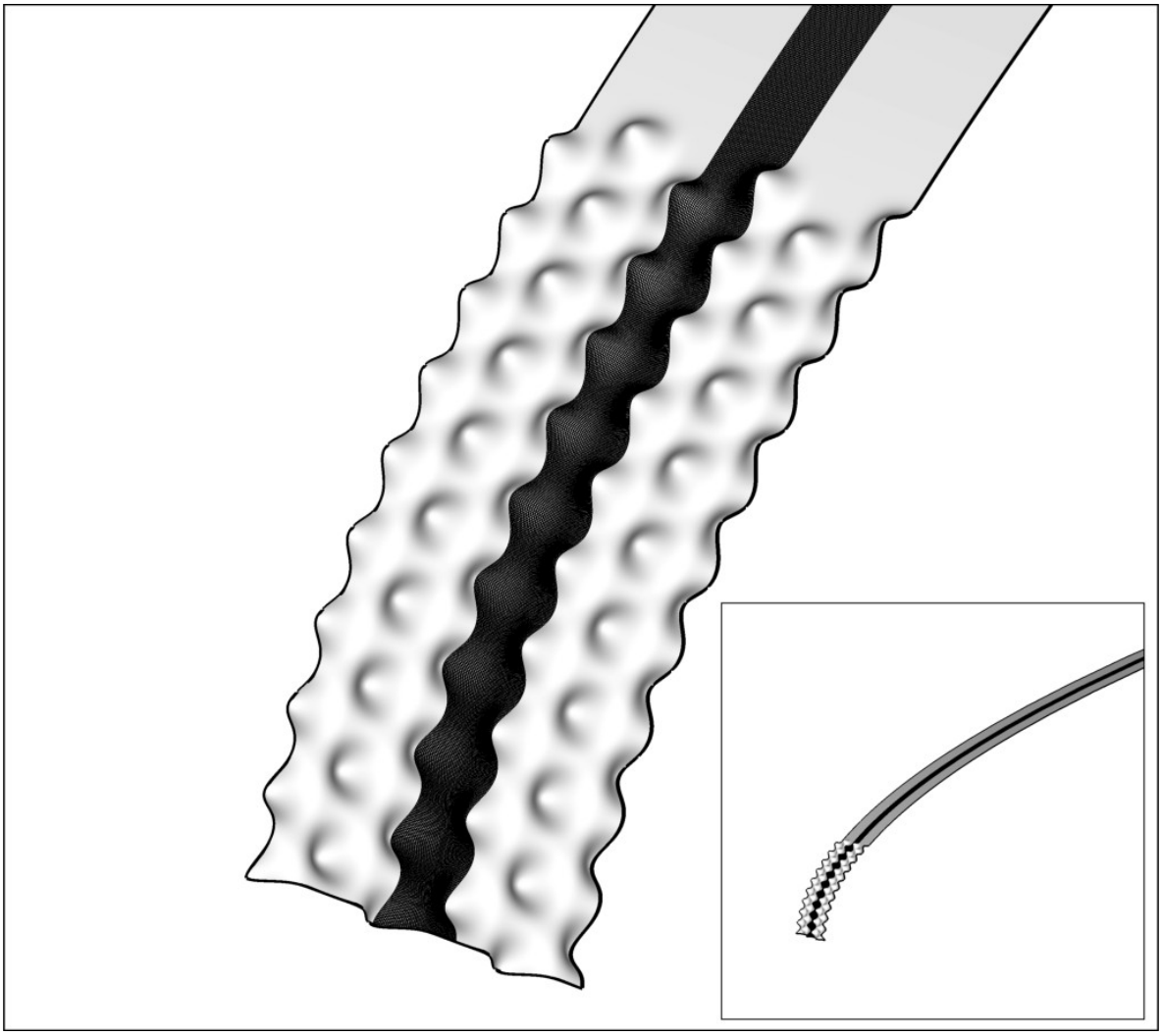

Figure 41: Baseline roughness pattern used in the current study.

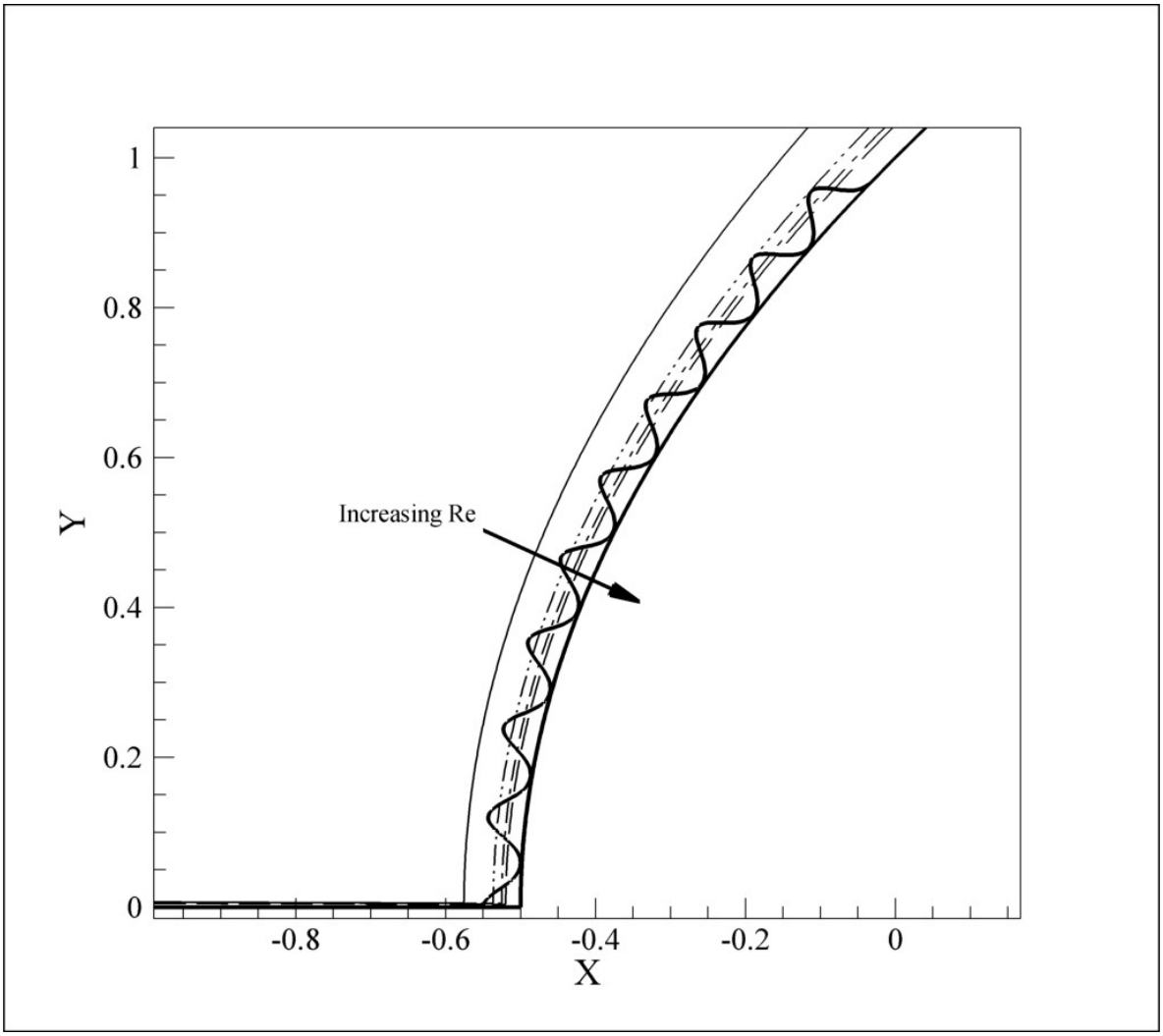

Figure 42: Comparison of the baseline roughness pattern with the two-dimensional laminar boundary-layer thickness for leading edge Re of 1000, 5000, 10,000 and 15,000.

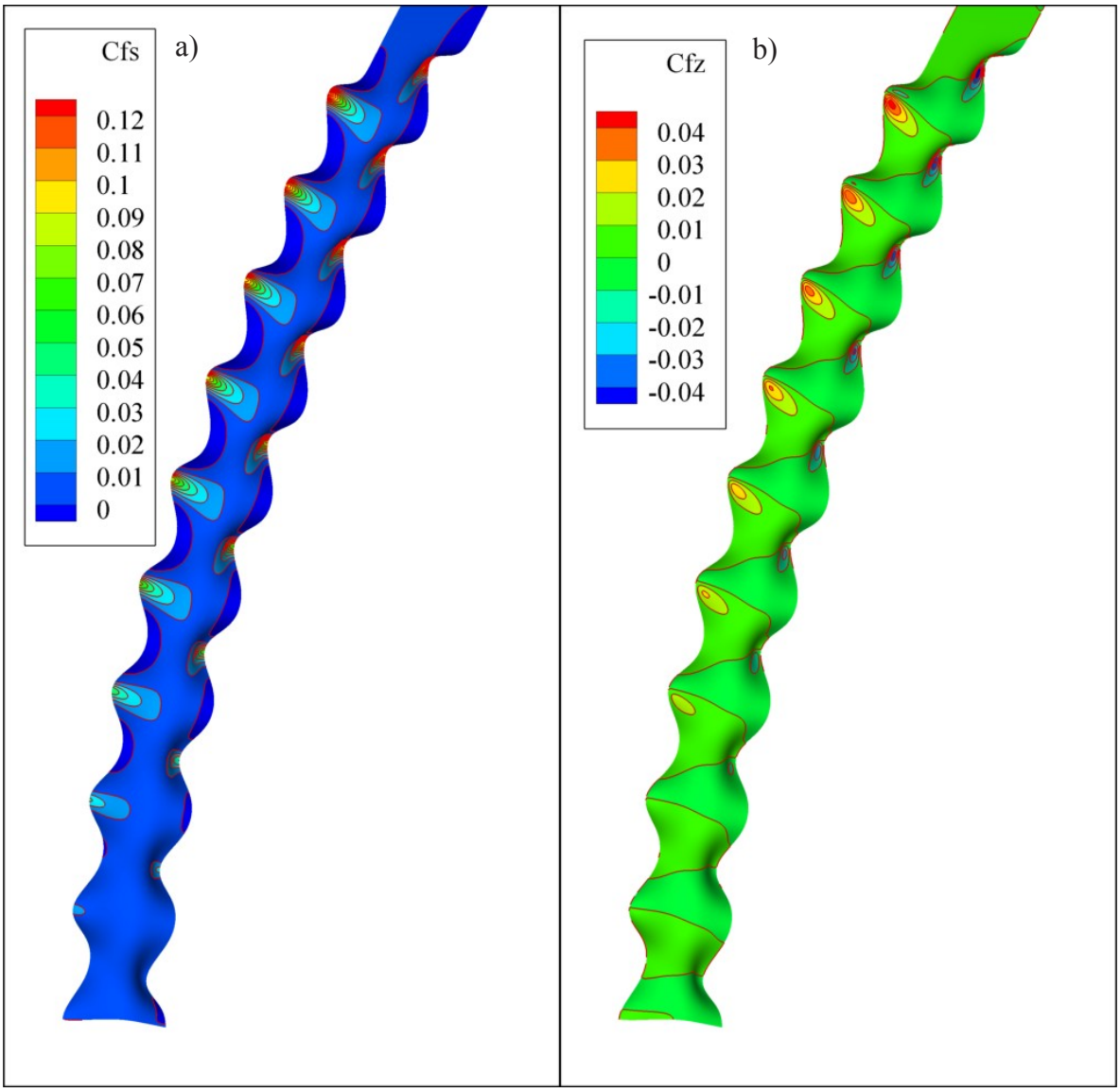

Figure 43: a) Streamwise and b) spanwise skin friction for flow over the roughness field at Re=5000.

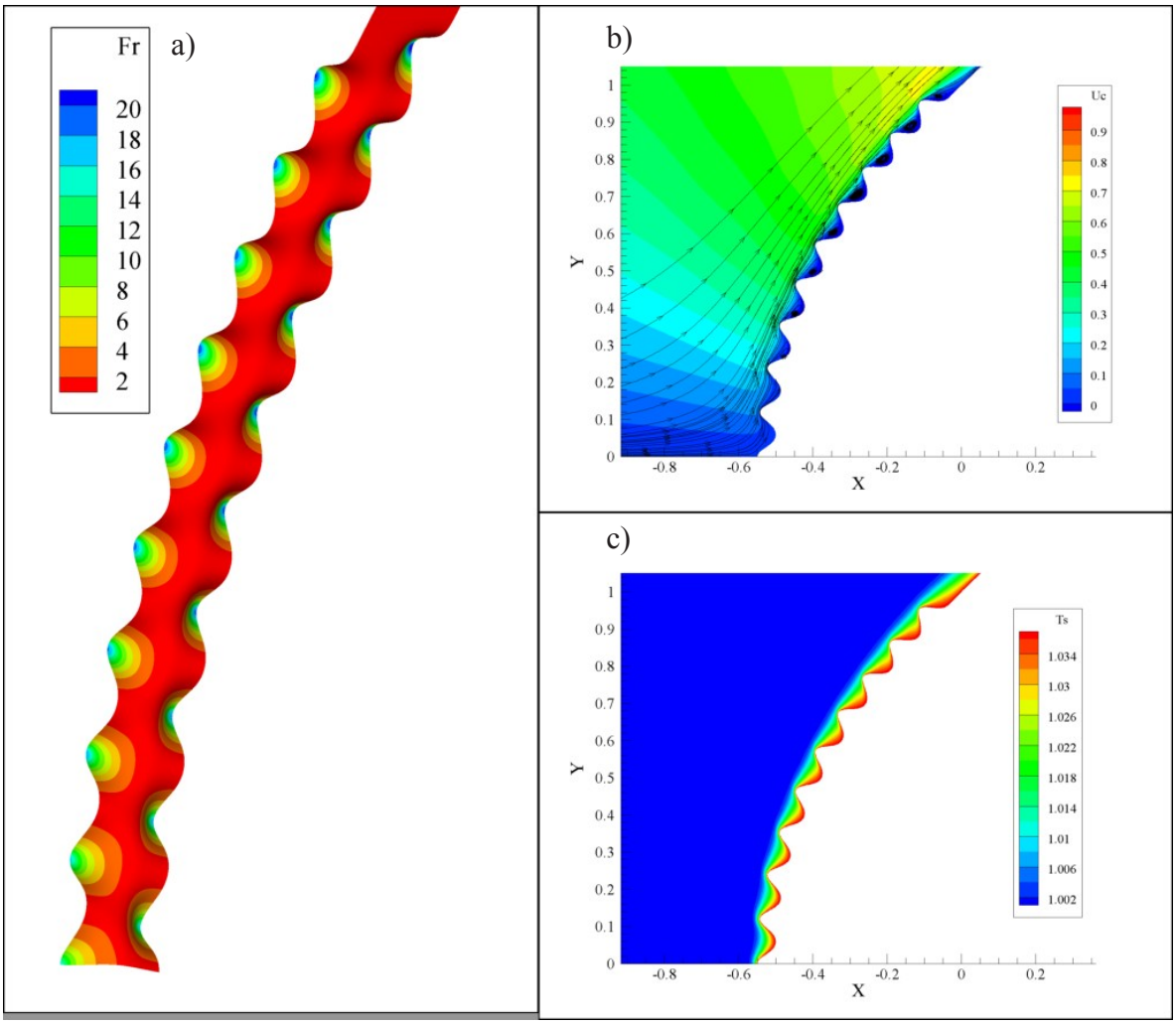

Figure 44: Contours of a) Frossling number, b) streamwise velocity, *Uc*, and c) static temperature, over the roughness field at Re=5000.

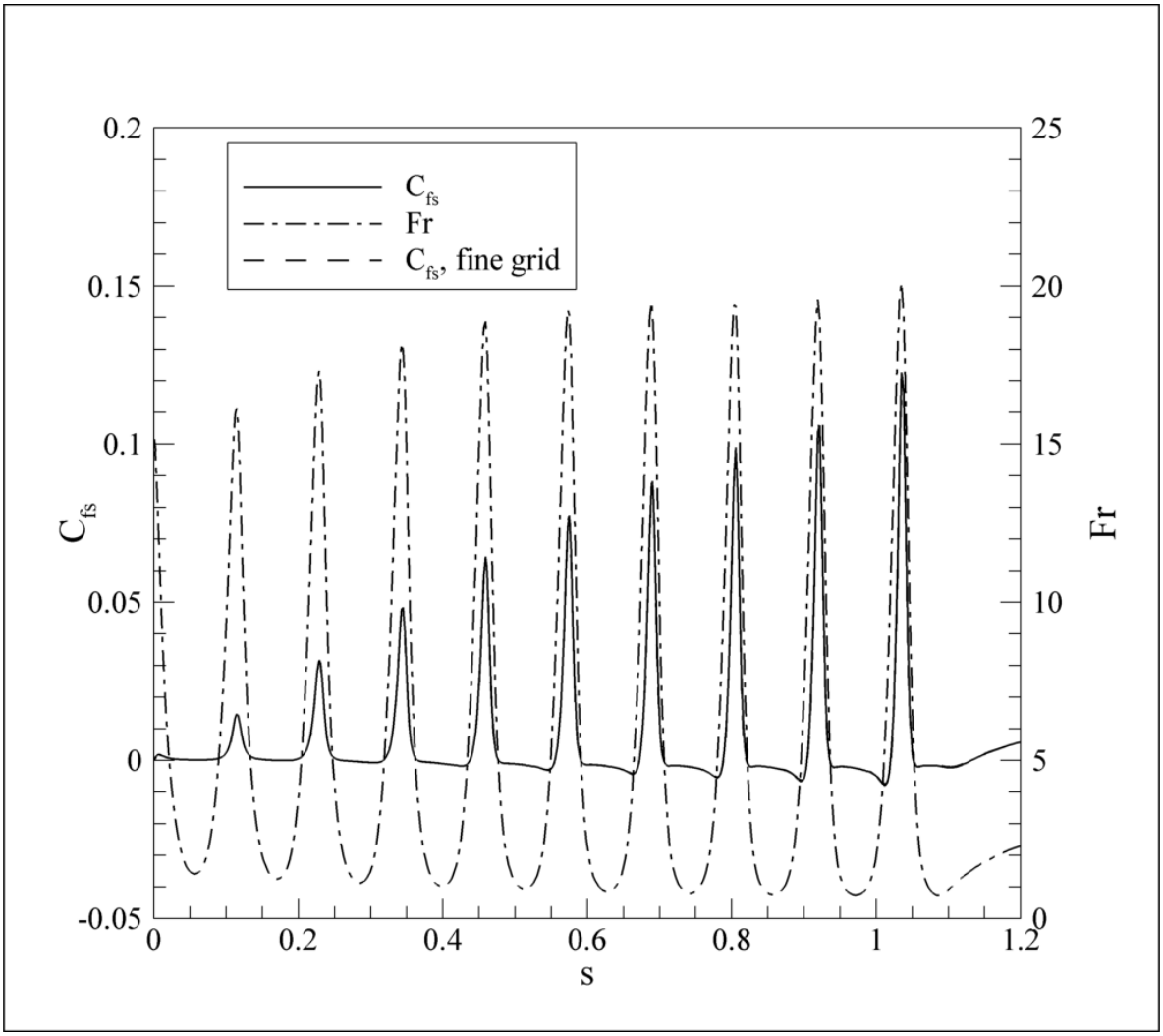

Figure 45: Streamwise skin-friction and convective heat transfer for flow over distributed roughness, Re=5000. The fine grid solution is also shown for the streamwise skin-friction.

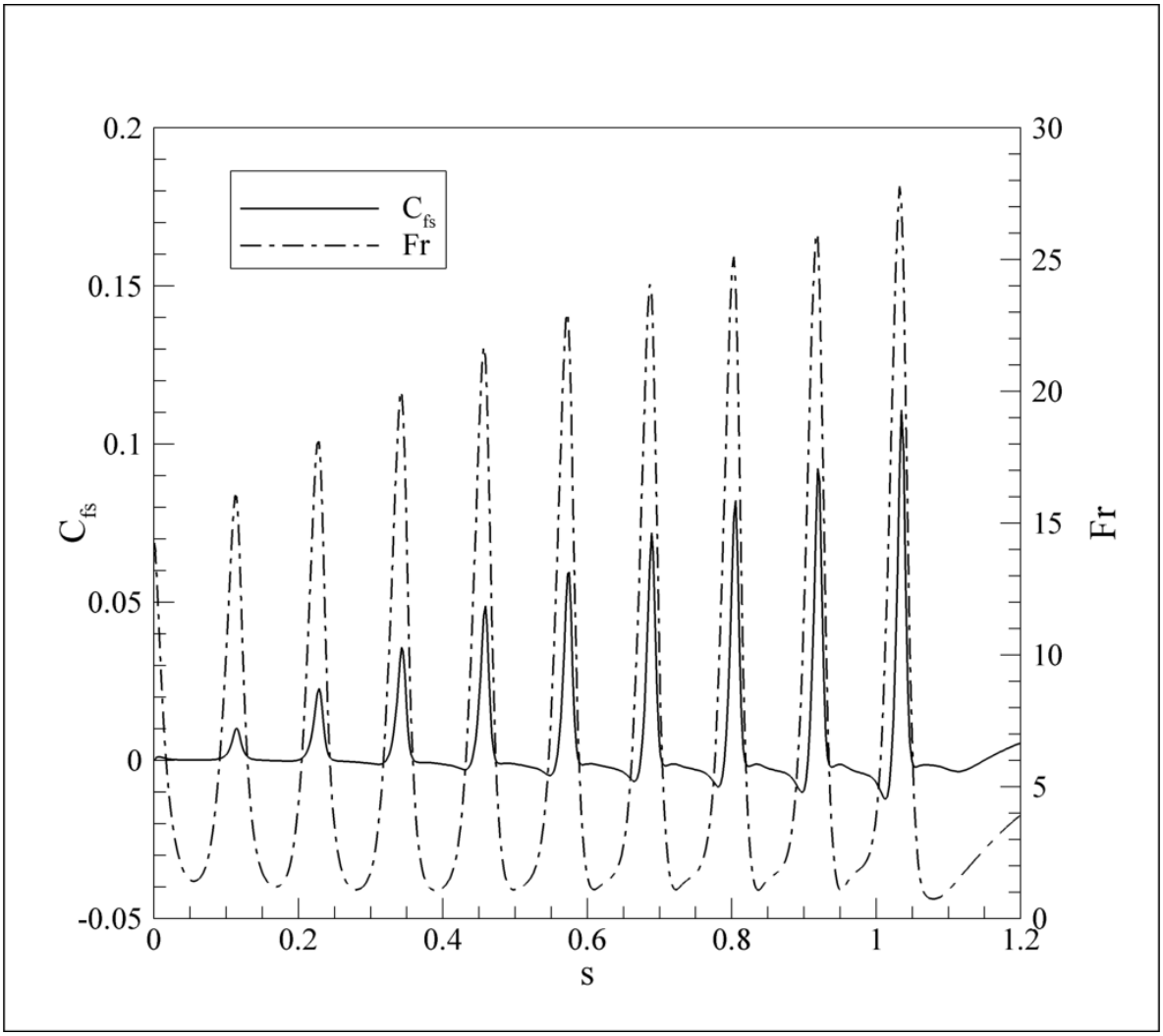

Figure 46: Streamwise skin-friction and convective heat transfer for flow over distributed roughness, Re=10,000.

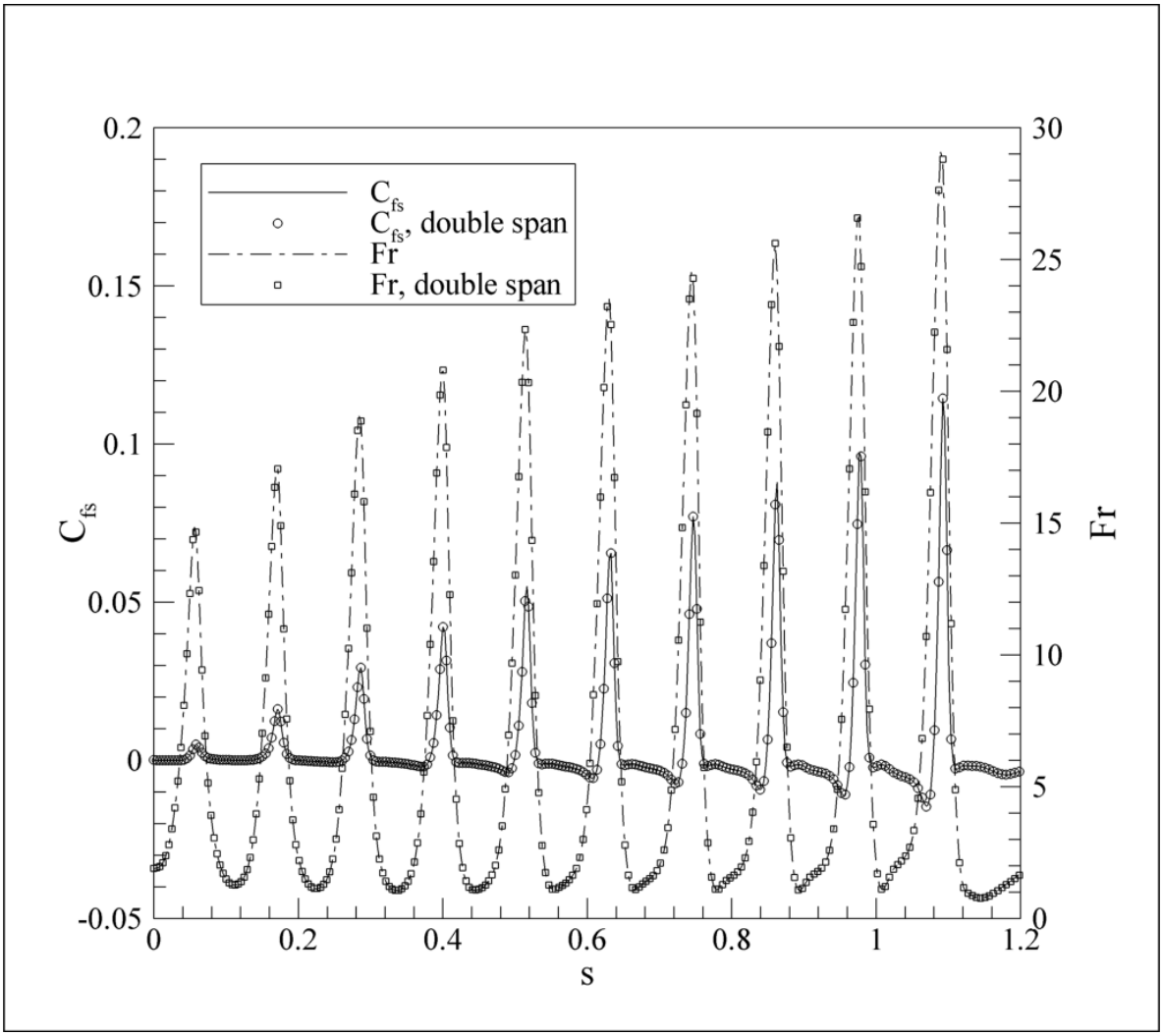

Figure 47: Effect of doubling the computational spanwise domain on the streamwise skin-friction and convective heat transfer at the right symmetry plane (Re=10,000).

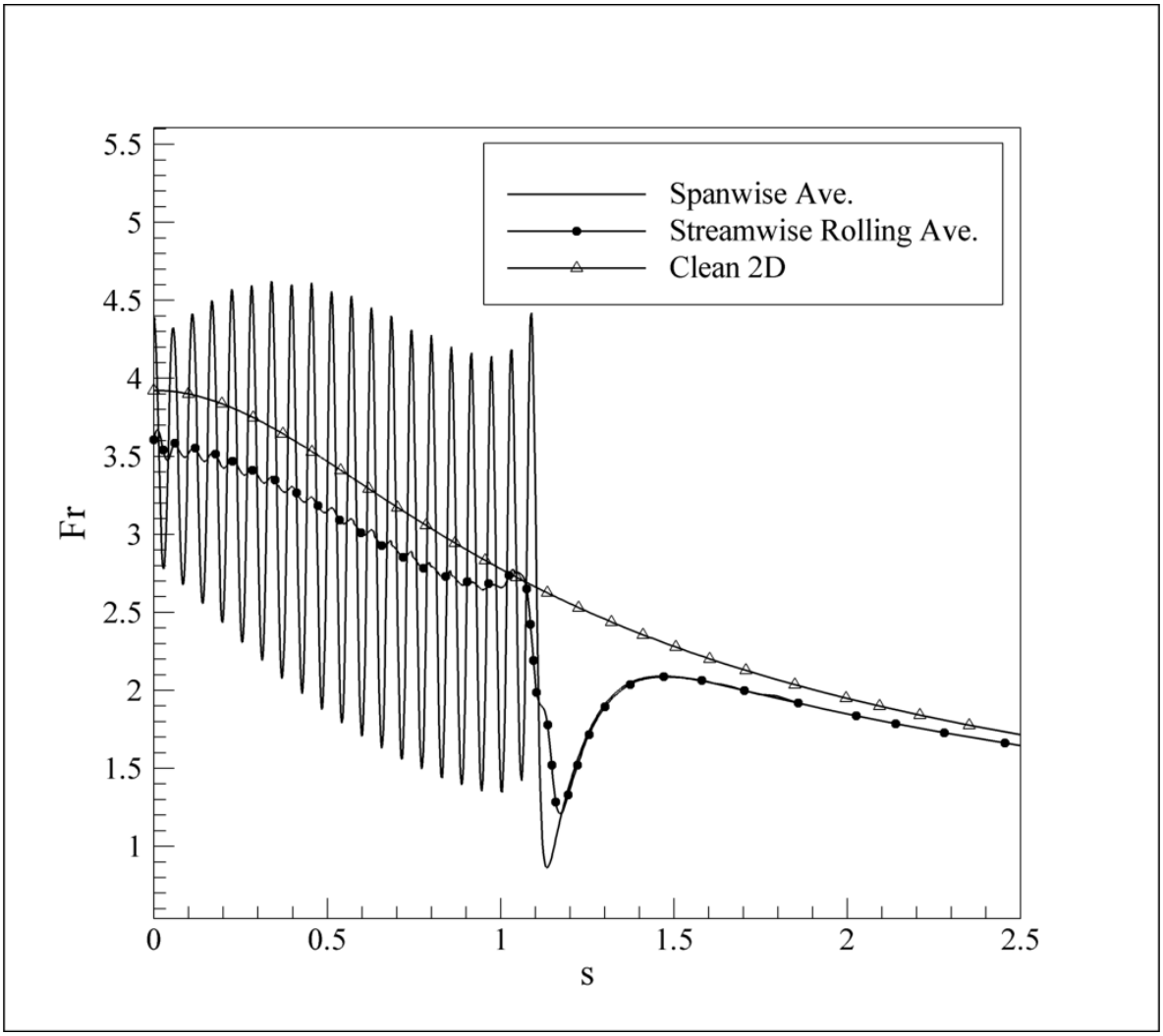

Figure 48: Comparison of various methods for evaluating the convective heat transfer. Re=5000. The width of the window for the rolling average is approximately equal to the roughness spacing.

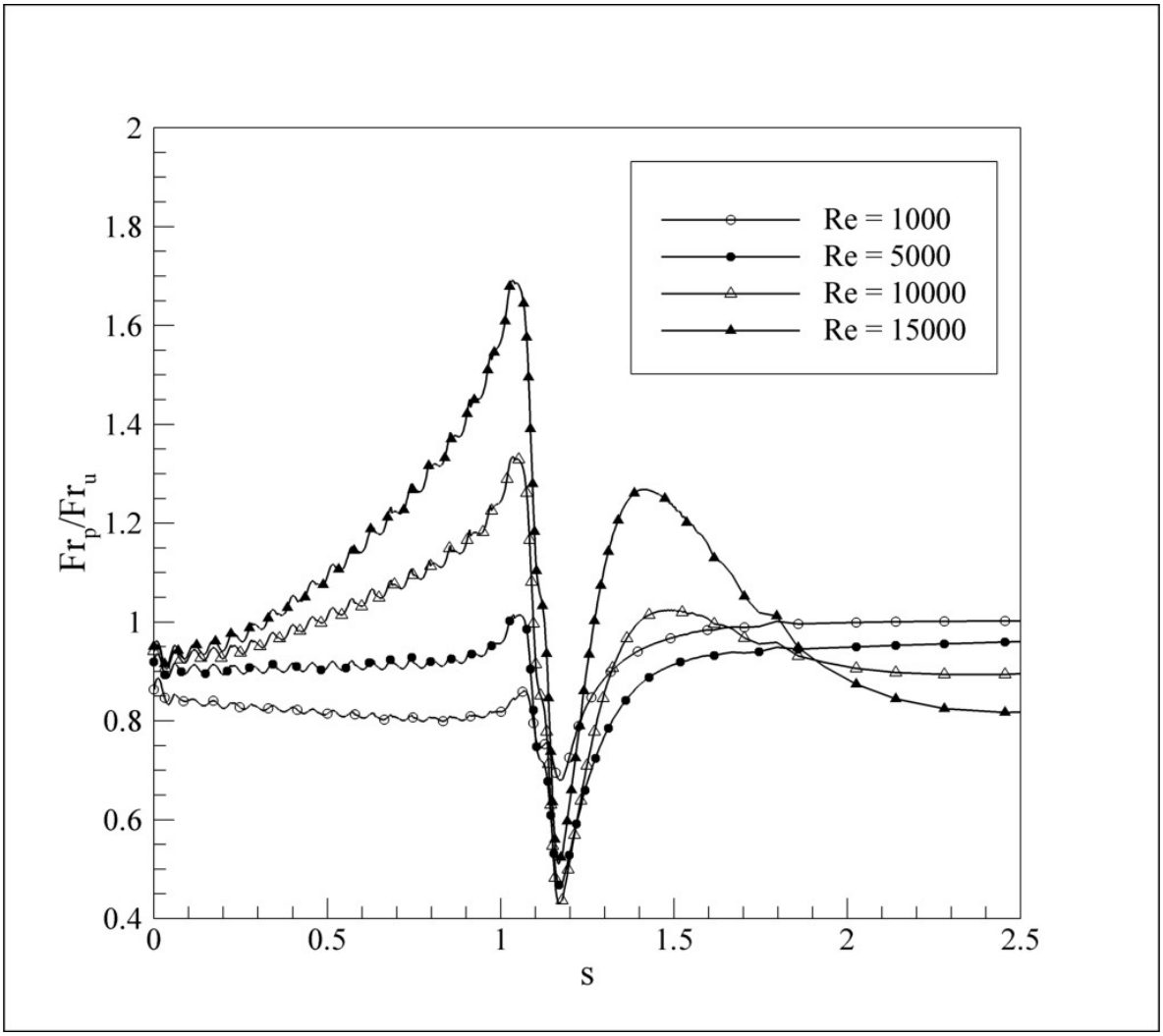

Figure 49: Relative increase in convective heat transfer due to leading edge roughness as a function of the Reynolds number.

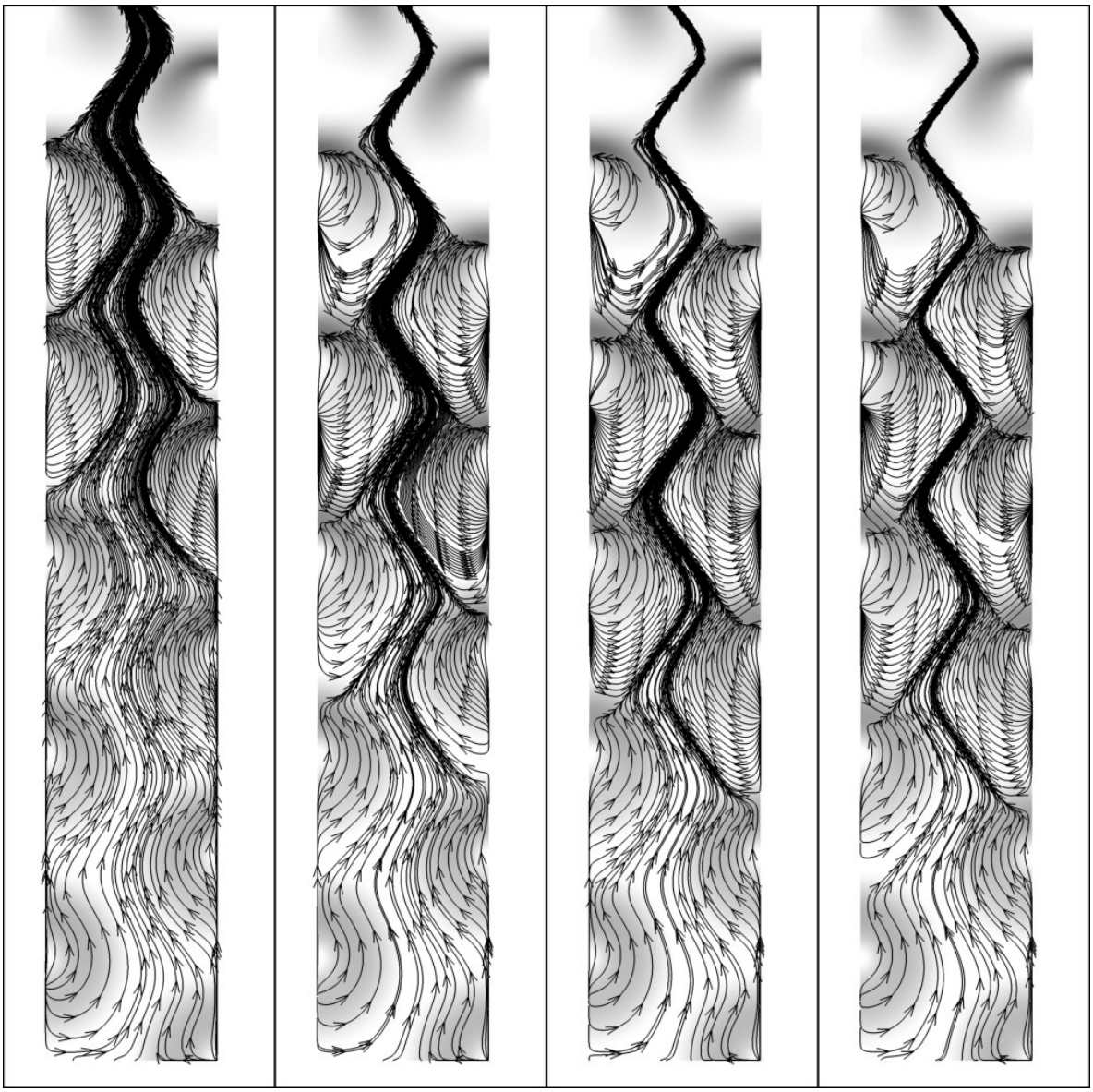

Figure 50: Variation of the surface streamline pattern as a function of the Reynolds number. Plots are, from left to right, Re = 1000, 5000, 10000, 15000.

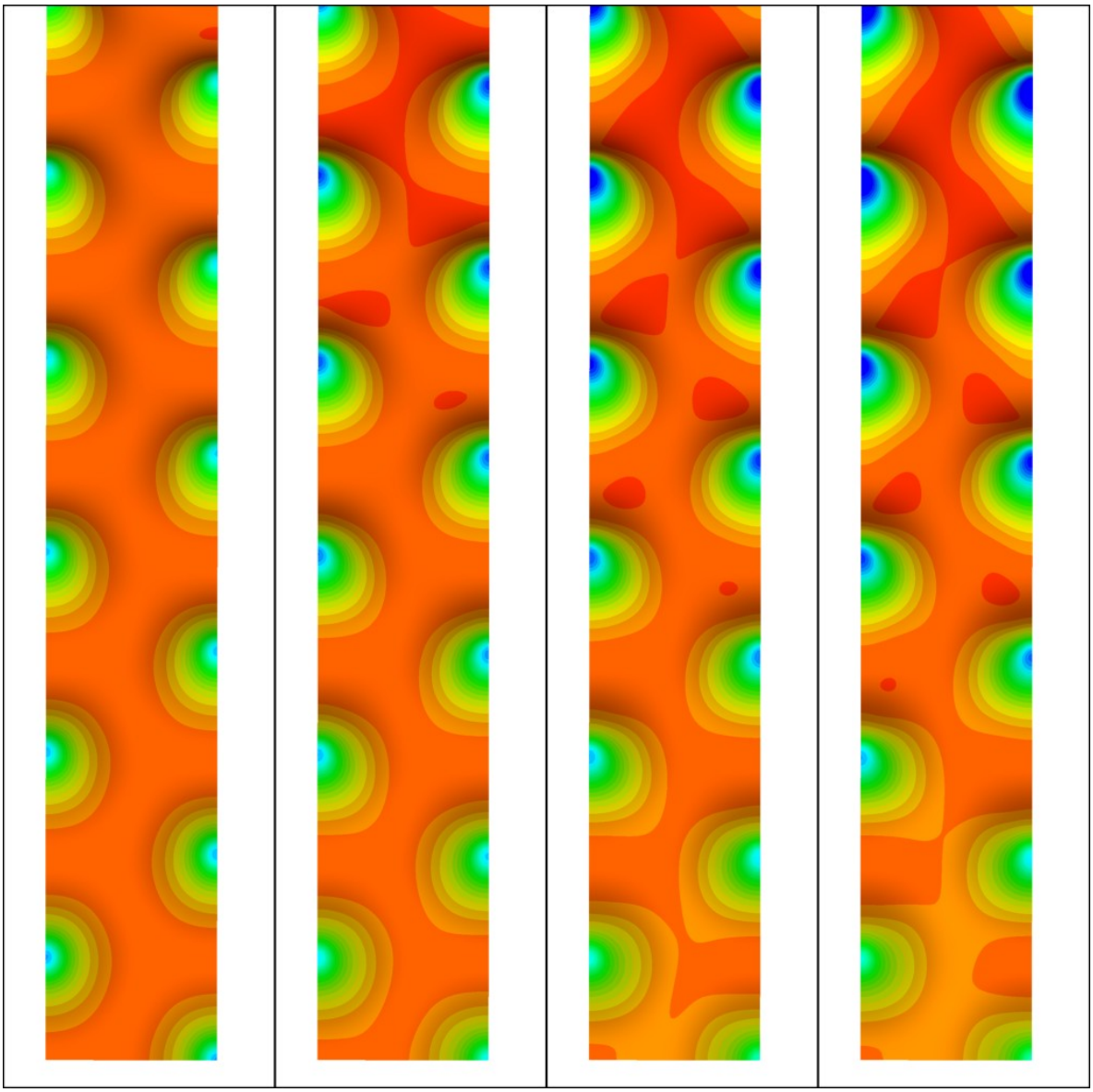

Figure 51: Variation of the surface heat transfer as a function of the Reynolds number. Blue regions are increased cooling, red regions are reduced cooling. Plots are, from left to right, Re = 1000, 5000, 10000, 15000.

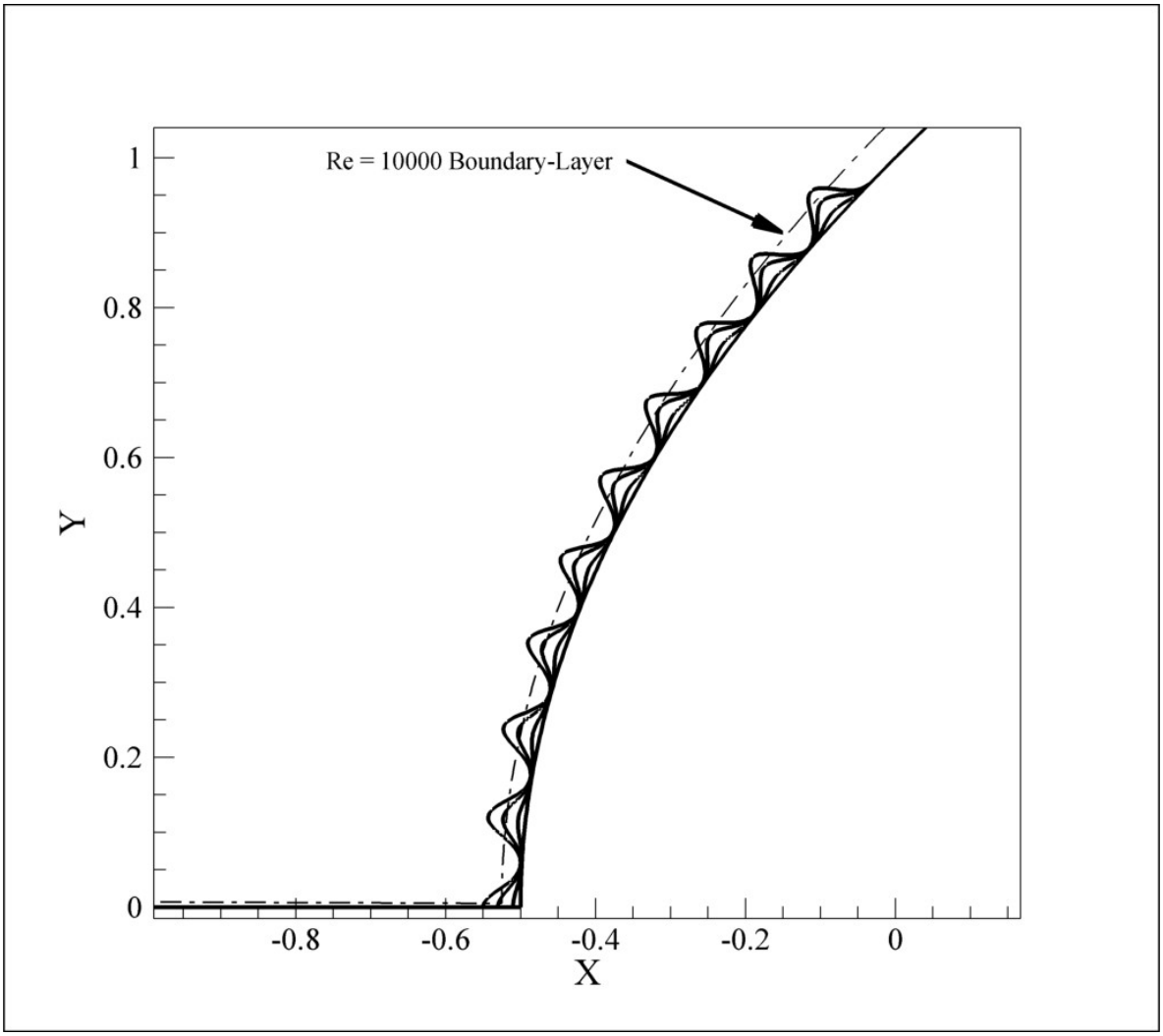

Figure 52: Comparison of the various roughness heights with the two-dimensional laminar boundary-layer thickness at Re = 10000. k = 0.01, 0.03 and 0.05.

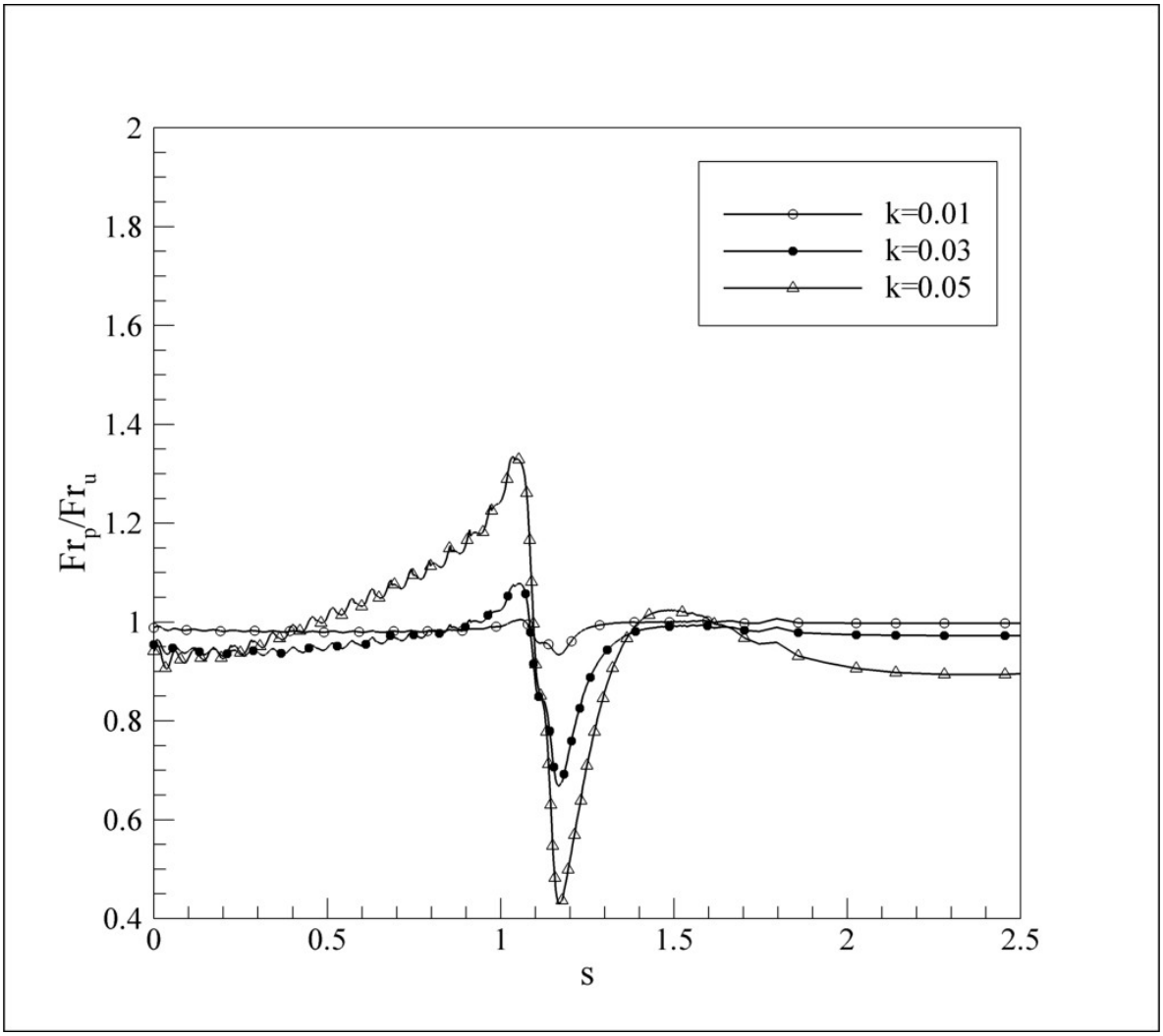

Figure 53: Relative increase in convective heat transfer due to leading edge roughness as a function of the roughness height, k.

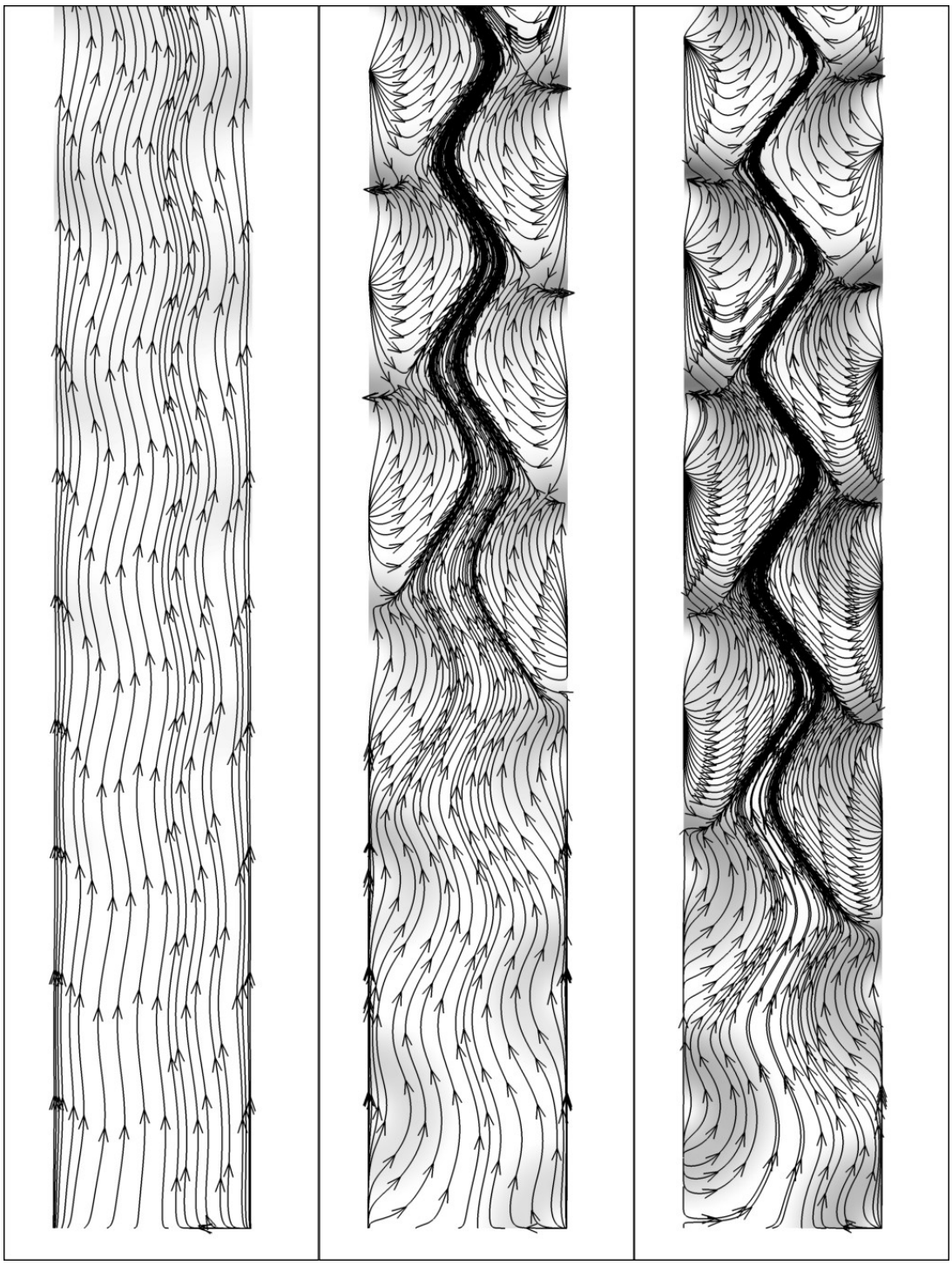

Figure 54: Variation of the surface streamline pattern as a function of the roughness height. Plots are, from left to right, k=0.01, 0.03, 0.05.

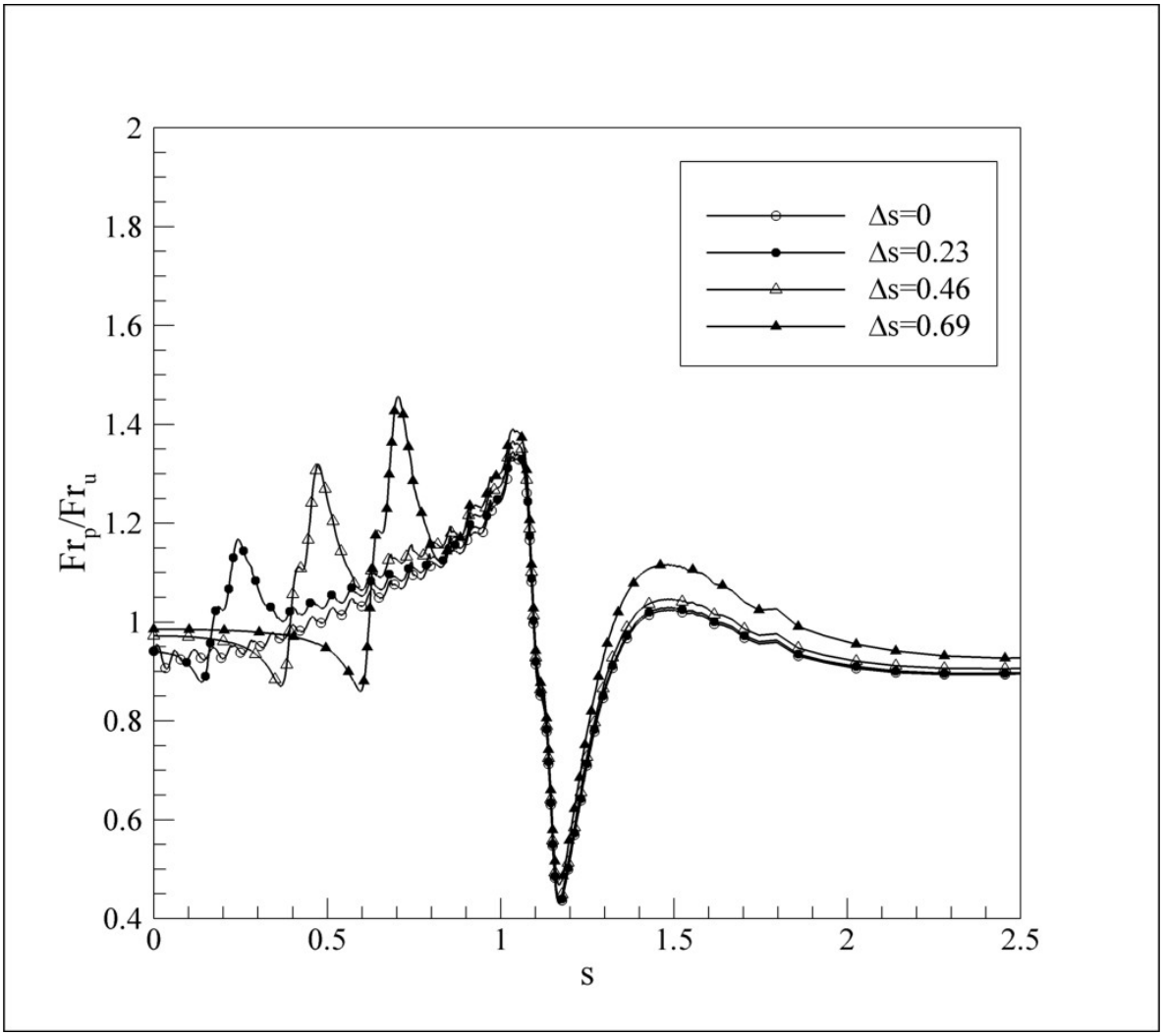

Figure 55: Relative increase in convective heat transfer due to variation in the starting point of the roughness field, i.e. the smooth region length Δs.

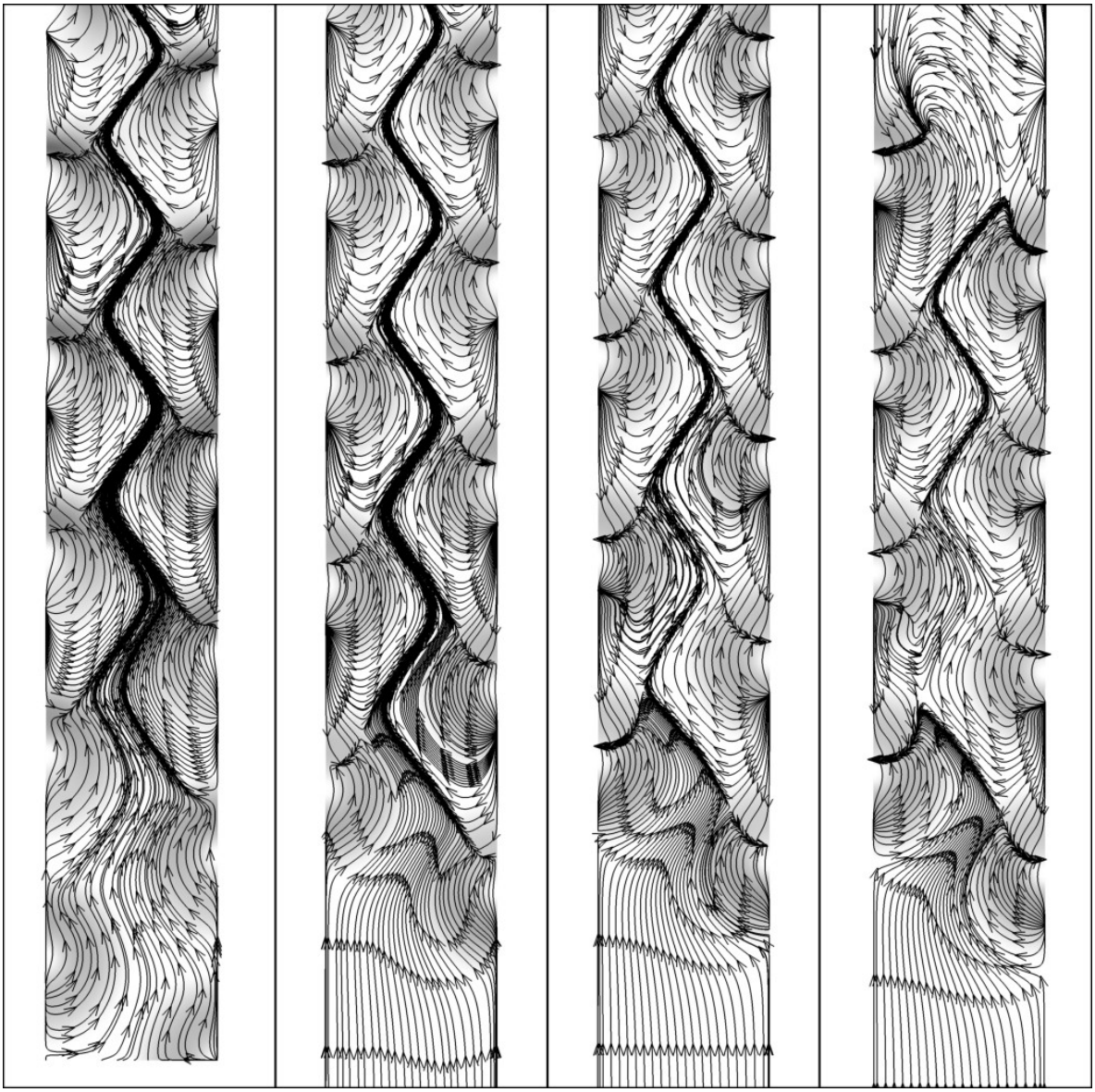

Figure 56: Variation of the surface streamline pattern as a function of the roughness field starting point, i.e. smooth region effect. Length of smooth region is, from left to right, $\Delta s = 0$ (at stagnation line), 0.23, 0.46 and 0.69.

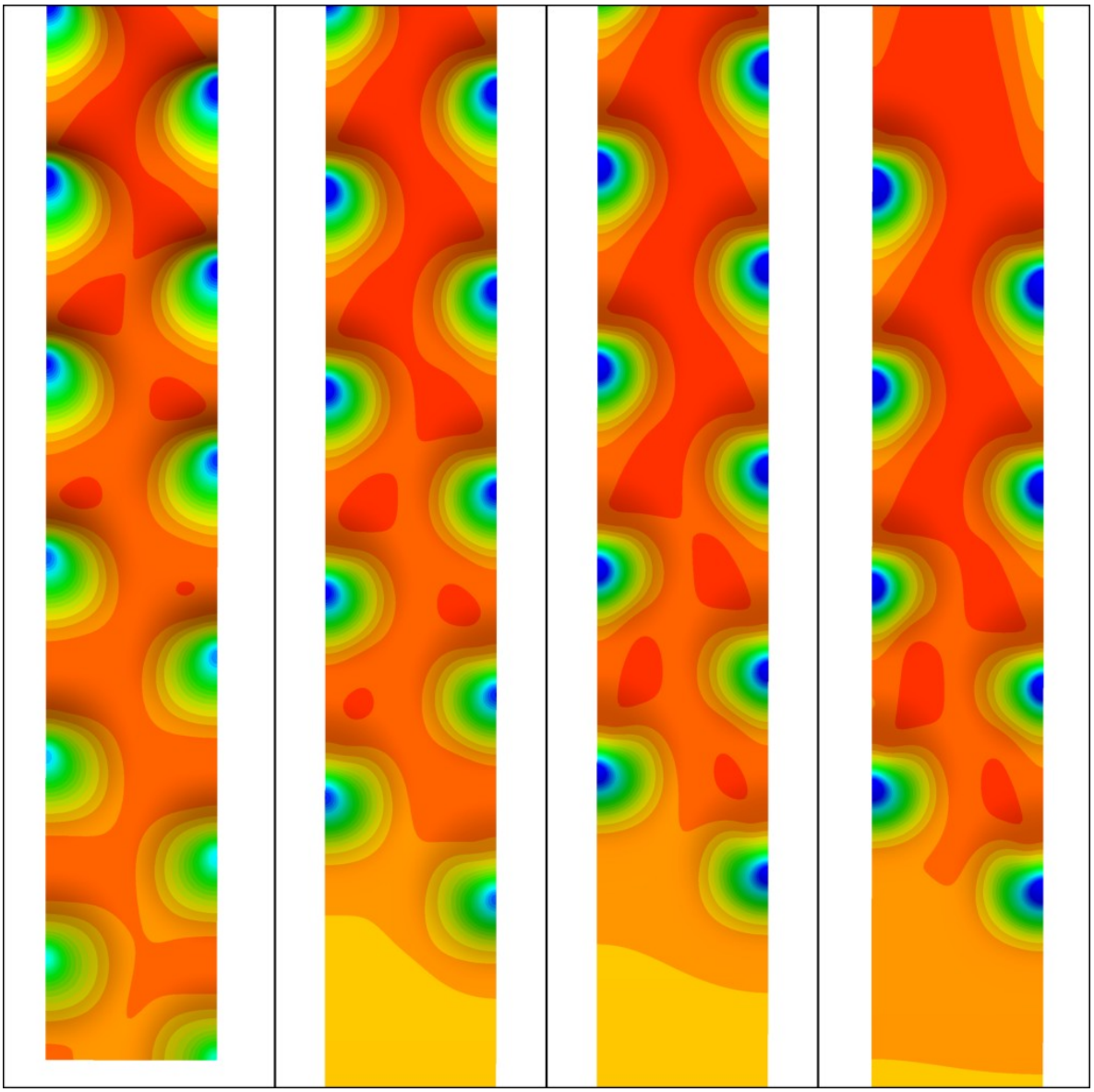

Figure 57: Variation of the convective heat transfer as a function of the roughness field starting point, i.e. smooth region effect. Length of smooth region is, from left to right, $\Delta s = 0$, 0.23, 0.46 and 0.69. Blue regions are increased cooling, red regions are reduced cooling.

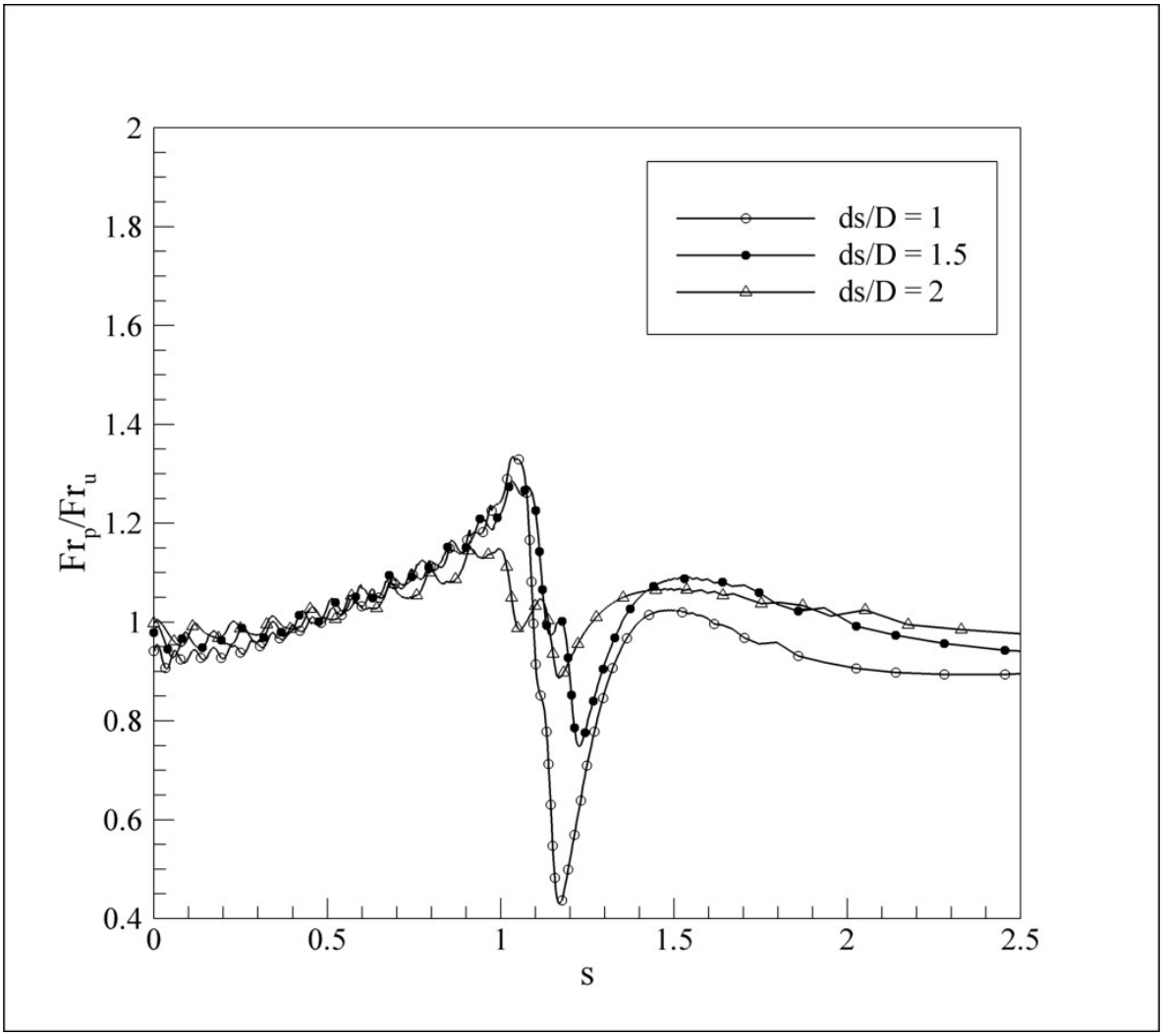

Figure 58: Relative increase in convective heat transfer due to variation in the roughness spacing, ds/D.

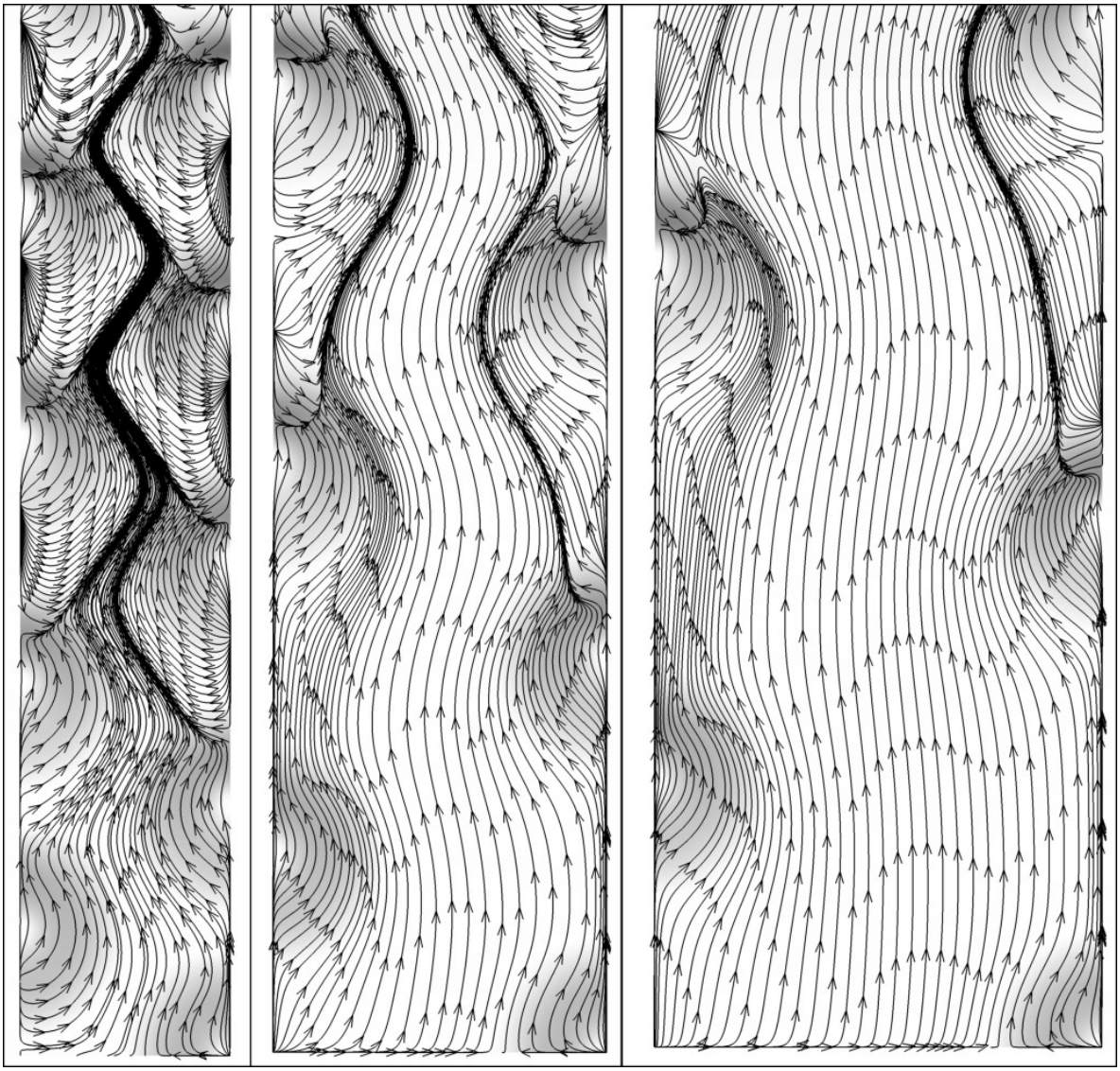

Figure 59: Variation of the surface streamline pattern as a function of the roughness spacing. Roughness spacing is, from left to right, ds/D = 1, 1.5 and 2.

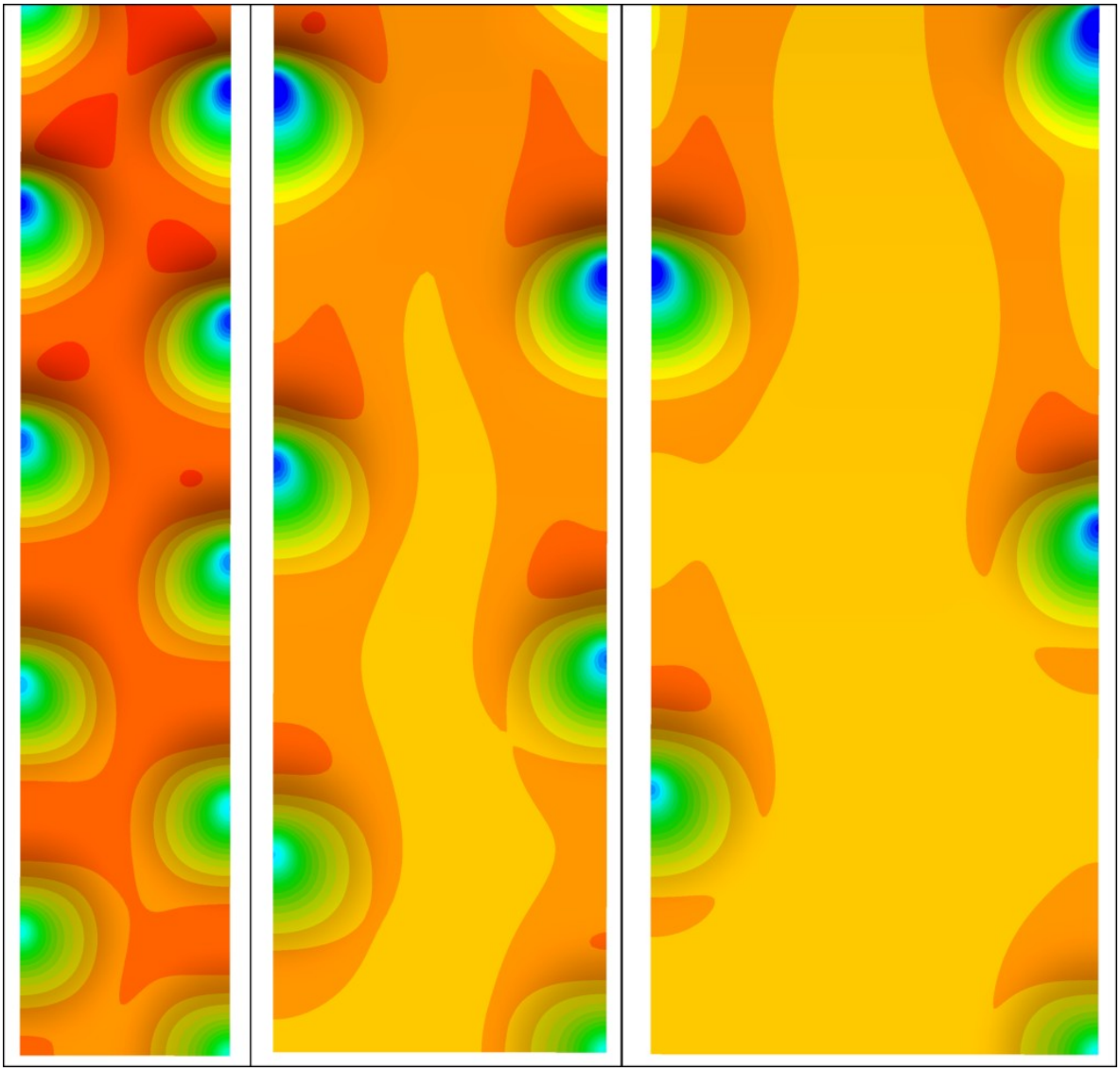

Figure 60: Variation of the convective heat transfer as a function of the roughness spacing. Roughness spacing is, from left to right, ds/D = 1, 1.5 and 2. Blue regions are increased cooling, red regions are reduced cooling.

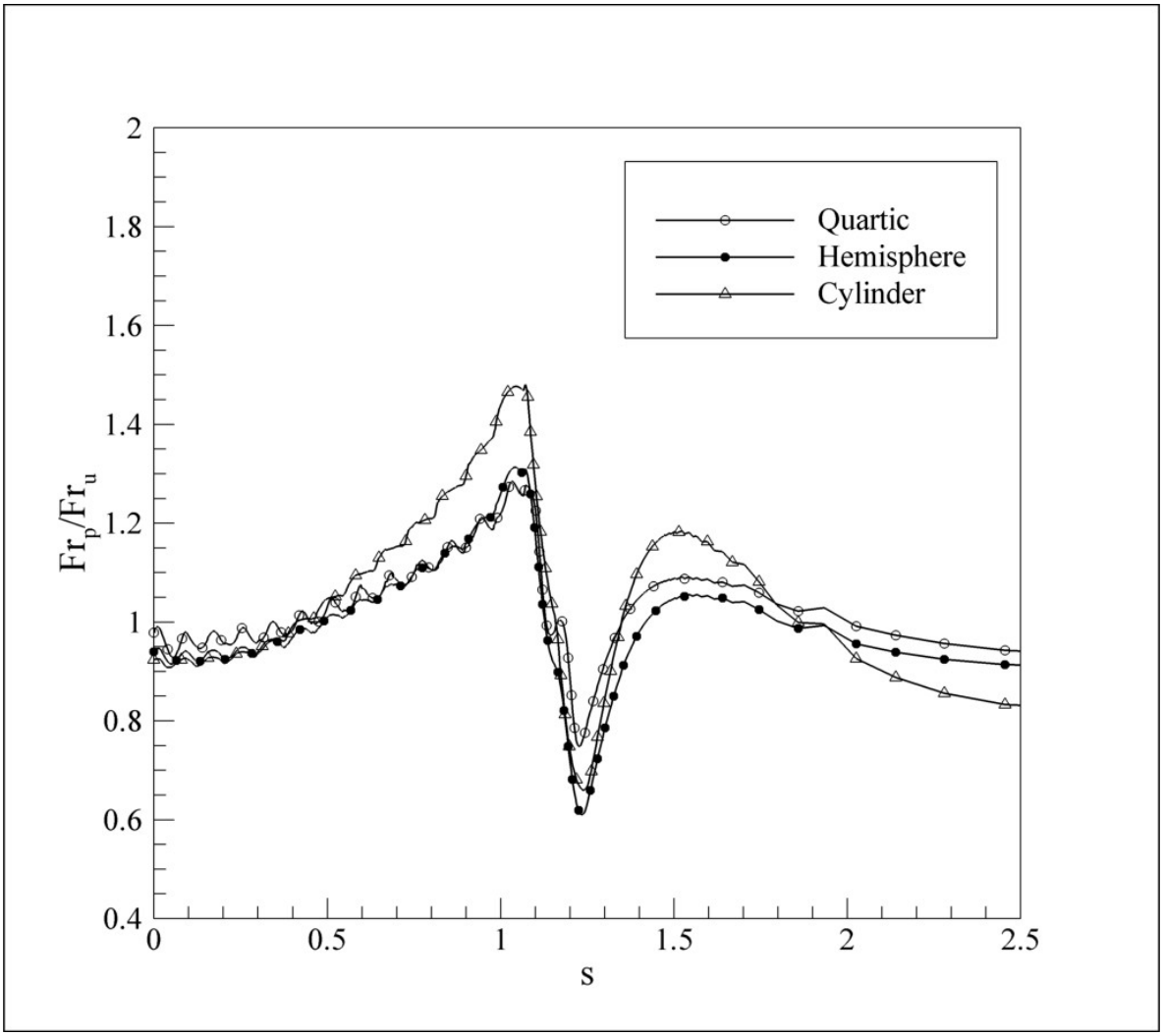

Figure 61: Relative increase in convective heat transfer due to variation in the roughness shape (see Figure 13).

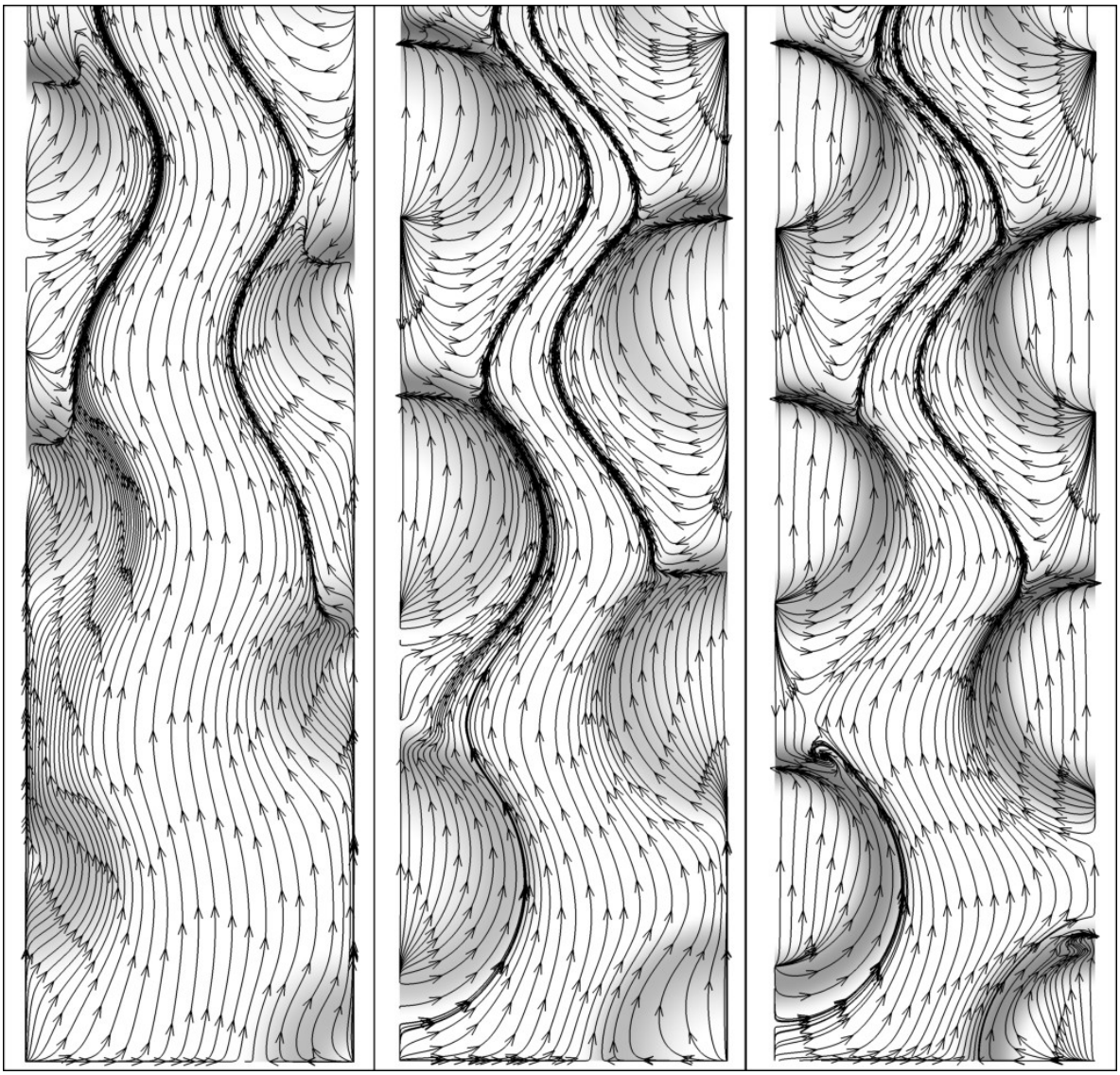

Figure 62: Variation of the surface streamline pattern as a function of the roughness shape. Roughness shapes are, from left to right, quartic, hemisphere and cylinder.

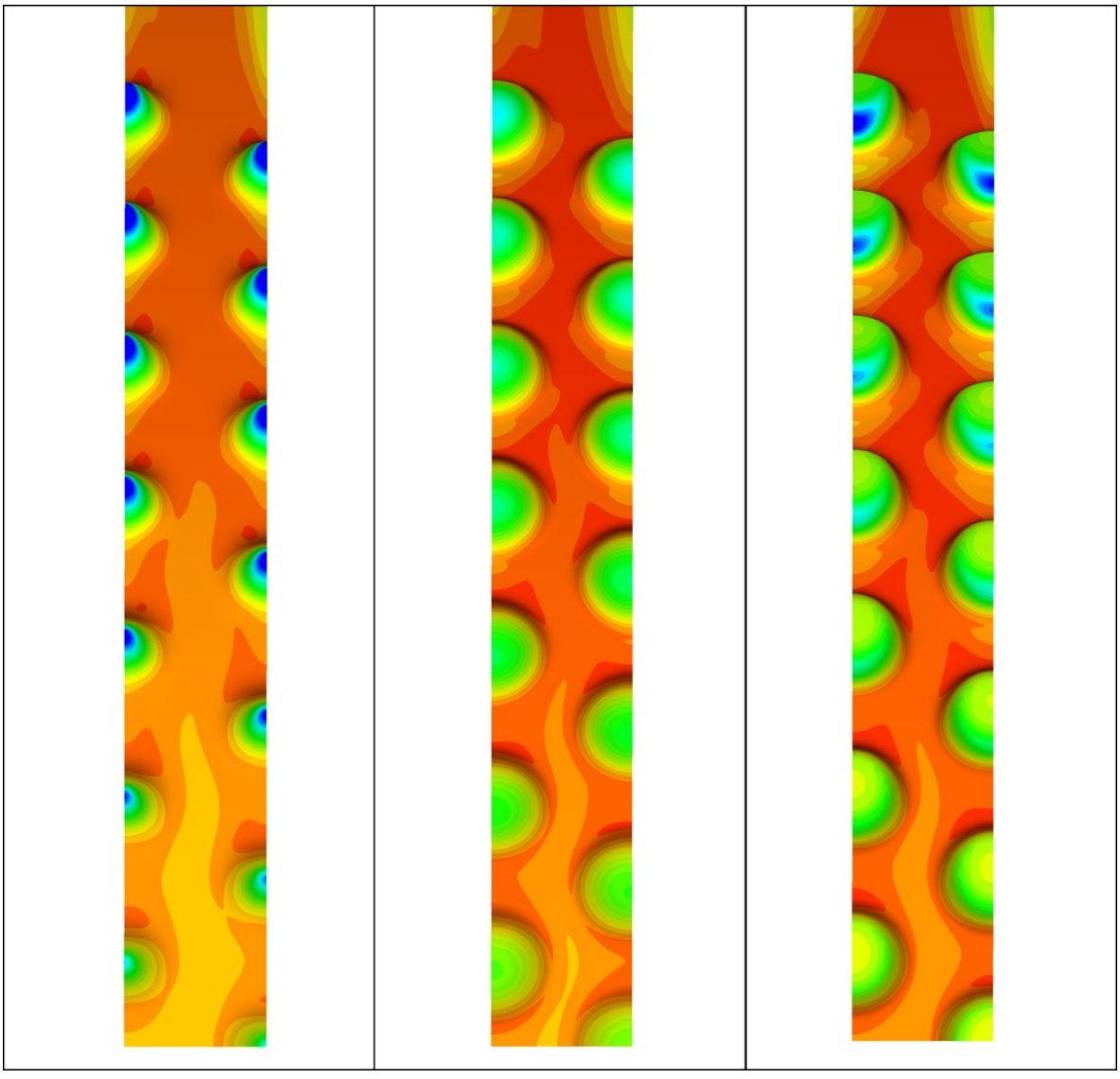

Figure 63: Comparison of convective heat transfer for various roughness shapes. Roughness shapes are, from left to right, quartic, hemisphere and cylinder. Blue regions are increased cooling, red regions are reduced cooling.

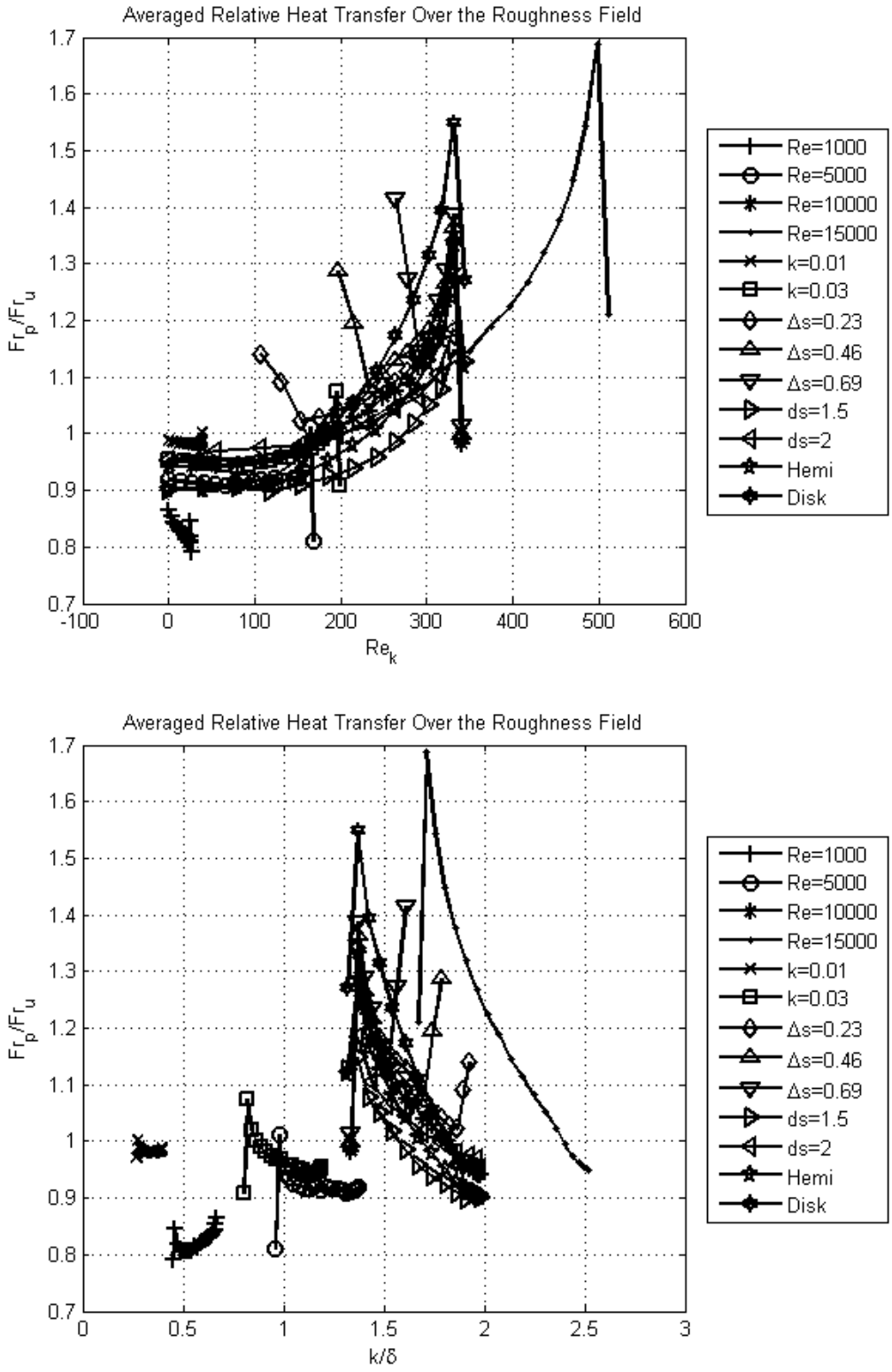

Figure 64: Average relative heat transfer as a function of Re_k and k/δ.

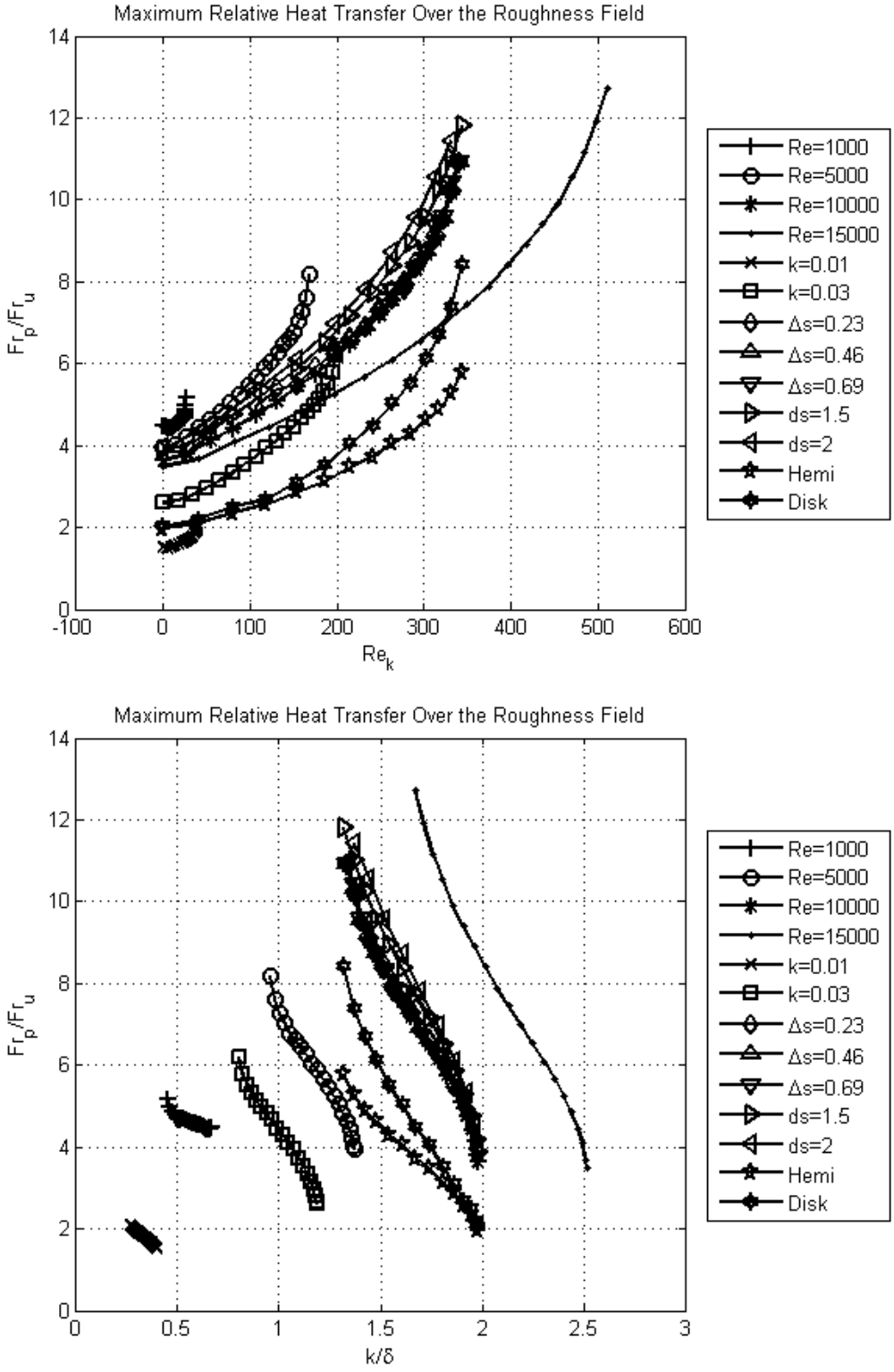

Figure 65: Maximum relative heat transfer as a function of Re_k and k/δ.

APPENDIX: DETAILS OF THE NUMERICAL EQUATIONS

This appendix gives a summary of the equations being solved for the multi-phase condensed-layer study and a detailed derivation of the incompressible Navier-Stokes equations used for the three-dimensional distributed roughness study.

Summary of the Condensed-Layer Equations

Streamfunction equation:

$$\Omega = \eta_Y^2 \Psi_{\eta\eta} + \eta_{YY} \Psi_\eta \quad . \tag{A.1}$$

Vorticity-transport equation:

$$\eta_Y \Psi_\eta \Omega_X - \eta_Y \Psi_X \Omega_\eta = \eta_Y^2 \Omega_{\eta\eta} + \eta_{YY} \Omega_\eta \quad . \tag{A.2}$$

Wall-normal momentum equation (in terms of the air pressure gradient):

$$\beta_\eta = 0 \quad . \tag{A.3}$$

Transmission of film thickness to the outer flow:

$$F_\eta = 0 \quad . \tag{A.4}$$

No slip condition at the wall:

$$\Psi = \Psi_\eta = 0 \quad . \tag{A.5}$$

Equation for the film thickness:

$$\frac{\partial F}{\partial T} + \frac{\partial}{\partial X}\left[\Omega(X,0)\frac{F^2}{2} - \beta\frac{F^3}{3} + \Sigma\frac{F^3}{3}\left(\frac{\partial^3 F}{\partial X^3} + \frac{\partial^3 F_{ice}}{\partial X^3}\right)\right] = 0 \quad , \tag{A.6}$$

where

$$F = F_{water} - F_{ice} \quad . \tag{A.7}$$

Approach to Prandtl shear at the far-field:

$$\eta_Y \Psi_\eta = Y + F_{water} - 1 \quad , \tag{A.8}$$

where

$$\Sigma = \frac{\mu_{air}^2}{R_B^3 \lambda^4 h^7} \quad . \tag{A.9}$$

Derivation of the Incompressible Navier-Stokes Equations

The Navier-Stokes equations in vector notation are given by the vorticity transport equation,

$$\vec{V} \cdot \nabla \vec{\omega} = \vec{\omega} \cdot \nabla \vec{V} + Re^{-1} \nabla^2 \vec{\omega} \quad , \tag{A.10}$$

and the equation for the velocity potential,

$$\vec{\omega} = \nabla \times \vec{V} = \nabla \times \nabla \times \vec{A} \quad . \tag{A.11}$$

Transformation to Contravariant Coordinates

(A.10) and (A.11) are transformed using

$$(\xi', \eta') = C(x, y) \quad \text{and} \quad \zeta' = z \quad , \tag{A.12}$$

where C is a Conformal coordinate transformation. In this case

$$h_1 = h_2 = h \quad \text{And} \quad h_3 = 1 \quad . \tag{A.13}$$

In this scenario the general vector transformations are given by

$$\nabla \phi = \frac{1}{h} \frac{\partial \phi}{\partial x_1} \hat{e}_1 + \frac{1}{h} \frac{\partial \phi}{\partial x_2} \hat{e}_2 + \frac{\partial \phi}{\partial x_3} \hat{e}_3 \quad , \tag{A.14}$$

$$\nabla \cdot \vec{\Phi} = \frac{1}{h^2} \left\{ \frac{\partial}{\partial x_1} (\Phi_1 h) + \frac{\partial}{\partial x_2} (\Phi_2 h) + \frac{\partial}{\partial x_3} (\Phi_3 h^2) \right\} \quad , \tag{A.15}$$

$$\nabla^2 \phi = \frac{1}{h^2} \left\{ \frac{\partial}{\partial x_1} \left(\frac{\partial \phi}{\partial x_1} \right) + \frac{\partial}{\partial x_2} \left(\frac{\partial \phi}{\partial x_2} \right) + \frac{\partial}{\partial x_3} \left(h^2 \frac{\partial \phi}{\partial x_3} \right) \right\} \quad , \tag{A.16}$$

$$\begin{aligned}\nabla\times\vec{\Phi}=&\frac{1}{h}\left[\frac{\partial}{\partial x_2}(\Phi_3)-\frac{\partial}{\partial x_3}(h\Phi_2)\right]\hat{e}_1\\&+\frac{1}{h}\left[\frac{\partial}{\partial x_3}(h\Phi_1)-\frac{\partial}{\partial x_1}(\Phi_3)\right]\hat{e}_2\\&+\frac{1}{h^2}\left[\frac{\partial}{\partial x_1}(h\Phi_2)-\frac{\partial}{\partial x_2}(h\Phi_1)\right]\hat{e}_3\quad,\end{aligned}\tag{A.17}$$

and

$$\begin{aligned}&\nabla\times\nabla\times\vec{\Phi}=\\&\frac{1}{h}\left[\frac{\partial}{\partial x_2}\left\{\frac{1}{h^2}\left[\frac{\partial}{\partial x_1}(h\Phi_2)-\frac{\partial}{\partial x_2}(h\Phi_1)\right]\right\}-\frac{\partial}{\partial x_3}\left\{\left[\frac{\partial}{\partial x_3}(h\Phi_1)-\frac{\partial}{\partial x_1}(\Phi_3)\right]\right\}\right]\hat{e}_1\\&+\frac{1}{h}\left[\frac{\partial}{\partial x_3}\left\{\left[\frac{\partial}{\partial x_2}(\Phi_3)-\frac{\partial}{\partial x_3}(h\Phi_2)\right]\right\}-\frac{\partial}{\partial x_1}\left\{\frac{1}{h^2}\left[\frac{\partial}{\partial x_1}(h\Phi_2)-\frac{\partial}{\partial x_2}(h\Phi_1)\right]\right\}\right]\hat{e}_2\\&+\frac{1}{h^2}\left[\frac{\partial}{\partial x_1}\left\{\left[\frac{\partial}{\partial x_3}(h\Phi_1)-\frac{\partial}{\partial x_1}(\Phi_3)\right]\right\}-\frac{\partial}{\partial x_2}\left\{\left[\frac{\partial}{\partial x_2}(\Phi_3)-\frac{\partial}{\partial x_3}(h\Phi_2)\right]\right\}\right]\hat{e}_3\quad.\end{aligned}\tag{A.18}$$

Applying these transformations to (A.10) gives

$$\begin{aligned}&\frac{\partial(h\omega_1)}{\partial t}+\frac{\partial}{\partial\eta'}(V_2\omega_1-V_1\omega_2)+\frac{\partial}{\partial\zeta'}\{h(V_3\omega_1-V_1\omega_3)\}\\&=Re^{-1}\frac{\partial}{\partial\eta'}\left\{\frac{1}{h^2}\left[\frac{\partial}{\partial\eta'}(h\omega_1)-\frac{\partial}{\partial\xi'}(h\omega_2)\right]\right\}+\frac{\partial}{\partial\zeta'}\left\{\left[\frac{\partial}{\partial\zeta'}(h\omega_1)-\frac{\partial}{\partial\xi'}(\omega_3)\right]\right\}\end{aligned}\tag{A.19}$$

for ω_1 and

$$\begin{aligned}&h^2\frac{\partial\omega_3}{\partial t}+\frac{\partial}{\partial\xi'}\{h(V_1\omega_3-V_3\omega_1)\}+\frac{\partial}{\partial\eta'}\{h(V_2\omega_3-V_3\omega_2)\}\\&=Re^{-1}\frac{\partial}{\partial\xi'}\left\{\left[\frac{\partial}{\partial\xi'}(\omega_3)-\frac{\partial}{\partial\zeta'}(h\omega_1)\right]\right\}+\frac{\partial}{\partial\eta'}\left\{\left[\frac{\partial}{\partial\eta'}(\omega_3)-\frac{\partial}{\partial\zeta'}(h\omega_2)\right]\right\}\quad.\end{aligned}\tag{A.20}$$

for ω_3. Applying the transformations to (A.11) gives

$$\omega_1 = \frac{1}{h}\left[\frac{\partial}{\partial \eta'}\left\{\frac{1}{h^2}\frac{\partial(h\theta)}{\partial \eta'}\right\} + \frac{\partial^2(h\theta)}{\partial \zeta'^2} + \frac{\partial^2 \psi}{\partial \xi' \partial \zeta'}\right] ,$$

$$\omega_2 = \frac{1}{h}\left[\frac{\partial^2 \psi}{\partial \eta' \partial \zeta'} - \frac{\partial}{\partial \xi'}\left\{\frac{1}{h^2}\frac{\partial(h\theta)}{\partial \eta'}\right\}\right] \qquad \text{(A.21)}$$

$$\text{and} \quad \omega_3 = \frac{1}{h^2}\left[-\frac{\partial^2(h\theta)}{\partial \xi' \partial \zeta'} - \frac{\partial^2 \psi}{\partial \xi'^2} - \frac{\partial^2 \psi}{\partial \eta'^2}\right] .$$

The relationship between the velocity vector and the stream-like functions to be used in (A.19) and (A.20) is,

$$\vec{V} = \frac{1}{h}\frac{\partial \psi}{\partial \eta'}\hat{e}_1 + \frac{1}{h}\left[-\frac{\partial(h\theta)}{\partial \zeta'} - \frac{\partial \psi}{\partial \xi'}\right]\hat{e}_2 + \frac{1}{h^2}\frac{\partial(h\theta)}{\partial \eta'}\hat{e}_3 \quad . \qquad \text{(A.22)}$$

Transformation for Potential Flow and Computational Parameters

The vector components in the preceding section are transformed to remove the potential flow solution and remove some of the conformal coordinate scale factors,

$$\begin{Bmatrix} \psi \\ h\theta \\ h\omega_1 \\ h\omega_2 \\ \omega_3 \end{Bmatrix} = \begin{Bmatrix} \Psi + \bar{\psi} \\ \Theta \\ \Omega_1 \\ \Omega_2 \\ \Omega_3 \end{Bmatrix} , \qquad \text{(A.23)}$$

where $\bar{\psi}$ is the two-dimensional streamfunction given by the potential flow solution past the clean parabola. With this transformation the vorticity transport equations become

$$\begin{aligned} &\frac{\partial \Omega_1}{\partial t} - \frac{1}{h^2}V_2\Omega_1\frac{\partial h}{\partial \eta'} + \frac{1}{h}V_2\frac{\partial \Omega_1}{\partial \eta'} + \frac{1}{h}\Omega_1\frac{\partial V_2}{\partial \eta'} + \frac{1}{h^2}V_1\Omega_2\frac{\partial h}{\partial \eta'} \\ &+ V_3\frac{\partial \Omega_1}{\partial \zeta'} + \Omega_1\frac{\partial V_3}{\partial \zeta'} - hV_1\frac{\partial \Omega_3}{\partial \zeta'} - h\Omega_3\frac{\partial V_1}{\partial \zeta'} = Re^{-1}\left(-\frac{2}{h^3}\frac{\partial \Omega_1}{\partial \eta'}\frac{\partial h}{\partial \eta'}\right. \\ &\left. + \frac{1}{h^2}\frac{\partial^2 \Omega_1}{\partial \eta'^2} + \frac{2}{h^3}\frac{\partial \Omega_2}{\partial \xi'}\frac{\partial h}{\partial \eta'} - \frac{1}{h^2}\frac{\partial^2 \Omega_2}{\partial \xi' \partial \eta'} + \frac{\partial^2 \Omega_1}{\partial \zeta'^2} - \frac{\partial^2 \Omega_3}{\partial \xi' \partial \zeta'}\right) , \end{aligned} \qquad \text{(A.24)}$$

for Ω_1 and

$$h^2\frac{\partial \Omega_3}{\partial t}+V_1\Omega_3\frac{\partial h}{\partial \xi'}+h\Omega_3\frac{\partial V_1}{\partial \xi'}+hV_1\frac{\partial \Omega_3}{\partial \xi'}-\Omega_1\frac{\partial V_3}{\partial \xi'}-V_3\frac{\partial \Omega_1}{\partial \xi'}$$
$$+V_2\Omega_3\frac{\partial h}{\partial \eta'}+h\Omega_3\frac{\partial V_2}{\partial \eta'}+hV_2\frac{\partial \Omega_3}{\partial \eta'}-\Omega_2\frac{\partial V_3}{\partial \eta'}-V_3\frac{\partial \Omega_2}{\partial \eta'} \qquad \text{(A.25)}$$
$$=Re^{-1}\left(\frac{\partial^2\Omega_3}{\partial \xi'^2}-\frac{\partial^2\Omega_1}{\partial \xi'\partial \zeta'}+\frac{\partial^2\Omega_3}{\partial \eta'^2}-\frac{\partial^2\Omega_2}{\partial \eta'\partial \zeta'}\right),$$

for Ω_3. Applying the transformation to (A.21) gives

$$\Omega_1=\frac{-2}{h^3}\frac{\partial \Theta}{\partial \eta'}\frac{\partial h}{\partial \eta'}+\frac{1}{h^2}\frac{\partial^2\Theta}{\partial \eta'^2}+\frac{\partial^2\Theta}{\partial \zeta'^2}+\frac{\partial^2\Psi}{\partial \xi'\partial \zeta'},$$

$$\Omega_2=\frac{\partial^2\Psi}{\partial \eta'\partial \zeta'}-\frac{1}{h^2}\frac{\partial^2\Theta}{\partial \xi'\partial \eta'}+\frac{2}{h^3}\frac{\partial \Theta}{\partial \eta'}\frac{\partial h}{\partial \xi'} \qquad \text{(A.26)}$$

$$\text{and}\quad -h^2\Omega_3=\frac{\partial^2\Theta}{\partial \xi'\partial \zeta'}+\frac{\partial^2\Psi}{\partial \xi'^2}+\frac{\partial^2\Psi}{\partial \eta'^2}.$$

The relationship between the velocity vector and the stream-like functions is

$$\vec{V}=\frac{1}{h}\left[\frac{\partial \Psi}{\partial \eta'}+\frac{\partial \bar{\psi}}{\partial \eta'}\right]\hat{e}_1+\frac{1}{h}\left[-\frac{\partial \Theta}{\partial \zeta'}-\frac{\partial \Psi}{\partial \xi'}-\frac{\partial \bar{\psi}}{\partial \xi'}\right]\hat{e}_2+\frac{1}{h^2}\frac{\partial \Theta}{\partial \eta'}\hat{e}_3 \quad . \qquad \text{(A.27)}$$

Elimination of terms using Continuity and Solenoidality

The solver being used in the current study is a block tri-diagonal solver which inverts the equations for the four unknowns Ψ, Θ, Ω_1 and Ω_3. Therefore Ω_2 is treated as a guessed value from the previous iteration. In addition, any terms involving the derivative of the second component of velocity introduce mixed derivatives into the vorticity transport equations. When using a second order central difference scheme for these terms they cannot be included directly in the inversion process. Therefore, this section details the method of using the continuity equation and solenoidality condition to eliminate as many terms

involving V_2 and Ω_2 as possible. The continuity equation in contravariant coordinates is given by

$$\nabla\cdot\vec{V}=\frac{1}{h^2}\left\{\frac{\partial}{\partial\xi'}\left(hV_1\right)+\frac{\partial}{\partial\eta'}\left(hV_2\right)+\frac{\partial}{\partial\zeta'}\left(h^2V_3\right)\right\}=0 \quad . \tag{A.28}$$

Expanding derivatives gives

$$h\frac{\partial V_1}{\partial\xi'}+V_1\frac{\partial h}{\partial\xi'}+h\frac{\partial V_2}{\partial\eta'}+V_2\frac{\partial h}{\partial\eta'}+h^2\frac{\partial V_3}{\partial\zeta'}=0 \quad . \tag{A.29}$$

Solving for the term involving a derivative of V_2 gives

$$\frac{\partial V_2}{\partial\eta'}=-\frac{\partial V_1}{\partial\xi'}-V_1\frac{1}{h}\frac{\partial h}{\partial\xi'}-V_2\frac{1}{h}\frac{\partial h}{\partial\eta'}-h\frac{\partial V_3}{\partial\zeta'} \quad . \tag{A.30}$$

Now multiply (A.30) by $(1/h)\Omega_1$ to give

$$\frac{1}{h}\Omega_1\frac{\partial V_2}{\partial\eta'}=-\frac{1}{h}\Omega_1\frac{\partial V_1}{\partial\xi'}-\frac{1}{h^2}\Omega_1V_1\frac{\partial h}{\partial\xi'}-\frac{1}{h^2}\Omega_1V_2\frac{\partial h}{\partial\eta'}-\Omega_1\frac{\partial V_3}{\partial\zeta'} \quad , \tag{A.31}$$

which will allow elimination of the corresponding term in (A.24). Note that as a bi-product, other terms are eliminated in (A.24) as well. Similarly multiply (A.30) by $h\Omega_3$ to give

$$h\Omega_3\frac{\partial V_2}{\partial\eta'}=-h\Omega_3\frac{\partial V_1}{\partial\xi'}-V_1\Omega_3\frac{\partial h}{\partial\xi'}-V_2\Omega_3\frac{\partial h}{\partial\eta'}-h^2\Omega_3\frac{\partial V_3}{\partial\zeta'} \quad , \tag{A.32}$$

which allows elimination of the corresponding term in (A.25).

The solenoidality condition in contravariant coordinates is given by

$$\nabla\cdot\vec{\Omega}=\frac{1}{h^2}\left\{\frac{\partial}{\partial\xi'}\left(\Omega_1\right)+\frac{\partial}{\partial\eta'}\left(\Omega_2\right)+\frac{\partial}{\partial\zeta'}\left(h^2\Omega_3\right)\right\}=0 \quad . \tag{A.33}$$

Expanding the derivatives in this equation and solving for the term that involves the second component of vorticity, Ω_2, gives

$$\frac{\partial \Omega_2}{\partial \eta'} = -\frac{\partial \Omega_1}{\partial \xi'} - h^2 \frac{\partial \Omega_3}{\partial \zeta'} \quad . \tag{A.34}$$

Multiplying (A.34) by $(-1/h)V_1$ gives

$$-\frac{1}{h} V_1 \frac{\partial \Omega_2}{\partial \eta'} = \frac{1}{h} V_1 \frac{\partial \Omega_1}{\partial \xi'} + h V_1 \frac{\partial \Omega_3}{\partial \zeta'} \quad , \tag{A.35}$$

which will allow elimination of the corresponding term in (A.24). In addition, differentiating (A.34) with respect to ξ' and multiplying by $(-1/h^2)$ gives

$$-\frac{1}{h^2} \frac{\partial^2 \Omega_2}{\partial \xi' \partial \eta'} = \frac{1}{h^2} \frac{\partial^2 \Omega_1}{\partial \xi'^2} + \frac{2}{h} \frac{\partial \Omega_3}{\partial \zeta'} \frac{\partial h}{\partial \xi'} + \frac{\partial^2 \Omega_3}{\partial \xi' \partial \zeta'} \quad , \tag{A.36}$$

which will allow the elimination of terms in (A.24) which are multiplied by the inverse of the Reynolds number. Note once again that, as a bi-product, a fortuitous elimination of other mixed derivatives is achieved. Multiplying (A.34) by $-V_3$ gives

$$-V_3 \frac{\partial \Omega_2}{\partial \eta'} = V_3 \frac{\partial \Omega_1}{\partial \xi'} + h^2 V_3 \frac{\partial \Omega_3}{\partial \zeta'} \quad , \tag{A.37}$$

which will allow elimination of the corresponding term in (A.25). In addition, differentiating (A.34) with respect to ζ' and multiplying by -1 gives

$$-\frac{\partial^2 \Omega_2}{\partial \eta' \partial \zeta'} = \frac{\partial^2 \Omega_1}{\partial \xi' \partial \zeta'} + h^2 \frac{\partial^2 \Omega_3}{\partial \zeta'^2} \quad , \tag{A.38}$$

which will allow elimination terms in (A.25) which are multiplied by the inverse of the Reynolds number.

The net result of this section is that (A.31), (A.35) and (A.36) are applied to (A.24) while (A.32), (A.37) and (A.38) are applied to (A.25). When this is done the resulting equations are

$$\frac{\partial \Omega_1}{\partial t}-\frac{2}{h^2}V_2\Omega_1\frac{\partial h}{\partial \eta'}+\frac{1}{h}V_2\frac{\partial \Omega_1}{\partial \eta'}+\frac{1}{h^2}V_1\Omega_2\frac{\partial h}{\partial \eta'}+\frac{1}{h}V_1\frac{\partial \Omega_1}{\partial \xi'}-\frac{1}{h}\Omega_2\frac{\partial V_1}{\partial \eta'}$$
$$+V_3\frac{\partial \Omega_1}{\partial \zeta'}-h\Omega_3\frac{\partial V_1}{\partial \zeta'}-\frac{1}{h}\Omega_1\frac{\partial V_1}{\partial \xi'}-\frac{1}{h^2}\Omega_1V_1\frac{\partial h}{\partial \xi'}=Re^{-1}\left(\frac{1}{h^2}\frac{\partial^2\Omega_1}{\partial \eta'^2}\right. \quad \text{(A.39)}$$
$$\left.-\frac{2}{h^3}\frac{\partial \Omega_1}{\partial \eta'}\frac{\partial h}{\partial \eta'}+\frac{2}{h^3}\frac{\partial \Omega_2}{\partial \xi'}\frac{\partial h}{\partial \eta'}+\frac{\partial^2\Omega_1}{\partial \zeta'^2}+\frac{1}{h^2}\frac{\partial^2\Omega_1}{\partial \xi'^2}+\frac{2}{h}\frac{\partial \Omega_3}{\partial \zeta'}\frac{\partial h}{\partial \xi'}\right) \ ,$$

for Ω_1 and

$$h^2\frac{\partial \Omega_3}{\partial t}+hV_1\frac{\partial \Omega_3}{\partial \xi'}-\Omega_1\frac{\partial V_3}{\partial \xi'}+hV_2\frac{\partial \Omega_3}{\partial \eta'}-\Omega_2\frac{\partial V_3}{\partial \eta'}+h^2V_3\frac{\partial \Omega_3}{\partial \zeta'}-h^2\Omega_3\frac{\partial V_3}{\partial \zeta'}$$
$$=Re^{-1}\left(\frac{\partial^2\Omega_3}{\partial \xi'^2}+\frac{\partial^2\Omega_3}{\partial \eta'^2}+h^2\frac{\partial^2\Omega_3}{\partial \zeta'^2}\right) \ , \quad \text{(A.40)}$$

for Ω_3 .

Transformation for The Roughness Shape

The transformation to incorporate the roughness via the Prandtl transposition is

$$\xi=\xi' \ , \quad \eta=\eta'-f(\xi,\zeta) \quad \text{and} \quad \zeta=\zeta' \ . \quad \text{(A.41)}$$

Applying this transformation to the vorticity transport equations gives

$$h^2\frac{\partial \Omega_1}{\partial t}-2V_2\Omega_1\frac{\partial h}{\partial \eta'}+hV_2\frac{\partial \Omega_1}{\partial \eta}+V_1\Omega_2\frac{\partial h}{\partial \eta'}+hV_1\frac{\partial \Omega_1}{\partial \xi}-hf_\xi V_1\frac{\partial \Omega_1}{\partial \eta}$$
$$-h\Omega_2\frac{\partial V_1}{\partial \eta}+h^2V_3\frac{\partial \Omega_1}{\partial \zeta}-h^2f_\zeta V_3\frac{\partial \Omega_1}{\partial \eta}-h^3\Omega_3\frac{\partial V_1}{\partial \zeta}+h^3f_\zeta\Omega_3\frac{\partial V_1}{\partial \eta}$$
$$-h\Omega_1\frac{\partial V_1}{\partial \xi}+hf_\xi\Omega_1\frac{\partial V_1}{\partial \eta}-\Omega_1V_1\frac{\partial h}{\partial \xi'}=Re^{-1}\left(-\left[\frac{2}{h}\frac{\partial h}{\partial \eta'}+f_{\xi\xi}+h^2f_{\zeta\zeta}\right]\frac{\partial \Omega_1}{\partial \eta}\right. \quad \text{(A.42)}$$
$$+\left[\left(1+f_\xi^2\right)+h^2f_\zeta^2\right]\frac{\partial^2\Omega_1}{\partial \eta^2}+\frac{\partial^2\Omega_1}{\partial \xi^2}+h^2\frac{\partial^2\Omega_1}{\partial \zeta^2}+\frac{2}{h}\frac{\partial \Omega_2}{\partial \xi}\frac{\partial h}{\partial \eta'}$$
$$\left.-\frac{2}{h}f_\xi\frac{\partial \Omega_2}{\partial \eta}\frac{\partial h}{\partial \eta'}+2\mathrm{h}\frac{\partial \Omega_3}{\partial \zeta}\frac{\partial h}{\partial \xi'}-2\mathrm{h}f_\zeta\frac{\partial \Omega_3}{\partial \eta}\frac{\partial h}{\partial \xi'}-2f_\xi\frac{\partial^2\Omega_1}{\partial \xi\partial \eta}-2h^2f_\zeta\frac{\partial^2\Omega_1}{\partial \eta\partial \zeta}\right)$$

for Ω_1 and

$$
\begin{aligned}
&h^2\frac{\partial \Omega_3}{\partial t}+hV_1\frac{\partial \Omega_3}{\partial \xi}-hf_\xi V_1\frac{\partial \Omega_3}{\partial \eta}-\Omega_1\frac{\partial V_3}{\partial \xi}+f_\xi\Omega_1\frac{\partial V_3}{\partial \eta}+hV_2\frac{\partial \Omega_3}{\partial \eta}\\
&-\Omega_2\frac{\partial V_3}{\partial \eta}+h^2V_3\frac{\partial \Omega_3}{\partial \zeta}-h^2f_\zeta V_3\frac{\partial \Omega_3}{\partial \eta}-h^2\Omega_3\frac{\partial V_3}{\partial \zeta}+h^2f_\zeta\Omega_3\frac{\partial V_3}{\partial \eta}\\
&=Re^{-1}\left(\frac{\partial^2\Omega_3}{\partial\xi^2}+\left(1+f_\xi^2+h^2f_\zeta^2\right)\frac{\partial^2\Omega_3}{\partial\eta^2}+h^2\frac{\partial^2\Omega_3}{\partial\zeta^2}-\left(f_{\xi\xi}+h^2f_{\zeta\zeta}\right)\frac{\partial\Omega_3}{\partial\eta}\right.\\
&\qquad\left.-2f_\xi\frac{\partial^2\Omega_3}{\partial\xi\,\partial\eta}-2h^2f_\zeta\frac{\partial^2\Omega_3}{\partial\eta\,\partial\zeta}\right)\quad .
\end{aligned}
\tag{A.43}
$$

for Ω_3. Applying the transformation to (A.26) gives

$$
\begin{aligned}
\Omega_1=&\frac{-2}{h^3}\frac{\partial\Theta}{\partial\eta}\frac{\partial h}{\partial\eta'}+\frac{1}{h^2}\frac{\partial^2\Theta}{\partial\eta^2}+\frac{\partial^2\Theta}{\partial\zeta^2}+f_\zeta^2\frac{\partial^2\Theta}{\partial\eta^2}-f_{\zeta\zeta}\frac{\partial\Theta}{\partial\eta}-2f_\zeta\frac{\partial^2\Theta}{\partial\eta\,\partial\zeta}\\
&-f_\zeta\frac{\partial^2\Psi}{\partial\xi\,\partial\eta}+\frac{\partial^2\Psi}{\partial\xi\,\partial\zeta}+f_\xi f_\zeta\frac{\partial^2\Psi}{\partial\eta^2}-f_\xi\frac{\partial^2\Psi}{\partial\eta\,\partial\zeta}-f_{\xi\zeta}\frac{\partial\Psi}{\partial\eta}\quad ,
\end{aligned}
$$

$$
\Omega_2=\frac{\partial^2\Psi}{\partial\eta\,\partial\zeta}-f_\zeta\frac{\partial^2\Psi}{\partial\eta^2}+\frac{2}{h^3}\frac{\partial\Theta}{\partial\eta}\frac{\partial h}{\partial\xi'}-\frac{1}{h^2}\frac{\partial^2\Theta}{\partial\xi\,\partial\eta}+f_\xi\frac{1}{h^2}\frac{\partial^2\Theta}{\partial\eta^2}
\tag{A.44}
$$

$$
\begin{aligned}
\text{and}\quad -h^2\Omega_3=&\frac{\partial^2\Psi}{\partial\eta^2}+\frac{\partial^2\Psi}{\partial\xi^2}+f_\xi^2\frac{\partial^2\Psi}{\partial\eta^2}-f_{\xi\xi}\frac{\partial\Psi}{\partial\eta}-2f_\xi\frac{\partial^2\Psi}{\partial\xi\,\partial\eta}\\
&-f_\zeta\frac{\partial^2\Theta}{\partial\xi\,\partial\eta}+\frac{\partial^2\Theta}{\partial\xi\,\partial\zeta}+f_\xi f_\zeta\frac{\partial^2\Theta}{\partial\eta^2}-f_\xi\frac{\partial^2\Theta}{\partial\eta\,\partial\zeta}-f_{\xi\zeta}\frac{\partial\Theta}{\partial\eta}\quad .
\end{aligned}
$$

The relationship between the velocity vector and the stream-like functions is

$$
\vec{V}=\frac{1}{h}\left[\frac{\partial\Psi}{\partial\eta}+\frac{\partial\bar{\psi}}{\partial\eta'}\right]\hat{e}_1+\frac{1}{h}\left[-\frac{\partial\Theta}{\partial\zeta}+f_\zeta\frac{\partial\Theta}{\partial\eta}-\frac{\partial\Psi}{\partial\xi}+f_\xi\frac{\partial\Psi}{\partial\eta}-\frac{\partial\bar{\psi}}{\partial\xi'}\right]\hat{e}_2+\frac{1}{h^2}\frac{\partial\Theta}{\partial\eta}\hat{e}_3\quad .
\tag{A.45}
$$

The velocity derivatives present in (A.42) and (A.43) can be evaluated using (A.45) such that the vorticity transport equations are written entirely in terms of the vorticity components and the stream-like functions. It can be shown that these derivatives are given by

$$
\frac{\partial V_1}{\partial\xi}=\frac{-1}{h}V_1\left(\frac{\partial h}{\partial\xi'}+f_\xi\frac{\partial h}{\partial\eta'}\right)+\frac{1}{h}\left[\frac{\partial^2\Psi}{\partial\xi\,\partial\eta}+\frac{\partial^2\bar{\psi}}{\partial\xi'\,\partial\eta'}+f_\xi\frac{\partial^2\bar{\psi}}{\partial\eta'^2}\right]\quad ,
\tag{A.46}
$$

$$\frac{\partial V_1}{\partial \eta}=\frac{-1}{h}V_1\frac{\partial h}{\partial \eta'}+\frac{1}{h}\left[\frac{\partial^2 \Psi}{\partial \eta^2}+\frac{\partial^2 \bar{\psi}}{\partial \eta'^2}\right] \quad , \tag{A.47}$$

$$\frac{\partial V_1}{\partial \zeta}=\frac{-1}{h}f_\zeta V_1\frac{\partial h}{\partial \eta'}+\frac{1}{h}\left[\frac{\partial^2 \Psi}{\partial \eta \partial \zeta}+f_\zeta\frac{\partial^2 \bar{\psi}}{\partial \eta'^2}\right] \quad , \tag{A.48}$$

$$\frac{\partial V_3}{\partial \xi}=\frac{-2}{h}V_3\left(\frac{\partial h}{\partial \xi'}+f_\xi\frac{\partial h}{\partial \eta'}\right)+\frac{1}{h^2}\frac{\partial^2 \Theta}{\partial \xi \partial \eta} \quad , \tag{A.49}$$

$$\frac{\partial V_3}{\partial \eta}=\frac{-2}{h}V_3\frac{\partial h}{\partial \eta'}+\frac{1}{h^2}\frac{\partial^2 \Theta}{\partial \eta^2} \tag{A.50}$$

$$\text{and} \quad \frac{\partial V_3}{\partial \zeta}=-\frac{2}{h}f_\zeta V_3\frac{\partial h}{\partial \eta'}+\frac{1}{h^2}\frac{\partial^2 \Theta}{\partial \eta \partial \zeta} \quad . \tag{A.51}$$

Transformation for The Grid Stretching

The last transformation is application of the one-dimensional grid stretching laws in each of the three coordinate directions. This transformation is given by

$$\bar{\xi}=f_1(\xi) \quad , \quad \bar{\eta}=f_2(\eta) \quad \text{and} \quad \bar{\zeta}=f_3(\zeta) \quad . \tag{A.52}$$

The stretching transformations alter the various terms in one direction only. For example, a first order derivative is transformed by

$$\frac{\partial \Psi}{\partial \xi}=\frac{\partial \bar{\xi}}{\partial \xi}\frac{\partial \Psi}{\partial \bar{\xi}} \quad , \tag{A.53}$$

and a mixed derivative is transformed by

$$\frac{\partial^2 \Psi}{\partial \xi \partial \eta}=\frac{\partial \bar{\xi}}{\partial \xi}\frac{\partial \bar{\eta}}{\partial \eta}\frac{\partial^2 \Psi}{\partial \bar{\xi} \partial \bar{\eta}} \quad . \tag{A.54}$$

The only additional terms in the governing equations are introduced by second order derivatives of the same coordinate direction. For example

$$\frac{\partial^2 \Psi}{\partial \xi^2} = \left(\frac{\partial \bar{\xi}}{\partial \xi}\right)^2 \frac{\partial^2 \Psi}{\partial \bar{\xi}^2} - \frac{\partial^2 \bar{\xi}}{\partial \xi^2} \frac{\partial \Psi}{\partial \bar{\xi}} \quad . \tag{A.55}$$

Therefore the governing equations are relatively unchanged from the previous section and will not be repeated here.

Boundary Conditions

At the surface, a no-slip boundary condition is applied which requires setting each component of (A.45) to zero. The result is

$$\Psi = -\bar{\psi} \quad \text{and} \quad \frac{\partial \Psi}{\partial \eta} = -\frac{\partial \bar{\psi}}{\partial \eta'} \tag{A.56}$$

for Ψ and

$$\Theta = \frac{\partial \Theta}{\partial \eta} = 0 \tag{A.57}$$

for Θ. The derivation of these equations is given in Chapter 3. (A.56) and (A.57) allow the evaluation of any derivative in the wall-normal direction for either Ψ or Θ terms. For example, the second order wall-normal derivative of Ψ is

$$\frac{\partial^2 \Psi}{\partial \eta^2} = \left(\frac{\partial \bar{\eta}}{\partial \eta}\right)^2 \frac{\partial^2 \Psi}{\partial \bar{\eta}^2} - \frac{\partial^2 \bar{\eta}}{\partial \eta^2} \frac{\partial \Psi}{\partial \bar{\eta}} \quad . \tag{A.58}$$

Using the second equation in (A.56) and applying a second order central difference at the wall gives

$$\frac{\Psi_{i2k} - \Psi_{i0k}}{2\Delta \bar{\eta}} = \left(\frac{\partial \bar{\eta}}{\partial \eta}\right)^{-1} \frac{\partial \bar{\psi}}{\partial \eta'} \quad , \tag{A.59}$$

or solving for the "fictitious" point below the surface gives

$$\Psi_{i0k} = \Psi_{i2k} - 2\Delta \bar{\eta} \left(\frac{\partial \bar{\eta}}{\partial \eta}\right)^{-1} \frac{\partial \bar{\psi}}{\partial \eta'} \quad . \tag{A.60}$$

Applying a second order central difference at the surface to (A.58) gives

$$\frac{\partial^2 \Psi}{\partial \eta^2} = \left(\frac{\partial \bar{\eta}}{\partial \eta}\right)^2 \frac{\Psi_{i2k} - 2\Psi_{i1k} + \Psi_{i0k}}{(\Delta \bar{\eta})^2} - \frac{\partial^2 \bar{\eta}}{\partial \eta^2} \frac{\Psi_{i2k} - \Psi_{i0k}}{2\Delta \bar{\eta}} \quad . \tag{A.61}$$

Substituting (A.60) into (A.61) gives

$$\frac{\partial^2 \Psi}{\partial \eta^2} = \left(\frac{\partial \bar{\eta}}{\partial \eta}\right)^2 \frac{2\Psi_{i2k} - 2\Psi_{i1k}}{(\Delta \bar{\eta})^2} - \frac{2}{\Delta \bar{\eta}} \frac{\partial \bar{\eta}}{\partial \eta} \frac{\partial \bar{\psi}}{\partial \eta'} - \frac{\partial^2 \bar{\eta}}{\partial \eta^2} \left(\frac{\partial \bar{\eta}}{\partial \eta}\right)^{-1} \frac{\partial \bar{\psi}}{\partial \eta'} \quad . \tag{A.62}$$

Thus any wall-normal derivative can be evaluated in terms of known quantities at grid points at or adjacent to the surface. A similar expression can be developed for the second derivative of Θ at the wall,

$$\frac{\partial^2 \Theta}{\partial \eta^2} = \left(\frac{\partial \bar{\eta}}{\partial \eta}\right)^2 \frac{2\Theta_{i2k} - 2\Theta_{i1k}}{(\bar{\eta})^2} \quad . \tag{A.63}$$

These expressions can be substituted for the appropriate terms in (A.44) in order to be able to evaluate the vorticity components at the surface.

At the η far-field the two-dimensional potential flow solution is recovered. This is accomplished by eliminating any streamwise or spanwise velocity components that would not be present in the pure potential flow, that is

$$\frac{\partial \Psi}{\partial \eta} = \frac{\partial \Theta}{\partial \eta} = 0 \quad . \tag{A.64}$$

Therefore, at the η far-field the velocity components, (A.45), have the form

$$\vec{V} = \frac{1}{h} \frac{\partial \bar{\psi}}{\partial \eta'} \hat{e}_1 + \frac{1}{h} \left[-\frac{\partial \Theta}{\partial \zeta} - \frac{\partial \Psi}{\partial \xi} - \frac{\partial \bar{\psi}}{\partial \xi'} \right] \hat{e}_2 + 0\, \hat{e}_3 \quad . \tag{A.65}$$

Note that there are components of the wall-normal velocity component, V_2, in (A.65) which are not part of the potential flow solution. This allows the possibility of flow displacement due to the presence of the roughness. Since the flow at the η far-field is a potential flow

solution there is no vorticity, therefore

$$\Omega_1=\Omega_2=\Omega_3=0 \quad . \tag{A.66}$$